2018

Bio-Functionalized Graphene Field-Effect Transistors For The Detection Of Nucleic Acids And Drug Targets

Ramya Vishnubhotla
University of Pennsylvania, rvi@sas.upenn.edu

Bio-Functionalized Graphene Field-Effect Transistors For The Detection Of Nucleic Acids And Drug Targets

Abstract

The need for scalable, rapid, sensitive, label-free detection of small biomolecules and chemicals such as proteins, nucleic acids or market drugs is central to the field of biomolecular and chemical sensing. Detection of these biomolecules and chemicals is relevant for early disease diagnostics and therapeutic drug monitoring to prolong lifespans, treat patients in a brief timeframe, and decrease medical costs. Various ailments, such as cancers, are the source of up-regulation or down-regulation of certain biomolecules, or "biomarkers" in human fluids, and are indicative of the presence of the disease when compared to human fluids from a healthy subject. By detecting these biomarkers in low concentrations, or by tracking their change in concentration in human samples, scientists could create an effective early disease diagnostics tool that would be used at the point-of-care. In parallel, detection of market drugs in human samples could replace the need for more expensive and time-consuming analytical techniques such as liquid chromatography-mass spectrometry (LC-MS).

The work presented here explores the necessary proof-of-concept for the creation of point-of-care devices for medical diagnostics and therapeutic drug monitoring. It details the process of synthetic nucleic acid detection down to attomolar concentrations, the detection of single base-pair mismatches in nucleic acid strands, and drug target detection in concentrations (1-10 ng/mL) far less than those found in human fluid, the latter for the purpose of therapeutic drug monitoring or "drug compliance" testing. Such sensitivity could only be achieved with the nanomaterial graphene, a two-dimensional allotrope of carbon with the highest electron mobility at room temperature of any material currently known, and with exceptional robustness and biocompatibility. The work here is based on the use of graphene field-effect transistors, or GFETs, for nucleic acid and drug target sensing, and further explores the various uses of graphene for protein and pH sensing, as well as binding of protein-nanoparticle assemblies and neuropeptide-receptor binding, through either rigid or flexible substrates.

Degree Type
Dissertation

Degree Name
Doctor of Philosophy (PhD)

Graduate Group
Physics & Astronomy

First Advisor
Alan T. Johnson

Keywords
biosensing, field-effect transistor, graphene, nanomaterials, ssDNA

Subject Categories
Condensed Matter Physics | Nanoscience and Nanotechnology | Physics

BIO-FUNCTIONALIZED GRAPHENE FIELD-EFFECT TRANSISTORS FOR THE DETECTION OF NUCLEIC ACIDS AND DRUG TARGETS

Ramya Vishnubhotla

A DISSERTATION

in

Physics and Astronomy

Presented to the Faculties at the University of Pennsylvania

in

Partial Fulfillment of the Requirements for the Degree of

Doctor of Philosophy

2018

Supervisor of Dissertation

_____

A.T. Charlie Johnson, Professor, Department of Physics & Astronomy.

Graduate Group Chairperson

_____

Joshua Klein, Professor, Department of Physics & Astronomy.

Dissertation Committee

Lee Bassett, Assistant Professor, Department of Electrical & Systems Engineering.

Charles Kane, Christopher H. Browne Distinguished Professor, Department of Physics and Astronomy.

Justin Khoury, Professor and Undergraduate Chair, Department of Physics & Astronomy.

Alison Sweeney, Assistant Professor, Department of Physics and Astronomy.

BIO-FUNCTIONALIZED GRAPHENE FIELD-EFFECT TRANSISTORS FOR THE DETECTION

OF NUCLEIC ACIDS AND DRUG TARGETS

COPYRIGHT

2018

Ramya Vishnubhotla

Above all, for Ammamma, the toughest woman I know.

And for Thatha, a physicist that I never got to discuss physics with.

Acknowledgements

Firstly, I would like to thank my thesis advisor, Dr. A.T. Charlie Johnson, without whom this work would not have been possible. Charlie's mentoring provided me with the freedom to pursue projects that interested me, in the timeframe that I needed, and whichever hours I chose to work. This has allowed me to become an independent scientist, and I am grateful for the experience to have learned on my own and from others in the lab, and develop my research preferences as a physicist throughout my graduate career.

I would like to thank Dr. Jinglei Ping, my graduate school mentor, for teaching me so much about graphene, its functionalization, the physics and chemistry of nucleic acid detection, and, arguably most important: data analysis. Without Jinglei's mentorship, I would not be ready to graduate at this time, nor would I feel confident to proceed to the next step in my career. A thank you must also be extended to current and former group members: to Dr. Pedro Ducos and Dr. Madeline Diaz-Serrano, for teaching me graphene growth and graphene field effect transistor fabrication; to Dr. Zhaoli Gao, for his assistance and further mentorship concerning basically everything from data analysis to device fabrication troubleshooting; to Dr. Nicholas Kybert and Dr. Carl Naylor for always making me laugh, calming me down when I was stressed, and for willingly discussing project ideas with me, and to Dr. Mitchell Lerner, for convincing me to join this lab five years ago. I have never once regretted the decision.

It is crucial that I also acknowledge the work put in by the students I have mentored: undergraduates Amey Vrudhula, Kelsey Steinke, Abigail Lee, Olivia Saouaf, Adithya

My sincerest gratitude to the many family members who have made this possible. To my father, Dr. Lakshmanna Vishnubhotla, for giving me an education, and for teaching me the value of one; to my mother, Kalyani Vishnubhotla, for her emotional support and reliability; to my brother, Anooj Vishnubhotla, for being my closest ally in both childhood and adulthood; to my boyfriend, Matthew Neder, for his love, and to the countless cousins, aunts and uncles, nieces and nephews in my extended family, for all the long phone conversations and gatherings, which have further reminded me how important family is, and have put my graduate school hardships into perspective.

A huge thank you to my friends, both near and far: Inayat Bajwa, Leigh Schaefer, Christina Krawiec, Laasya Madduri, Rekha Roarty, Shruthi Baskaran, Ben Heidorn, Rachel Chin, Christopher Kehayias, Christoph Kammer, Antoine Galand, Meet Vora, Rajatesh Gudibande (and many more), for their friendship inside and outside of the lab, which has gotten me through some very stressful days.

Thank you to the wonderful and talented women and men, instructors and students at Balance MMA, and to my boxing coach, Carlos Mainor, all for teaching me how to fight, and providing me with peace of mind and confidence.

Last but certainly not least, thank you to my high school physics teachers, Mark and Nancy Misage at Westlake High School in Austin, Texas, for making me fall in love with physics in the first place.

ABSTRACT

BIO-FUNCTIONALIZED GRAPHENE FIELD-EFFECT TRANSISTORS FOR THE DETECTION OF NUCLEIC ACIDS AND DRUG TARGETS

Ramya Vishnubhotla

A.T. Charlie Johnson

The need for scalable, rapid, sensitive, label-free detection of small biomolecules and chemicals such as proteins, nucleic acids or market drugs is central to the field of biomolecular and chemical sensing. Detection of these biomolecules and chemicals is relevant for early disease diagnostics and therapeutic drug monitoring to prolong lifespans, treat patients in a brief timeframe, and decrease medical costs. Various ailments, such as cancers, are the source of up-regulation or down-regulation of certain biomolecules, or "biomarkers" in human fluids, and are indicative of the presence of the disease when compared to human fluids from a healthy subject. By detecting these biomarkers in low concentrations, or by tracking their change in concentration in human samples, scientists could create an effective early disease diagnostics tool that would be used at the point-of-care. In parallel, detection of market drugs in human samples could replace the need for more expensive and time-consuming analytical techniques such as liquid chromatography-mass spectrometry (LC-MS).

The work presented here explores the necessary proof-of-concept for the creation of point-of-care devices for medical diagnostics and therapeutic drug monitoring. It details

the process of synthetic nucleic acid detection down to attomolar concentrations, the detection of single base-pair mismatches in nucleic acid strands, and drug target detection in concentrations (1-10 ng/mL) far less than those found in human fluid, the latter for the purpose of therapeutic drug monitoring or "drug compliance" testing. Such sensitivity could only be achieved with the nanomaterial graphene, a two-dimensional allotrope of carbon with the highest electron mobility at room temperature of any material currently known, and with exceptional robustness and biocompatibility. The work here is based on the use of graphene field-effect transistors, or GFETs, for nucleic acid and drug target sensing, and further explores the various uses of graphene for protein and pH sensing, as well as binding of protein-nanoparticle assemblies and neuropeptide-receptor binding, through either rigid or flexible substrates.

Keywords: *graphene, field-effect transistor, ssDNA, biosensing, nanomaterials*

Table of Contents

List of Figures

List of Tables

Chapter 1: Overview of Thesis

Since the discovery of graphene, the research surrounding it has expanded from its characterization and the study of its physical properties to the application of the nanomaterial for various sensing endeavors. Graphene related research is particularly exciting because of the unique properties of the material, including high sensitivity and robustness which make it an excellent candidate for the detection of biomolecular and chemical targets through a scalable methodology. Benefits of such sensitive detection reach beyond academia and create promise in the fields of engineering and medical diagnostics.

It has been shown that the change in concentration of certain biomolecules, such as nucleic acids, proteins, or volatile organic compounds (VOCs) can up-regulate or down-regulate in human fluids when a patient suffers from a specific ailment. The change in concentration of these "biomarkers", as they are called, is indicative of the presence of the disease and their detection could serve as an inexpensive, rapid method for early disease diagnostics. This could lead to prolonging lifespans for diseases such as pancreatic cancer or ovarian cancer, for which there are currently no standard early-detection methods. Consequentially, patients suffering from these diseases are generally not diagnosed until the late stages of the cancer, leading to a low survival rate and sometimes, high medical bills.

Through the detection of market drugs for therapeutic drug monitoring, these devices have the potential to replace current analytical techniques, such as gas/liquid chromatography-mass spectrometry (GC-MS, LC-MS), which are expensive and time-

consuming. Therefore, the research surrounding the development of scalable devices that aim to address these clinical issues through low-concentration detection is essential not just for the advancement of science and engineering, but for modern medicine as well.

The work presented in this thesis focuses on the proof-of-concept of graphene field-effect transistors for the detection of nucleic acids and drug targets in addition to employing it as a sensing medium for protein detection, pH sensing, protein-nanoparticle assembly detection, and measuring neuropeptide-receptor binding, all as initial steps for eventual disease diagnostics or drug detection in human samples that could be used at the point-of-care.

The technical background details of nanomaterials are found in Chapter 2, which describes the properties of low-dimensional materials. Beginning with graphene, this chapter explains why physicists believed it couldn't exist in a thermodynamically stable form before discussing its eventual discovery and superior electronic properties. Later, this chapter touches on other low-dimensional materials, such as transition metal dichalcogenides (TMDs) and carbon nanotubes (CNTs) as sensing-medium alternatives to graphene. This chapter also discusses the insulator, hexagonal boron nitride (hBN), which can be paired with graphene or TMDs to block interactions with dangling bonds on a SiO_2 substrate, or act as a protective layer from photoresist contamination during device fabrication. Each of these alternative nanomaterials is appealing and has its own exclusive characteristics, but none of them are as effective for sensing as graphene, which is central to this thesis.

Chapter 3 describes the graphene growth, transfer and characterization processes. Graphene was grown *via* chemical vapor deposition in-lab on a copper foil substrate and

transferred using an electrolysis bubbling method. Raman spectroscopy verified the high-quality nature of the low-defect, monolayer graphene, and atomic force microscopy (AFM) determined the surface-cleanliness and height of the sample. Optical microscopy confirmed the continuous nature of the film. This chapter ends with how field-effect transistors operate and are measured.

In Chapter 4, the fabrication method of these field-effect transistors is explained, which includes photolithography, thermal evaporation and oxygen plasma etching. Later in this chapter, the cleaning, surface chemistry and functionalization steps are described, followed by data collection and analysis of the sensors.

Chapter 5 illustrates some of the uses of graphene FETs for nucleic acid detection and market drug detection. Here, it is shown that GFETs are adept at detecting ssDNA down to concentrations of 1 fM and later, 1 aM, as well as being able to detect single base pair mismatches between probe and target DNA strands. Furthermore, GFETs demonstrate detection of a long target strand (100 nucleotides) with a short probe (20 nucleotides). Next, this chapter discusses graphene aptasensors for the detection of market drugs, such as the HIV treatment market drug tenofovir, as well as an azole class antifungal drug. The purpose of these graphene aptasensors is for therapeutic drug monitoring, or, in other words, drug compliance, at the point of care. The benefit is the potential to serve as a replacement for more laborious lab techniques, such as liquid chromatography-mass spectrometry (LC-MS), which are expensive, time-consuming and require the employment of highly-skilled lab technicians. These graphene aptasensors detected drug concentrations down to ~1 ng/mL for tenofovir and ~ 10 ng/mL for the azole antifungal drug, both of which are much lower than what is found in the human body.

Chapter 6 discusses the uses of graphene sensors for the detection of other biomolecules, such as the protein HER3, which is a biomarker for breast cancer, flexile graphene devices for pH sensing in complex fluids, graphene devices for protein-nanoparticle assembly detection and graphene devices for measuring the binding between neuropeptides and their receptors. Each of these projects explores new uses for graphene and its ability for sensing.

Chapter 7 concludes this work and gives an overview of the thesis and the type of projects that can develop from moving forward in this field of research, including the impact this type of research could make on various fields beyond science and engineering, such as healthcare and its associated costs.

Chapter 8 gives some background information about the thesis dedication.

Chapter 2: Graphene Discovery, Properties, and Beyond Graphene

Low-dimension materials such as graphene, transition metal dichalcogenides (TMDs), and carbon nanotubes (CNTs) show promise for the development of novel, scalable, and point-of-care biosensors and chemical sensors due to high electron mobility, superior sensitivity, and biocompatibility when compared with more traditional device channels like silicon or gallium arsenide.

Section 2.1 of this chapter discusses why theorists believed graphene could not exist in a stable form, followed by the discovery of graphene in 2004 by Geim and Novoselov through a method known as mechanical exfoliation. This discovery was a significant breakthrough in condensed matter physics, and motivated scientists to study graphene in addition to other novel 2D materials. This section also explains the methods for acquiring graphene through both mechanical exfoliation and chemical vapor deposition (CVD), including the benefits of CVD graphene over exfoliated graphene for scalable sensors.

Section 2.2 is dedicated to the properties of graphene, most notably its lack of a band gap, its high electron mobility, and its sensitivity. These qualities are what make graphene such a desirable material for low-concentration sensing.

In section 2.3, we briefly explore other low-dimension semiconducting nanomaterials, including transition metal dichalcogenides (TMDs) and carbon nanotubes (CNTs). While these materials do not possess the same sensitivity as graphene, their devices have their

own benefits, such as ease of fabrication and a band gap, and have been incorporated into various types of biomolecular and chemical sensors.

In section 2.4, we introduce a different 2D material, the insulator hexagonal boron nitride (hBN). This material has a very similar lattice structure compared to graphene, making it appropriate for stacking on top of or underneath graphene, either to serve as a screening layer from dangling bonds on a SiO_2 substrate, or atop graphene, as a protective layer against contamination. Additionally, it can also serve as a protective layer atop TMDs to prevent degradation in atmosphere.

2.1 Graphene Discovery, Exfoliated Graphene and CVD Graphene

Until recently, many two-dimensional (2D) materials were theorized but not explicitly studied, as they simply had not yet been discovered. The material that spurred the fascination with 2D materials was graphene, an allotrope of carbon of sp^2 hybridization, and, in more general terms, a single atomic layer of graphite, more commonly known as pencil lead. The structure of graphene consists of carbon atoms arranged in a continuous honeycomb lattice.

For years, graphene was said to be unstable in physical form due to its sensitivity to thermal fluctuations which were assumed to be so strong that they would displace atoms in the lattice[1,2]. However, in 2004, Geim and Novoselov at the University of Manchester proved this to be incorrect, and showed that a rigid substrate can provide stability for the graphene film. Interestingly, it was also discovered that graphene is visible to the naked eye provided a substrate of SiO_2 with a thickness of ~ 285nm [3].

The discovery of graphene has humble beginnings, and was done so through the "scotch-tape method", or "mechanical exfoliation" method, where Geim and Novoselov used store-bought scotch-tape and adhered it to the surface of graphite, removing a thin film. By repeatedly pulling apart this film into thinner and thinner films with the tape, they were able to isolate a single atomic layer of graphite in a stable form in small flakes[4]. Thus, graphene was born and its research expanded [5].

This breakthrough led to the Nobel prize in physics in 2010 for Geim and Novoselov, and a further boost in interest in the study of graphene. Since then, a second type of graphene

has garnered a great deal of attention, and that is chemical vapor deposition (CVD) graphene. In this form, graphene is "grown" on a metallic substrate in continuous, large-area sheets using a carbon gas source, high heat (~1000 C) and sometimes, low pressure[6,7].

Benefits and caveats exist for both exfoliated and CVD graphene. Exfoliated graphene is the most pristine, low-defect form of graphene available. Its mobilities can reach up to 10,000 cm^2/Vs on an oxidized silicon substrate [4], and as high as 200,000 cm^2/Vs when suspended[8], and takes minimal time to synthesize. Unfortunately, exfoliated graphene flakes are quite small (~ 1-100 μm), and as a result, it is difficult to achieve precise placement of them in application.

CVD graphene is wafer-scale, and can be grown in sheets of several square inches[9] (see Appendix A). Because of its large-area nature, the scientist has more control over her experiments and applications and can dictate the size and placement of the graphene film. This creates the possibility of scalable graphene devices, where the scalability factor is crucial for both applications and statistically relevant results. However, mobilities for CVD graphene are much lower compared to exfoliated graphene's, around 1,000-3,000 cm^2/Vs for good quality, monolayer CVD graphene devices[10,11]. This difference in quality is most likely from the formation of defects in the lattice during CVD growth, combined with exposure to chemicals during the transfer process, neither of which presents itself in mechanical exfoliation sample preparation. For more information on CVD graphene growth and transfer, please see Chapter 3. Various cleaning methods are employed to reduce the contamination for CVD devices, but are never able to achieve an

unadulterated state of the graphene. However, such challenges come with the territory of application.

Despite the limited uses of graphene outside of research, the material shows promise for future applications, on which this thesis sheds more light.

2.2 Properties of Graphene

Graphene, a 2D allotrope of carbon with sp^2 hybridization exists as a single atomic layer of carbon atoms arranged in a honeycomb lattice. Graphene's unit cell contains two atoms, making up the "A" and "B" sublattices, and it has a lattice constant of 2.46 angstroms (Å), a carbon-carbon bond length of $a = 1.42$Å, and its basis vectors (a_1, a_2) and reciprocal lattice vectors (b_1, b_2), written in terms of a are:

$$a_1 = \frac{a}{2}\left(3, \sqrt{3}\right) \quad a_2 = \frac{a}{2}\left(3, -\sqrt{3}\right) \tag{2.1}$$

$$b_1 = \frac{2\pi}{3a}\left(1, \sqrt{3}\right) \quad b_2 = \frac{2\pi}{3a}\left(1, -\sqrt{3}\right) \tag{2.2}$$

The two sublattices of the graphene structure can be seen in **Figure 2.2.1** [4]:
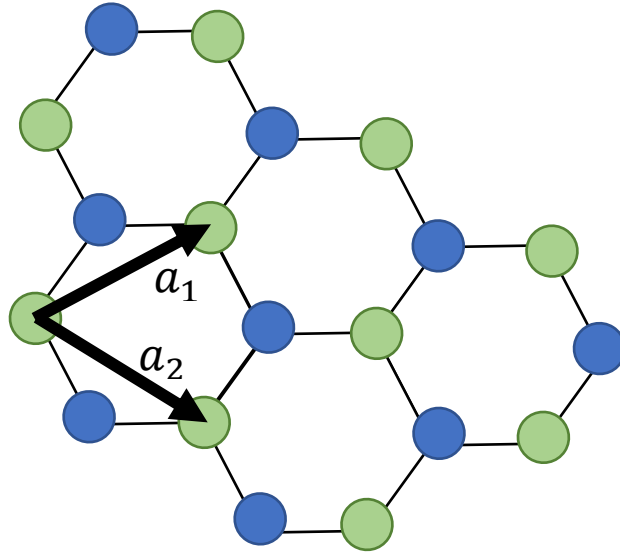
Fig 2.2.1 *Graphene honeycomb lattice showing basis vectors and separate sub-lattices in blue and green.*

To further understand the lattice of graphene and the properties that arise from it, **Figure 2.2.2** demonstrates the first Brillouin zone (FBZ) of graphene, which is defined as a primitive cell in reciprocal space, and can be found by drawing lines to the nearest neighbors of an atom and bisecting each of these lines perpendicularly to enclose the FBZ. There are a total of six points at the edge of the FBZ of graphene known as "Dirac points"[12], although only two differing values exist, labeled K and K' in **Figure 2.2.2**[13]. Their values are stated in **Equation 2.3**.
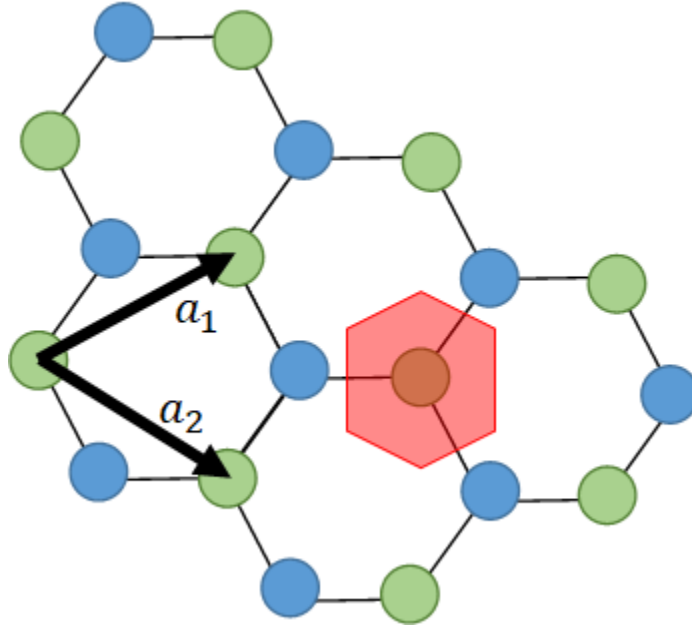
Figure 2.2.2. *First Brillouin zone (red) of the graphene honeycomb lattice, with 6 Dirac points. Of these six points, there are only two differing values, labeled as K and K'.*

$$K = \frac{2\pi}{3a}\left(1, \frac{1}{\sqrt{3}}\right) \quad K' = \frac{2\pi}{3a}\left(1, \frac{-1}{\sqrt{3}}\right) \qquad (2.3)$$

The values for K and K' are necessary for the tight binding model for graphene, which

represents the meeting of the valence and conduction band at these six Dirac points at the

edge of the FBZ, described by the following equation:

$$E = \pm\gamma_0\sqrt{1 + 4cos^2\left(\frac{k_y a}{2}\right) + 4\cos\left(\frac{k_y a}{2}\right)\cos\left(\frac{\sqrt{3}k_x a}{2}\right)} \qquad (2.4)$$

Here, γ_0 represents the nearest-neighbor hopping energy, which is 2.5 eV based on

density functional theory[13]. By inputting the values for k_x and k_y based on the values for

K and K' in **Equation 2.3**, we see that at the edge of the FBZ, the energy is zero,

meaning there is no band gap for graphene (**Figure 2.2.3**). Due to the lack of a band gap,

there is an inability to ever have a zero current flow, or "turn off" the device[14]. Its lack of

a band gap allows it to conduct both holes and electrons, categorizing it as "ambipolar"[3].
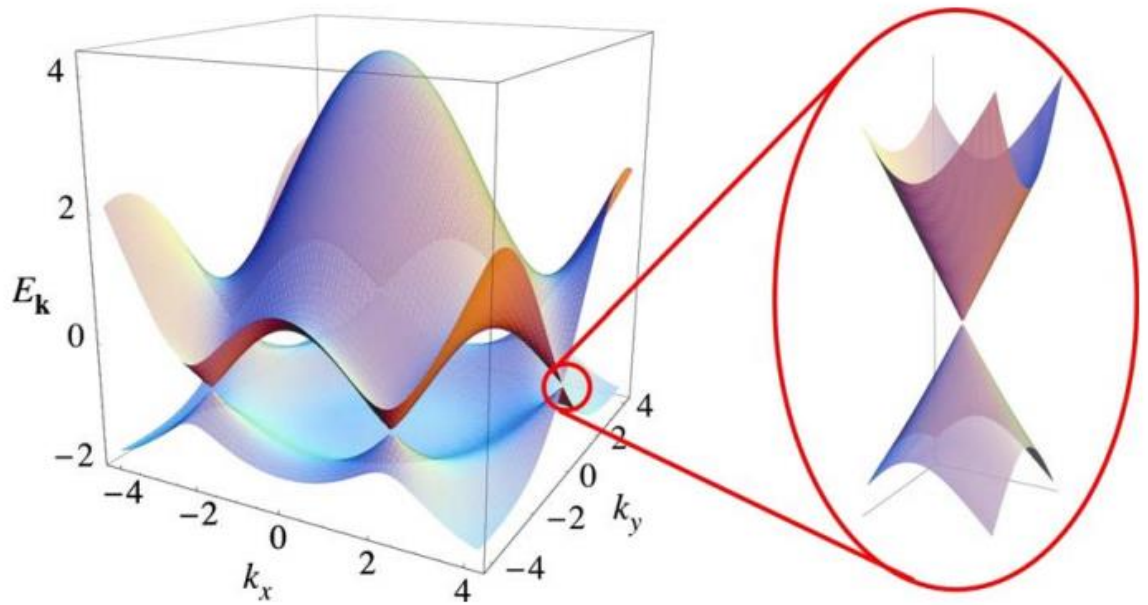
Fig 2.2.3. *Graphene band structure demonstrating the lack of bandgap, where the valence and conduction bands meet at the Dirac point [Ref: electronic properties of graphene]*

Despite graphene's superior mobility and sensitivity as every atom of the surface is exposed, it is not ideal for digital logic devices, as its lack of a band gap leaves it inefficient for modern-day electronics. This could be counteracted by engineering a band gap in graphene by doping it with atoms of a different element, such as boron or nitrogen[15], or patterning it into nanoribbons (GNRs)[16], which are thin strips of graphene for which there is a band gap coming from a lateral confinement of electrons in the GNR (usually being less than 50 nm in width). However, doping can lead to decreased electron mobility, and GNR patterning is not a viable process for scalable fabrication. Thus, the sensitivity and scalability of large-area CVD graphene is what makes it most suitable for biosensing techniques, where an on/off property is irrelevant, and the surface can be large enough, with every atom exposed, to detect biomolecules and chemicals in low concentrations.

Graphene's high electron mobility is ascribed to the massless nature of fermions in the material[17], meaning that the appropriate equation to describe the charge carriers is not the Schrodinger equation, but the Dirac equation. This is shown through the Dirac-like Hamiltonian:

$$\hat{H} = \hbar v_F \begin{pmatrix} 0 & k_x - ik_y \\ k_x + ik_y & 0 \end{pmatrix} \qquad \textbf{(2.5)}$$

For which the solution is:

$$E = \hbar v_F \boldsymbol{\sigma} \bullet \boldsymbol{k} \qquad \textbf{(2.6)}$$

From this solution, we can see that the energy of the electrons in graphene are dependent on the Fermi velocity v_F which plays the role of the speed of light, the Pauli matrix $\boldsymbol{\sigma}$,

and the momentum **k**. The Fermi velocity for electrons in graphene is ~ 10^6 $\frac{m}{s}$.[3] The

electron mobility, or speed at which charge carriers travel in graphene, is greater at room

temperature than those found in any other material measured[18], and is described through

the following equation:

$$v_d = \mu E \tag{2.7}$$

In this relationship, v_d is the drift velocity, or average velocity, of the charge carriers, μ

is the mobility, and E is the electric field. Therefore, because the drift velocity of the

charge carriers in graphene is so high due to their massless nature, the mobility of these

carriers will also be high for some fixed electric field.

2.3 Beyond Graphene: Transition Metal Dichalcogenides and Carbon Nanotubes

Apart from graphene, FET sensing can be carried out with other materials such as transition metal dichalcogenides (TMDs) or carbon nanotubes (CNTs). TMDs are semiconductors with a band gap that take the form MX_2, where 'M' is a transition metal and 'X' is a chalcogen atom (S Se, Te). This lattice layout is shown in **Figure 2.3.1**. In this structure, element 'M' is sandwiched between layers of element 'X' – this defines a single layer of the TMD. The most widely studied TMD is molybdenum disulfide, or MoS_2, which has an indirect bandgap of 1.23 eV that is tunable[19], robust[20], and has exceptional photoresponsivity[21].
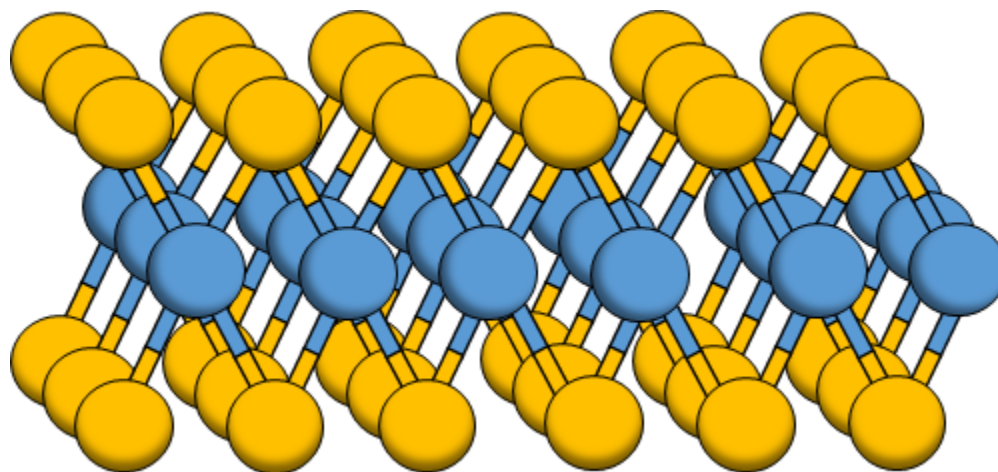
Fig 2.3.1 *MoS_2 lattice with molybdenum atoms in blue and sulfur atoms in yellow*

MoS_2 can be synthesized both with the exfoliation method[22] and through CVD growth, although placement of the material is challenging, as it often grows in flakes[23,24], though there have been some reports of large-area CVD MoS_2 growth[25,26]. In the past, MoS_2 has

been used for the detection of opioids[27], gas sensing of CO, CO_2 and NO^{28}, and detection of biomolecules such as prostate specific antigen[29].

A benefit of MoS_2 (and other TMD) devices is that there is less photolithographic contamination than graphene devices, as the CVD flakes do not need to be patterned in the device channel[27] (please see Chapter 4 for more information on device fabrication), although placement of the flakes on the substrate can be imprecise.

One study has reported the growth and transfer of full sheets of CVD grown MoS_2 in dimensions of 2x2 inches[30], although, currently, there are no other reports of executing this method successfully and with limited contamination.

Beyond MoS_2, there are a number of other TMD materials that have been used for various applications, such as tungsten disulfide (WS_2) used for humidity sensing[31], gas sensing for acetone and NO_2[32], and devices incorporated with graphene for DNA hybridization sensing[33]. $MoTe_2$ has been used for gas sensing of NO_2 and NH_3[34] and for adsorption of various SF_6 decomposition molecules[35]. Tungsten ditelluride (WTe_2) is another TMD that can be grown *via* CVD[36,37], although due to its sensitivity to atmosphere and its relative newness, there are currently no reports for WTe_2 sensors. While these additional TMDs are interesting and hold their own unique properties, they are still problematic for fabricating scalable arrays of FETs for low-concentration sensing, either due to their lack of sensitivity compared to graphene, or their instability in atmosphere.

Apart from 2D materials, sensors can also be fabricated with carbon nanotubes, sometimes described as 1D carbon, or graphene "rolled" into a cylinder. They are a

viable option for sensing purposes and exist as single-walled NTs or multiwall NTs, which describe many concentric CNTs, and possess a band gap.

The chirality of the nanotube, or angle at which it is rolled, determines its properties, and is described by the equation below:

$$C = na_1 + ma_2 \tag{2.8}$$

where C is the circumference of the nanotube and is comprised of the integer sum of the graphene basis vectors a_1 and a_2 with 'm' and 'n' being integers[38].

Carbon nanotubes can be grown *via* CVD, and may also be purchased synthetically. The biggest deterrent to CVD-grown CNTs is the fact that approximately one third of them will be metallic, compromising the on-off ratio. The desired CNT type for FET sensors is semiconducting, and therefore, it is beneficial to purchase nanotubes with the desired chirality and properties in a water-soluble fluid. In the past, CNTs have been used for glucose sensing[39], prostate cancer biomarker detection[40], Lyme disease detection[41], and complex vapor mixtures[42]. CNT FETs do not need to undergo any photoresist exposure following attachment to their substrate, and, if they are purchased commercially in a solution, can be pipetted by hand onto the desired device area. Even with these benefits, CNTs are, ultimately, less sensitive than graphene, as CNT networks will not be perfectly continuous like a graphene film.

Despite neither TMDs nor CNTs possessing the electron mobility or sensitivity that graphene does, these materials do, indeed, have a band gap, meaning that they are more realistic for use in modern-day electronics than graphene, and each has its ease of use/fabrication over scalable graphene devices.

2.4 A Two-Dimensional Insulator: Hexagonal Boron Nitride

A different type of low-dimensional material is hexagonal boron-nitride (hBN), which consists of alternating boron and nitrogen atoms in the 'A' and 'B' sublattices in a 2D hexagonal lattice structure similar to that of graphene, and can be obtained *via* exfoliation or through CVD growth. This material, an insulator with a band gap of 5.2 eV [43], has a lattice mismatch of only 1.5% when compared to graphene[44] and can therefore be stacked neatly on top of or underneath graphene.

By stacking it underneath, one can prevent graphene's charge carriers from interfering with dangling bonds of a SiO_2 substrate, maintaining the graphene's high electron mobility[45-47]. Alternately, hBN can be stacked atop graphene for scalable device fabrication, and behaves as a protective layer for graphene against photolithographic contamination. Atop metals, hBN serves as a protective layer from oxidation in air[48], and can also be used as a protective layer for TMDs, making it an interesting and versatile material for improving the quality of GFET of TMD-FET sensors. Please see Appendix B for growth details on hBN.

Chapter 2 Conclusions

Graphene is an unusual material with alluring properties such as high robustness and superior electron mobility at room temperature. Despite the long-held belief that graphene could not exist in a stable state, Geim and Novoselov from the University of Manchester isolated flakes of graphene *via* mechanical exfoliation in 2004, which led to the Nobel Prize in Physics in 2010, the shortest time between discovery and award in Nobel Prize history. Its superior sensitivity makes it an excellent nanomaterial for sensing.

Although graphene is central to this work, there are other nanomaterials that are worth researching and exploring, such as semiconducting transition metal dichalcogenides (TMDs), and the 1D version of graphene, carbon nanotubes (CNTs), which can be purchased with the desired chirality, and which have been studied long before graphene was discovered. The benefits of TMDs and CNTs is that they pose fewer contamination obstacles during device fabrication, as they are smaller area than large-area CVD graphene and do not need to be patterned, and they possess a band gap, which graphene lacks. Because of this band gap, these materials are more suitable for digital logic technology, as they can be turned "on" and "off".

Finally, hexagonal boron nitride (hBN), an insulator that can be exfoliated or grown through CVD, is another intriguing nanomaterial with a similar lattice structure of that of graphene, and which is advantageous when used in conjunction with graphene or even TMDs to improve device sensitivity and quality.

Both TMDs and CNTs have their own benefits and challenges in sensing, although neither possess the sensitivity of graphene, which is the most suitable of these materials for biomolecular and chemical detection. However, this cannot be achieved without good quality graphene, which will be discussed in the next chapter.

Chapter 2 References

1   Peierls, R. Quelques propriétés typiques des corps solides. *Annales de l'institut Henri Poincaré* **5**, 177-222 (1935).

2   Laundau, L. D. Zur Theorie der phasenumwandlungen II. *Physikalische Zeitschrift der Sowjetunion* **11**, 26-35 (1937).

3   Geim, A. K. & Novoselov, K. S. The rise of graphene. *Nature Materials* **6**, 183 (2007).

4   Novoselov, K. S. *et al.* Electric Field Effect in Atomically Thin Carbon Films. *Science* **306**, 666-669 (2004).

5   Pham, V. P., Jang, H.-S., Whang, D. & Choi, J.-Y. Direct growth of graphene on rigid and flexible substrates: progress, applications, and challenges. *Chem. Soc. Rev.* **46**, 6276-6300 (2017).

6   Kim, K. S. *et al.* Large-scale pattern growth of graphene films for stretchable transparent electrodes. *Nature* **457**, 706 (2009).

7   Xuesong, L., Luigi, C. & S., R. R. Synthesis of Graphene Films on Copper Foils by Chemical Vapor Deposition. *Advanced Materials* **28**, 6247-6252 (2016).

8   Bolotin, K. I. *et al.* Ultrahigh electron mobility in suspended graphene. *Solid State Communications* **146**, 351-355 (2008).

9   Ping, J., Vishnubhotla, R., Vrudhula, A. & Johnson, A. T. C. Scalable Production of High-Sensitivity, Label-Free DNA Biosensors Based on Back-Gated Graphene Field Effect Transistors. *ACS Nano* **10**, 8700-8704, doi:10.1021/acsnano.6b04110 (2016).

10   Rajesh *et al.* Genetically Engineered Antibody Functionalized Platinum Nanoparticles Modified CVD-Graphene Nanohybrid Transistor for the Detection of Breast Cancer Biomarker, HER3. *Adv. Mater. Inter.* **3** (2016).

11   Gao, Z. *et al.* Scalable Production of Sensor Arrays Based on High-Mobility Hybrid Graphene Field Effect Transistors. *ACS Applied Materials & Interfaces* **8**, 27546-27552 (2016).

12   Wallace, P. R. The Band Theory of Graphite. *Physical Review* **71**, 622-634 (1947).

13   Castro Neto, A. H., Guinea, F., Peres, N. M. R., Novoselov, K. S. & Geim, A. K. The electronic properties of graphene. *Reviews of Modern Physics* **81**, 109-162 (2009).

14   Wang, H., Hsu, A., Wu, J., Kong, J. & Palacios, T. Graphene-Based Ambipolar RF Mixers. *IEEE Electron Device Letters* **31**, 906-908 (2010).

15   S., P. L. *et al.* Synthesis, Structure, and Properties of Boron- and Nitrogen-Doped Graphene. *Advanced Materials* **21**, 4726-4730 (2009).

16   Han, M. Y., Özyilmaz, B., Zhang, Y. & Kim, P. Energy Band-Gap Engineering of Graphene Nanoribbons. *Physical Review Letters* **98**, 206805 (2007).

17   Novoselov, K. S. *et al.* Two-dimensional gas of massless Dirac fermions in graphene. *Nature* **438**, 197 (2005).

18   Bolotin, K. I., Sikes, K. J., Hone, J., Stormer, H. L. & Kim, P. Temperature-Dependent Transport in Suspended Graphene. *Physical Review Letters* **101**, 096802 (2008).

19   Zhu, J. *et al.* Thickness-dependent bandgap tunable molybdenum disulfide films for optoelectronics. *RSC Adv.* **6**, 110604-110609 (2016).

20   Kobayashi, K. & Yamauchi, J. Electronic structure and scanning-tunneling-microscopy image of molybdenum dichalcogenide surfaces. *Physical Review B* **51**, 17085-17095 (1995).

21   Li, X. & Zhu, H. Two-dimensional MoS2: Properties, preparation, and applications. *J. Materiomics* **1**, 33-44 (2015).

22   Li, H., Wu, J., Yin, Z. & Zhang, H. Preparation and Applications of Mechanically Exfoliated Single-Layer and Multilayer MoS2 and WSe2 Nanosheets. *Accounts of Chemical Research* **47**, 1067-1075 (2014).

23   Wang, X., Feng, H., Wu, Y. & Jiao, L. Controlled Synthesis of Highly Crystalline MoS2 Flakes by Chemical Vapor Deposition. *Journal of the American Chemical Society* **135**, 5304-5307 (2013).

24   Schmidt, H. *et al.* Transport Properties of Monolayer MoS2 Grown by Chemical Vapor Deposition. *Nano Letters* **14**, 1909-1913 (2014).

25   Yi-Hsien, L. *et al.* Synthesis of Large-Area MoS2 Atomic Layers with Chemical Vapor Deposition. *Advanced Materials* **24**, 2320-2325 (2012).

26   Li, L. *et al.* A General Method for the Chemical Synthesis of Large-Scale, Seamless Transition Metal Dichalcogenide Electronics. *Advanced Materials* **30**, 1706215 (2018).

27   Naylor, C. H. *et al.* Scalable Production of Molybdenum Disulfide Based Biosensors. *ACS Nano* **10**, 6173-6179, (2016).

28   Shokri, A. & Salami, N. Gas sensor based on MoS2 monolayer. *Sensors and Actuators B: Chemical* **236**, 378-385 (2016).

29   Lee, J. *et al.* Two-dimensional Layered MoS2 Biosensors Enable Highly Sensitive Detection of Biomolecules. *Scientific Reports* **4**, 7352 (2014).

30   Ma, D. *et al.* A universal etching-free transfer of MoS2 films for applications in photodetectors. *Nano Research* **8**, 3662-3672 (2015).

31   Luo, Y. *et al.* Tungsten disulfide (WS2) based all-fiber-optic humidity sensor. *Opt. Express* **24**, 8956-8966 (2016).

32   Ko, K. Y. *et al.* Improvement of Gas-Sensing Performance of Large-Area Tungsten Disulfide Nanosheets by Surface Functionalization. *ACS Nano* **10**, 9287-9296 (2016).

33   Rahman, M. S., Hasan, M. R., Rikta, K. A. & Anower, M. S. A novel graphene coated surface plasmon resonance biosensor with tungsten disulfide (WS2) for sensing DNA hybridization. *Optical Materials* **75**, 567-573 (2018).

34   Zhihong, F. *et al.* Highly sensitive MoTe 2 chemical sensor with fast recovery rate through gate biasing. *2D Materials* **4**, 025018 (2017).

35   Wang, D.-W. *et al.* MoTe2: A Promising Candidate for SF6 Decomposition Gas Sensors with High Sensitivity and Selectivity. *iEEE Electron Dev. Lett.* **9**, 292-295 (2017).

36   Naylor, C. H. *et al.* Large-area synthesis of high-quality monolayer 1T'-WTe 2 flakes. *2D Materials* **4**, 021008 (2017).

37   Jiadong, Z. *et al.* Large-Area and High-Quality 2D Transition Metal Telluride. *Advanced Materials* **29**, 1603471 (2017).

38   Dresselhaus, M. S., G. Dresselhaus, and P. Avouris. Carbon nanotubes : synthesis, structure, properties, and applications. *Topics in applied physics*, 447 (2001).

39   Lerner, M. B. *et al.* Scalable, non-invasive glucose sensor based on boronic acid functionalized carbon nanotube transistors. *Applied Physics Letters* **102**, 183113 (2013).

40   Lerner, M. B. *et al.* Hybrids of a Genetically Engineered Antibody and a Carbon Nanotube Transistor for Detection of Prostate Cancer Biomarkers. *ACS Nano* **6**, 5143-5149 (2012).

41   Lerner, M. B., Dailey, J., Goldsmith, B. R., Brisson, D. & Johnson, A. T. C. Detecting Lyme Disease Using Antibody-Functionalized Single-Walled Carbon Nanotube Transistors. *Biosensors & bioelectronics* **45**, 163-167 (2013).

42   Kybert, N. J., Lerner, M. B., Yodh, J. S., Preti, G. & Johnson, A. T. C. Differentiation of Complex Vapor Mixtures Using Versatile DNA–Carbon Nanotube Chemical Sensor Arrays. *ACS Nano* **7**, 2800-2807 (2013).

43   Hoffman, D. M., Doll, G. L. & Eklund, P. C. Optical properties of pyrolytic boron nitride in the energy range 0.05---10 eV. *Physical Review B* **30**, 6051-6056 (1984).

44   Wang, J., Ma, F. & Sun, M. Graphene, hexagonal boron nitride, and their heterostructures: properties and applications. *RSC Advances* **7**, 16801-16822 (2017).

45   Qi, J. Z. *et al.* Electronic Transport in Heterostructures of Chemical Vapor Deposited Graphene and Hexagonal Boron Nitride. *Small* **11**, 1402-1408 (2015).

46   Dean, C. R. *et al.* Boron nitride substrates for high-quality graphene electronics. *Nature Nanotechnology* **5**, 722 (2010).

47   Gannett, W. *et al.* Boron nitride substrates for high mobility chemical vapor deposited graphene. *Applied Physics Letters* **98**, 242105 (2011).

48   Galbiati, M., Stoot, A. C., Mackenzie, D. M. A., Bøggild, P. & Camilli, L. Real-time oxide evolution of copper protected by graphene and boron nitride barriers. *Scientific Reports* **7**, 39770 (2017).

Chapter 3: Graphene Growth, Transfer and Characterization

Proper growth of graphene and its characterization are crucial aspects of graphene sensor fabrication to ensure high quality devices. Here, the methods of graphene growth and transfer are explained, along with graphene film characterization to verify the quality of the nanomaterial.

This chapter begins with Section 3.1, defining the standardized growth of wafer-scale CVD graphene on a copper foil substrate, before moving on to its transfer through a low-contamination electrolysis bubbling method.

Section 3.2 describes the characterization process of the graphene film *via* Raman spectroscopy, which uses a laser to measure the low-energy vibrational and rotational modes of a material's lattice. The process depends on the inelastic scattering of the laser's photons as they interact with the material's lattice, creating a unique spectrum of the material.

In Section 3.3, atomic force microscopy (AFM) is presented as a second means of material characterization, which uses a cantilever and tip to scan the surface of materials to determine their height.

Optical microscopy, the simplest method of characterization, is explained in Section 3.4, and is employed to ensure the continuity and lack of bilayer growth in the film. Without good quality growth and transfer steps, or high-quality graphene, the yield of the sensors will be low and ineffective at detecting molecules.

The chapter ends with section 3.5, which focuses on the structure of the leading type of graphene sensor in this work, the graphene field-effect transistor, and how it operates.

3.1 Graphene Growth and Transfer

Graphene is grown in-lab *via* a method known as chemical vapor deposition (CVD). This process utilizes a low-pressure furnace, H_2 and Ar carrier gases and methane as a carbon feedstock to produce continuous, large-area, low-defect monolayer graphene on a copper foil substrate. Graphene nucleates around defects on the surface of the copper foil, adatoms, and surface contaminants, and the carbon atoms from the methane detach from the hydrogen in the methane molecules and adsorb onto the copper foil, resulting in a layer of graphene[1]. The H_2 is necessary to etch away carbon that is not of the sp^2 hybridization[2]. More details on this process are provided in Appendix A.

To transfer graphene, the copper foil with graphene was coated with a sacrificial layer of polymethyl methacrylate (PMMA, A4 950, Microchem) to improve visibility of the film and provide structural support, and baked at 150 C for 2 min to ensure proper adhesion of the PMMA to the graphene. Transfer was carried out *via* an electrolysis bubbling method[3] in a 0.05 M sodium hydroxide (NaOH) solution connected to a power source of voltage 20 V with the cathode resting in the NaOH solution and the anode connected to the Cu foil/graphene/PMMA stack. Upon immersion of the stack in the solution, the circuit is completed and current begins to flow. H_2 bubbles form at the interface of the graphene/PMMA stack and the Cu foil, and the two separate (**Fig 3.1.1**), leaving the graphene/PMMA film floating in the NaOH solution.
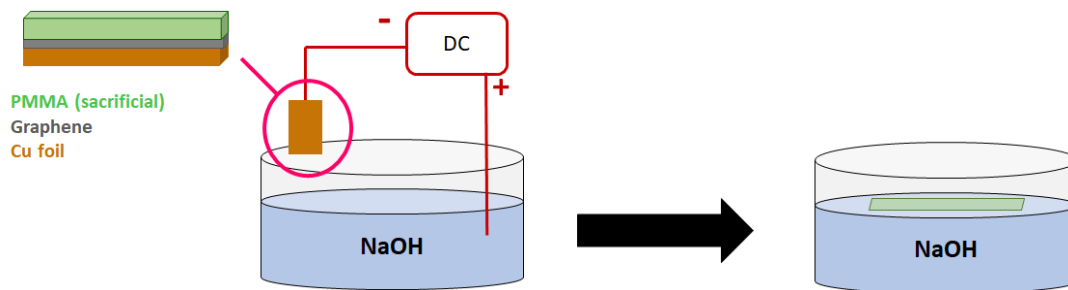
Fig. 3.1.1 *Electrolysis bubbling method of graphene with 0.05M sodium hydroxide (NaOH) solution with the anode connected to the copper foil/graphene/PMMA stack and the cathode in the NaOH solution. This leaves a film of graphene/PMMA floating in the solution.*

The film was then transferred to a series of deionized (DI) water baths to remove the NaOH residue, and finally transferred onto the desired substrate and left to dry for ~1 hour. The benefit of this transfer method compared to others, for example, using copper etchant[4] is that it is low-contamination, as NaOH residue is easier to remove than copper etchant, and that it is a rapid process.

Once the graphene/PMMA stack is dry, the sample is baked at 150 C for 2 minutes to ensure adhesion of the graphene to the substrate. Next, the PMMA is removed with acetone and the sample rinsed with IPA and dried with compressed N_2.

At this point, what is left is a clean graphene film on the desired substrate. The following steps for fabrication are explained in more detail in Chapter 4.

3.2 Raman Spectroscopy of Graphene

Raman spectroscopy is a highly useful technique to provide information about the quality of a nanomaterial. This method of characterization uses a laser to measure the low-energy vibrational and rotational modes of the material's lattice, creating a unique "fingerprint" of the material. It relies on inelastic scattering of the laser's photons which interact with the lattice, causing a shift in the photons' energies and providing information about the lattice itself. Here, Raman spectroscopy was carried out on bare, un-transferred graphene on copper foil.

Raman profiles of the graphene grown in-lab were consistent with good-quality, monolayer graphene, exhibiting the correct placement and intensity of the three most important bands, the D band, the G band, and the G', or 2D band. The D band, ~ 1300 cm^{-1}, represents the defects in the graphene caused by sp^3 hybridized carbon. The G band, at ~ 1600 cm^{-1}, describes the in-plane vibrational mode involving sp^2 carbon-carbon bonds, and the G' band, or the 2D band, found ~ 2700 cm^{-1}, is the second order of the D band, the result of a two phonon lattice vibrational process, is the strongest band in the spectrum, and does not represent defects[5].

For high quality, monolayer graphene, the ratio between the 2D/G peaks is ~2, with a very low D/G ratio (< 0.05)[6]. This can be seen in **Fig. 3.2.1**, which shows the Raman spectrum of monolayer graphene on copper foil. From this Raman spectrum, we verify that the graphene quality is high and ready for use in sensing.
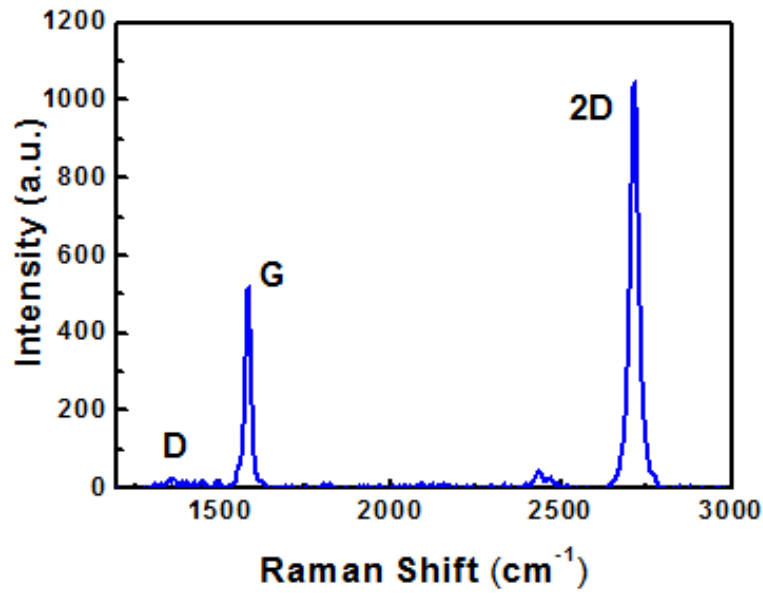
Figure 3.2.1. *Raman spectrum of monolayer graphene on copper foil, with a low D peak and a ratio of ~2 between the 2D and G peaks.*

This spectrum looks very different than the spectrum for graphite, for which the G peak

far exceeds the height of the 2D peak[7]:
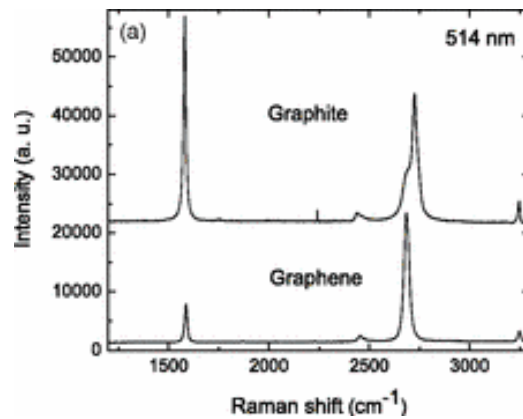
Figure 3.2.2. *Raman spectrum of graphite compared to graphene*

3.3 Atomic Force Microscopy of Graphene

Scanning probe microscopy methods are standard for determining the quality of samples, especially ultra-thin samples such as 2D materials. One such form of scanning probe microscopy is atomic force microscopy (AFM), which aims to provide information about the height of thin materials by wielding a cantilever with a thickness of a few nanometers to scan the surface of the sample. When the surface is scanned in tapping mode, the cantilever oscillates close to its resonant frequency while moving laterally across the surface of the sample. As the cantilever and tip come into contact with the sample, the cantilever varies in distance from the substrate depending on the height of the material (**Fig. 3.3.1**). This distance variation is due to the damping of the cantilever's oscillations coming from the intramolecular forces between the atoms of the sample and the tip.
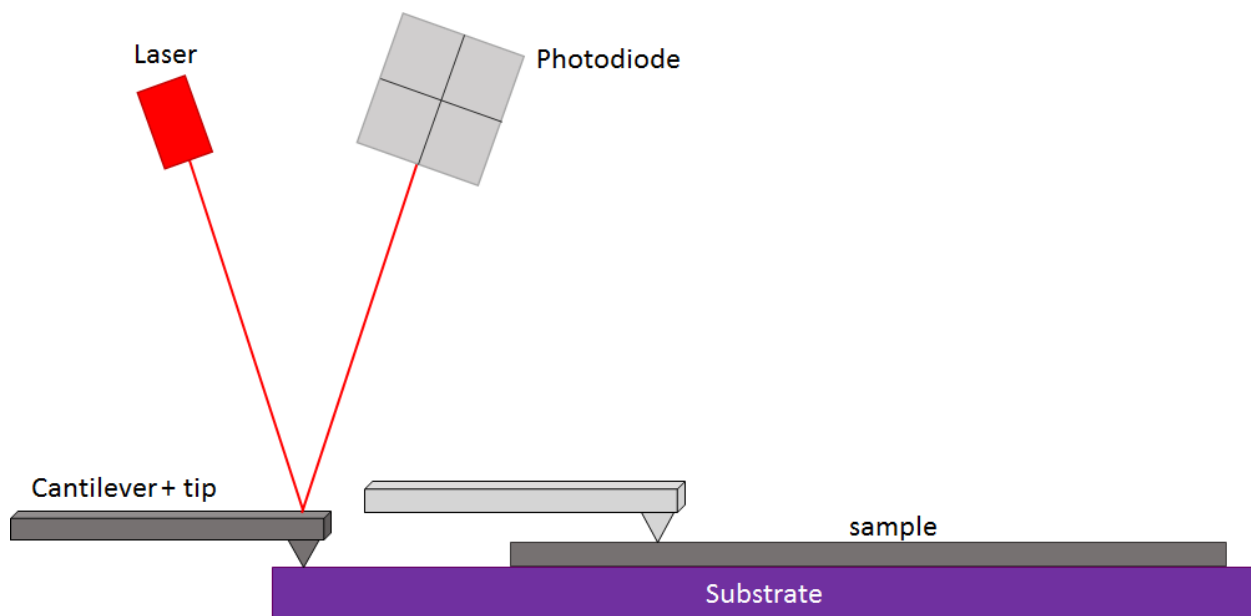
Figure 3.3.1 *Atomic force microscopy schematic. A cantilever scans the surface of the substrate and sample in a tapping mode and increases or decreases in height depending on the thickness of the scanned material, yielding a height profile.*

AFM is sensitive to even atomically thin films, making it excellent for scanning materials like graphene and verifying that no bilayer or amorphous growth is present. Additionally, upon scanning the surface, it can determine the surface roughness and cleanliness of the sample, as the height profile will change due to contamination.

AFM profiles for bare graphene on a SiO_2 substrate yield a height of ~1 nm with a Bruker Icon AFM in tapping mode, where the cantilever and tip continuously tap the sample while scanning the surface. A height of ~1 nm is the expected experimental value for graphene on this type of substrate[8] (**Fig. 3.3.2**).

It behooves the experimentalist to conduct AFM on a substrate where the graphene is visible, seen through a small camera in the AFM set-up. Otherwise, it is impossible to know where (or what) one is scanning. Therefore, AFM directly on the copper foil substrate is not an option, as there is a need for color contrast. AFM scans for graphene are typically carried out on a SiO_2 substrate of ~ 285 nm, so that the graphene film is visible. The necessity of film visibility is to locate an effective place for scanning, usually beginning with the edge of a small tear in the center of the film, as the edges of the full film are often contaminated from transfer, where PMMA residue can be stubborn to remove and can result in an inaccurate height profile. To create a sample of graphene on SiO_2, the film must be transferred *via* the electrolysis bubbling method mentioned in section 3.1.
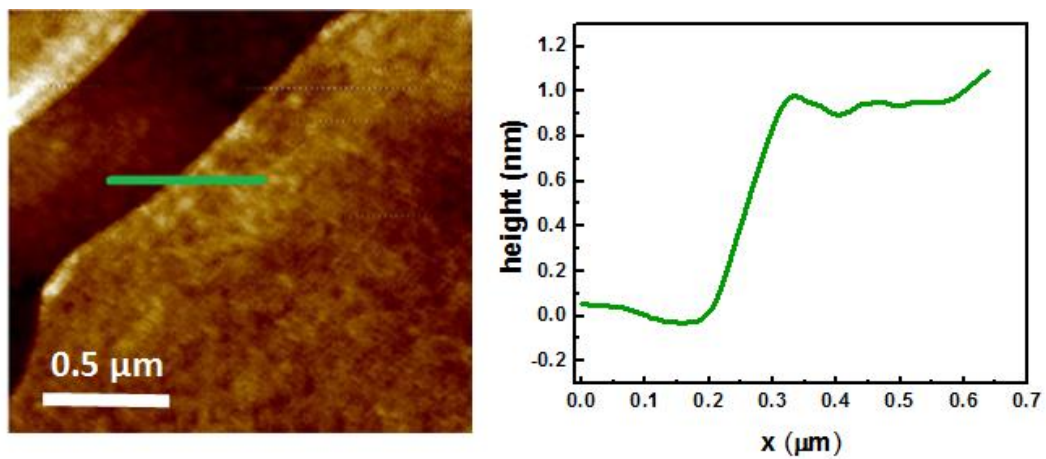
Figure 3.3.2. *Atomic force microscopy of bare graphene on SiO₂ (left) and height profile associated with the image (right), showing a height of ~1 nm.*

3.4 Optical Microscopy of Graphene

The final characterization for graphene, and the simplest, is optical microscopy. By observing the graphene under magnification, one can determine the existence of bilayer growth (often seen as darker areas on the graphene), and, moreover, ascertain the continuity of the sample, as discontinuous graphene leads to poor device quality and yield. Optical microscopy is helpful because the Raman laser only provides information about the quality of small areas of the graphene, but not necessarily the continuity, and AFM only provides information about the cleanliness and continuity of small areas (a few µm).

Therefore, optical microscopy, when used on high magnification, is the best way to determine continuity, as without a continuous sheet, problems may arise with adhesion to the substrate during device fabrication. **Figure 3.4.1** represents continuous monolayer graphene on a SiO_2 substrate.
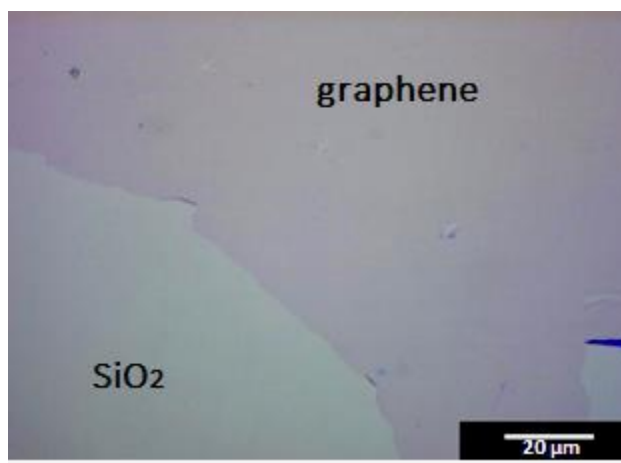
Figure 3.4.1 *Continuous, monolayer bare graphene on SiO_2*

In the event that the graphene contains significant bilayer growth, which will appear as spotty, darker areas under an optical microscope, a possible fix to the growth recipe is to either decrease the methane flow, or to decrease the time of the growth. If the film is discontinuous in its growth, which will appear as hexagonal flakes that are beginning to form a film, with empty spaces in between, then the graphene growth step should be extended by a few minutes (see Appendix A for more details on the graphene growth recipe).

3.5 Electrical Characterization of Graphene Field-Effect Transistors

The high-quality, monolayer, large-area graphene described in this thesis is used primarily for the fabrication of field-effect transistors (FETs), which are pervasive in modern electronics. A field-effect transistor is an electrical device with three terminals: a gate, a source, and a drain. A fixed "bias voltage" (V_B) is applied across the source and drain, and an electric field associated with the "gate voltage" (V_G) alters the Fermi level of the conducting channel, and thus, modulates the flow of current through this channel. Typically, for devices described here, the substrate is SiO_2 of thickness ~285 nm on heavily doped p-type silicon.

The most frequently employed type of FET is the metal-oxide semiconductor FET, or MOSFET, which incorporates semiconductors such as silicon, which are used to form the channel[9]. Although there is an abundance of silicon, it possesses a band gap, and silicon devices have been well studied and understood for decades, it simply does not have the same level of detection sensitivity as graphene, as every atom of the lattice is not exposed as in the case of graphene, nor does it have the high electron mobility of graphene at room temperature. Therefore, while silicon is a viable choice for modern day electronic devices such as computers and smartphones that need to be turned on and off, it is not the best option for low-concentration biomolecular or chemical sensing.

The work presented here centers around graphene FETs on a Si/SiO_2 wafer, with silicon as the gate of the device and silicon dioxide acting as the gate dielectric. CVD graphene serves as the channel, with source and drain electrodes of chromium and gold (5 nm, 40 nm, respectively). Unlike metal-semiconducting devices, which have a potential energy

barrier for the electrons to overcome, known as the Schottky barrier, GFET devices

possess no such barrier, and instead have Ohmic contact (conductor-conductor junction)

between their metal electrodes and graphene channel, classifying the devices as "non-

rectifying". Owing to the fact that graphene is an excellent conductor of both electrons

and holes and therefore, there is no potential energy barrier for electrons to overcome

between the electrodes and the channel. In these devices, the silicon gate and the

graphene channel are capacitively coupled, illustrated in the schematic below (**Fig. 3.5.1**)
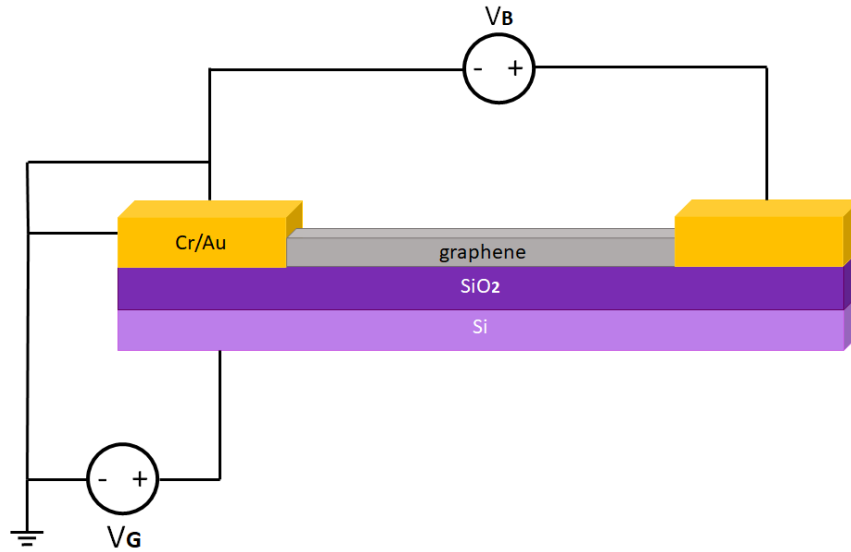
Figure 3.5.1. *Schematic of a graphene field effect transistor with chromium (Cr) and gold (Au) contacts, a bias voltage across the source and drain (V_B), and a gate voltage (V_G) from the source to the silicon/silicon dioxide body.*

All readout was done electronically by sweeping the gate of the device. This resulted in a

profile of current versus gate voltage (I-V_G) which provides information about the

electron mobility in the GFETs and the Dirac voltage, or "Dirac point", described as the

minimum point of conductance. For bare graphene, the Dirac voltage generally lies

between 0-10 V, with mobilities up to about 2,000-2,500 cm^2/Vs, and a GFET device

yield of $> 90\%$ [10]. An example of a single such device is shown in the figure below:
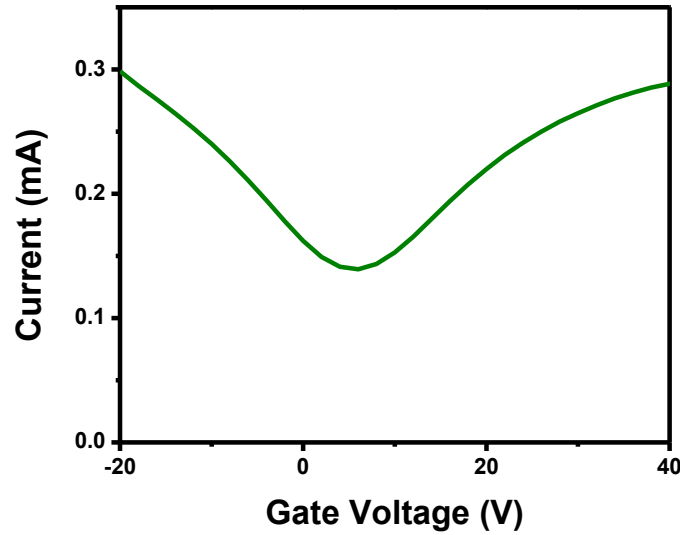
Figure 3.5.2. *I-V$_G$ characteristics of a single GFET, with a Dirac voltage between 0-10 V*

In this graph, the current never reaches zero, and the Dirac voltage is roughly 3-4 V. In

theory, the Dirac voltage should be zero, as explained in Chapter 2, section 2, and the

mobility thousands of cm^2/Vs higher than 2,000-2,500 cm^2/Vs. Unfortunately, dangling

bonds on the SiO_2 surface can interfere with these values, and the use of the substrate is

not avoidable in this instance. High mobilities can be achieved with suspended graphene,

however, these devices are difficult to engineer in large quantities, and therefore, this is

not a suitable method for scalable fabrication.

The details of the I-V$_G$ curve and how it changes due to chemical functionalization on the

surface of the graphene will be explained in more detail in Chapter 4.

Chapter 3 Conclusions

The verification of proper graphene growth and quality is critical for fabricating high-caliber graphene devices with superior sensitivity. By using Raman spectroscopy, one can determine the nature of the graphene on a copper foil substrate and confirm that it is monolayer. With atomic force microscopy, the cleanliness and height of the sample can be measured, and finally, by using optical microscopy at high magnification (50x, 100x) of graphene on a SiO_2 substrate, the continuity of the film becomes apparent. Without a clean transfer method and film quality verification from the necessary characterization steps, it is likely that device quality can be poor due to contamination or discontinuous growth.

Once the quality of the graphene has been established, the next step is its use in graphene biosensors, or, in the case of this work, graphene field effect transistors (GFETs), and measurements of their electrical characteristics for data collection. The fabrication, functionalization, and data collection of these biosensors is discussed in the next chapter.

Chapter 3 References

1   Luo, Z. *et al.* Effect of Substrate Roughness and Feedstock Concentration on Growth of Wafer-Scale Graphene at Atmospheric Pressure. *Chemistry of Materials* **23**, 1441-1447 (2011).

2   Gan, L. & Luo, Z. Turning off Hydrogen To Realize Seeded Growth of Subcentimeter Single-Crystal Graphene Grains on Copper. *ACS Nano* **7**, 9480-9488 (2013).

3   Gao, L. *et al.* Repeated growth and bubbling transfer of graphene with millimetre-size single-crystal grains using platinum. *Nature Communications* **3**, 699 (2012).

4   Van Ngoc, H., Qian, Y., Han, S. K. & Kang, D. J. PMMA-Etching-Free Transfer of Wafer-scale Chemical Vapor Deposition Two-dimensional Atomic Crystal by a Water Soluble Polyvinyl Alcohol Polymer Method. *Scientific Reports* **6**, 33096 (2016).

5   Ferrari, A. C. Raman spectroscopy of graphene and graphite: Disorder, electron–phonon coupling, doping and nonadiabatic effects. *Solid State Communications* **143**, 47-57 (2007).

6   Malard, L. M., Pimenta, M. A., Dresselhaus, G. & Dresselhaus, M. S. Raman spectroscopy in graphene. *Physics Reports* **473**, 51-87 (2009).

7   Ferrari, A. C. *et al.* Raman Spectrum of Graphene and Graphene Layers. *Physical Review Letters* **97**, 187401 (2006).

8   Nemes-Incze, P., Osváth, Z., Kamarás, K. & Biró, L. P. Anomalies in thickness measurements of graphene and few layer graphite crystals by tapping mode atomic force microscopy. *Carbon* **46**, 1435-1442 (2008).

9   Kim, S. O. & Kim, H. J. Fabrication of n-metal–oxide semiconductor field effect transistor with Ta2O5 gate oxide prepared by plasma enhanced metalorganic chemical vapor deposition. *J. of Vacuum Sci & Tech B* **12**, 3006-3009 (1994).

10   Vishnubhotla, R. *et al.* Scalable graphene aptasensors for drug quantification. *AIP Advances* **7**, 115111 (2017).

<u>Chapter 4: Graphene Field Effect Transistor Fabrication and Functionalization</u>

After verification of the high quality of the graphene and its effective, clean transfer to a desired substrate, the next step is the fabrication of graphene field-effect transistors (GFETs) and the functionalization of these devices for sensing. Upon fabrication completion, the devices are functionalized with a linker molecule, followed by a probe molecule which is tailored to bind specifically to a desired target. AFM verified the binding of each of these functionalization steps to the surface of the graphene.

In section 4.1, we describe the fabrication procedure including photolithography, thermal evaporation, oxygen plasma etching, and annealing to create arrays of GFETs ready for functionalization. In section 4.2, we explore the functionalization of the graphene's surface with a linker molecule and the probe molecule and ascertain their binding through atomic force microscopy (AFM). Section 4.3 explains the binding of the target to the probe.

The collection of data *via* an all-electronic readout method is illustrated in section 4.4, where the current is measured as a function of gate voltage (V_G). The shift of the Dirac voltage is defined, and how this shift can be quantified in terms of the amount of charge on the graphene's surface. Finally, this chapter ends with section 4.5, and how the data of current and gate voltage is analyzed by a linear fitting of the hole branch of the curves.

4.1 GFET Fabrication

To fabricate GFETs, a Si/SiO$_2$ wafer was patterned using traditional photolithography and thermal evaporation. The details of this process are explained in Appendix C, and result in arrays of scalable GFETs.

The final step of the GFET fabrication process before chemical functionalization was annealing. Annealing requires exposing the sample to heat and gas flow to either correct defects in a lattice, as is the case for the copper foil during graphene growth, or, in this instance, to decrease contamination of the GFETs from photoresist residue. The GFETs were annealed at 225 C with argon flow of 1000 sccm and hydrogen flow of 250 sccm for one hour. The end result at this stage was low-contamination graphene FETs ready for functionalization. GFET yield was over 90%, with a Dirac point between 0-10V. This can be seen in **Figure 4.1.1** (below), which shows one GFET (left) under optical microscopy, and the I-V$_G$ characteristics of GFETs in one array, with high yield and good device uniformity.

The details of I-V$_G$ data collection and analysis will be described in more detail later in this chapter.
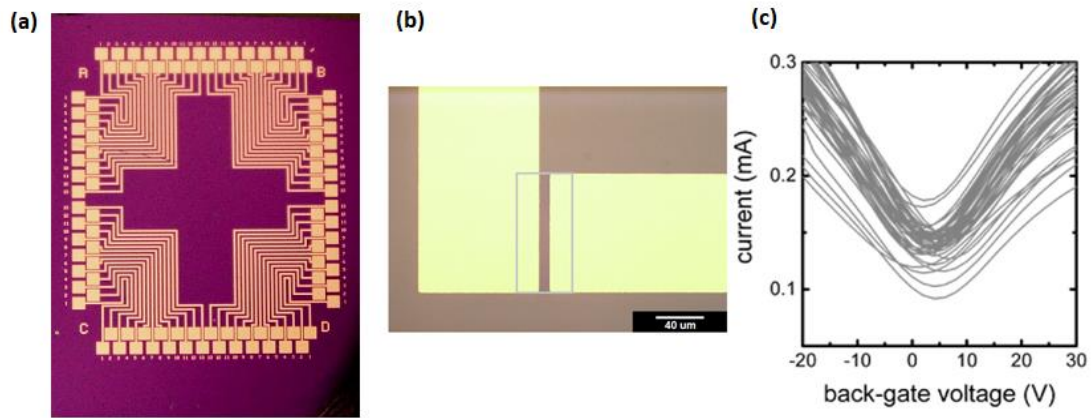
Figure 4.1.1 *(a) Single "chip" with 52 GFETs, 13 in each quadrant; (b) magnified image of a single GFET, with a grey box depicting placement of the graphene channel; (c) I-V_G curves for GFETs on one chip, with a yield of > 90%.*

4.2 GFET Linker and Probe Molecule Functionalization

The molecules used to functionalize a GFET depend on the most effective method for trapping the desired target molecule. The focus of this thesis is the sensing of nucleic acids and drug targets, and one highly effective linker molecule for detecting these targets is 1-pyrenebyuteric N-hydroxysuccinimide ester (Sigma Aldrich), also known as "Pyrene-NHS", or "P-BASE". This molecule forms a non-covalent bond with the carbon atoms through π-π stacking between the aromatic rings of P-BASE and the graphene. Other linker molecules, such as diazonium salt, may also be used, although diazonium salt creates a covalent (therefore, perturbative) bond with graphene, and can induce defects in the graphene and affect the electronic properties unfavorably[1,2].

Beginning immediately after the annealing step, the GFETs were soaked in a 1 mM solution of the solvent dimethylformamide (DMF) and P-BASE for ~20 hours to ensure full coverage of the P-BASE on the graphene. Afterward, they were removed from the DMF solution and rinsed with DMF, IPA and DI water.

Following P-BASE attachment, the second functionalization step was attachment of the "probe" molecule. A probe molecule is a molecule that specifically binds to the desired target. For single strand DNA (ssDNA) target detection, the probe was the complementary DNA strand.

If the target was a drug molecule, then an aptamer, or a series of nucleotides in a particular orientation selected to bind to a specific target acted as the appropriate probe. The correct aptamer for a target can be found through "synthetic evolution of ligands through exponential enrichment", or SELEX, which is a combinational chemistry

technique involving some 10^{12}-10^{18} randomly generated DNA strand sequences in various orientations carefully being selected through several rounds of exposure to the target molecule[3]. Those that bind fully or partially are kept for the next round, and all other sequences are discarded, eventually leading to a few select aptamers that bind strongly to the desired target. The SELEX method has proven successful for various target molecules, including the HIV drug tenofovir[4], an azole-class antifungal drug[5], glucagon receptors[6], as well as proteins, cells, and microorganisms[7].

Determination of a selective probe molecule is a vital step, as without it, there can be no target detection, or worse, one could have non-selective binding of the probe to other molecules. When the linker molecule is Pyrene-NHS, the binding of the probe to the NHS group is imperative. This was carried out by use of a synthetic probe molecule, which was either ssDNA for the detection of a ssDNA target, or an aptamer for drug detection, each with an amine group attached to one end. The related crosslinker chemistry equation is shown below (ThermoFisher Scientific):

| NHS Ester Reagent | | Primary Amine on Protein | | Stable Conjugate (amide bond) | | NHS |

$$(\textbf{4.1})$$
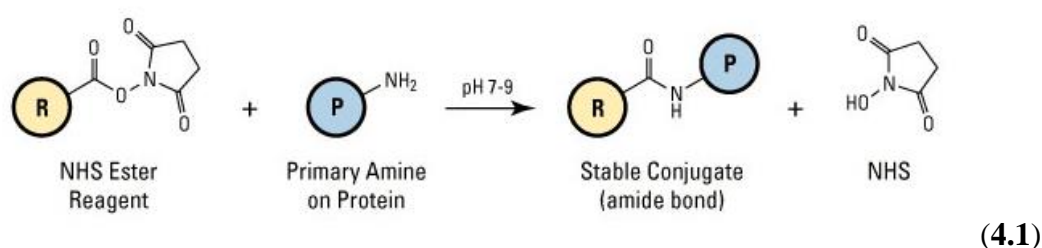
Here, "R" represents the pyrene with its NHS group attached, and "P" is the probe molecule with an amine group at one end. In this instance, incubation was executed in DI water, and the end result was the probe-amine combination taking the place of the NHS group, which detached and got washed away through cleaning steps[8]. Through this linker

chemistry, the probe was bound to the P-BASE and became immobilized on the

graphene, assuming the necessary configuration, which was either rigid for ssDNA, or

some unknown configuration through heat treatment for an aptamer. All probe solutions

were kept at the same concentration, regardless of the experiment, which was 1 μM. The

GFETs incubated in the probe solution for approximately 3 hours, at which point they

were rinsed with DI water and dried with compressed N_2. Atomic force microscopy

determined the binding of these molecules to the graphene. Seen in **Fig. 4.2.1**, it is

evident that the P-BASE and probe molecule attached properly, as the height profile

increased after each functionalization step, as expected. The height profile of graphene on

SiO_2 was what was expected, around ~1 nm. Although the thickness of a graphene film is

around 0.34 nm, because of dangling bonds on the SiO_2, the thickness, experimentally,

can end up being closer to 1 nm.

Pyrene-NHS atop graphene yields a height of an additional ~1 nm, and with the binding

of the probe (~1 nm), the overall height of the sample was around 3 nm above the

substrate, which is in agreement with the accepted sizes of the molecules[9].
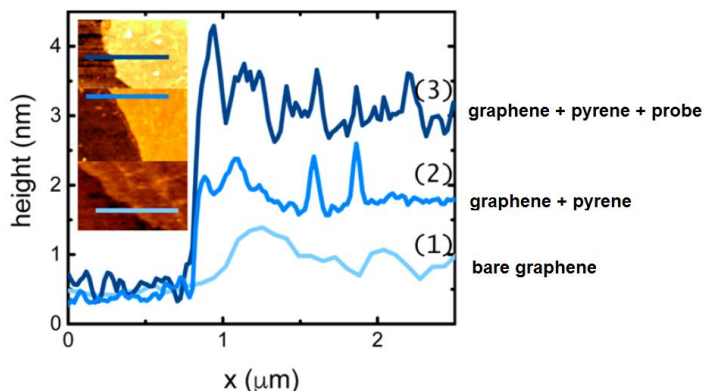
Figure 4.2.1 *Atomic force microscopy images of bare graphene on SiO₂, then
functionalized with pyrene-NHS, and again with probe DNA*

Next, the devices were exposed to the desired target molecule, which was left to bind to

the probe, discussed in more detail in the following section.

4.3 GFET Target Molecule Binding

Target molecule binding was generally the same. Following probe attachment, the target solution of a known concentration was pipetted onto the chip and incubated in a humid environment, anywhere from 30 minutes to 4 hours, depending on the target strand length and concentration. This is because long DNA strands need more time to hybridize with their probes fully and low concentration solutions need more time to diffuse through the fluid medium. Assuming correct selection of the probe molecule for the desired target, the target molecule should bind to the probe and nothing else, given proper cleaning steps after each functionalization step.

A schematic of this binding is seen in **Fig. 4.3.1**, where the P-BASE is bound to the graphene, shown as aromatic rings in the image, and the probe molecule, in red, is bound to the pyrene through the cross-linking chemistry of **Equation 4.1**. It was then able to hybridize into a double helix upon exposure to the target, in blue, which is its perfect complementary strand.
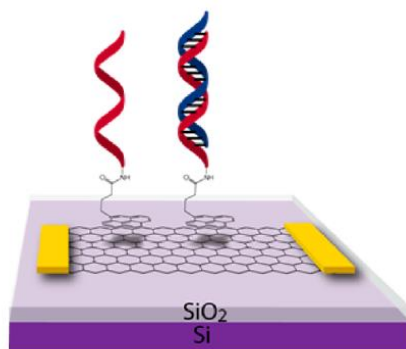
Figure 4.3.1 *Graphene field effect transistor schematic with pyrene, probe DNA (red) and target DNA (blue)*

If detecting a drug target, then an aptamer with an amine group at the end acted as the probe, as mentioned in the previous section.

For examples of other types of linker, probe and target molecules, see Chapter 6.

4.4 Functionalized GFET Data Collection

Data for the GFETs was collected *via* an all-electronic readout method by sweeping the gate voltage and measuring the associated current. This resulted in a profile of current versus gate voltage, or I-V_G. From the I-V_G characteristics, we were able to determine the position of the Dirac voltage, and more importantly, the shift in the Dirac voltage based on the target attachment. In order to measure this shift, the GFET characteristics were measured after probe molecule attachment and again after target molecule attachment. The shift in the Dirac voltage of the GFETs between these two steps is related to the target's composition and, in the case of ssDNA, its length. Dirac voltage shifts are due to the chemical gating effect, which occurs when a target molecule of negative/positive charge binds to the probe molecule and as a result, induces an increase in the positive/negative charge carriers in the graphene channel, thus shifting the Dirac voltage to the right/left, respectively[10].

For DNA, the strands are diluted in a solution of DI water. The DNA strands deprotonate in the water due to the ionization of the phosphate groups, and acquire a negative charge for both the probe and the target. Because of this charge, and due to the chemical gating effect, the Dirac voltage shifts in the positive direction, ascribed to an induced increase in the positive charge carriers in the graphene channel. This can be seen in **Figure 4.4.1**.
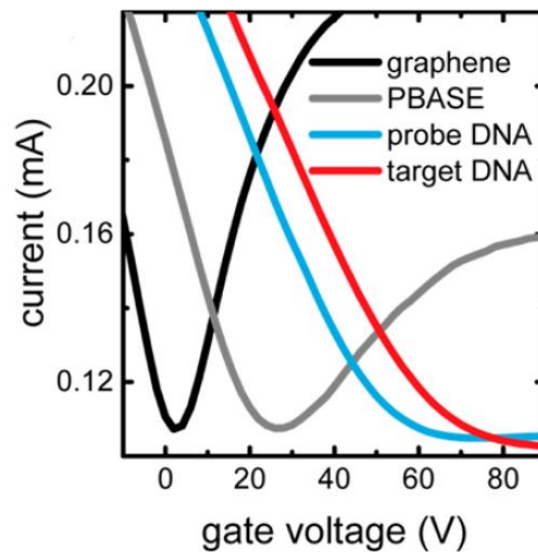
Figure 4.4.1 *Functionalization of plain graphene with pyrene (grey), probe (blue) and target (red) molecules. Each of these steps creates a shift in the Dirac point, or minimum point of conductance, due to the chemical gating effect.*

Since the probe and the target strands both become negatively charged prior to attachment, it seems counterintuitive that binding would occur for two negatively charged strands without the help of an ionic solution. However, graphene creates an exception to this, as both positive and negative charge carriers can be induced in the material. Binding of the negatively charged probe molecule engenders an increase in the positive charge carriers in the graphene, which balances out the negative charge of the probe. As a result, the target molecule, which is also negatively charged, can bind to its probe without the aid of an ionic solution.

The shifts of these curves can be quantified into an associated charge for each functionalization step by recalling that in the GFET, the graphene and the silicon are capacitively coupled. The relationship between charge and shift in the Dirac voltage can be expressed as a combination of the following equations:

$$Q=C\Delta V \text{ and } C=\frac{K\varepsilon_0 A}{d} \qquad\qquad (\textbf{4.2})$$

Here, Q represents the amount of charge coming from the functionalization step, C is the capacitance, ΔV is the shift in the Dirac voltage due to said functionalization step, K is the dielectric constant, in this case, about 3.9 for SiO_2, ε_o is the commonly known permittivity constant of 8.85 x 10^{-12} F/m, A is the area of the plates, in this instance, the area of the channels, which is 10μm x 100μm, and d is the distance between the plates, or the thickness of the oxide, which is 285 nm for these devices.

Looking at **Figure 4.4.1**, the shift in the Dirac voltage from probe to target is ~20V, which, according to **Equation 4.2**, corresponds to a charge of 2.42x10^{-12} Coulombs.

4.5 Data Analysis

I-V_G curves of the graphene FETs were analyzed in OriginPro 8 by fitting the following equation to the hole branch, or left-handed linear branch of the curves:

$$I^{-1} = [e\alpha\mu(V_G - V_D)]^{-1} + I_S^{-1} \qquad (4.3)$$

Here, I represents the current, μ is the charge carrier mobility, V_G is the back-gate voltage, V_D the Dirac voltage, α the constant relating gate voltage to carrier number density, and I_S is the saturation constant due to short-range scattering. This equation gives the Dirac voltage and mobility of each GFET. The Dirac voltage of each device was recorded after probe attachment and again after target attachment, and the shift associated with each device was averaged, with the error being the standard deviation of the mean.
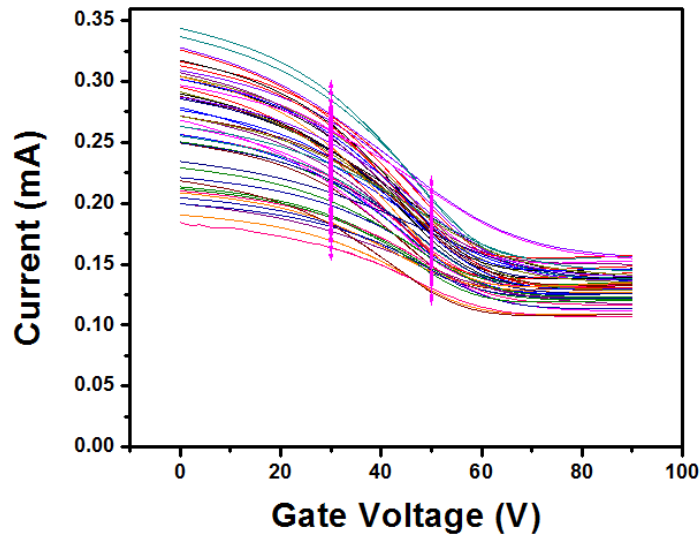
Figure 4.5.1 *OriginPro fitting of the hole branch for GFETs to extract the Dirac voltage using fitting **Equation 4.3**;*

Each Dirac shift average is attributed to a specific target of a known concentration. This process was repeated several times for various target concentrations, and one for baseline solution, to determine the true value of the target signals.

Any baseline salt solution will undoubtedly have charge, and create a shift of its own, even without any target molecules. In this case of DI water, although water molecules are neutrally charged, they do create a small shift when bound to the graphene's surface. This is most likely due to the autoionization of water, and creates a shift in the Dirac voltage in the positive direction, usually between 4-6 V.

After testing the GFETs at various target concentrations (with one "chip" per concentration), a relationship between relative Dirac shift and concentration became apparent, which takes on Hill-Langmuir behavior for ligand-receptor binding and provides information about the limit of detection, the saturation limit, and the dissociation constant, all described in more detail in the next chapter.

Chapter 4 Conclusions

In this chapter, a standardized process for graphene FET arrays has been described, in addition to how to keep contamination of these sensors to a minimum to preserve the quality of the graphene and produce a high device yield.

Upon completion of the fabrication and cleaning steps, the GFETs were ready to be used for sensing purposes, and were functionalized with the necessary linker molecules and probe molecules for detection of nucleic acids and drug targets, both of which can be done with nucleic acid probes, either through single strand DNA or aptamers. The chapter ends with data collection and analysis of these sensors through an all-electronic readout method, as well as how the electronic properties are altered due to the binding of molecules to the graphene.

The next chapter (Chapter 5) goes into detail concerning the detection of nucleic acids and drug targets using the devices that were described in this chapter.

Chapter 4 References

1   Lerner, M. B. *et al.* Scalable Production of Highly Sensitive Nanosensors Based on Graphene Functionalized with a Designed G Protein-Coupled Receptor. *Nano Letters* **14**, 2709-2714 (2014).

2   Huang, P., Jing, L., Zhu, H. & Gao, X. Diazonium Functionalized Graphene: Microstructure, Electric, and Magnetic Properties. *Accounts of Chemical Research* **46**, 43-52 (2013).

3   Chai, C., Xie, Z. & Grotewold, E. in *Plant Transcript. Fact.: Meth. Prot.*   249-258 (2011).

4   Vishnubhotla, R. *et al.* Scalable graphene aptasensors for drug quantification. *AIP Advances* **7**, 115111 (2017).

5   Wiedman, G. R. *et al.* An Aptamer-Based Biosensor for the Azole Class of Antifungal Drugs. *mSphere* **2** (2017).

6   Wang, G. *et al.* Selection and characterization of DNA aptamer against glucagon receptor by cell-SELEX. *Sci. Rep.* **7**, 7179 (2017).

7   Darmostuk, M., Rimpelova, S., Gbelcova, H. & Ruml, T. Current approaches in SELEX: An update to aptamer selection technology. *Biotechnol. Adv.* **33**, 1141-1161 (2015).

8   Kuila, T. *et al.* Chemical functionalization of graphene and its applications. *Progress in Materials Science* **57**, 1061-1105 (2012).

9   Liu, Y. *et al.* Giant enhancement in vertical conductivity of stacked CVD graphene sheets by self-assembled molecular layers. *Nat. Commun.* **5**, 5461 (2014).

10   Lerner, M. B. *et al.* Toward quantifying the electrostatic transduction mechanism in carbon nanotube molecular sensors. *J Am Chem Soc* **134**, 14318-14321 (2012).

Chapter 5: Graphene-DNA Hybrid Biosensors for Nucleic Acid and Drug Target Detection

Graphene's high sensitivity lends itself to be an excellent material for biomolecular and chemical detection. Nucleic acids, in particular, are proven biomarkers for various diseases, most notably, different types of cancers such as pancreatic, colon, and breast cancer. The detection of synthetic nucleic acids in low concentrations diluted in DI water with DNA-decorated graphene field effect transistors serves as a primary step towards eventual point-of-care diagnosis through human fluid samples.

Graphene aptasensors, or GFETs functionalized with aptamers, which are series of nucleotides selected to bind to a specific target, are an interesting and convenient type of device for low-concentration market drug detection. The purpose of market drug sensing is to act as a more rapid and inexpensive method for therapeutic drug monitoring (TDM) in place of traditional methods such as liquid/gas chromatography mass spectrometry (LC-MS)/(GC-MS), which are time-consuming, costly, and require the employment of highly skilled personnel.

Section 5.1 details the techniques and results for detecting ssDNA with GFETs down to concentrations of 1 fM and detecting single base pair mismatches between a ssDNA probe molecule and its complementary target.

Section 5.2 serves as an extension of section 5.1, where GFETs were prepared for detecting ssDNA in lower concentrations than 1 fM. A limit of ~ 1 aM was reached by increasing the length of the probe and target DNA strands. The GFETs also demonstrated

that they could detect a long target (100 nucleotides) by using a short probe (20

nucleotides) with an increase in signal.

In section 5.3, we explore graphene functionalized with aptamers, or series of nucleotides

selected to bind to a particular target, for the detection of the HIV drug, tenofovir. These

graphene aptasensors, as they are called, can detect tenofovir down to concentrations of 1

ng/mL, which is lower than what is found in the human body for patients taking this

medication.

Section 5.4 uses a method known as "systematic evolution of ligands by experimental

enrichment", or "SELEX" to select an aptamer for an azole class of antifungal drug. The

process relied on a large library, in this case, one of over 10^{14} sequences, exposed to the

target. The sequences that produced no binding with the target were removed, and the

cycle was repeated in this manner until the correct sequence for target binding was left.

This aptamer was then used for fabrication of graphene aptasensors to detect the drug

down to concentrations of ~10 ng/mL.

5.1 Scalable Graphene Field Effect Transistors for Nucleic Acid Detection

Abstract

Scalable production of all-electronic DNA biosensors with high sensitivity and selectivity is a critical enabling step for research and applications associated with detection of DNA hybridization. We have developed a scalable and very reproducible (> 90% yield) fabrication process for label-free DNA biosensors based upon graphene field effect transistors (GFETs) functionalized with single-stranded probe DNA. The shift of the GFET sensor Dirac point voltage varied systematically with the concentration of target DNA. The biosensors demonstrated a broad analytical range and limit of detection of 1 fM for 60-mer DNA oligonucleotide. In control experiments with mismatched DNA oligomers, the impact of the mismatch position on the DNA hybridization strength was confirmed. This class of highly sensitive DNA biosensors offers the prospect of detection of DNA hybridization and sequencing in a rapid, inexpensive, and accurate way.

Introduction

All-electronic DNA biosensors offer considerable promise for rapid genetic screening and nucleic acid detection for gene-expression investigations, pharmacogenomics, drug discovery, and molecular diagnostics[1]. In order to enable these applications, the electronic DNA biosensors need to be sensitive, selective, and based upon a scalable fabrication process. Wafer-scale graphene, a one-atom thick sheet of carbon with

59

remarkable electronic sensitivity, outstanding biocompatibility[2], and extremely low signal-to-noise ratio[3], can be prepared *via* chemical vapor deposition[4,5]. However, very few previous reports on graphene field-effect-transistors (GFETs) for DNA sensing[6-10] were based on scalable fabrication methods. To this point there are no reports of more than 10 functional devices fabricated on a single chip, and the sensitivity has been limited to 100 fM[7].

Here we describe the development of scalable biosensors based on back-gated GFETs with for detection of DNA (**Fig. 5.1.1 a**) with sensitivity as low as 1 fM ($\sim 6 \times 10^5$ DNA molecules in a 1 mL drop). We prepared graphene by chemical vapor deposition (CVD) and fabricated GFETs with conventional photolithography. The GFETs demonstrated high yield ($> 90\%$) and consistent transport properties. The GFETs were functionalized using a well-controlled chemical treatment that enabled high surface coverage with single-stranded probe DNA. DNA biosensors created in this way exhibit a wide analytical range (three decades in concentration) and excellent selectivity against non-complementary DNA oligomers. The sensitivity of the DNA biosensors depends systematically on the length of the oligomer, and for 60-mer DNA 1 fM limit of detection was achieved. The response calibration curves of the DNA biosensors were in excellent agreement with predictions of the Sips model[11] for DNA-hybridization. Our control experiments confirmed that sensor responses were determined by hybridization between the probe and target DNA oligomers, and the results were consistent with earlier reports of hybridization using DNA microarrays. Our methodology has the potential to be developed into a rapid and convenient point-of-care tool with clinically relevant sensitivity.
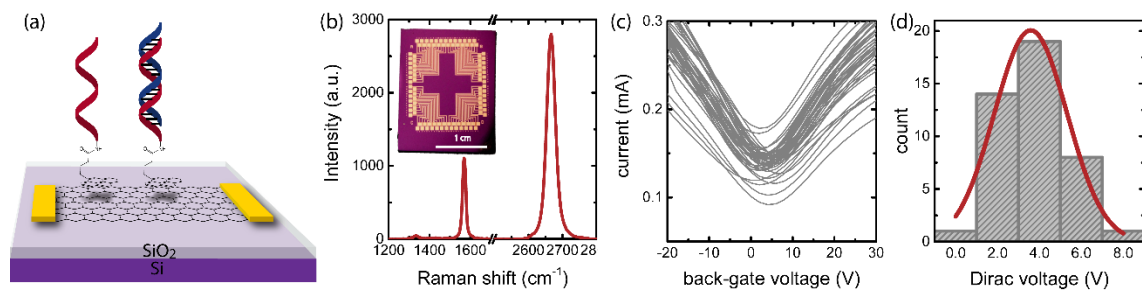
Figure 5.1.1 *(a) Detection of DNA by a graphene field-effect transistor functionalized with complementary DNA. (b) Raman spectrum of the channel region of a graphene field effect transistor (GFET) after processing. Inset: Optical micrograph of an array of 52 GFETs. (c) I-V_G characteristics for an array of 52 GFET devices showing excellent reproducibility. (d) Histogram of the Dirac voltage extracted from the I-V_G characteristics of panel (b) along with a Gaussian fit to the data (red curve).*

Fabrication Process

A 2.5 × 2.5 cm graphene sample was prepared *via* chemical vapor deposition on a copper growth substrate and transferred using an electrolysis bubbling method[12] onto a 2 × 2.5 cm oxidized silicon substrate with pre-fabricated, 45-nm thick Cr/Au electrodes for an array of 52 GFETs. We find that this transfer method effectively limits contamination, doping, and damage associated with graphene transfer. The GFET channels were then defined using photolithography and oxygen plasma etching (**Fig. 5.1.1 b, inset**). The sensor array was cleaned by annealing in an argon/hydrogen atmosphere before further characterization or chemical functionalization (see Methods for additional details of the fabrication process). This method is compatible with scale up to thousands of GFETs or more, as well as integration with prefabricated CMOS signal processing circuitry[13].

The graphene in the GFET channels was single-layer with low defect density, as verified by the 2D/G ratio (~2) and the minimal D peak intensity in the Raman spectrum[14] (**Fig. 5.1.1 b**). The excellent quality of the graphene enables consistent GFET transport properties and high fabrication yield (>90%), based on more than 30 arrays fabricated for

this experiment. As shown in **Fig. 5.1.1 c**, the current-gate voltage (I-V_G) characteristics for all 52 GFETs in a single array are very similar. The Dirac point of the GFETs, where the I-V_G characteristic has a minimum, lies in a narrow range near zero back-gate voltage, 3.6 ± 4.0V (**Fig. 5.1.1 d**), indicating low doping effects induced in our methodology.
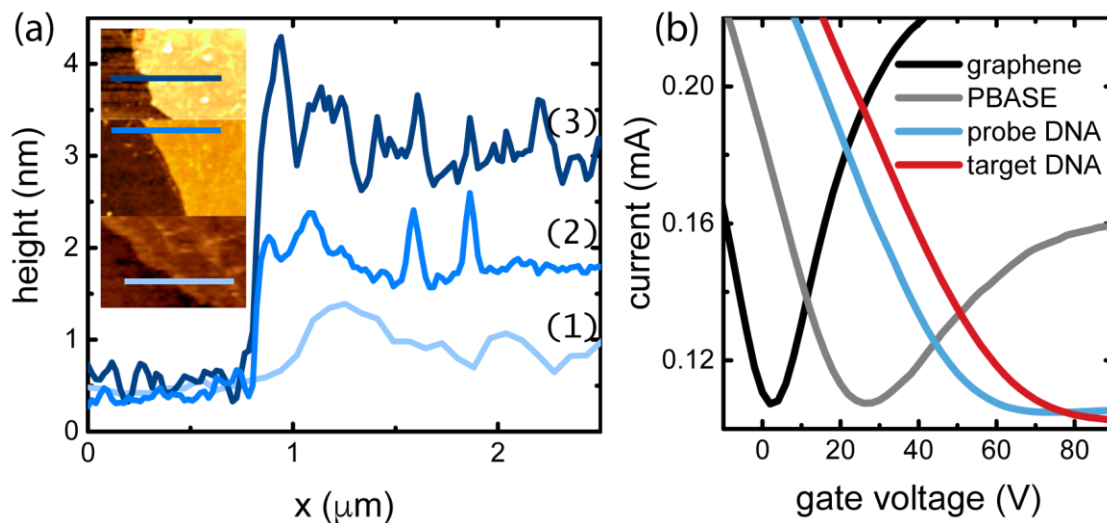
Figure 5.1.2 *(a) AFM line scans of (1) annealed graphene, (2) PBASE-functionalized graphene, and (3) graphene functionalized with PBASE and aminated DNA. Inset: AFM images showing the scan lines plotted in the main figure. Scan lines are 2.5 μm. Z-scale 8 μm. (b) I-V_G characteristics for a typical GFET that was annealed, functionalized with PBASE, reacted with 22mer aminated probe DNA, and exposed to 10 nM target DNA in deionized water.*

After annealing, the GFET channels were functionalized by incubation for 20 hrs in a solution of the bifunctional linker molecule 1-Pyrenebutyric acid N-hydroxysuccinimide ester (PBASE) in dimethylformamide (DMF) (See Methods for details). The aromatic pyrenyl group of PBASE binds to the basal plane of graphene through the non-covalent π-π interaction[15,16]. This process yields a uniform, ~ 1 nm thick monolayer[17] of self-assembled PBASE on the graphene (see linescan (1) in **Fig. 5.1.2 a)**, except at wrinkles (~

nm high) in the CVD graphene created by the transfer process[18]. The aminated (5') probe DNA (22mer, 40mer, or 60mer) was then bound to the PBASE linker by a N-hydroxysuccinimide (NHS) crosslinking reaction (See Methods for details). Due to the high coverage of the PBASE monolayer, the probe DNA molecules were immobilized on the graphene channel at such high density that individual DNA molecules could not be distinguished in AFM images (**Fig. 5.1.2 a**) acquired using a NCST AFM cantilever (Nano World). The average height increase of the GFET due to attachment of the 22mer probe DNA is ~ 1.2 nm, consistent with the molecular size. After attachment of the probe DNA, GFET DNA biosensors were tested against the complementary single strand DNA "target" and various controls.

Results and Discussion

The I-V_G characteristics of the GFET devices were measured in the dry state[5] after each step of functionalization chemistry and again after exposure to the target. The value of the Dirac voltage for each I-V_G characteristic is determined using a curve-fitting method[19] through the equation

$$I^{-1} = \left[e\alpha\mu(V_{bg} - V_D)\right]^{-1} + I_s^{-1}. \tag{5.1}$$

Here I is the current, μ the mobility, V_{bg} the back-gate voltage, V_D the Dirac voltage, α=7.2 $\times$ 10^{16} cm^{-2} V^{-2} the constant relating gate voltage to carrier number density, and I_s the saturation current due to short-range scattering[20]. Formation of the PBASE monolayer leads to an increase in V_D of ~ 23 $\pm$ 3.3 V (**Fig. 5.1.2 b**). This is explained by considering

chemical gating effects associated with residual water on the device surface. Here, we assume that NHS groups are hydrolyzed into carboxyl groups, which deprotonate and acquire a negative charge. Attachment of 22mer probe DNA led to a further 40V increase in the Dirac voltage, which is explained quantitatively through the chemical-gating effect[19] of probe-DNA molecules that become negatively charged due to ionization of phosphate groups in residual water. This Dirac voltage shift corresponds to an increase in the positive (hole) carrier density in the graphene by $\sim 3.0 \times 10^{12}$ cm^{-2}. Assuming chemical gating of 22 negative charges for each oligomer, the density of immobilized probe DNA is $\sim 1.3 \times 10^3$ μm^{-2}, more than an order of magnitude higher than the level of protein attachment achieved using a very similar functionalization approach[5,19]. This corresponds to a separation of ~ 25 nm between DNA molecules, consistent with the uniform DNA coverage observed by AFM (**Fig. 5.1.2 a**).

In response experiments, all 52 GFET sensors on a single chip were tested against a solution with a known concentration of target DNA or a related control in deionized water. The Dirac voltage of the *I-V$_G$* characteristic showed a reproducible shift to positive voltage, ΔV_D, as seen in Fig. 4.1.2 (b). To compare results across the three different DNA targets, for each concentration tested we plot the Dirac voltage shift relative to DV_D^0, the shift measured upon exposure to pure deionized water, i.e., $DV_D^{REL} = DV_D - DV_D^0$, with the results shown in **Fig.5.1.3 a**. For all DNA oligomers tested, the relative shift varied systematically with target concentration, and it is ascribed to an increase in the positive carrier concentration in the GFET channel induced by the negatively-charged phosphate groups of target DNA molecules that have hybridized with probe DNA on the GFET surface.
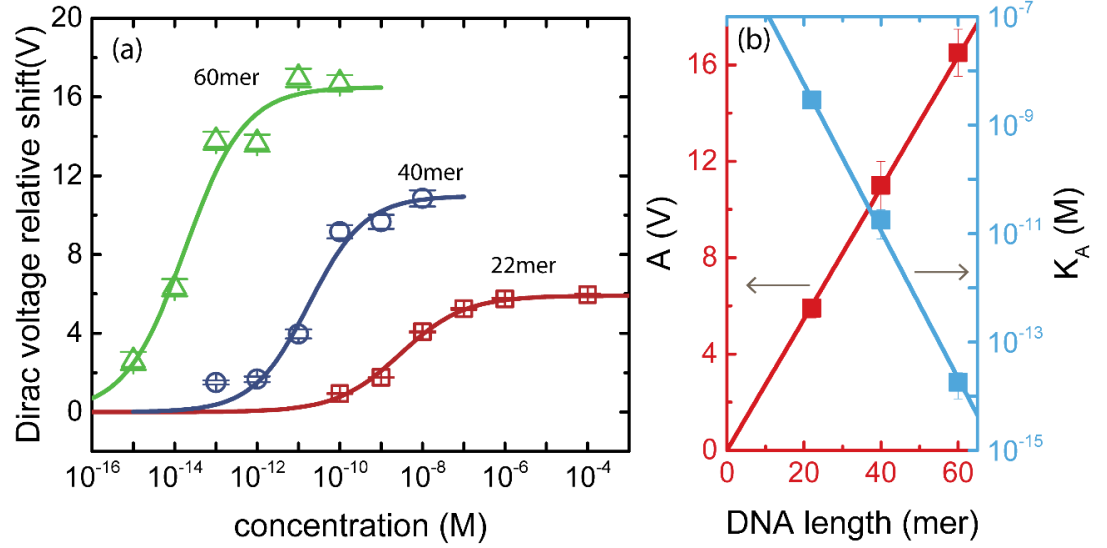
Figure 5.1.3 *(a) Relative Dirac voltage shift as a function of concentration for DNA targets of different lengths. Error bars (standard deviation of the mean) are approximately equal to the size of the plotted point. Solid curves are fits to the data based on the Sips model. (b) Variation of the fit parameters A (red data) and K_A (blue data) in Eqn. (1) with DNA oligomer length. The red and blue lines are fits to the data, as discussed in the main text.*

The Sips model[11,21] for describing DNA hybridization provides an excellent fit to the measured data for ΔV_D^{REL} as a function of target concentration:

$$\Delta V_D^{REL} = A \frac{(c/K_A)^a}{1+(c/K_A)^a} \tag{5.2}$$

where c is the concentration of the target DNA solution, A the maximum response with all binding sites occupied, and K_A the equilibrium dissociation constant. The parameter a in the Sips model represents a Gaussian distribution of DNA binding energies where $a=1$ corresponds to single binding energy level. The best fit to the data for the 22mer target yields fit parameter values: $A = 5.9 \pm 0.4$ V, $K_A = 2.9 \pm 0.9$ nM, and $a = 0.56 \pm 0.07$. The analytic range of the fit (**Fig. 5.1.3 a**) covers three orders of magnitude, from ~100 pM to ~100 nM, with sensitivity ~1.4 V/decade. The dataset presented in **Fig. 5.1.3 a** indicates

that GFET-based DNA biosensors can differentiate between DI water and a solution containing the 22mer target at a concentration of < 100 pM. Although this is higher than an earlier report[7] with a detection limit of 100 fM for 20mer DNA, our approach offers the advantages of scalable fabrication and device miniaturization (52 devices per array). The best fit value of K_A, 2.4 ± 0.8 nM, agrees well with that expected for 20-mer DNA hybridization[22], 1.7 nM. The best fit value of $a = 0.56 \pm 0.07$ implies a heterogeneous adsorption isotherm with a distribution of binding energies rather than a single value DNA-DNA binding energy, which would yield $a = 1$. This binding energy distribution is assumed to reflect significant interactions between the probe and/or target DNA and the graphene surface[23].

	A	K_A	a
22mer	5.9 ± 0.4 V	2.9 ± 0.9 nM	0.56 ± 0.07
40mer	11.0 ± 1.0 V	17.8 ± 9.8 pM	0.64 ± 0.14
60mer	16.5 ± 1.0 V	18.1 ± 9.0 fM	0.60 ± 0.17

Table 5.1.1 *Fitting parameters for all probe DNA sequences tested.*

We also tested GFET DNA biosensors based on 40mer probe DNA and 60mer probe DNA. As shown in **Fig. 5.1.3 a**, the limit of detection (LOD) using 40mer probe DNA is ~ 100 fM, and the 60mer target DNA was reliably detected at a concentration of 1 fM (~ 6×10^5 DNA molecules in a 1 mL drop). The Sips model fit parameters for the three probe DNA sequences are shown in Table 1. The distribution function index is roughly the same for the different DNA targets, indicating comparable degree of binding energy heterogeneity. The fit values for A and K_A demonstrate two advantages of using longer DNA oligomers.

First, the maximum signal level (A) increases nearly linearly with DNA length, at a rate of 0.27 V/mer (see **Fig. 5.1.3 b**, red data points). This is assumed to reflect that the charge carried by each DNA chain increases as the DNA length increases, enhancing the chemical gating effect on the graphene and leading to a proportionately larger Dirac voltage shift. Second, the dissociation constant decreases exponentially for longer DNA. As seen in **Fig. 5.1.3 b**, in the $\log(K_A)$-length relationship is approximately linear, with slope of -0.225 ± 0.024. This is in good agreement with the slope of -0.138 ± 0.006 that was found using a quartz crystal microbalance approach[22].

Multiple control experiments were conducted with 22mer DNA biosensors to verify that the biosensor responses reflected specific binding of the complementary target DNA. A variety of control samples were used, with all control solutions having a concentration of 1 μM in DI water. In **Fig. 5.1.4**, we report the results as the Dirac voltage shift induced by the target or control at a concentration of 1 μM, relative to the shift induced by pure DI water. The target 22mer DNA gives the largest value for the relative Dirac Voltage shift (ΔV_D^{REL}=5.7 ± 0.4 V), which is expected since it should have the highest binding affinity for the probe DNA and therefore the largest associated change in GFET carrier concentration. The single base-mismatch controls are expected to interact more weakly with the probe DNA. It is intriguing to note that the control with a single base-mismatch at the 5' end shows a slight response decrease (~ +4.6 ± 0.7 V or 80 ± 12% of that for the target DNA), while the response to control DNA with the mismatch at the center is strongly suppressed (+0.7 ± 0.5 V), only ~10% of that for the target DNA. Experiments based on DNA oligonucleotide microarrays[24,25] show similar effects in how the response depends on the position of a single base mismatch. The reason why a mismatch at the center of the

strand has such a strong effect on hybridization can be understood through a positional-dependent-nearest-neighbor model[25,26]. The control oligomer with two mismatches, one at the center and one at the 5' end, gave a sensor response that was indistinguishable from the response to DI water, and the same was true for the response to a 1 μM solution of a random sequence DNA oligomer (32% consistent with the target DNA).
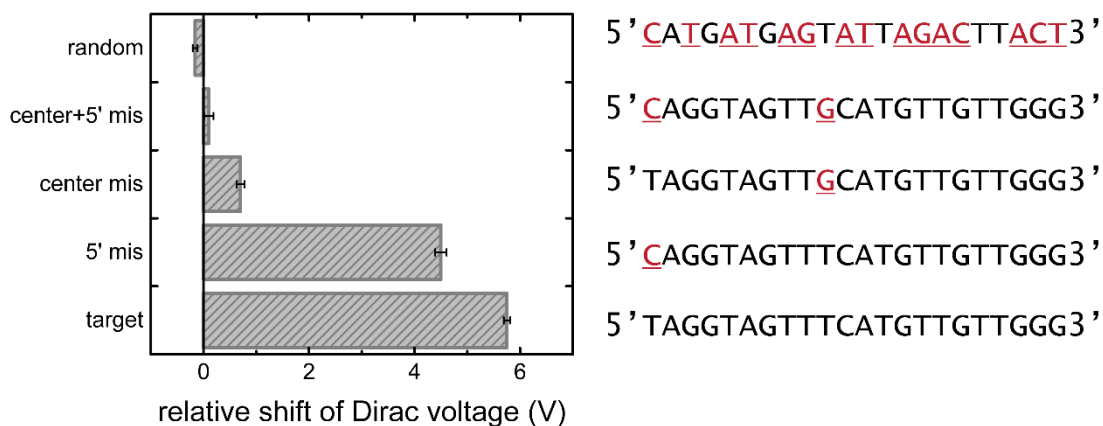
Figure 5.1.4 *Relative response of GFET-based 22mer DNA biosensors to the target sequence and various controls, all at a concentration of 1 μM. The base sequences of the oligomers tested are listed, with mismatches shown in red. Starting from the bottom, the oligomers tested are: target DNA, single mismatch at the 5' end, single mismatch at the center, two mismatches at the 5' end and the center, and random sequence DNA. Error bars are standard deviation of the mean.*

Conclusions

We have developed a scalable fabrication approach for arrays of graphene-based DNA biosensors with all-electronic readout, and we measured their responses to the complementary DNA target and multiple control oligomers. The fabrication process is based upon conventional photolithographic processing and should be suitable for mass production. The GFETs fabricated for the experiments were of very high quality, as evidenced by Raman spectroscopy, Atomic Force Microscopy, and electronic measurements. The DNA biosensors have a wide analytical range and a sensitivity that

depends systematically on the length of the DNA. For 60mer DNA, we achieved a detection limit of 1 fM, enabled by the use of graphene as the transduction material, functionalized with high coverage of probe DNA. Measured sensor responses over a range of six orders of magnitude in concentration were well fit by the Sips model. Control experiments verified that the sensor response was derived from specific binding of the probe DNA to the target DNA, and also confirmed that the complementary DNA with a mismatch at the center hybridizes much more weakly with the probe DNA than at the 5' end.

5.2 Graphene Field Effect Transistors for ssDNA at aM Concentrations and Capture of Long Targets with Short Probes

The work presented here also appears, in some form, in the publication: Vishnubhotla, Ping, Sriram, Dickens, Mandyam, Adu-Beng, Johnson, **2018** *(in preparation)*

Abstract

Graphene-enabled biosensors can be produced in a scalable manner at reasonable cost, and they show significant promise for sensitive detection of small molecules and biomarkers such as proteins, single strand nucleic acids, aptamers, and drug targets. Here, we describe an approach that enables a limit of detection of ~ 1 aM of a ssDNA target, or about 100 strands per mL of deionized water, without amplification. Furthermore, we have shown that a short probe (20mer) has the capability to trap a longer target strand (100mer) with a proportional increase in signal, as expected for an electrostatic transduction mechanism. These results show the potential utility of this technology in nucleic acid detection for disease diagnostics.

Introduction

Graphene field effect transistors (GFETs) show great promise as a platform for DNA detection. GFET DNA sensors can be implemented without need for molecular labeling, which offers reduced complexity and cost compared to more conventional sensor approaches based on PCR, optical detection, or electrochemistry.[27] Early reports showing sub-pM sensitivity[7] and single nucleotide polymorphism (SNP) detection[28] were based on fabrication approaches suitable only for few-device production. More recently, scalable fabrication methods were developed for GFET DNA sensors for detection of complementary single strand nucleic acid targets at fM concentrations with excellent

specificity against single base pair mismatches[29]. GFET-based DNA sensors might eventually find use in multiple domains, including cancer detection based on the presence of cell-free nucleic acids in body fluids.[30,31] Through the use of DNA aptamers, reproducible graphene aptasensors have also been used for detection of small molecule targets[32-34]. These reports were based on graphene grown by chemical vapor deposition, a large-area material in a "layer" format that is compatible with photolithographic processing, which enables reproducible performance across devices and fabrication runs[35]. This gives graphene advantages over one-dimensional nanomaterials (e.g., carbon nanotubes[36] and silicon nanowires[37]) or two-dimensional materials that are less well developed, including the transition metal dichalcogenides[38,39].

The promise of GFETs for nucleic acid detection motivates efforts to enhance the limit of detection for this system. Here, we demonstrate two methods for improving the sensitivity of DNA-graphene biosensors functionalized with single-stranded probe DNA strand for detection of the complementary target strand detection. First, we found that increasing the length of the probe and target to 80 nucleotides each (80mer) enabled a limit of detection (LOD) of ~1 aM without amplification, representing a 1000x improvement over earlier reports[6,7,28,29]. Second, we used a short probe (20mer) to bind to a section of a longer target (100mer), which in the best case led to a ~3x increase in output signal, offering another possibility to lower the LOD for long targets.

For these experiments, monolayer graphene was grown *via* CVD on a copper foil substrate (~ 8 cm x 10 cm) using methane as the carbon feedstock[40]. We used a wafer-scale process where the full graphene film was coated with a sacrificial layer of polymethyl methacrylate (PMMA) and transferred using an electrochemical hydrolysis

method onto a 4-inch Si/SiO$_2$ wafer[12], where electrodes for 11 arrays of 52 GFET sensors had been previously fabricated using photolithography and thermal evaporation of Cr/Au electrodes (5 nm/40 nm; Figure 1). A second round of photolithography followed by O$_2$ plasma etching was used to define the GFET channels with dimensions 10 μm x 100 μm. After photolithographic processing and etching, the GFETs were cleaned in 1165 (Microposit), acetone and IPA, dried with N$_2$, and annealed to remove resist residues with a final device yield exceeding 90%. The quality of the graphene after processing was assessed using Raman spectroscopy, which showed a 2D/G peak ratio of ~ 2, and a low D/G ratio, consistent with that of low-defect, monolayer graphene[14].

(a) (b)
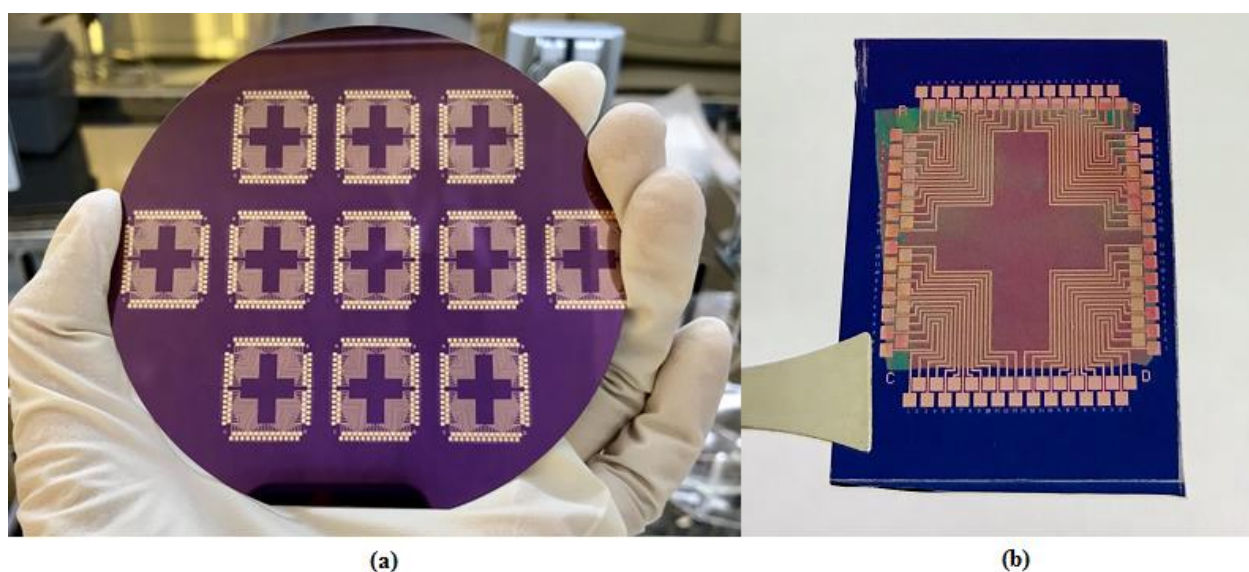
Figure 5.2.1 *(a) Example of a 4-inch substrate used for wafer-scale processing. Four inch wafer patterned with 11 arrays of field effect transistors. (b) graphene-PMMA film on patterned wafer substrate*

For chemical functionalization, the GFET array was first incubated in a 1 mM solution of the linker molecule 1-pyrenebutyric acid N-hydroxysuccinimide ester (P-BASE), which

binds to the graphene surface by non-covalent π-π stacking and allows for immobilization of the probe molecule on the graphene's surface.

This step was immediately followed by incubation in a 1 µM solution of aminated probe ssDNA in deionized (DI) water for 3 hours, followed by rinsing with DI water and drying with compressed N_2 to complete the biosensor fabrication. These functionalization steps yielded full coverage of pyrene and probe DNA on the graphene's surface, which was verified by atomic force microscopy (AFM) (**Fig. 5.2.2**), which confirmed the height profiles expected for as-grown graphene (~1 nm), graphene functionalized with P-BASE (~ 1.5 nm), and graphene functionalized with P-BASE and probe ssDNA (~1.5 nm).
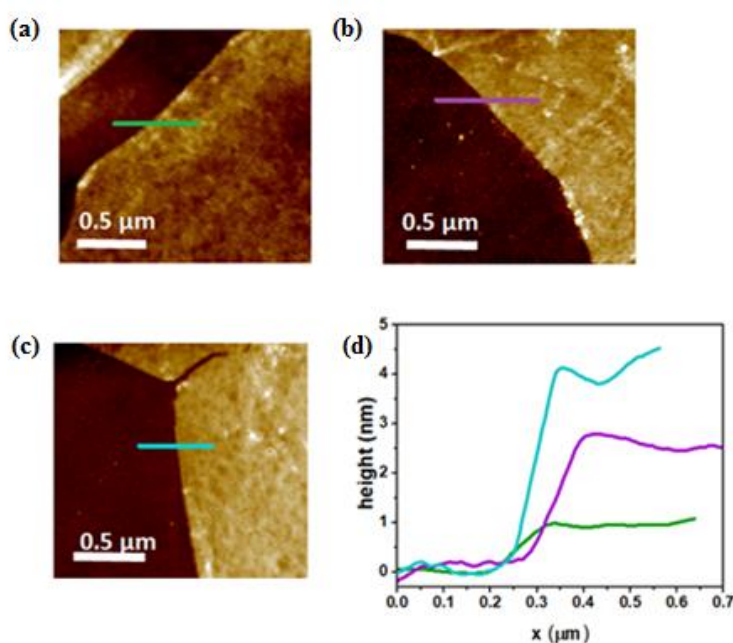
Figure 5.2.2. *Atomic force microscopy with z-scale nm height of ~ 3.5 nm for bare graphene (a), graphene functionalized with pyrene (b) and graphene functionalized with pyrene and an aminated 20mer probe DNA strand (c). The height profiles (d) were as expected for graphene on bare SiO_2 (~1 nm), pyrene (~1.5 nm) and probe DNA (~1.5 nm), verifying that each molecule is binding as expected during functionalization.*

To test the sensor response, the current – gate voltage characteristic (I-V_G) was measured for each device in the array, and the array was then exposed to a solution of target DNA at a known concentration in DI water to allow for target binding. Following incubation in the target solution, the array was blown dry, and the I-V_G curve was measured again for each device (see Methods for more details on sensor fabrication, functionalization, and testing). The signal transduction mechanism is assumed to be the "chemical gating" effect[41], where deprotonation of the phosphate backbone of bound target DNA leaves it negatively charged, leading to an increase in the hole carrier density in the GFET. This leads to a reproducible positive shift in the Dirac voltage, ΔV_D, which varies systematically with the concentration of target DNA in the solution. The sensor response is reported as this Dirac voltage shift, relative to ΔV_0, the shift observed for DI water with no added target:

$$\Delta V_D^{REL}(c) = \Delta V_D(c) - \Delta V_0 . \tag{5.3}$$

Current versus gate voltage statistics of the GFETs showed over a 90% device yield through a standardized growth/transfer process[42], with a Dirac voltage of approximately 10 V, and an average mobility of ~2,000 cm^2/Vs (**Fig 5.2.3 a**) both of which are promising for statistically accurate results. Data was quantified by measuring the shift of the Dirac voltage through I-Vg characteristics measurements, following probe and target attachment, which is seen in **Fig. 5.2.3**.
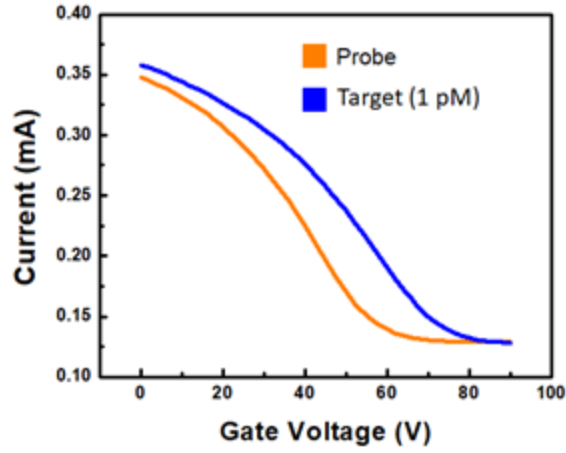
Figure. 5.2.3. *I-Vg shift between probe and target of ~ 20V for attachment of a 1 pM target*

To accurately quantify the shift in the Dirac voltage between probe and target attachment, the following equation was used to fit the hole branch of the I-V$_G$ curves:

$$I^{-1} = \left[e\alpha\mu\left(V_{bg} - V_D\right)\right]^{-1} + I_S^{-1} \tag{5.1}$$

Here, I represents the current, μ is the charge carrier mobility, V_{bg} is the back-gate voltage, V_D the Dirac voltage, α the constant relating gate voltage to carrier number density, and I_S is the saturation constant due to short-range scattering[20].

Building on our earlier report where a 1 fM LOD was achieved with a 60mer probe and target,[1] probe and target strands of length 80 were used to achieve the goal of aM scale detection. The sensor response was reported as the measured Dirac voltage shift (**Equation 5.3**) for many different concentrations. The relationship between this known

75

target concentration and the relative Dirac voltage shift can be described by the Sip's model for DNA hybridization.[11]

$$\Delta V_D^{REL} = A\,\frac{(c/K_A)^n}{1+(c/K_A)^n} \qquad\qquad (5.2)$$

where A represents the maximum response with all binding sites occupied, c is the DNA concentration, K_A is the dissociation constant and is the concentration producing half occupation of a binding site, and n is the Hill coefficient, which expresses the degree to which the DNA interacts with its surroundings, where $n=1$ denotes no interaction. It also indicates the relationship between target concentration and chain length on signal strength, in that a longer chain is comprised of a greater amount of charge, has greater binding affinity, and as a result, lowers the dissociation constant while increasing the shift in the Dirac voltage for a given concentration. This is demonstrated in **Figure 5.2.4 a** for an 80mer probe and target and its dissociation constant, K_A, which was found to be ~ 0.9 fM ± 0.38 fM. Although this value is lower than K_A for a 60mer, it does not quite follow the expected linear trend between K_A versus chain length[22].

According to Guo et. al, DNA maintains a roughly rod-like structure up until ~75 nucleotides, about half the accepted value of the persistence length. This persistence length quantifies the stiffness of polymers and is due to the electrostatic effects of the strand that dominate for longer chain sequences and result in twisting and bending of the strands. Based on Guo's study, it is believed that at 80 nucleotides, full hybridization is unable to occur due to the loss of rigidity in the DNA strand, thus influencing the value of K_A[43]. The commencement of the non-linear behavior can be seen in **Fig. 5.2.4 b**, where K_A begins to deviate from the expected linear behavior. Our data is in agreement with

Guo et. al, as non-linearity becomes apparent around ~75 nucleotides, likely due to the

cessation of a rod-like structure as electrostatic effects in the chain begin to dominate.
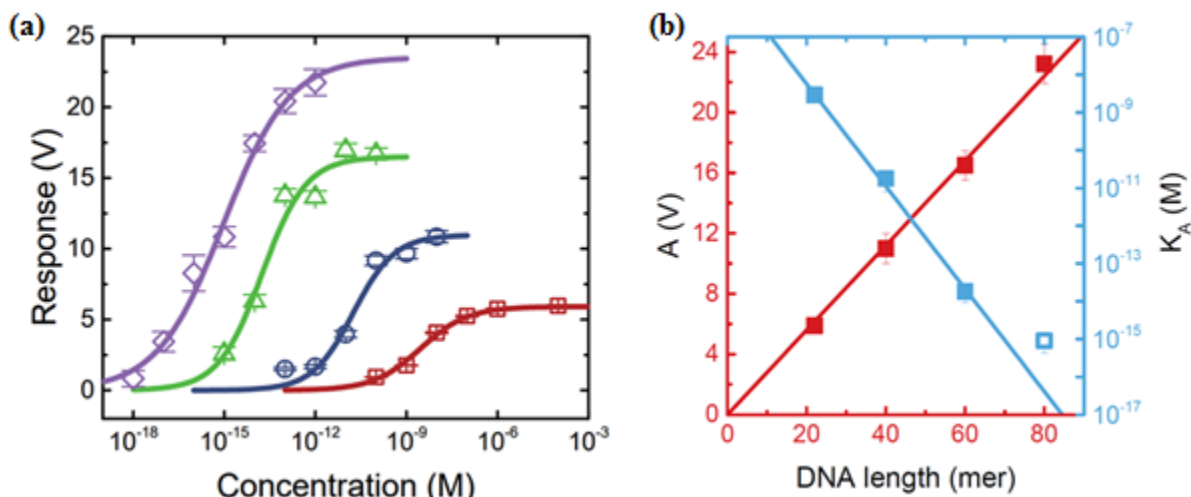
Figure 5.2.4. *(a) Hill-Langmuir curve of Dirac voltage shift versus target concentration of 80mer probe/target (purple) with a K_A of 0.9 fM and a detection limit of ~ 1 aM, compared to our previous study that tested 22mer (red), 40mer (blue) and 60mer (green)[1]; (b) Relationship between K_A and DNA length. Note that the relationship between K_A and length ceases linear behavior for higher strand lengths.*

In addition to reaching a LOD of 1 aM, experimentation confirmed that a short probe

(20mer) is adept at trapping a longer target (100mer) depending on the probe's placement

along the target sequence. Three different probes, each 20 nucleotides in length, were

used to detect a 100mer target strand. Of these three probes, one was complementary to

the 20 nucleotides at the 3' end of the 100mer target, another complementary to the 20

nucleotides at the 5' end of the 100mer target, and the last being complementary to the

middle 20 nucleotides of the 100mer target. All probe concentrations were 1 µm and all

target concentrations were 10 nM.

The various probe and target lengths, along with placement, are described in **Table 5.2.1**. Here, it is evident that although a 20mer probe-target combination provides a considerable signal at a 10 nM concentration normalized to a baseline of DI water (ΔV_D^{REL}), the signal is much larger for a 20mer probe that binds to a 100mer strand in the middle. This is due to the electrostatic transduction mechanism, and is roughly equal to the signal from a 40mer probe/target combination at the same concentration, which yields a LOD of 100 fM[1]. These results exhibit that the chemical gating effect is still appreciable even with partial binding of the target, provided that the probe binds to the center of the target. We notice a trivial signal for a 20mer probe binding to a 100mer target at either the 3' end or the 5' end, possibly due to the loss of rigidity of the 100mer strand length combined with uneven weighting of the target about the probe, hindering the binding and therefore the signal, although this is still not well understood.

Name	Description	ΔV_D^{REL}
"20"	**20**mer probe/20mer target	3.8 ± 0.69 V
"100 M"	20mer probe for **M**iddle 20 nucleotides of **100**mer	11.76 ± 0.77 V
"100 3P"	20mer probe for 20 nucleotides at **3'** end of **100**mer	-0.84 ± 0.7 V
"100 5P"	20mer probe for 20 nucleotides at **5'** end of **100**mer	1.07 ± 0.45 V

Table 5.2.1. *Table clarifying the probe/target combinations and binding placement of short probe/long target compared to a probe/target of equal length and the Dirac shift associated for each combination.*

Table 5.2.1 shows that a 100mer target with a 20mer probe in the middle ('100M') yields a signal roughly three times the signal of a 20mer probe/target combination, illustrated in **Fig.5.2.5**.

78
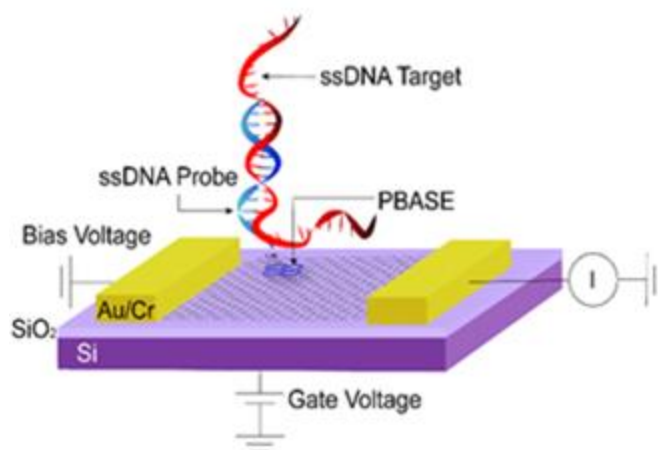
Figure 5.2.5. *20mer probe DNA binding to the 20 nucleotides in the middle of a 100mer target sequence.*

This portion of the study verifies that long target detection is possible, and does not require the use of an equally long probe, and that nucleotides that do not hybridize can still contribute to the electrostatic signal.

Conclusions

This study demonstrates that reaching ~ 1 aM sensitivity of ssDNA targets with ssDNA probes on graphene biosensors is possible without amplification by increasing both the length of the probe and target DNA strands. Furthermore, graphene has exhibited its ability to trap a long target using a short probe, yielding a signal roughly 3 times in magnitude, provided binding of the probe to the middle of the target. The results presented here have been discovered through the use of scalable, sensitive back-gated graphene field effect transistors which are rapid and inexpensive to fabricate, making them ideal for point-of-care diagnostics. Improving detection limits of nucleic acids down to the aM range through this methodology is directly correlated with early disease

diagnosis for ailments with nucleic acid biomarkers for which biomarker upregulation might occur in very small concentrations and with nucleic acid strands that are thousands of nucleotides in length. This report details the lowest detection limit with graphene FETs up to this point.

Methods

Graphene Growth Please refer to Appendix A

Graphene Transfer

A sacrificial layer of polymethyl methacrylate (PMMA, A4 950K) was spin-coated onto the surface of the graphene on Cu foil. Transfer of graphene was carried out *via* an electrolysis bubble method utilizing a NaOH solution (0.05 M) with one electrode attached to the Cu foil and another in contact with the NaOH solution. The formation of H_2 bubbles at the interface of the PMMA/graphene and the Cu foil separated the film from the foil, and the film was then transferred to a series of DI water baths to remove NaOH residue before finally being transferred onto the desired substrate, a Si/SiO_2 wafer with an array of Cr/Au electrodes (5 nm/40 nm) that had been previously fabricated using photolithography and physical vapor deposition.

GFET Fabrication

Please refer to Appendix C

GFET Functionalization

GFETs were soaked in a 1 μM solution of P-BASE and dimethylformamide (DMF) for ~20 hours to ensure uniform coverage of the P-BASE onto the graphene. The devices were then removed from the DMF bath and soaked in a series of DMF, IPA, and DI

water baths for 2 minutes each before being dried with N_2. The chip was incubated in an aminated probe molecule solution, also of 1 μM in DI water for 3 hours before being rinsed with DI water and dried with N_2. To attach the target, a target solution of known concentration in DI water was pipetted onto the chip and left to incubate in a humid environment either for 30-60 minutes (20mer, 20mer/100mer), 2.5 hours (concentrations above Ka), or 4 hours (aM concentrations) before being rinsed with DI water again and dried with N_2. I-V_G curves were measured following probe attachment and target attachment, so as to determine the concentration-dependent shift in the Dirac voltage.

5.3 GFETs for HIV Drug Detection

Abstract

Simpler and more rapid approaches for therapeutic drug-level monitoring are highly desirable to enable use at the point-of-care. We have developed an all-electronic approach for detection of the HIV drug tenofovir based on scalable fabrication of arrays of graphene field-effect transistors (GFETs) functionalized with a commercially available DNA aptamer. The shift in the Dirac voltage of the GFETs varied systematically with the concentration of tenofovir in deionized water, with a detection limit less than 1 ng/mL. Tests against a set of negative controls confirmed the specificity of the sensor response. This approach offers the potential for further development into a rapid and convenient point-of-care tool with clinically relevant performance.

Introduction

Therapeutic drug monitoring (TDM) is crucial for treating patients safely and appropriately as well as for developing new medications. It is particularly important to oversee the consumption of drugs with narrow therapeutic ranges and marked pharmacokinetic variability in target concentrations that are difficult to monitor, and drugs known to cause adverse effects[44] both in individuals and communities. Conventional TDM, however, is based on analytical techniques, such as liquid chromatography and mass spectrometry (LC-MS) that are expensive, time-consuming, and not suitable for clinical use[45]. In this study, we describe the fabrication of nanosensors potentially useful for monitoring the HIV

medication tenofovir, with a methodology that leverages the remarkable sensitivity of the two-dimensional material graphene[2], a highly reproducible and robust fabrication method for graphene field effect transistors (GFETs), and an effective, commercially-obtained aptamer with high affinity for tenofovir, a relevant drug metabolite.

Aptamers are oligonucleotide biorecognition elements selected to bind to a particular target[46], for which there are relatively few reports of use with scalable GFETs[47-50]. It is also possible to integrate aptamer biorecognition layers with metal-oxide-silicon field effect transistors (MOSFETs) using an extended gate geometry[51]. The aptamer used here was obtained commercially (Base Pair Technologies) and has been selected to bind to a metabolite of the HIV market prodrug tenofovir alafenamide. Tenofovir detection is of particular interest as the medication is often used to treat patients affected with HIV by reducing the virus count in the blood of the patient, and therefore decreasing the chance of the development of AIDS. Additionally, hepatitis B virus (HBV) is an accompanying ailment in HIV patients, and tenofovir treatments have shown to reduce the likelihood of HBV forming drug-resistant mutations, making it more suitable for the treatment of HIV than competing drugs[52]. In 2015, Koehn et al reached tenofovir detection limits of 0.5 ng/mL in plasma and cell samples using a method based on liquid chromatography-mass spectrometry (LC-MS)[53]. Such testing is potentially useful for monitoring therapy and to prevent drug accumulation and toxicity in patients with kidney or liver problems. However, despite the fact that this detection limit is much more sensitive than required for TDM of tenofovir, the cost and slow speed of LC-MS make the approach inconvenient for a clinical setting. All-electronic nano-enabled sensors offer a promising pathway towards a low-cost, rapid testing method suitable for use in the clinic or home.

Here we report development of scalable graphene aptasensors for tenofovir based on back-gated GFETs functionalized with a tenofovir aptamer with a limit of detection of approximately 300 pg/mL ($\sim$1 nM). We prepared graphene by chemical vapor deposition and fabricated GFETs using a robust and reproducible photolithographic process, with the GFETs showing a high yield (>90%) and consistent electronic properties[29]. The chemical functionalization procedure provided high surface coverage with the aptamer, as determined using atomic force microscopy (AFM). The aptasensors showed a wide useful range (about a factor of 1000 in concentration) and high selectivity against related drug compounds. Our approach offers the potential for further development into a rapid and convenient point-of-care tool with clinically relevant performance.

Experiments were based on arrays of 52 devices, with graphene grown by chemical vapor deposition (CVD) on a catalytic copper foil using methane as the carbon feedstock. The monolayer graphene film was transferred onto a pre-patterned array of Cr/Au contacts on an Si/SiO$_2$ wafer (chip size of 2.5 cm x 2 cm) through an electrolysis bubbling method[12]. The quality of the graphene was confirmed *via* Raman spectroscopy (**Fig. 5.3.1 a**), showing 2D/G ratio of about 2, as expected for monolayer graphene[14]. GFET channels (10 μm x 100 μm) were defined using photolithography and plasma etching, and the completed GFET arrays (**Fig. 5.3.1 b,c**) were cleaned by annealing in forming gas to minimize contaminants. Additional details of the fabrication are provided in the Methods section.
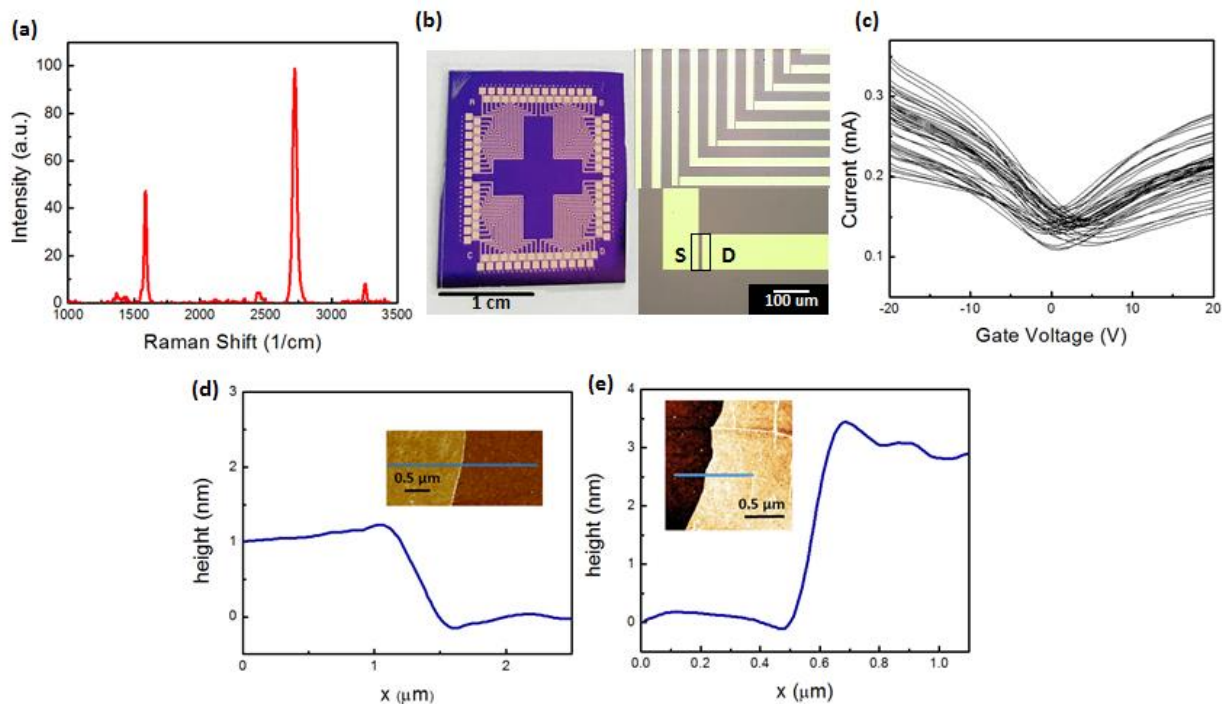
Figure 5.3.1. (*a*) *Raman spectrum of chemical-vapor-deposition-grown graphene on copper foil.* (*b*) *Three optical images of the sensor array. The left panel is a photograph of an array of 52 graphene field effect transistors (GFETs). The right panel has two optical micrographs at different magnifications. The top micrograph shows a region with vertical source electrodes and horizontal drain electrodes. The lower micrograph is zoomed in to show a single GFET, with a box outlining the graphene channel.* (*c*) *Current-gate voltage characteristic of graphene field effect transistors, showing good device uniformity.* (*d*) *Atomic Force Microscope (AFM) line scan for annealed graphene on SiO2. The height of the graphene is ~1 nm, as expected for monolayer graphene after transfer onto SiO2. Inset: AFM topographic image with the scan line indicated in blue.* (*e*) *AFM line scan of annealed graphene on SiO2 after functionalization with 1-Pyrenebutyric acid N-hydroxysuccinimide ester linker and the tenofovir aptamer. The step height is ~3 nm, consistent with the expected heights for the molecular structure. Inset: AFM topographic image with the scan line shown in blue.*

Current-backgate voltage (I-V$_G$) measurements showed good device-to-device uniformity across the array (**Fig. 5.3.1 d**), and the I-V$_G$ characteristics were analyzed by fitting the data to the form[19]:

$$I^{-1} = \left[e\alpha\mu(V_{bg} - V_D) \right]^{-1} + I_S^{-1} \qquad\qquad (5.1)$$

where I is the measured current, μ the carrier mobility, V_{bg} the back-gate voltage, V_D the

Dirac voltage, α the constant relating gate voltage to carrier number density, and I_S the

saturation constant due to short-range scattering[20]. The best fit values for the Dirac

voltage and carrier mobility were typically in the range 0-5 V (2.35 $\pm$ 1.76 V) with an

average mobility of 2,654 $\pm$ 115 cm^2/V-s.

As-fabricated GFETs were functionalized with a commercial tenofovir aptamer using a

well-controlled chemical treatment. First, the GFET array was incubated for ~ 20 hours

in a solution of the linker molecule 1-Pyrenebutyric acid N-hydroxysuccinimide ester (P-

BASE) at a concentration of 1μM in dimethylformamide (DMF). P-BASE is known to

bind with high affinity to graphene *via* π-π stacking[15]. Following the instructions of the

manufacturer, the aminated tenofovir aptamer solution (1 μM in phosphate-buffer of pH

= 7.6) underwent a heat treatment in order to obtain the desired conformation of the

aptamer, and the devices were incubated in this solution for 3 hours following pyrene

attachment. Results of the functionalization process were visualized by AFM (**Fig. 5.3.1

d,e**). The height of bare graphene on silicon oxide was ~ 1 nm, while after binding of the

linker and aptamer, the height of the structure had increased to ~ 3 nm, consistent with

expectations given the molecular structures as well as our earlier report for

functionalization of graphene with single-stranded DNA using the same linker

molecule[29].

For testing of sensor responses, all 52 aptasensors in a single array were tested against a

solution with a known concentration of tenofovir or a related control compound in

deionized (DI) water. The solution was pipetted onto the array and left for one hour in order to allow the tenofovir target to bind to the aptamer layer. After incubation, we observed a consistent shift of the Dirac point to more positive gate voltage (**Fig. 5.3.2 a**), ΔV_D. The sensor array response was taken to be the average Dirac voltage shift relative to ΔV_D^0, the shift measured upon exposure to deionized water: $\Delta V_D^{REL} = \Delta V_D - \Delta V_D^0$. This relative shift varied systematically with tenofovir concentration (**Fig. 5.3.2 b**) and is attributed to an increase in the hole concentration in the GFET due to chemical gating[41] induced by tenofovir binding. Tenofovir contains an amine group and a phosphate group, so it is expected to take on a charge of –e at pH 7.

The Hill-Langmuir model for ligand binding in equilibrium provides an excellent fit to the data for ΔV_D^{REL} as a function of tenofovir concentration

$$\Delta V_D^{REL} = A \frac{(c/K_a)^n}{1+(c/K_a)^n} + Z \qquad (5.2)$$

In this equation, *A* represents the maximum response with all binding sites occupied, *c* is the tenofovir concentration, K_a is the tenofovir concentration producing half occupation of a binding site, and *n* is the Hill coefficient. For the data in **Fig. 5.3.2 b**, the best-fit parameters are *A*= 9.2 ± 0.2 V, K_a = 3.8 ± 1.5 ng/mL, and *n* = 1.1 ± 0.3, which is consistent with independent binding of the target[54]. Assuming a charge of –e for tenofovir, the shift of ~9 V corresponds to a tenofovir density of 1.1×10^3 μm^{-2} when binding is saturated. The GFET tenofovir aptasensors described here have a limit of detection below 1 ng/mL, comparable to that reported for LC-MS, but implemented in a simpler, manufacturable, all-electronic format.

To verify that the sensor response reflected specific binding of tenofovir to the aptamer, tests were conducted against three different HIV drugs as negative controls (lamivudine, abacavir, and emtricitabine), each at a concentration of 200 ng/mL, which for tenofovir would saturate the sensor response. As shown in **Fig. 5.3.2 b**, the sensor response to emtricitabine was zero within statistical error, while abacavir and lamivudine gave small but statistically significant responses. This is ascribed to a degree of structural similarity between these compounds and tenofovir that allows for some small binding probability to the aptamer. In a separate control experiment, an array of unfunctionalized graphene FETs was tested against tenofovir at a concentration of 3 μg/mL, a concentration that would saturate the response of the graphene aptasensor. As shown in **Fig. 5.3.2 b**, the response of the FET array was zero, within statistical error. Overall the results of these control experiments provide strong evidence that the aptasensor response to tenofovir reflects specific binding to the immobilized aptamer.
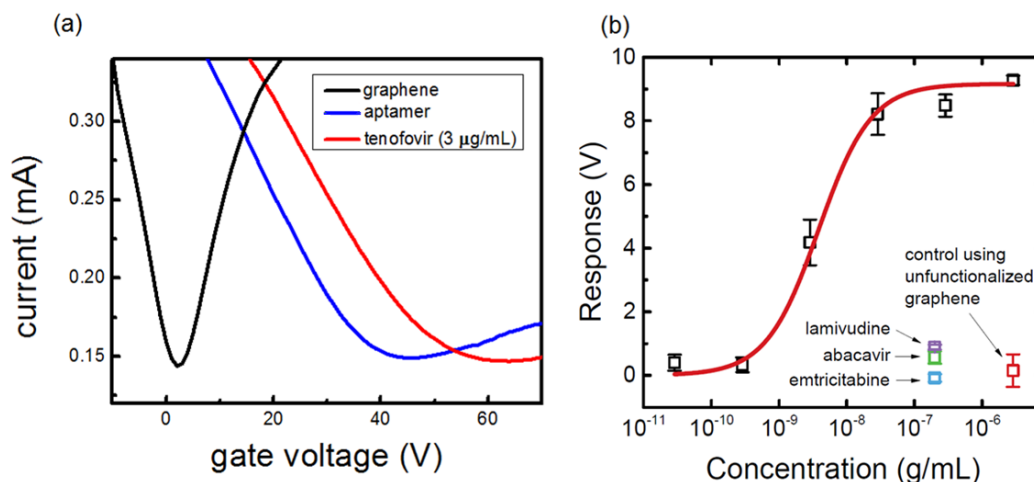
Figure 5.3.2. (*a*) *I-V$_G$ curves for an as-fabricated graphene field effect transistor (GFET; black data), the GFET after functionalization with the aptamer (blue data) and after exposure to tenofovir at 3 μg/mL. (**b**) Relative Dirac voltage shift as a function of tenofovir concentration. The error bars are calculated as the standard error of the mean. The red curve is a fit to the data based upon the Langmuir-Hill model as described in the text. The*

limit of detection is < 1 ng/mL. Data points associated with negative control experiments are also shown; when no error bar is plotted, the error bar is smaller than the size of the plotted symbol. The near null response for the negative controls provides very strong evidence that the dose-response curve reflects specific binding of the tenofovir target and the aptamer.

Conclusions

We have successfully created a scalable approach for fabrication of arrays of GFET-based aptasensors and demonstrated sensitive (~1 nM) and specific detection of the target tenofovir, with a process based on CVD-grown graphene and photolithographic processing, making it suitable for scale-up to industrial production[35]. Our GFET aptasensors have a wide analytical range and sensitivity comparable to LC-MS. Further work is required to optimize the aptasensor performance when applied to real human samples, but their simpler electronic format could make them more suitable for use in a point-of-care setting. For this work, the aptamer was obtained commercially, but we have recently extended the approach to a novel aptamer against azole class antifungal drugs[55], suggesting the ability to incorporate any aptamer into this process.

Methods

Growth of Large-Area graphene by CVD Please refer to Appendix A

Graphene Transfer Please refer to Appendix A

GFET Fabrication Please refer to chapter 4 Section 1

GFET Functionalization and Testing

To functionalize the GFET channels, the chip was placed in a solution of 25 mL of dimethylformamide (DMF, Thermo Fisher) and 2 mg of 1-Pyrenebutyric acid N-

hydroxysuccinimide ester (P-BASE, Sigma Aldrich), for 20 hours. After this time, the chip was removed, sprayed with DMF and soaked in DMF (2 min), sprayed with IPA and soaked in IPA for 2 min, and finally, sprayed with DI water and soaked in DI water (2 min) before being removed and dried with compressed N_2 gas. AFM imaging of samples after this attachment step showed a height of ~2 nm for graphene plus P-BASE (data not shown). To prepare the aptamer solution, 10 μL of a 100 μM aptamer/DI water solution was diluted in 10 mL of phosphate buffer solution ($MgCl_2$, 1mM, pH = 7.4), which was heated from 35 °C to 90 °C, held at 90 °C for 15 minutes, and cooled to room temperature to obtain the necessary configuration of the aptamer. The devices were incubated in this solution for 3 hours. After aptamer attachment (which further increased the AFM height to ~3 nm for graphene, P-BASE and aptamer, as seen in **Fig. 5.3.1 e**), the array was thoroughly cleaned with DI water.

The I-V_G curves of the aptamer functionalized GFET array were measured using a bias voltage of 100 mV, while the gate voltage was swept over the range 0 – 90 V, with a step size of 2V and a scan rate of ~ 0.3 V/s. Next, a tenofovir/DI water solution of known concentration was pipetted onto the chip and left to incubate for one hour in a humid environment to prevent evaporation of the solution and allow for specific binding of tenofovir to the aptamer surface. After incubation, the sample was again thoroughly washed with DI water and blown dry. Finally, the I-V_G curves were measured again, and the data was analyzed to determine the Dirac voltage shift due to target binding.

5.4: Graphene Aptasensors for the Azole Class of Antifungal Drugs

Abstract

This technical report describes the development of an aptamer for sensing azole antifungal drugs during therapeutic drug monitoring. Modified synthetic evolution of ligands through exponential enrichment (SELEX) was used to discover a DNA aptamer recognizing azole class antifungal drugs. This aptamer undergoes a secondary structural change upon binding to its target molecule, as shown through fluorescence anisotropy-based binding measurements. Experiments using circular dichroism spectroscopy revealed a unique G-quadruplex structure that was essential and specific for binding to the azole antifungal target. Aptamer-functionalized graphene field effect transistor (GFET) devices were created and used to measure the strength of binding of azole antifungals to this surface. In total, this aptamer and the supporting sensing platform provide a valuable tool for therapeutic drug monitoring of patients with invasive fungal infections.

Importance

We have developed the first aptamer directed toward the azole class of antifungal drugs and a functional biosensor for these drugs. This aptamer has a unique secondary structure that allows it to bind to highly hydrophobic drugs. The aptamer works as a capture component of a graphene field effect transistor device. These devices can provide a quick and easy assay for determining drug concentrations. These will be useful for therapeutic

drug monitoring of azole antifungal drugs, which is necessary to deal with the complex

drug dosage profiles.

Introduction

Understanding a drug's pharmacokinetics is crucial to safely and effectively treating

patients. Unfortunately, drug levels in patients can vary significantly, and the factors

contributing to this variability are frequently misunderstood. For some critically ill

patients, it is essential to gauge levels of a drug in real time. The best therapeutic

management can be achieved by maintaining a therapeutic level in a patient's

bloodstream and by optimizing individual dosage regimens. These analyses generally

rely upon trough and peak monitoring and real-time kinetic drug modeling. For this

reason, therapeutic drug monitoring (TDM) of some drugs is a critical component of

successful therapy[44]. It is particularly important to monitor drugs with narrow therapeutic

ranges, marked pharmacokinetic variability, target concentrations that are difficult to

monitor, and known to cause adverse events.

The azole antifungal drugs posaconazole, fluconazole, voriconazole, and itraconazole are

an important class of lanosterol 14α-demethylase enzyme-inhibiting molecules[56], which

compromise fungal cell membranes by preventing the synthesis of the key component

ergosterol[57]. A number of these drugs are highly hydrophobic, which creates analytical

challenges. Furthermore, because of their hydrophobic nature it is difficult to know how

much of the drug is freely available in the blood at any given time. Wide variances in the

pharmacokinetics of critically ill patients have been observed for triazole drugs like

voriconazole and posaconazole, which has resulted in a need for TDM[58]. Furthermore,

posaconazole and voriconazole have been shown to have drastically different

bioavailabilities depending on how they are administered and if they are coadministered

with other drugs[59,60]. Therapeutic drug monitoring in conjunction with antifungal therapy

has been shown to promote a more favorable outcome than in non-TDM groups[61].

Unfortunately, TDM requires blood to be drawn from patients and then drug levels in

blood to be evaluated by analytical instrumentation at some later point in time. Analytical

techniques such as liquid chromatography (LC) and mass spectrometry (MS) require

skilled staff and resources that are not found in all hospitals[45]. These barriers become

especially difficult to overcome when treating patients in community hospitals, at home,

or in resource-limited settings. Effective methods for sensing small drug molecules in

blood samples would make it easier to determine drug concentrations.

Any effective TDM method requires a way to capture the drug target from a patient

sample. Antibodies provide specificity and sensitivity as a capture probe, but they are

typically unstable over a wide range of assay conditions. As a more robust alternative,

oligonucleotide-based aptamer capture probes were developed here as a stable and

selective capture molecule for small-molecule drugs. Oligonucloetide aptamers can bind

to a wide variety of target molecules with high affinity. Such oligonucleotides (i.e., DNA

and RNA libraries of 10^{14} to 10^{16} molecules) can be quickly synthesized and screened

using *in vitro* synthetic evolution of ligands through exponential enrichment (SELEX)

methods[46,62].

In this report, azole-specific aptamers were created by using a modified SELEX method

to screen a library of more than 10^{14} DNA sequences. Furthermore, graphene field effect

transistors (GFETs) were developed as a biosensing platform for detection of azole

antifungal drugs with these aptamers. These devices represent a newly emerging type of biosensor that relies on electronic measurements of the transistor itself rather than the flow of an electrolyte solution, binding of antibodies, or fluorescence labeling. Taken together, these results provide a possible path forward for development of an azole antifungal sensing device with potential broader downstream capability of improving therapeutic drug monitoring of small-molecule drugs.

Results

SELEX process results

Azole-binding aptamers were generated from a random 40-mer library using a modified SELEX process (**Fig. 5.4.1**). PCR output and Oligreen dye intensity were used to track the enrichment of posaconazole binders. The output of the PCR experiments for each selection round was plotted after both 15 and 25 cycles of PCR amplification. In addition, the intensity of Oligreen dye on DNA-containing counter-SELEX and SELEX (target) beads (**Fig. 5.4.2 a, b**) was used to track enrichment. During rounds of increased pressure, such as rounds 5 and 6, the total PCR output initially decreased but then recovered over the next rounds. This pattern was most evident past round 10, when the beads were first washed with the competitive molecule fluconazole. This wash allowed for weakly binding molecules to be eluted from the sample. Denaturing polyacrylamide gels were used to assess whether or not the aptamer's molecular weight changed during SELEX. Each round displays two bands, which are a result of leftover double-stranded DNA not digested by λ exonuclease (**Fig. 5.4.3 a**). The single-strand bands from rounds 1 to 10 are the same size as the single-strand control library. The larger bands from rounds 11, 12, and 13 are distinct from the library band even when denatured (**Fig. 5.4.3 c**). Each

band was separated as described in the Materials and Methods section and further

analyzed. This study also included several control sequences to further investigate the

importance of the structure of the round 13 aptamer (Rd 13): Rd 13 Scrambled (S), Rd 13

T6, and Rd 13 T1 were created with various middle lengths. Rd 13 Scrambled was

carefully reordered from the original sequence to fully prevent the formation of G-

quadruplex structures. The two other sequences maintained the G-quadruplex regions but

with two different distances between them.

Rd 13	CGGGGGGAGGCGGAGGGAGGACTGGGG CTTCATTGACGTTCTTCACAGTAGGGGTAA GGGCTTAGGTGGTTGGTGCCTG
Rd 9	CGCGGGGAGGAGGAGGCAGACTGGGGCT TCTTTGACGTTC
Rd 13 S	GCTGTGTGCGTGAGTGGAGTGCGCGCGA GAGTGAGTGCGGTGAGAGATTCGGTGTG CGTGTCGTGATGAATGCGACCGG
Rd 13 T6	CGGGGGGAGGCGGAGGGAGGACTGGGG CTGTAGGGGTAAGGGCTTAGGTGGTTGGT GCCTG
Rd 13 T1	CGGGGGGAGGCGGAGGGAGGACTGGGT GGGGTAAGGGCTTAGGTGGTTGGTGCCTG

Figure 5.4.1 *Possible stem-loop structures of Rd 13 and Rd 9 along with the control sequences*
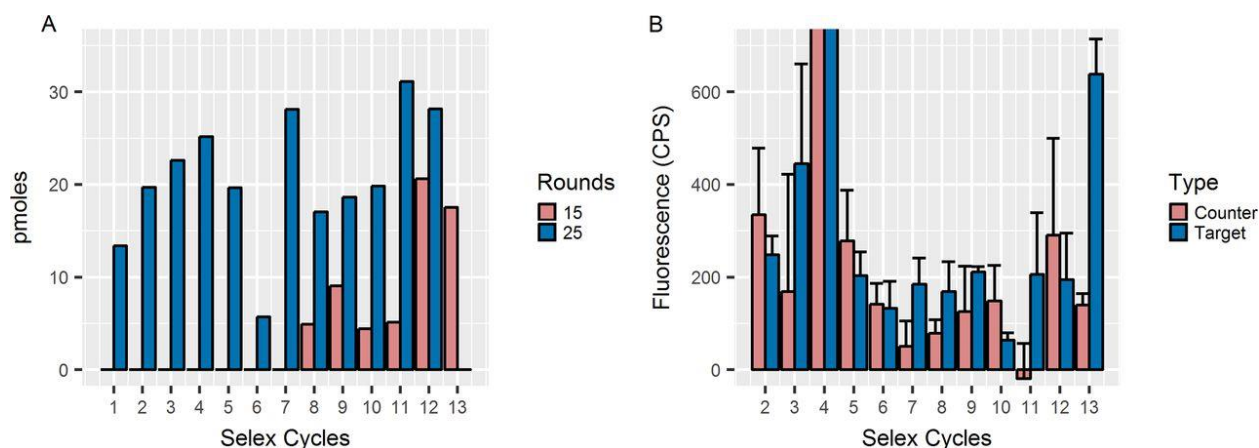
Figure 5.4.2 *(A) After rounds 5 and 6, the PCR output decreased due to increased pressure. The output increased in later rounds, and amplification can even be seen after only 15 cycles of PCR as opposed to 25 cycles. In panel B, the fluorescence intensity of the Oligreen dye from aptamer samples incubated with posaconazole (target)-labeled beads increased relative to control beads as binders were enriched.*
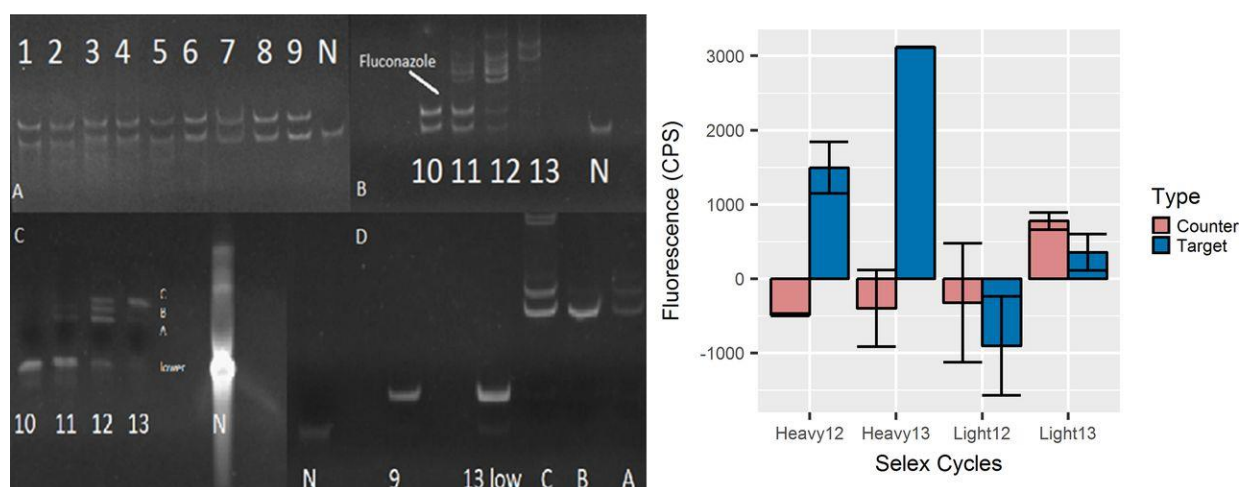
Figure 5.4.3 *After the addition of fluconazole, there were bands that were higher in molecular weight than the starting library, N40 (lane N), and the original sequences. A denaturing polyacrylamide gel (panel C) highlights the fact that these bands were, in fact, aptamers with unique molecular weights and not aggregates of the smaller original library sequence N40. The relative binding capabilities of the heavy and light bands were different from those of the control (counter-SELEX) and target (posaconazole) labeled beads, respectively. Light bands from rounds 12 and 13 showed little preference for either type of beads. The heavy bands, however, bound significantly better to the target labeled beads than the control beads. Negative values occurred when emission at 525 nm was below that at 505 nm. Lanes C, B, and A in panel D correspond to the separated bands C, B, and A in panel C.*

Selection of best sequence

After separation, the "heavy" and "light" bands were analyzed separately for their binding capabilities. The light bands of rounds 12 and 13, those the same length as the library, do not bind to the target (**Fig. 5.4.3**). The heavy bands, however, bound significantly better to the posaconazole-labeled beads versus the control beads and were used for further studies. The heavy bands from round 13 as well as the sample from round 9 were sequenced.

The sequence for Rd 9 is the same size, 40 bases, as the original library. The sequence for Rd 13 is almost double that size at 79 bases. A significant portion of the Rd 9 sequence (in red in **Fig. 5.4.1**) is found in the Rd 13 sequence. Additionally, QGRS mapping was used to predict the existence of G-quadruplex structure in these sequences[63]. The Rd 9 sequence contains one predicted G-quadruplex stretch, highlighted in **Fig. 5.4.1**. Interestingly, the Rd 13 sequence contains two regions of predicted G-quadruplex structure. Stem-loop structure-predicting software was used to map the room temperature (298-K) structures of these aptamers[64]. These predictions show that while Rd 9 forms a stem-loop structure with a single arm, Rd 13 has two separate arms. These features became a major focus of the further study of these aptamers.

Binding affinity of azole drug aptamers

Fluorescence anisotropy experiments were used to determine the dissociation constants (*Kd*s) for the posaconazole-aptamer complex[63,64]. These experiments measured the ability of a boron-dipyrromethene (BODIPY)-labeled posaconazole (PosBD) to rotate in solution. Inhibited rotation, due to aptamer binding, was detected as a change in

anisotropy. In these experiments, only the Rd 13 aptamer caused an increase in anisotropy from titrations of a constant PosBD concentration with increasing amounts of DNA aptamers (**Fig. 5.4.4**). The control library and Rd 9 fail to bind to the PosBD. It should be noted that the control library contains the primer sequences, bringing the total length to 86 nucleotides. This fact suggests that the difference in molecular weights between Rd 13 and Rd 9 is not the sole reason for the difference in anisotropy. The dissociation constant when fitting to the fraction bound (F_{bound}) is 2.7 ± 1.2 μM. The overall dissociation constant for PosBD might be weaker than that of posaconazole given the fact that PosBD was not used for SELEX. The differences in anisotropy changes were further used to probe the specificity of the aptamer for the target. Specificity was interrogated with respect to two other BODIPY-labeled molecules: isavuconazole (ISV), which is chemically similar to posaconazole, and caspofungin (CSF), which is chemically dissimilar since it is an echinocandin class drug. Titration of 100 pmol of Rd 13 aptamer into a 125-μl solution containing 100 pmol of PosBD causes a greater anisotropy change than titration into 100 pmol of BODIPY-labeled ISV or CSF (**Fig. 5.4.5**). Titration of Rd 9 or the library into 100 pmol of PosBD causes little to no change in anisotropy. The truncated versions T6 and T1 cause less of an anisotropy change, although Rd 13 T6 is not significantly different (**Fig. 5.4.5 b**). The Rd 13 Scrambled aptamer did not cause a significant anisotropy change compared to a control such as EDTA and hence did not bind to PosBD. These results indicated that the G-quadruplex structure is necessary for binding.
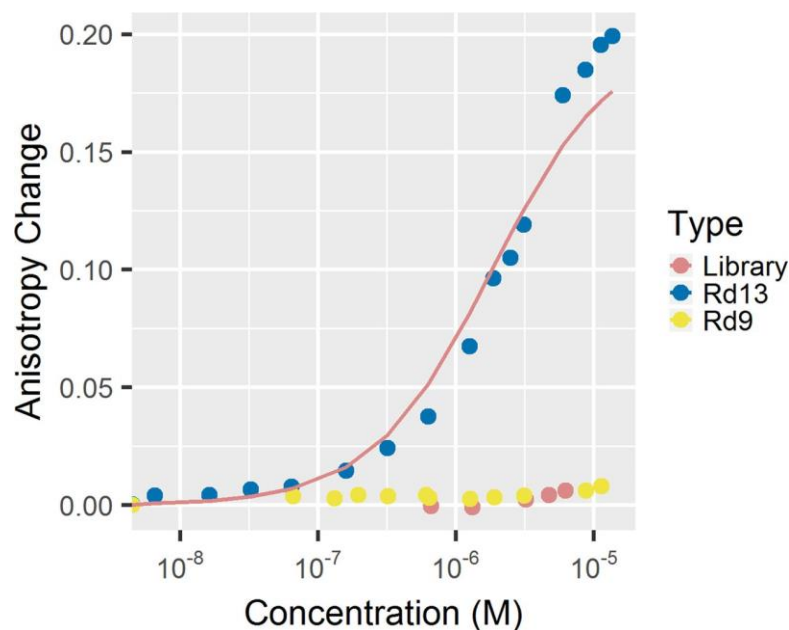
Figure 5.4.4 *PosBD anisotropy changed when the aptamer was titrated into 100 pmol of PosBD per 125 μl. (Example traces are shown.) The anisotropy changed neither with the earlier round (round 9) nor with the control library.*
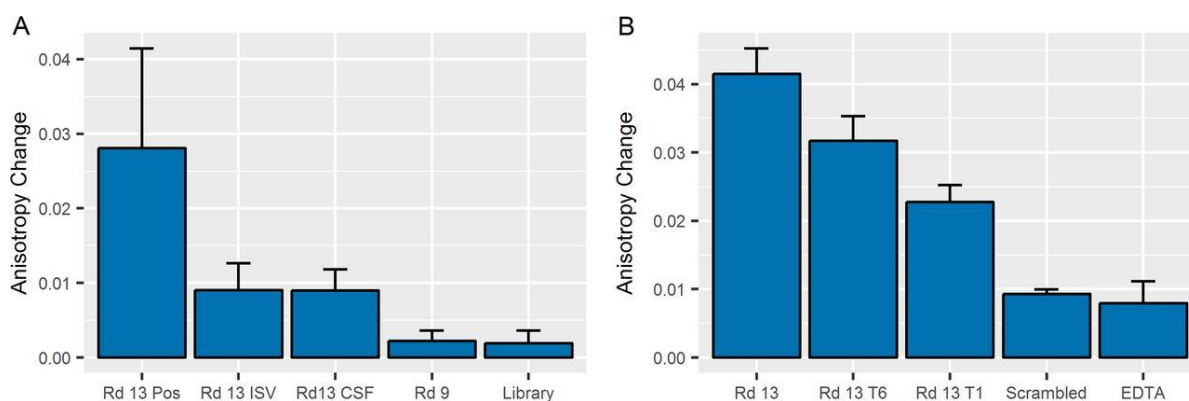
Figure 5.4.5 *One hundred picomoles of aptamer (Rd 13, Rd 9, or the library) was titrated into 100 pmol of various BODIPY-labeled drugs (posaconazole [Pos], isavuconazole [ISV], and caspofungin [CSF]) (A). Titration of Rd 13 into PosBD caused a significant change in anisotropy. Titration of Rd 13 into other BODIPY-labeled drugs or Rd 9/library into PosBD caused little changes in anisotropy. These data suggested that Rd 13 binds best to posaconazole. Aptamers of different lengths were titrated into 100 pmol of PosBD (B). The full-length Rd 13 aptamer caused the greatest change in anisotropy, and the truncated and scrambled versions showed decreased amounts of anisotropy change. The scrambled version only caused a change proportional to that caused by a chelator, EDTA.*

Binding competition assay

The aptamers developed in this study bind to azole class antifungal drug targets, specifically to those with the exposed terminal azole group like posaconazole. High specificity is important for downstream diagnostic devices to prevent false-positive readings. The anisotropy experiments were modified slightly to develop a competitive assay to further probe specificity. This experiment showed the relative abilities of various drugs to replace PosBD in the aptamer complex (**Fig. 5.4.6**). As expected, posaconazole displaces the greatest amount of PosBD. The related drugs fluconazole and itraconazole replace fewer PosBD molecules. The chemically distinct echinocandin antifungal drugs micafungin and caspofungin had little effect. Of the azole drugs, itraconazole is the most hydrophobic. The smaller amount of PosBD replacement with itraconazole versus posaconazole suggests that binding is not solely driven by hydrophobic effects. Secondary structure plays a large part in the binding of azole targets to these aptamers.
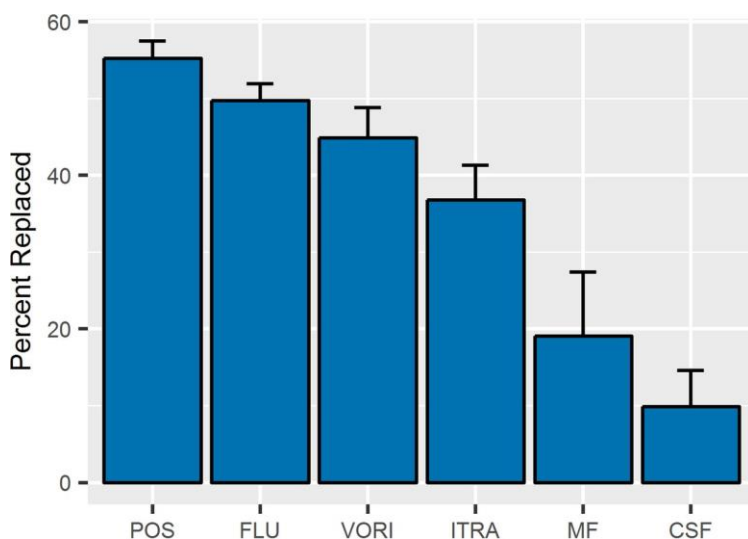
Figure 5.4.6 *After initial PosBD incubation, the aptamer was heated at 70°C in the presence of posaconazole (Pos), fluconazole (Flu), itraconazole (Itra), voriconizole (Vori), micofungin (MF), or caspofungin (CSF) and then cooled on ice. The percentage replaced was calculated as a function of the loss in anisotropy.*

CD spectroscopy and secondary structure analysis

Circular dichroism (CD) spectroscopy experiments were conducted to probe the folding

of these aptamers in the presence of salts and posaconazole. CD spectroscopy is a

technique that is widely used in biophysics to predict secondary structures of

biomolecules[65]. Molecules such as nucleotides and proteins can contain structures that

will interact differently with left- and right-polarized light, which can be detected by CD

spectroscopy. Secondary structure controls the complex formation of aptamers and target

molecules. As these aptamers all contained multiple stretches of guanine residues, there is

a high possibility that they form G-quadruplex structures. The CD spectra of Rd13 are

characteristic of G-quadruplex folded DNA, with a maximum at 260 nm and a minimum

at 240 nm (**Fig. 5.4.7 a**)[66,67]. Addition of magnesium chloride to the solution both

increases the signal at 260 nm and decreases the signal at 240 nm. This suggests that the

aptamer forms a G-quadruplex structure in low-salt buffer, which is slightly enhanced

with the addition of salts. In contrast, the signal is not altered significantly by adding

posaconazole in the absence of divalent salts (**Fig. 5.4.7 b**). The most drastic change

occurs when the aptamers are exposed to a combination of both posaconazole and salts.

The aptamers Rd 9 and Rd 13 show similar CD signals in 0.2 mM magnesium chloride.

A G-quadruplex structure formed with Rd 9 and Rd 13 but not with Rd 13 Scrambled

(**Fig. 5.4.7 c**). When 100 μM posaconazole was added, there was a change in the CD

signal for Rd 9 and Rd 13. With posaconazole, the spectrum for Rd 9 changes to contain

a maximum at 230 nm and a drastic minimum at 280 nm (**Fig. 5.4.7 d**). The spectra for

Rd 13 in magnesium chloride with posaconazole contain two maxima at about 230 and

270 nm with a minimum above 300 nm. The Rd 13 Scrambled sequence does not

undergo any further change in secondary structure. The G-quadruplex structure of Rd 13

forms in the presence of salt, and this structure then changes when the target is added.
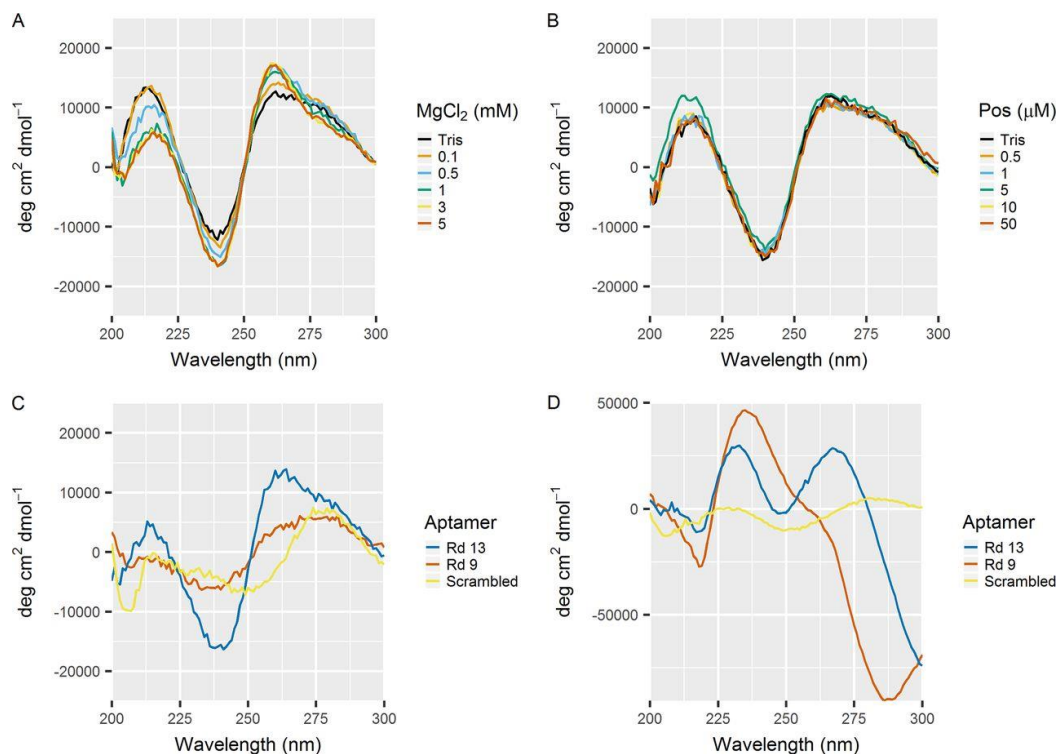
Figure 5.4.7 *Addition of magnesium chloride to the Rd 13 aptamer enhances G-quadruplex folding (A), but addition of posazonazole alone does not (B). This is seen in an increase in the maximum at 260 nm and a decrease in the minimum at 240 nm. Both Rd 13 and Rd 9 exhibit G-quadruplex structure in 0.2 mM magnesium chloride salt (C). The structure changes drastically in the presence of magnesium chloride and 100 μM posaconazole (D). The Rd 13 Scrambled aptamer does not change, but Rd 9 now contains a peak of 230 nm and a minimum at 280 nm and Rd 13 contains two peaks at 230 nm and 260 nm with a new minimum peak above 300 nm.*

GFETs

Graphene field effect transistors (GFETs) are a robust platform for detecting the binding

of small molecules to a surface[68]. As a transistor, GFETs allow for the flow of charge

between a gate and a source over a single sheet of carbon atoms. This sheet is extremely

sensitive to changes or binding above it, seen as a change in the Dirac voltage needed for

charge to flow. When combined with GFET devices, these aptamers act in an induced-fit

manner, which allows them to function as a small-molecule capture arm on a supported surface. GFET devices functionalized with amino-Rd 13 were used to measure the posaconazole concentration (**Fig. 5.4.8**). Posaconazole was diluted from dimethyl sulfoxide (DMSO) into SELEX buffer as described above. The sensor output signal was taken to be the Dirac voltage shift, measured relative to the shift induced upon exposure to pure buffer. As concentrations of posaconazole were increased from 0.01 μg/ml to 100 μg/ml, the relative Dirac voltage shift increased to upwards of −6 V. The variation of the relative Dirac voltage shift with concentration was well fit by a model based on the Langmuir-Hill theory of equilibrium binding, where the dissociation constant of the aptamer is a fitting parameter[5]. The best-fit value of 1.8 ± 0.5 μg/ml (2.6 ± 0.7 μM) is in good agreement with the value of 2.7 ± 1.2 μM derived from the anisotropy assay. In a negative-control experiment, treatment with the echinocandin drug caspofungin produced a negligible shift in the gate threshold voltage, providing strong evidence that the sensor response reflects specific binding of the target to the aptamer probe. The observed values of the relative Dirac voltage shift are in a range similar to that of a similarly designed aptamer-based GFET biosensor biosensing for an HIV drug[33]. These data suggest that Rd 13 aptamer chemically attached to the GFET surface binds posaconazole in a similar fashion to free Rd 13 aptamer in solution.
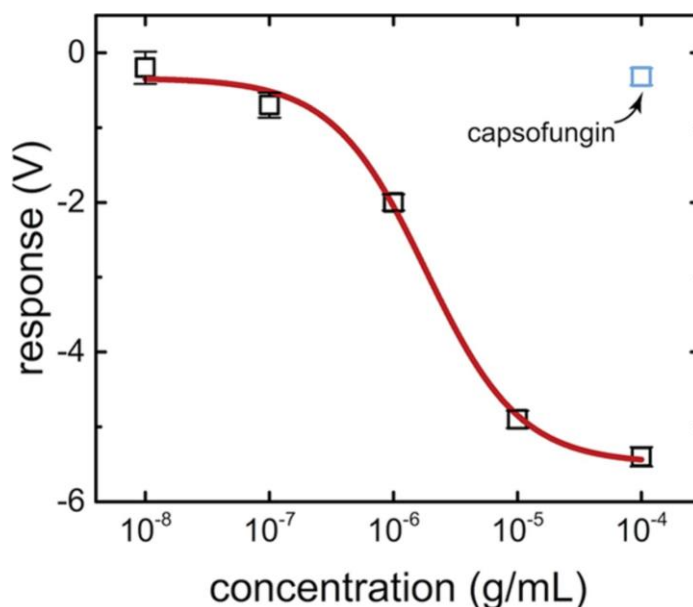
Figure 5.4.8 *The aptamer-based GFET devices showed a detectable threshold Dirac voltage shift between 0.1 mg/ml and 0.1 μg/ml with posaconazole (Pos) and none with CSF. The red curve indicates a fit to a Hill-Langmuir equation. The fit values, especially the low microgram-per-milliliter range are therapeutically relevant concentrations of azole class antifungal drugs.*

Discussion

Therapeutic drug monitoring requires a method of capturing molecules and separating

them from a sample for analysis. This report highlights the development of an azole drug-

capturing oligonucleotide using the SELEX process and the discovery of a unique

structure that allows it to bind azole antifungal drugs. Circular dichroism

spectrophotometry showed that this oligonucleotide works as a scaffold with two sections

of G-quadruplex folds. Large protein target aptamers have been made before using two

separate G-quadruplexes linked chemically to bind at separate sites[69]. These types of

folds rarely interacted with smaller, hydrophobic molecules due to the highly charged

nature of single-stranded DNA (ssDNA). The larger Rd13 aptamer was likely generated

as a result of the interaction between single G-quadruplex-containing aptamers. When

azole drugs bind to these aptamers, a structural change occurs. The CD spectra of these changes are similar to CD spectra for B→Z DNA transitions[70,71]. This type of dual-G-quadruplex aptamer proved ideal for capturing small hydrophobic molecules. The anisotropy binding experiments show that the poly(G) region is essential for target binding. When bound to the surface of a graphene field effect transistor, the aptamer works as a capture arm. This arm collects posaconazole from the sample, which leads to a change in the GFET gate voltage. The azole "aptasensor" adds to the list of other aptamer-based sensing devices[72,73]. Unlike these other devices, however, GFET aptamer biosensors have the potential to function without the need for secondary antibodies, fluorophores, or electrochemical mediators[29]. The versatility of the oligonucleotide-based biosensor opens the door to numerous different applications.

Taken together, the unique structure and binding properties of the oligonucleotide provided with the sensitivity of graphene field effect transistors could prove useful for therapeutic drug monitoring. Posaconazole and the other azole class antifungal drugs exhibit strong hydrophobicity and protein binding. Despite this fact, this aptamer binds specifically to azole drugs. There are other aptamers directed toward clinically interesting drugs, such as the aminoglycoside antibiotics and antiretroviral drugs among others[74,75]. The work presented here provides the first basic step toward effective therapeutic drug monitoring: a method of capturing and sensing the drug. These other aptamers could also be utilized as capture arms for a graphene-based sensing platform. The next step will involve testing patient samples and validating their usefulness in clinic. In the near future, aptamer-based GFET biosensors could be mass produced for a fraction of the cost of other methods such as liquid chromatography-mass spectrometry (LC-MS). These tests

can be performed in a manner of minutes, negating the need for culture-based methods, which can take upwards of 24 to 48 h. Such devices will allow clinicians to quickly assess azole concentrations in a patient's blood and provide them with the additional care that they need.

Materials and Methods

The N40 DNA aptamer library was purchased from TriLink BioTechnologies, Inc. (Ronkonkoma, NY). Other oligonucleotides, including amino-functionalized oligonucleotides, were synthesized by IDT (Coralville, IA), Sigma-Aldrich (St. Louis, MO), and Biosearch Technologies (Novato, CA). Carboxyl Dynabeads (14305D), the Oligreen single-stranded DNA (ssDNA) assay kit, and BODIPY fluorescent dye were purchased from Life Technologies, Inc. (Carlsbad, CA). Streptavidin-conjugated magnetic beads and λ exonuclease were purchased from New England Biolabs (Boston, MA). Azole drugs were purchased from Santa Cruz Biotechnologies (Dallas, TX). All other reagents and solvents were purchased from Thermo Fisher Scientific (Waltham, MA). Graphene devices were fabricated in-house using methods described in previous work.

SELEX process

The aptamer library from TriLink BioTechnologies was prepared by dissolving 1 nmol of DNA in 100 µl of SELEX buffer (140 mM sodium chloride, 2 mM potassium chloride, 5 mM magnesium chloride, 2 mM calcium chloride, 0.05% Tween in 20 mM pH 7.4 Tris buffer). The library was heated at 94°C for 3 min, placed on ice for 5 min, and then

incubated at room temperature (25°C) for 5 min. Next, the DNA library was incubated

for 1 h at 50°C and 2 h at room temperature and then in later rounds for 10 min at 50°C

and 20 min at room temperature. For the first round, the library was incubated with 1 mg

of unlabeled carboxyl Dynabeads (counter-SELEX). The beads were carefully

concentrated using a magnet. The library was then incubated with 1 mg of posaconazole-

labeled beads for 1 h at 50°C and 2 h at room temperature. The beads were washed 3

times with 100 µl SELEX buffer and once with 100 µl Millipore water incubated with

1 nmol posaconazole in 20 µl of water with 0.01% DMSO for 1 h. The recovered DNA

was purified using a Zymo Research DNA preparation column. Recovered DNA was

amplified under two PCR conditions. First, the 20 µl of DNA was amplified using a

TaKaRa rTaq DNA polymerase enzyme. The mixture contained 2.5 µl (10 µM) forward

primer, 2.5 µl (10 µM) phosphorylated reverse primer, 5 µl (2.5 mM) deoxynucleoside

triphosphates (dNTPs), 5 µl 10× $MgCl_2$ buffer, 0.5 µl (2.5 U) rTaq enzyme, 20 µl DNA,

and 14.5 µl Millipore water. PCR was performed under the following conditions: an

initial round at 94°C for 5 min and then 15 cycles of 94°C for 30 s, 50°C for 30 s, and

72°C for 1 min followed by a final 5 min of extension at 72°C. This sample was then

treated as is with 1 µl (5 U) λ exonuclease and incubated at 37°C for 30 min. This

mixture was purified using a Zymo column, and the output was checked for absorbance

at 260 nm using a Nanodrop spectrophotometer. If the yield was less than 1 pmol, an

additional PCR was conducted as described above but substituting 10 cycles for the 15

cycles. Further rounds of SELEX included the following modifications: for rounds 2

through 5, 200 pmol beads was used instead of 1 nmol. After round 5, incubation times

were decreased to 30 min for counter-SELEX and then 10 min at 50°C and 20 min at

room temperature. After round 6, the bead capacity was decreased to 20 pmol. In rounds 11 to 13, beads were incubated for 1 h with 1 µl of 1 M fluconazole in 20 µl, first as an additional competitive wash, before washing with posaconazole.

SELEX result tracking

In each round, 1 µl of DNA-incubated control beads and 1 µl of DNA-incubated posaconazole-labeled beads were saved after washing with water but before posaconazole elution. The DNA content was assessed using a 1:800 solution of Oligreen dye in 20 mM Tris buffer with 2 mM EDTA at pH 7.5, and the samples were analyzed using a Photon Technology International (PTI) fluorometer. PCR output was measured using a Nanodrop spectrophotometer. DNA size was investigated by running an 8% polyacrylamide gel, and denaturing gels were run using an 8% polyacrylamide gel with 8 M urea in SDS buffer after loading DNA treated with formamide at 100°C. Sequencing of various rounds was performed by Macrogen (Rockville, MD) to determine the sequence for that round.

Fluorescence binding experiments

Purified bands and synthesized sequences were prepared by taking 2 pmol and dissolving them in 100 µl SELEX buffer. These solutions were heated at 94°C for 3 min, on ice for 5 min, and at room temperature for 5 min. The samples were incubated with 20 pmol posaconazole-labeled and unlabeled beads at 50°C for 10 min and room temperature for 20 min. The samples were then washed 2 times with water, and 125 µl of a 1:800 dilution of Oligreen dye was added. Samples were then heated at 94°C for 3 min, the beads were

concentrated, and the supernatant was collected. Samples were excited at 480 nm with emission scanning from 500 to 550 nm. The fluorescence was recorded as counts per second at 520 nm minus the counts per second at 505 nm.

Fluorescence anisotropy binding experiments

Fluorescence anisotropy experiments were conducted using a PTI fluorometer with fluorescence polarizers. One hundred picomoles of BODIPY-labeled posaconazole (PosBD) was added from DMSO (1 µl) to 125 µl of modified SELEX buffer (140 mM sodium chloride, 2 mM potassium chloride, 5 mM magnesium chloride, 2 mM calcium chloride in 20 mM Tris buffer, pH 7.4)[64]. Fluorescence anisotropy experiments were recorded using a polarizer system, and the G-factor was calculated manually for each run but consistently fell within 0.44 to 0.45. Anisotropy measurements were recorded first for 2 min. After the initial 2 min, aliquots of aptamers from 1 to 2,000 pmol were added, and samples were equilibrated for 5 min. The value of the anisotropy was taken to be the average anisotropy of the last 60 s after equilibration. Anisotropy values were plotted as the change in anisotropy:

$$\Delta\langle r\rangle(C) = \langle r\rangle(C) - \langle r\rangle_0 \tag{5.3}$$

These values were used to calculate a bound fraction (F_{bound}):

$$F_{bound}(C) = \frac{\Delta\langle r\rangle(C)}{\Delta\langle r\rangle_{max}} \tag{5.4}$$

The bound fraction was further used to calculate a dissociation constant (K_d) by fitting to

$$F_{bound}(C) = \frac{C}{C + K_d} \tag{5.5}$$

Fluorescence anisotropy competition assays

Competition assays were performed using the same measurement techniques described above for binding assays. In this experiment, 50 pmol of PosBD was added from DMSO into 125 μl of modified SELEX buffer, and the anisotropy was recorded for 2 min. One thousand picomoles of aptamer was then added and allowed to equilibrate for 10 min. After this time, 1,000 pmol of an unlabeled drug molecule was added, and the solution was heated up to 70°C for 3 min and cooled on ice for 2 min. The heat-ice cycle was performed twice. The anisotropy was then recorded again for another 5 min. The percentage of PosBD replaced was calculated as

$$\% \text{ replaced} = 100 \times \frac{\langle r \rangle_{\text{aptamer, drug}} - \langle r \rangle_0}{\langle r \rangle_{\text{aptamer}} - \langle r \rangle_0}$$

(5.6)

The percentage replaced equals 100 multiplied by the anisotropy with aptamer and drug replacement minus the initial anisotropy divided by the anisotropy caused by the aptamer alone minus the initial anisotropy.

CD experiments

Experiments were performed using an Aviv model 420 CD spectrophotometer. All aptamer samples were prepared at a 10 μM concentration in 20 mM Tris buffer (pH 7.4). Increasing amounts of salts and/or azole antifungal drugs were added, and the CD spectra were recorded from 300 nm to 200 nm.

GFET functionalization and testing

The chemical vapor deposition (CVD) method with a methane source was used to grow graphene, which was then transferred via electrolysis onto a patterned Si/SiO_2 surface. This surface contained chromium and gold electrodes, and the graphene channels

between them were further defined through photolithography and annealed in an argon-hydrogen environment. GFETs were incubated in 1-pyrenebutyric acid *N*-hydroxysuccinimide ester (P-base) and dimethylformamide for 20 h. After this incubation, the devices were further incubated in a solution of phosphate-buffered saline (PBS; pH 7.6) containing the Rd 13 aptamer for 3 h. The devices were heated from 70 to 90°C, held at this temperature for 15 min, and then allowed to cool down to room temperature. In order to test the devices, the I-V_G properties (ideal transistor's current-to-gate voltage) of GFETs were determined with posaconazole and caspofungin.

Chapter 5 Conclusions

Despite graphene's lack of a band gap, its immense sensitivity can be exploited for sensing purposes, where graphene sensors are adept at detecting single base-pair mismatches, the placement of the mismatch in the chain, and target DNA strands down to concentrations of 1 aM.

Furthermore, graphene aptasensors are effective at detecting market drugs down to ng/mL concentrations, which provides an alternative to current chemical detection methods, such as LC-MS, which are expensive and laborious.

This type of technology is advantageous for in-clinic, point-of-care diagnostics, due to its rapid methodology and low cost. The next chapter explores the uses of graphene sensors for detection of other molecules beyond nucleic acids and drug targets.

Chapter 5 References

1   Sassolas, A., Leca-Bouvier, B. D. & Blum, L. J. DNA Biosensors and Microarrays. *Chem. Rev.* **108**, 109-139 (2008).

2   Chung, C. *et al.* Biomedical Applications of Graphene and Graphene Oxide. *Accounts of Chemical Research* **46**, 2211-2224 (2013).

3   R., G. B., Ye, L., Zhengtang, L. & T., J. A. Temperature dependence of the noise amplitude in graphene and graphene oxide. *Phys. Status Solidi (RRL)* **3**, 178-180 (2009).

4   Li, X. *et al.* Large-Area Synthesis of High-Quality and Uniform Graphene Films on Copper Foils. *Science* **324**, 1312-1314 (2009).

5   Lerner, M. B. *et al.* Scalable Production of Highly Sensitive Nanosensors Based on Graphene Functionalized with a Designed G Protein-Coupled Receptor. *Nano Letters* **14**, 2709-2714 (2014).

6   Zheng, C. *et al.* Fabrication of Ultrasensitive Field-Effect Transistor DNA Biosensors by a Directional Transfer Technique Based on CVD-Grown Graphene. *ACS Applied Materials & Interfaces* **7**, 16953-16959 (2015).

7   Xu, G. *et al.* Electrophoretic and field-effect graphene for all-electrical DNA array technology. *Nat. Commun.* **5**, 4866 (2014).

8   Xiaochen, D., Yumeng, S., Wei, H., Peng, C. & Lain-Jong, L. Electrical Detection of DNA Hybridization with Single-Base Specificity Using Transistors Based on CVD-Grown Graphene Sheets. *Adv. Mater.* **22**, 1649-1653 (2010).

9   Cai, B. *et al.* Ultrasensitive Label-Free Detection of PNA–DNA Hybridization by Reduced Graphene Oxide Field-Effect Transistor Biosensor. *ACS Nano* **8**, 2632-2638 (2014).

10   Chen, T.-Y. *et al.* Label-free detection of DNA hybridization using transistors based on CVD grown graphene. *Biosens. Bioelectron.* **41**, 103-109 (2013).

11   Sips, R. On The Structure of a Catalyst Surface. *J. Chem. Phys.* **16**, 490-495 (1948).

12   Gao, L. *et al.* Repeated growth and bubbling transfer of graphene with millimetre-size single-crystal grains using platinum. *Nature Communications* **3**, 699 (2012).

13   Huang, L. *et al.* Graphene/Si CMOS Hybrid Hall Integrated Circuits. *Sci. Rep.* **4**, 5548 (2014).

14   Ferrari, A. C. *et al.* Raman Spectrum of Graphene and Graphene Layers. *Physical Review Letters* **97**, 187401 (2006).

15   Katz, E. Application of bifunctional reagents for immobilization of proteins on a carbon electrode surface: Oriented immobilization of photosynthetic reaction centers. *J. Electroanal. Chem.* **365**, 157-164 (1994).

16   Chen, R. J., Zhang, Y., Wang, D. & Dai, H. Noncovalent Sidewall Functionalization of Single-Walled Carbon Nanotubes for Protein Immobilization. *J. Am. Chem. Soc.* **123**, 3838-3839 (2001).

17   Liu, Y. *et al.* Giant enhancement in vertical conductivity of stacked CVD graphene sheets by self-assembled molecular layers. *Nat. Commun.* **5**, 5461 (2014).

18   Ping, J. & Fuhrer, M. S. Carbon impurities on graphene synthesized by chemical vapor deposition on platinum. *J. Appl. Phys.* **116**, 044303 (2014).

19   Ping, J., Xi, J., Saven, J. G., Liu, R. & Johnson, A. T. C. Quantifying the effect of ionic screening with protein-decorated graphene transistors. *Biosens. Bioelectron.* **89**, 689-692 (2017).

20   Trushin, M. & Schliemann, J. Minimum Electrical and Thermal Conductivity of Graphene: A Quasiclassical Approach. *Phys. Rev. Lett.* **99**, 216602 (2007).

21   Halperin, A., Buhot, A. & Zhulina, E. B. Sensitivity, Specificity, and the Hybridization Isotherms of DNA Chips. *Biophys. J.* **86**, 718-730 (2004).

22   Okahata, Y. *et al.* Kinetic Measurements of DNA Hybridization on an Oligonucleotide-Immobilized 27-MHz Quartz Crystal Microbalance. *Anal. Chem.* **70**, 1288-1296 (1998).

23   Neenu, V. *et al.* Binding of DNA Nucleobases and Nucleosides with Graphene. *ChemPhysChem* **10**, 206-210 (2009).

24   Letowski, J., Brousseau, R. & Masson, L. Designing better probes: effect of probe size, mismatch position and number on hybridization in DNA oligonucleotide microarrays. *J. Microbiol. Methods* **57**, 269-278 (2004).

25   Peterson, A. W., Wolf, L. K. & Georgiadis, R. M. Hybridization of Mismatched or Partially Matched DNA at Surfaces. *J. Am. Chem. Soc.* **124**, 14601-14607 (2002).

26   Zhang, L., Miles, M. F. & Aldape, K. D. A model of molecular interactions on short oligonucleotide microarrays. *Nat. Biotechnol.* **21**, 818 (2003).

27   Drummond, T. G., Hill, M. G. & Barton, J. K. Electrochemical DNA sensors. *Nat. Biotechnol.* **21**, 1192, (2003).

28   Hwang, M. T. *et al.* Highly specific SNP detection using 2D graphene electronics and DNA strand displacement. *Proceedings of the National Academy of Sciences* **113**, 7088-7093, (2016).

29   Ping, J., Vishnubhotla, R., Vrudhula, A. & Johnson, A. T. C. Scalable Production of High-Sensitivity, Label-Free DNA Biosensors Based on Back-Gated Graphene Field Effect Transistors. *ACS Nano* **10**, 8700-8704, (2016).

30   Cai, H. *et al.* On-chip wavelength multiplexed detection of cancer DNA biomarkers in blood. *Biomicrofluidics* **10**, 064116, (2016).

31   Wang, Y. *et al.* Detection of tumor-derived DNA in cerebrospinal fluid of patients with primary tumors of the brain and spinal cord. *Proceedings of the National Academy of Sciences* **112**, 9704-9709, (2015).

32   Ke, X. *et al.* Graphene- and aptamer-based electrochemical biosensor. *Nanotechnology* **25**, 205501 (2014).

33   Vishnubhotla, R. *et al.* Scalable graphene aptasensors for drug quantification. *AIP Advances* **7**, 115111 (2017).

34   Zhang, X., Li, S., Jin, X. & Zhang, S. A new photoelectrochemical aptasensor for the detection of thrombin based on functionalized graphene and CdSe nanoparticles multilayers. *Chem. Commun.* **47**, 4929-4931, (2011).

35   Lerner, M. B. *et al.* Large scale commercial fabrication of high quality graphene-based assays for biomolecule detection. *Sens. Actuators B: Chem.* **239**, 1261-1267 (2017).

36   Yang, W. *et al.* Carbon nanomaterials in biosensors: Should you use nanotubes or graphene? *Angew. Chem., Int. Ed.* **49**, 2114-2138 (2010).

37   Cui, Y., Wei, Q. Q., Park, H. K. & Lieber, C. M. Nanowire nanosensors for highly sensitive and selective detection of biological and chemical species. *Science* **293**, 1289-1292 (2001).

38   Sarkar, D. *et al.* MoS2 Field-Effect Transistor for Next-Generation Label-Free Biosensors. *ACS Nano* **8**, 3992-4003, (2014).

39   Naylor, C. H. *et al.* Scalable Production of Molybdenum Disulfide Based Biosensors. *ACS Nano* **10**, 6173-6179, (2016).

40   Gao, Z. *et al.* Scalable Production of Sensor Arrays Based on High-Mobility Hybrid Graphene Field Effect Transistors. *ACS Appl. Mater. Interfaces* **8**, 27546-27552, (2016).

41   Lerner, M. B. *et al.* Toward quantifying the electrostatic transduction mechanism in carbon nanotube molecular sensors. *J Am Chem Soc* **134**, 14318-14321 (2012).

42   Rajesh *et al.* Genetically Engineered Antibody Functionalized Platinum Nanoparticles Modified CVD-Graphene Nanohybrid Transistor for the Detection of Breast Cancer Biomarker, HER3. *Advanced Materials Interfaces* **3**, n/a-n/a, (2016).

43   Guo, Z., Taubes, C. H., Oh, J.-E., Maher, L. J. & Mohanty, U. DNA on a Tube: Electrostatic Contribution to Stiffness. *The journal of physical chemistry. B* **112**, 16163-16169, (2008).

44   Andes, D., Pascual, A. & Marchetti, O. Antifungal Therapeutic Drug Monitoring: Established and Emerging Indications. *Antimicrob. Agents Chemother.* **53**, 24-34 (2009).

45   Grebe, S. K. G. & Singh, R. J. LC-MS/MS in the Clinical Laboratory – Where to From Here? *Clin. Biochem. Rev.* **32**, 5-31 (2011).

46   Tuerk, C. & Gold, L. Systematic evolution of ligands by exponential enrichment: RNA ligands to bacteriophage T4 DNA polymerase. *Science* **249**, 505-510 (1990).

47   Kwon, O. S. *et al.* Flexible FET-Type VEGF Aptasensor Based on Nitrogen-Doped Graphene Converted from Conducting Polymer. *ACS Nano* **6**, 1486-1493 (2012).

48   Ohno, Y., Maehashi, K. & Matsumoto, K. Label-Free Biosensors Based on Aptamer-Modified Graphene Field-Effect Transistors. *J. Am. Chem. Soc.* **132**, 18012-18013 (2010).

49   Wang, C. *et al.* A label-free and portable graphene FET aptasensor for children blood lead detection. *Scientific Reports* **6**, 21711 (2016).

50   An, J. H., Park, S. J., Kwon, O. S., Bae, J. & Jang, J. High-Performance Flexible Graphene Aptasensor for Mercury Detection in Mussels. *ACS Nano* **7**, 10563-10571 (2013).

51   Aliakbarinodehi, N. *et al.* Aptamer-based Field-Effect Biosensor for Tenofovir Detection. *Scientific Reports* **7**, 44409 (2017).

52   Dore, G. J. *et al.* Efficacy of Tenofovir Disoproxil Fumarate in Antiretroviral Therapy-Naive and -Experienced Patients Coinfected with HIV-1 and Hepatitis B Virus. *J. Infect. Dis.* **189**, 1185-1192 (2004).

53   Koehn, J., Ding, Y., Freeling, J., Duan, J. & Ho, R. J. Y. A Simple, Efficient, and Sensitive Method for Simultaneous Detection of Anti-HIV Drugs Atazanavir, Ritonavir, and Tenofovir by Use of Liquid Chromatography-Tandem Mass Spectrometry. *Antimicrob. Agents Chemother.* **59**, 6682-6688 (2015).

54   Weiss, J. N. The Hill equation revisited: uses and misuses. *FASEB Journal* **11**, 835-841 (1997).

55   Wiedman, G. R. *et al.* An Aptamer-Based Biosensor for the Azole Class of Antifungal Drugs. *mSphere* **2** (2017).

56   Sheehan, D. J., Hitchcock, C. A. & Sibley, C. M. Current and Emerging Azole Antifungal Agents. *Clin. Microbiol. Rev.* **12**, 40-79 (1999).

57   Ghannoum, M. A. & Rice, L. B. Antifungal agents: mode of action, mechanisms of resistance, and correlation of these mechanisms with bacterial resistance. *Clin Microbiol Rev* **12**, 501-517 (1999).

58   Jager, N. G. L., van Hest, R. M., Lipman, J., Taccone, F. S. & Roberts, J. A. Therapeutic drug monitoring of anti-infective agents in critically ill patients. *Expert Rev. Clin. Pharmacol.* **9**, 961-979 (2016).

59   Dolton, M. J., Brüggemann, R. J. M., Burger, D. M. & McLachlan, A. J. Understanding Variability in Posaconazole Exposure Using an Integrated Population Pharmacokinetic Analysis. *Antimicrob. Agents Chemother.* **58**, 6879-6885 (2014).

60   Dolton, M. J., Mikus, G., Weiss, J., Ray, J. E. & McLachlan, A. J. Understanding variability with voriconazole using a population pharmacokinetic approach: implications for optimal dosing. *J Antimicrob Chemother* **69**, 1633-1641 (2014).

61   Park, W. B. *et al.* The effect of therapeutic drug monitoring on safety and efficacy of voriconazole in invasive fungal infections: a randomized controlled trial. *Clin Infect Dis* **55**, 1080-1087 (2012).

62   Ellington, A. D. & Szostak, J. W. In vitro selection of RNA molecules that bind specific ligands. *Nature* **346**, 818 (1990).

63   Lea, W. A. & Simeonov, A. Fluorescence polarization assays in small molecule screening. *Expert Opin Drug Discov* **6**, 17-32 (2011).

64   Jing, M. & Bowser, M. T. Methods for measuring aptamer-protein equilibria: a review. *Anal Chim Acta* **686**, 9-18 (2011).

65   Greenfield, N. J. Using circular dichroism spectra to estimate protein secondary structure. *Nat. Protoc.* **1**, 2876-2890 (2006).

66   Paramasivan, S., Rujan, I. & Bolton, P. H. Circular dichroism of quadruplex DNAs: applications to structure, cation effects and ligand binding. *Methods* **43**, 324-331 (2007).

67   Nagatoishi, S., Tanaka, Y. & Tsumoto, K. Circular dichroism spectra demonstrate formation of the thrombin-binding DNA aptamer G-quadruplex under stabilizing-cation-deficient conditions. *Biochem Biophys Res Commun* **352**, 812-817 (2007).

68   Schwierz, F. Graphene transistors. *Nature Nanotech.* **5**, 487 (2010).

69   Hasegawa, H., Sode, K. & Ikebukuro, K. Selection of DNA aptamers against VEGF165 using a protein competitor and the aptamer blotting method. *Biotechnol Lett* **30**, 829-834 (2008).

70   Pohl, F. M. & Jovin, T. M. Salt-induced co-operative conformational change of a synthetic DNA: equilibrium and kinetic studies with poly (dG-dC). *J Mol Biol* **67**, 375-396 (1972).

71   Baker, E. S. & Bowers, M. T. B-DNA Helix Stability in a Solvent-Free Environment. *J. Am. Soc. Mass. Spectrom* **18**, 1188-1195 (2007).

72   Hu, R. *et al.* DLISA: A DNAzyme-Based ELISA for Protein Enzyme-Free Immunoassay of Multiple Analytes. *Anal. Chem.* **87**, 7746-7753 (2015).

73   Liu, J., Cao, Z. & Lu, Y. Functional Nucleic Acid Sensors. *Chem. Rev.* **109**, 1948-1998 (2009).

74   Stoltenburg, R., Nikolaus, N. & Strehlitz, B. Capture-SELEX: Selection of DNA Aptamers for Aminoglycoside Antibiotics. *J. Anal Methods Chem.* **2012**, 14 (2012).

75   Kammer, M. N. *et al.* Characterizing aptamer small molecule interactions with backscattering interferometry. *Analyst* **139**, 5879-5884 (2014).

Chapter 6: Graphene Devices for Sensing of Other Biomolecular and Chemical Targets: From Biomarker Proteins to pH in Complex Fluids

Aside from graphene sensors for nucleic acid detection, such devices can be devoted to the detection of other targets. This chapter contains details about graphene devices used for protein biomarker detection, protein-nanoparticle assemblies, pH sensing, and measuring neuropeptide and receptor binding.

Section 6.1 discusses the uses of GFETs, functionalized with platinum nanoparticles, for detection of the breast cancer HER3 protein biomarker. Section 6.2 recounts the use of graphene microelectrodes (GEs) on a kapton, of flexible plastic substrate, for sensing pH of complex fluids, including phosphate buffer solution (PBS), human serum, and a ferritin solution.

Section 6.3 also uses GEs for sensing the binding of the protein, ferritin, and a gold nanoparticle (AuNP). When the ferritin protein is in an "open" orientation, the AuNP can transfer Faradaic current through the device. When this pore is closed, no such charge transfer is possible. This project is unique, in that it demonstrates that graphene can also be used for understanding how two elements bind together. This leads into section 6.4, where GEs are used for measuring the binding between neuropeptides and their receptors.

This chapter is especially significant because it proves that graphene devices do not need to be confined to one specific target type, and that, in essence, graphene sensors can be used for any type of target, as long as an appropriate biochemical recognition element is identified, and provided the necessary steps are taken to account for background signal noise from the target solution medium.

6.1 Graphene Biosensors for Breast Cancer Protein Biomarker Detection

Abstract

Biosensors based on graphene field effect transistors (GFETs) decorated with antibody-functionalized platinum nanoparticles (PtNPs) are developed for the quantitative detection of breast cancer biomarker HER3. High-quality chemical vapor deposited graphene is prepared and transferred over gold electrodes microfabricated on an SiO_2/Si wafer to yield an array of 52 GFET devices. The GFETs are modified with PtNPs to obtain a hybrid nanostructure suitable for attachment of HER3-specific, genetically engineered thiol-containing single-chain variable fragment antibodies (scFv) to realize a biosensor for HER3. Physical and electrical characterization of Bio-GFET devices is carried out by electron microscopy, atomic force microscopy, Raman spectroscopy, and current–gate voltage measurements. A concentration-dependent response of the biosensor to HER3 antigen is found in the range 300 fg mL^{-1} to 300 ng mL^{-1} and is in quantitative agreement with a model based on the Hill–Langmuir equation of equilibrium thermodynamics. Based on the dose–response data, the dissociation constant is estimated to be 800 pg mL^{-1}, indicating that the high affinity of the scFv antibody is maintained after immobilization. The limit of detection is 300 fg mL^{-1}, showing the potential for PtNP/G-FETs to be used in label-free biological sensors.

Introduction

Cancer is a leading cause of death worldwide and a major public health concern. Breast cancer is the most common cancer among American women, except for skin cancers and is the second leading cause of cancer-related death for women in the United States[1]. During the past decade researchers have given enormous attention to the search for biomarkers for early detection of breast cancer. The human epidermal growth factor receptor family (HER) comprising four transmembrane receptors: HER1 (EGFR or ERBB1), HER2 (ERBB2), HER3 (ERBB3), and HER4 (ERBB4) play a key role in regulation of mammalian cell survival, proliferation, adhesion, and differentiation[2]. HER3 is implicated in tumorigenesis of numerous cancers including breast cancers[3,4], pancreatic cancers[5], gastric cancers[6], and colorectal cancers[7]. HER3 expression has prognostic value, since high levels of receptor expression are associated with significantly shorter survival time compared with patients who overexpress HER2[8]. For instance, it has been reported that both HER3 messenger RNA and protein were up-regulated in human breast cancers, where HER3 overexpression was found in the ratio of 50%–70%[9,10].

Normal physiological levels of HER3 range from 60 pg mL^{-1} to 2.55 ng mL^{-1}. However, in a pathological case, the HER3 level is abnormally increased up to 12 ng mL^{-1}.[11] High-sensitivity detection and accurate analysis of biomarker molecules in human fluid samples are vital for early detection, treatment, and management of cancer. The clinical measurement of cancer biomarkers has provided a great promise for early cancer detection and highly reliable predictions[12,13]. A typical heterogeneous immunoassay involves antibody immobilization, multiple steps of incubation and washing cycles,

followed by signal amplification and readout. From the initial antibody immobilization step to the final reading stage, the immunoassay result can usually take hours to days to obtain. Various techniques have been developed for cancer cell detection, including cytologic testing, fluorescent imaging, magnetic resonance imaging, computerized tomography, X-ray radiography, and ultrasound[14-17]. However, these techniques have disadvantages of high cost and long time required for either experimental process or instrumentation. Therefore, it is highly desirable to develop rapid, simple, and cost-effective methods for early detection of cancer cells in preclinical diagnosis for reduction in mortality for certain cancers. In this respect, point-of-care hand held devices offer promising alternatives to existing laboratory-based immunochemical assays.

Electrical detection methods like field-effect transistor (FET) based biosensors exhibit highly sensitive detection of chemical and biological species when designed so surface–analyte or ligand–receptor binding occurs very close to the FET channel[18]. Carbon-based nanomaterials such as carbon nanotubes[19-24], reduced graphene oxide (rGO)[25], and graphene[26-31] have received considerable attention for label-free FET-biosensors with high sensitivity because of their unique electrical properties and suitability for miniaturization in an array format. Compared to nanotubes and rGO, large-area graphene grown by chemical vapor deposition (CVD) offers advantages of overall electrical conductivity[32], device reproducibility, low noise, and superior carrier mobility[33], which are expected to lead to greater sensitivity. The direct immobilization of proteins on CNTs[34] or graphene oxide[25] has been reported to be unstable and washed off easily (unless covalent immobilization through special surface treatment and additional steps of carbodiimide chemistry of protein binding is involved), which results in undesirable

effects such as poor device sensitivity, poor reliability, and nonspecificity of the sensor. This has been avoided by stable biomolecular immobilization through metal nanoparticles on graphene[35], as their 3D geometry enables high bioreceptor loading with controlled orientation for ligand binding and thus are widely used in biosensing applications[36,37]. In this work, we use platinum nanoparticles (PtNPs; $\Phi = 6.4$ eV) instead of the more commonly used gold nanoparticles (AuNP; $\Phi = \approx 5.3$ eV) because PtNPs are reported to provide improved electrical signals in carbon nanotube-based FET biosensors[38,39]. This was attributed to enhanced electron transfer from the carbon nanotube channel ($\Phi = 4.9$ eV) to the PtNPs, thereby increasing the hole carrier density, leading to improved biosensor characteristics. Since the transduction mechanism in FET-based biosensors is largely electrostatic[18,40], the use of single-chain variable fragment antibodies (scFvs; 2–3 nm in size) in place of conventional antibodies (10–15 nm) is expected to offer performance advantages[23].

Here we report a novel strategy for scalable fabrication of arrays of graphene field effect transistors (GFETs) modified with Pt nanoparticles and then functionalized with HER3-specific scFv antibodies, as a proof-of-concept, to demonstrate selective and sensitive detection of the breast cancer biomarker protein HER3 in a buffer solution. The devices showed high sensitivity (limit of detection ≈ 300 fg mL^{-1}) and excellent specificity as indicated by multiple control experiments.

Results and Discussion

GFET devices were fabricated as described in the Experimental Section. Briefly, large-area monolayer graphene was prepared by low-pressure catalytic chemical vapor

deposition process on a copper foil with CH_4 as a precursor source. The graphene thin film was then transferred using a polymethyl methacrylate (PMMA) assisted "bubbling" transfer method onto a pre-patterned SiO_2/Si substrate with an array of 52 pairs of metal electrodes each having a dimension 100 μm wide separated with a 10 μm gap between the source and the drain electrode. After transfer, GFET channels were patterned using standard photolithography and oxygen etching, as described in **Figure 6.1.1** with a schematic representation of the GFETs fabrication. The GFETs were then annealed at 250 °C under flowing N_2 gas to remove residual photoresist contamination.
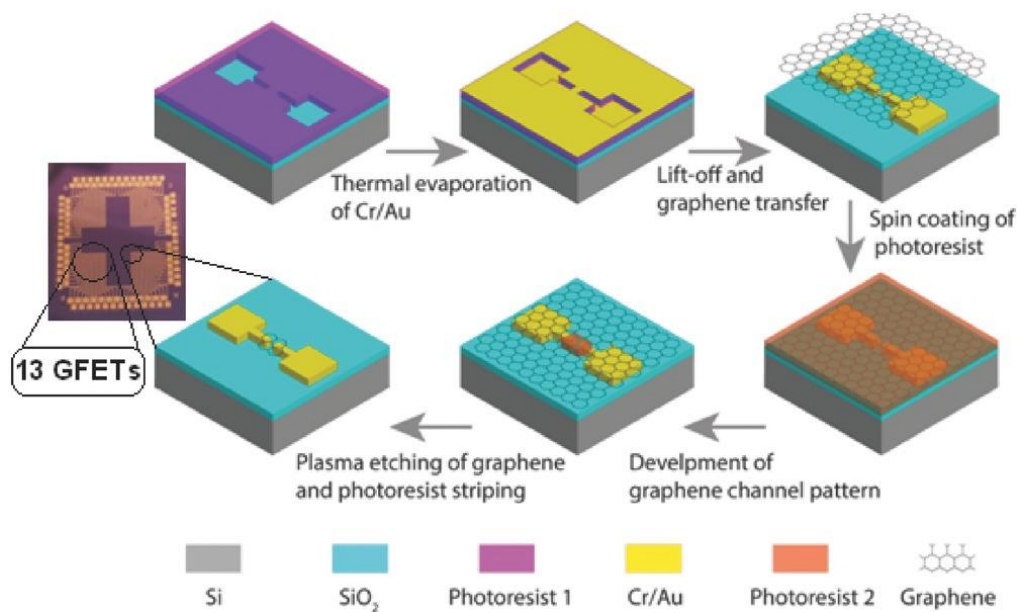
Figure 6.1.1 *Schematic representation of fabrication process for an array of 52 GFETs.*

The Raman spectrum of the GFET channel showed the G band at ≈1580 cm^{-1} and the 2D band at ≈2670cm^{-1}, with an I_G/I_{2D} intensity ratio of ≈0.6 (see Figure S1, "Supporting Information"). The symmetric 2D peak was well fit by a single Lorentzian with a full width half-maximum of 31 cm^{-1}, and the D (disorder) peak located at ≈1350 cm^{-1} was

nearly undetectable. All these findings are indicative of high-quality monolayer graphene[41,42], channel in GFETs after processing.

Figure 6.1.2 shows the stepwise chemical/biochemical modifications of the GFET channel used to create the biosensor device.
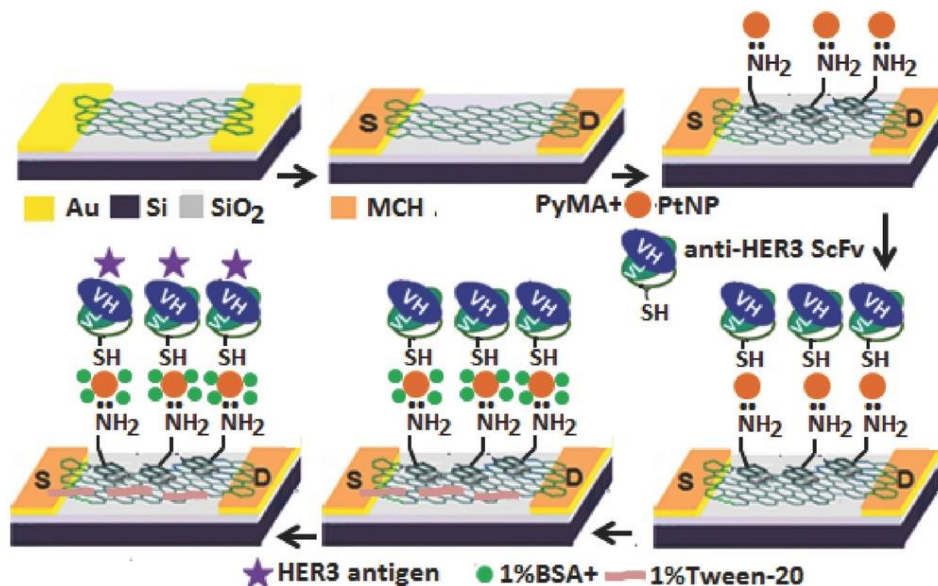
Figure 6.1.2 *Schematic of chemical and platinum nanoparticle modification of a GFET to create the biosensor structure.*

The GFETs were first modified with PtNPs by using the bifunctional linker, 1-methyl pyrene amine (PyNH$_2$), where the pyrene moiety binds to graphene via π–π linkage, and the terminal NH$_2$ binds to the PtNP by donating an electron pair[43]. High-resolution transmission electron microscopy was carried out on samples of graphene decorated with PtNPs (**Figure 6.1.3 a**) and showed that the ultrafine PtNPs were uniformly dispersed on the graphene surface. Typically the size distribution of Pt nanoparticles varied between 1 and 3.7 nm, with an average size of about 1.8 and 2.4 nm (inset in **Figure 6.1.3 a**). This has been further elucidated by scanning electron microscopy images (**Figure 6.1.3 b**) showing PtNPs uniformly distributed without agglomeration over the entire graphene

surface channel of the GFET; this platform successfully survived multiple washing and drying steps.
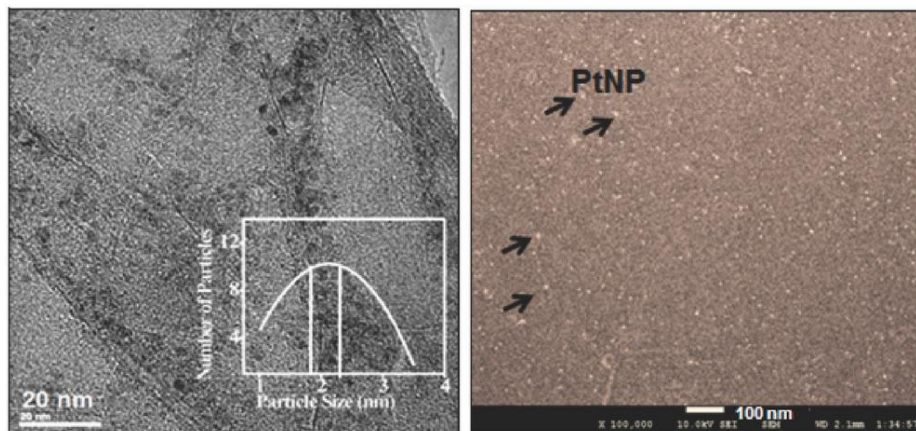
Figure 6.1.3 *a) TEM image of the PtNP-graphene nanohybrid. Inset: Size distribution of Pt nanoparticles, with an average size of about 1.8–2.4 nm; b) scanning electron image of a PtNP-graphene nanohybrid FET. Magnification is 100 000×, and the accelerating voltage is 10.0 kV.*

The PtNPs on the GFET were then functionalized by site-specific immobilization of HER3-specific scFv antibodies, which act as bio-receptor for immunoreaction with target HER3 antigen. We engineered the HER3 monoclonal antibody into an scFv antibody[44] with a pair of cysteine (thiol) residues inside the loop sequence bridging the V_H and V_L segments, allowing it to be immobilized on PtNPs embedded on graphene for the production of GFET-based biosensors. The electronic properties of Pt-decorated graphene change more significantly than that of intrinsic graphene after molecular adsorption of cysteine, which makes it a promising candidate for sensor development[45].

The atomic force microscopy (AFM) image in **Figure 6.1.4** shows further details of the device structure. Three height profiles were taken to probe the topography of CVD graphene, PtNP-graphene, and scFv immobilized on PtNP-graphene. From the height

126

profile, the thickness of the CVD-graphene sheet (**Figure 6.1.4 a**) is 0.3–0.5 nm,

consistent with monolayer graphene. After modification with PtNPs, the sample showed

a height profile of 2.0 ± 0.5 nm. This together with a fine particulate feature (**Figure**

6.1.4 b) of the hybrid structure showed that the PtNPs were well-distributed over the

graphene surface. After further modification with scFv antibodies (**Figure 6.1.4 c**), the

device showed a height profile of 4.0 ± 0.5 nm with globular features that are

significantly larger than the PtNP-graphene; the height difference of ≈ 2.0 nm is

consistent with the expected height of the scFv antibody (2.5 nm), indicating the

formation of scFv-PtNP conjugates bound to the GFET channel. Since scFv

immobilization occurs at room temperature, it is anticipated that the scFv is not denatured

during this process, which is confirmed by the sensing results presented below.
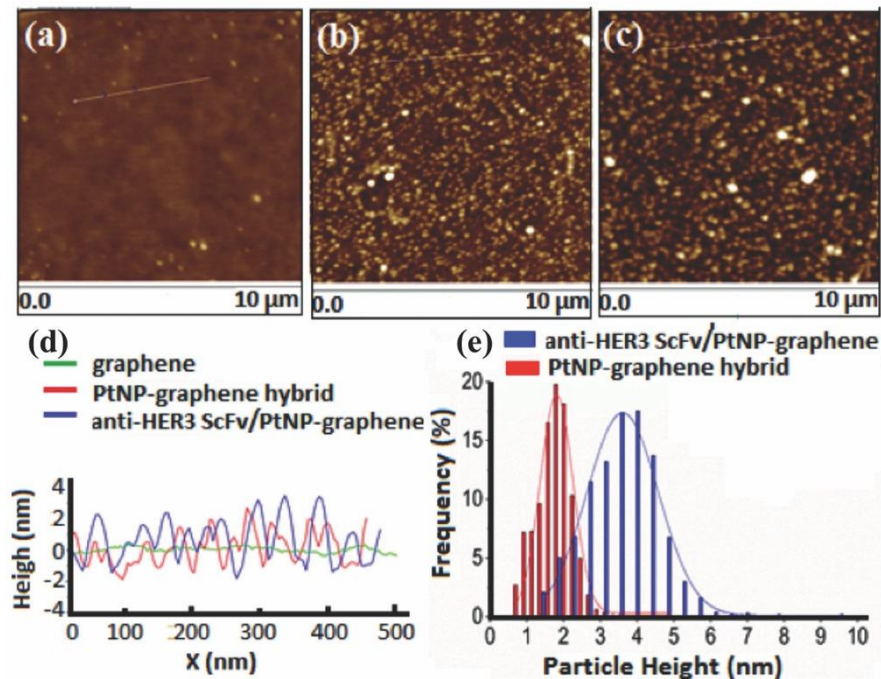
Figure 6.1.4 *Atomic force microscopy image of a) graphene, b) PtNP-graphene hybrid, and c) scFv/PtNP-graphene, all on Si/SiO₂. d) AFM line scans of the bare GFET, PtNP/GFETs, and scFv-functionalized PtNP/GFETs.*

We measured the source–drain current–gate voltage (I–V_g) characteristic of each device in an array of 52 GFETs fabricated on a single chip, before and after successive steps of (1) metal (Au) electrode surface passivation with 1-mercaptohexane (MCH), (2) GFET modification with PtNPs, and (3) scFv immobilization, to confirm the formation of the bio-GFET hybrid devices (see **Figure 6.1.5**). The Au source and drain electrodes were passivated with an MCH self-assembled monolayer to block nonspecific protein binding and thus avoid undesired surface contamination with scFv protein during bio-functionalization of the GFET channel. The device was rinsed thoroughly in water, and dried in a compressed air stream before taking measurements. All measurements were performed with a source–drain voltage of $V_{SD} = 50$ mV.
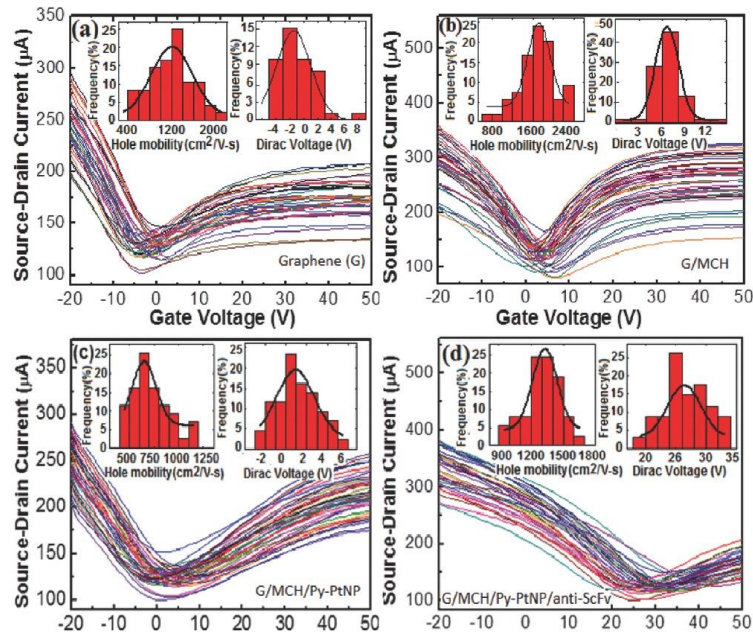
Figure 6.1.5 *Electrical characteristics of GFET devices at different stages of surface modification, with a representative set of 52 I–V$_g$ curves in each case. a) As-fabricated GFET, b) after electrode passivation with MCH, c) PtNP/GFET hybrid, and d) scFv-PtNP/GFET nanohybrid device. Insets in each case are histograms of carrier mobility and Dirac voltage along with Gaussian fits (black curves).*

The Dirac point voltage of the as-fabricated GFET was typically in the range −4.0 to +2.0 V, with an average carrier mobility (μ) of 1197 ± 56 cm^2 V^{-1} s^{-1} (**Figure 6.1.5 a**), which indicates a relatively clean transfer of graphene. After MCH passivation of the Au electrodes, a positive shift in the Dirac point was observed to be 6.5 ± 0.5 V with a comparatively high charge mobility, $\mu = 1719 \pm 31$ cm^2 V^{-1} s^{-1} (**Figure 6.1.5 a**). This may be understood in terms of a shift of the electrode Fermi level to an energy closer to the graphene valence bond, which reduces the Schottky barrier at the Au–graphene interface and enhances hole injection, as reported earlier for carbon nanotube FETs[46]. The PyNH$_2$:PtNP attachment on the GFET channel reduced the carrier mobility ($\mu = 651 \pm 21$ cm^2 V^{-1} s^{-1}) and caused a negative shift in the Dirac voltage to 0.92 ± 0.25 V, which is ascribed to increased scattering by the basic PyNH$_2$[18,47]. Following antibody attachment, the carrier mobility increased ($\mu = 1330 \pm 14$ cm^2 V^{-1} s^{-1}) with a positive shift in the Dirac voltage ($V_D = 26.4 \pm 1.0$ V), suggesting a decrease in carrier scattering by scFv attachment.

Figure 6.1.6 shows the I–V_g characteristics of an individual GFET device functionalized as described above and then treated with a blocking reagent (0.1% Tween 20 + 0.1% bovine serum albumin), which served as a barrier to nonspecific protein adsorption on the metal nanoparticles and GFET channel[48], followed by immunoreaction upon exposure to the HER3 antigen in buffer (pH 7.3) at concentrations in the range 300 fg mL^{-1} to 300 ng mL^{-1}. For each measurement, the GFET was incubated in a solution with a given HER3 concentration for 1 h, gently dried with compressed air, and then the I–V_g characteristic was measured. The Dirac voltage of the Bio-GFET showed a successive positive shift with increasing HER3 concentration. **Figure 6.1.6 a** shows the shifts in V_D for an

individual GFET at each successive stage of chemical modification/bio-functionalization with a shift (ΔV_D) of $\approx +7.0$ V upon exposure to 300 ng mL^{-1} HER3. **Figure 6.1.6 b** shows the response of an individual device to 30 ng mL^{-1} HER3 concentration in buffer with insets showing response to 300 fg mL^{-1} HER3 ($\Delta V_D \approx +1.7$ V) and pure buffer (with no HER3 antigen) as a negative control ($\Delta V_D < +1.0$ V). A significant positive shift in V_D was observed upon exposure to HER3 antigen, which is readily distinguishable from the very small response observed for a pure buffer sample. The observed Dirac voltage shifts may be attributed to electrostatic "chemical gating" of the GFET associated with increasing binding of antigen to scFv receptors bound on the graphene surface.
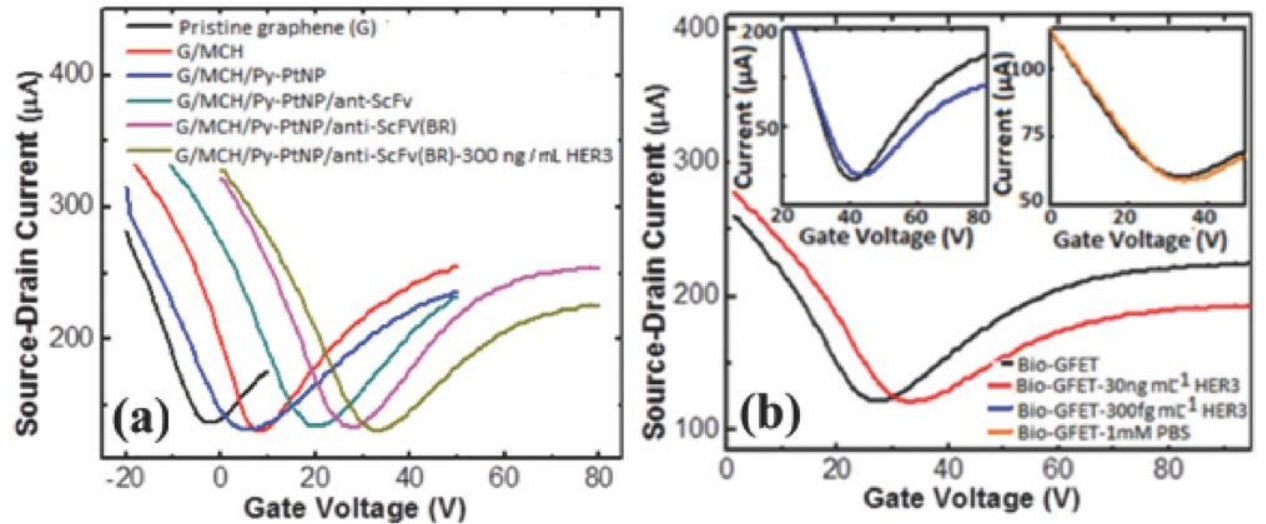
Figure 6.1.6 *a) Current–gate voltage (I–V$_g$) characteristics of a representative GFET device after fabrication and after each successive surface modification leading to formation of anti-HER3 scFv functionalized PtNP/GFET and on exposure to 300 ng mL^{-1} HER3 in PBS; b) The sensing performance of the device against 30 ng mL^{-1} HER3; Insets: (upper left) shows sensor response to 300 fg mL^{-1} HER3, and (upper right) sensor response to 1×10^{-3} M PBS (without antigen).*

There was a systematic dependence of the V_D shift with varying antigen HER3 concentration in the range 300 fg mL^{-1} to 300 ng mL^{-1}, with each concentration tested

independently on 6–10 functionalized devices for signal averaging and to avoid sample

contamination across trials. The variation of the average measured shift in the Dirac

voltage as a function of HER3 concentration is displayed in **Figure 6.1.7**, where the error

bars reflect the standard error of the mean. The sensor responses agree with a model

based on the Hill–Langmuir equation describing the equilibrium binding of a ligand by a

receptor[49].

$$\Delta V_D = A \frac{(c/K_d)^n}{1+(c/K_d)^n} + Z$$

(6.1)
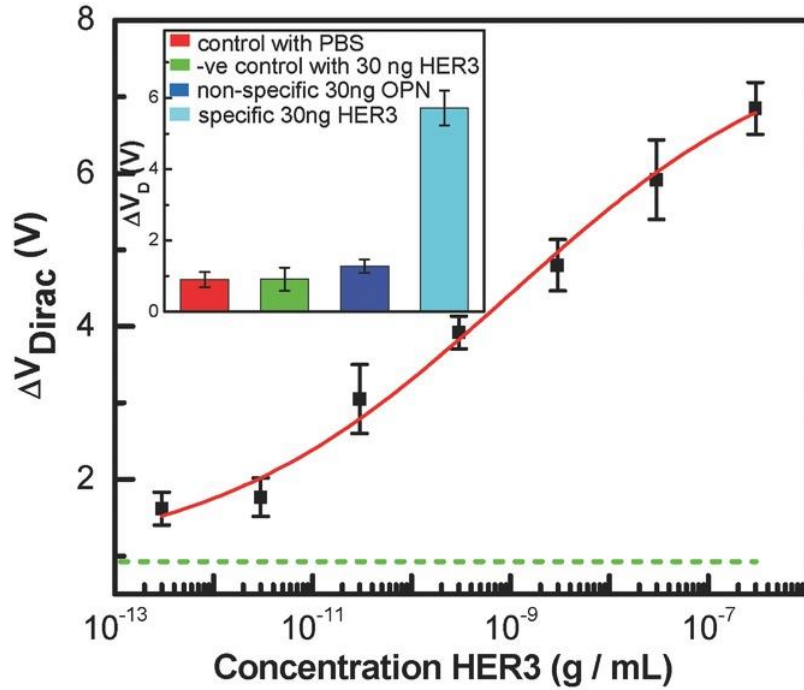
Figure 6.1.7 *Calibration curve of the biosensor device showing Dirac voltage shift (ΔV) response as a function of HER3 concentration (300 fg mL^{-1} to 300 ng mL^{-1}). The data are fit to a model based on the Hill–Langmuir equation (red curve); Inset: Comparison of device responses (ΔV_{Dirac}) for various control experiments. Fully prepared biosensor to target HER3 at 30 ng mL^{-1} (light blue bar). Fully prepared biosensor to negative controls plain PBS buffer (red bar) and non‑complementary protein marker osteopontin (OPN; dark blue bar). Also shown is the response in a negative control experiment where a device prepared without the scFv antibody was exposed to the target HER3 at 30 ng mL^{-1}(green bar).*

Here c is the HER3 antigen concentration, A is the sensor response at saturation when all binding sites are occupied, Z is an offset to account for the response to pure buffer, K_d is the dissociation constant describing the concentration at which half of available binding sites are occupied, and n is the Hill coefficient describing cooperativity of binding.

To construct the fit, the maximum response A and offset parameter Z were constrained to values that were sensible based on the response data and buffer response ($A = 6.85$ and $Z = 0.90$) while the parameters K_d and n were allowed to vary. The best-fit parameters were $K_d = 790 \pm 160$ pg mL^{-1} and $n = 0.29 \pm 0.01$. The low value of K_d indicates strong binding affinity of the scFv for HER3 antigen at the electrode surface, which may reflect high antibody loading of the PtNPs. A low value of $n = 0.29$ corresponds to negative cooperativity, under the (as yet untested) assumption of a linear relationship between sensor response and analyte binding. The value of the offset parameter $Z = 0.90$ is in good agreement with measured responses of devices to pure buffer (0.89 ± 0.2 V; indicated by the dashed line in **Figure 6.1.7**). The results indicate that a collection of 6–10 bio-GFET devices can readily differentiate between pure buffer ($\Delta V_D = 0.89 \pm 0.2$ V) and a solution containing 300 fg mL^{-1} (4.4×10^{-15} M) HER3 ($\Delta V_D = 1.76 \pm 0.2$ V). Multiple control experiments were conducted to gauge the specificity of the device (inset to **Figure 6.1.7**). A fully functionalized bio-GFET device was tested against 30 ng mL^{-1} osteopontin and the resulting response ($\Delta V_D = 0.91 \pm 0.2$ V) was indistinguishable from the device response to pure buffer ($\Delta V_D = 0.89 \pm 0.2$ V). A representative I–V_g characteristic is included as Figure S2 ("Supporting Information"). The response of an unfunctionalized GFET device (negative control) to 30 ng

mL^{-1} HER3 ($\Delta V_D = 1.19 \pm 0.2$ V) was again comparable to the buffer response, which is

significantly smaller than the response of a functionalized bio-GFET to the same HER3

concentration ($\Delta V_D = 5.71 \pm 0.49$ V) suggesting that bio-GFET response to HER3 target

reflects specific ligand–receptor binding with a negligible contribution from nonspecific

binding. Although a precise quantitative understanding of the transduction mechanism

remains to be developed, our results motivate the possibility that the present method

could be further optimized to develop a new class of scalable graphene-based nanohybrid

biosensors with the highly sensitive and specific chemical recognition characteristic of

the protein for a useful diagnostic test.

Conclusions

We demonstrated a novel scalable fabrication process for biosensor arrays based on

PtNP/graphene devices functionalized with an scFv with specific affinity for the breast

cancer biomarker protein HER3. The device exhibited a concentration-dependent

response over a wide concentration range of HER3, 300 fg mL^{-1} to 300 ng mL^{-1}($4.4 \times$

$10^{-15} - 4.4 \times 10^{-9}$ M) in PBS that was in excellent quantitative agreement with a model

based on the Hill–Langmuir equation of equilibrium thermodynamics. Since a wide range

of HER3 concentration is present in tumors cell lines, this is a much wider range of

detection than those (up to 2.4 pg mL^{-1}) reported by labeled impedimetric biosensors

using [Fe$_3$CN$_6$]$^{4-}$ redox probe, as label, for HER3 detection[50,51]. Control experiments

indicated that the HER3 specific scFv antibody retains its highly specific binding

characteristics on the PtNP/graphene hybrid structure, signifying the suitability of PtNPs

for efficient biomolecular immobilization for enhanced loading of antibodies on graphene

transistors. These observations of a good analytic range, high antigen–antibody

specificity, rapid response, and ease of use with a small sample volume makes this device superior to traditional immunoassay, suggesting its use as a point-of-care diagnostic tool.

Experimental Section

Device Fabrication: A source and drain electrode array was patterned on an SiO_2/Si water using a standard photolithographic liftoff process, based on a bilayer resist process of PMGI and Shipley 1813.5 nm Ti/40 nm Pd was then deposited by thermal evaporation, followed by the liftoff process with 1165 striper. Graphene synthesis was conducted with a low pressure chemical vapor deposition process. Cu foils were first cleaned with acetone and isopropyl alcohol (IPA), and then dried by N_2 gas. After the sample loading, the reaction chamber was pumped to a base pressure of ≈50 mTorr, followed by introduction of 80 sccm hydrogen (H_2) into the chamber. The furnace was heated to the process temperature of 1020 °C, followed by annealing of the Cu foil for 30 min. Methane (CH_4) was then introduced at a flow rate of 50 sccm for 35 min for graphene growth. The reactor was subsequently rapidly cooled to room temperature under a flow of 80 sccm H_2 and 50 sccm CH_4. The graphene monolayer was transferred onto the SiO_2/Si chip with metal electrodes by the PMMA-assisted "bubbling" transfer method[52]. After graphene transfer, GFET channels were patterned using standard photolithography, followed by oxygen plasma etching (1.25 Torr, 80 W, 30 min) and removal of residual photoresist by 1165 striper to yield an array of 52 GFET devices. GFETs were incubated in a colloidal mixture of 100 ppm PtNPs (Pt nanoparticles dispersion purchased from Sigma) and 5×10^{-3} M 1-methyl pyrene amine in methanol for 2 h, followed by extensive washing with methanol and IPA, and dried under flowing N_2 to yield the PtNP/GFET hybrid structure.

Expression and Purification of Anti-HER3 ScFv: The complete amino acid sequence of the variable heavy and light chains of the anti-HER3 A5 antibody was described previously[44]. An scFv version of the A5 antibody was expressed and purified as previously described[53]. Briefly, the pSYN-A5 scFv expression vector, which encodes for a 6×-HIS tagged version of the scFv, was transformed into TG1 *E. coli* and protein expression was induced through addition of 1×10^{-3} M IPTG (Isopropyl β-D-1-thiogalactopyranoside, Fisher Biotech) to a logarithmically culture. After 4 h of induction at 25 °C fully folded scFvs were extracted from the periplasmic space by osmotic shock in 30×10^{-3} M Tris-HCl (pH 8), 1×10^{-3} M EDTA, 20% sucrose (w/v). Protein was dialyzed into phosphate buffered saline and purified by sequential immobilized metal affinity chromatography (IMAC) and size exclusion chromatography.

Functionalization: A solution of scFv antibodies (3.2 µg mL^{-1}; pH 7.3) was pipetted onto the PtNP/GFET array in a humid environment to keep the solution from evaporating, over an incubation period of 1 h, causing PtNPs to be functionalized with scFv through binding of thiol groups of cysteine residues. After incubation, the chips were cleaned sequentially in two DI water baths under agitation for a total of 2 min, and then blown dry in a gentle stream of nitrogen.

Supporting Information

Supporting information can be found at DOI: 10.1002/admi.201600124

6.2 Flexible Graphene Biosensors for pH Sensing in Complex Fluids

Abstract

Advances in techniques for monitoring pH in complex fluids could have significant impact on analytical and biomedical applications ranging from water quality assessment to *in vivo* diagnostics. We developed flexible graphene microelectrodes (GEs) for rapid (< 5 seconds), very low power (femtowatt) detection of the pH of complex biofluids. The method is based on real-time measurement of Faradaic charge transfer between the GE and a solution at zero electrical bias. For an idealized sample of phosphate buffer solution (PBS), the Faradaic current varied monotonically and systematically with the pH with resolution of ~0.2 pH unit. The current-pH dependence was well described by a hybrid analytical-computational model where the electric double layer derives from an intrinsic, pH-independent (positive) charge associated with the graphene-water interface and ionizable (negative) charged groups described by the Langmuir-Freundlich adsorption isotherm. We also tested the GEs in more complex bio-solutions. In the case of a ferritin solution, the relative Faradaic current, defined as the difference between the measured current response and a baseline response due to PBS, showed a strong signal associated with the disassembly of the ferritin and the release of ferric ions at pH ~ 2.0. For samples of human serum, the Faradaic current showed a reproducible rapid (<20s) response to pH. By combining the Faradaic current and real time current variation, the methodology is potentially suitable for use to detect tumor-induced changes in extracellular pH.

Introduction

In vivo monitoring of pH is important in investigations of tissue metabolism, neurophysiology, and diagnostics[54]. Extracellular pH-sensing, though of great interest for cancer diagnosis and medical treatment[54-57], is currently based mainly on relatively slow fluorescent techniques such as fluorogenic pH probes[58,59] and fluorophore-decorated micelles[60]. Moreover, although optical methods hold promise for *in vivo* applications, improvement in detection platforms is still needed.[61] Other methods for *in vivo* measurement of tumor pH, including positron emission tomography (PET) radiotracers, magnetic resonance (MR) spectroscopy, and magnetic resonance imaging (MRI), are limited in sensitivity and require expensive instrumentation and exogenous and even radioactive indicators.[61] Electrical or electrochemical devices have the potential to be developed for *in vivo* pH monitoring but they are typically based on metal and glass, making them fragile and bulky. Existing approaches have additional disadvantages including the need for frequent recalibration, excessive power consumption, and lack of biocompatibility[54].

Flexible field-effect transistors (FETs) based on graphene, a biocompatible[62], chemically inert, and scalable[29] two-dimensional material with high quality pH-sensing properties[63-70], are promising for monitoring pH changes in biological systems. One important application is in cancer research and diagnostics since tumors demonstrate substantial reduction in extracellular pH[56,71,72] by 1.5 pH unit (from ~7.5 for healthy tissue to ~6.0 for tumor) but only moderate fluctuations in sodium concentration ($\sim 7\%$)[73] with respect to normal tissue. However, graphene FETs are commonly operated with ~ 100 mV source-drain bias and ~ 400 mV liquid-gate voltage. The application of these

potentials/biases may complicate device fabrication, scaling, and stability; perturb the system under investigation; and set a power (and thus size) constraint on the device. Since each gate-sweep measurement requires ~100 seconds to identify the charge neutrality point that characterizes the pH value, the pH measurement process with a FET is also relatively slow and may not be suitable for real-time monitoring.

Here we demonstrate the use of flexible graphene microelectrodes (GEs) [74] for rapid, bias-free pH measurement in phosphate buffer solution (PBS), ferritin solution in PBS (0.1 μM), and human serum. The GE fabrication process is based on scalable photolithographic approaches, and the measurements are conducted without using an external bias voltage [74], so the methodology is intrinsically low-power and minimally perturbative. We find that the spontaneous Faradaic charge transfer between the GE and PBS is modulated by the pH. The Faradaic current extracted from 5 seconds of charge measurement (20 times faster than graphene FETs)[63-70,75] varies systematically with the pH of PBS and is very insensitive to moderate fluctuations of the extracellular ionic strength that would be induced by a tumor (~7%). The GE response to pH is well described by a hybrid analytical/computational model where the electric double layer derives from an intrinsic, pH-independent (positive) charge associated with the graphene-water interface and ionizable (negative) charged groups described by the Langmuir-Freundlich adsorption isotherm. For the ferritin solution, we focus on the relative Faradaic current obtained by subtracting the baseline Faradaic current for PBS from that for the ferritin solution. The relative Faradaic current shows a very strong feature that we associate with the disassembly of the ferritin cage and the associated release of ferric ions into the solution. For human serum, the GE reaches equilibrium with the solution in short

time (~20 s) and also demonstrates remarkable performance: the Faradaic current responds systematically to pH in the range from 6.0 to 7.6 with high resolution (<0.2 pH unit); the differential current with respect to the pH flips sign and changes by ~ 150% as the pH decreases from 7.1 to 6.4. Together these findings suggest the suitability of the GE for both monitoring of biomolecular activity or protein disassembly in solution and for measurement of pH reduction expected for tumor extracellular fluid (1.5 pH unit)[55,71,72] *in vitro* or *in vivo*.

Results and Discussion

Inch-size graphene sheets for scalable electrode fabrication[29] were synthesized via low-pressure chemical vapor deposition on copper[76], and then transferred onto a flexible Kapton polyimide film with a pre-fabricated array of gold contacts. An Al_2O_3 sacrificial layer was deposited onto the sample by e-beam evaporation, and then the GE structures were defined using photolithography and oxygen plasma etching. This was followed by spin-coating of a 7-μm thick SU-8 2007 (Microchem) passivation layer, which was patterned to define 100 μm × 100 μm wells over the graphene electrodes. (See Experimental Section for further details of the device fabrication) An example of as-fabricated flexible devices is shown in **Figure 6.2.1 a.**
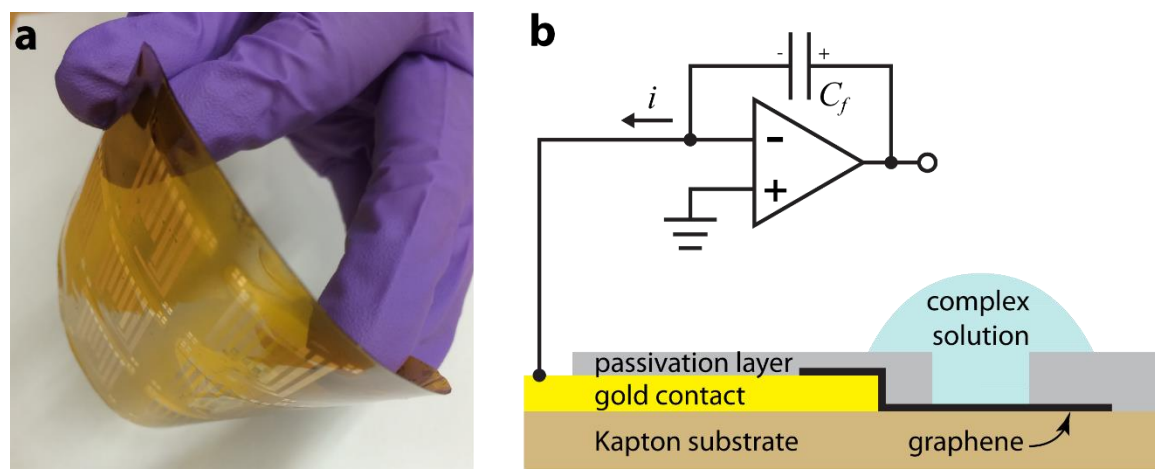
Figure 6.2.1. *(a) Graphene electrode devices on a flexible polyimide substrate. (b) Schematic of the device and the measurement configuration.*

The sub-pA Faradaic current between the GEs and the solution under test was measured using an electrometer (Keithley 6517a) with high resolution (~ fC) and low noise (0.75 fC/s peak-to-peak), as shown in **Figure 6.2.1 b**. The noninverting input of the electrometer was initially grounded. The GE was exposed to fluid samples with various pH values. To conduct the measurement, the graphene electrode was connected to the inverting input of the operational amplifier of the electrometer, and the charge transferred from the solution to graphene accumulated on the feedback capacitor C_f to provide the readout of the electrometer.

Modulation of Faradaic Current through pH Variation

First, we monitored the Faradaic charge transfer as a function of time for PBS (ionic strength 150 mM) as the pH was decreased from 11.2 to 2.2 and then increased back to 7.1 (**Figure 6.2.2 a**). For each pH value, the charge transferred from the solution to the graphene increased linearly with time, with the slope used to determine the Faradaic current i. In contrast to gate-sweep measurements for graphene FETs, where several

minutes might be needed to determine the shift in Dirac voltage that indicates the pH, the Faradaic current measurement described here was completed in less than 5 sec. The Faradaic current decreases monotonically with increasing pH, with excellent reproducibility, and minimal hysteresis (**Figure 6.2.2 b**). For pH > 3, the Faradaic current is negative, i.e., electrons are transferred from the solution to the graphene. At low pH (< 3), the Faradaic current is positive indicating that the proton concentration in the solution is large enough to reverse the direction of the current. The dependence of the Faradaic current on pH is approximately (but not exactly) linear, with a sensitivity of ~0.12 ± 0.01 pA/pH for pH in the range 2.2 – 11.2. We get an excellent fit to the data (red curve in **Figure 6.2.2 b**) using a model that incorporates the electric double layer and ionizable defect groups on graphene, as described in the following paragraphs.
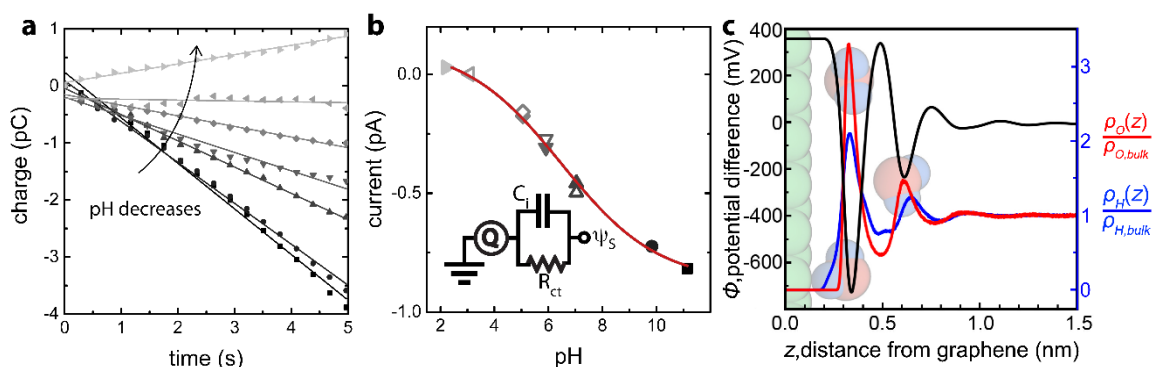
Figure 6.2.2. (*a*) *Real-time Faradaic charge transfer for phosphate buffer solution of various pH values. The solid lines are linear fits to the data.* (*b*) *The Faradaic current extracted from* ***a*** *as a function of the pH. The starting pH was 11.2. The Faradaic current was measured as the pH was decreased to 2.2 (solid symbols) and then increased to 7.1 (open symbols). The solid curve is a fit to an equation derived from* ***Equations 6.1-6.3*** *in the main text. Inset: Equivalent circuit for the graphene-solution interface.* (*c*) *Molecular simulations were used to calculate electrostatic potential $\Phi(z)$ (black) and densities of water hydrogen atoms (blue) and water oxygen atoms (red) as functions of z, the distance from the plane containing the graphene carbon nuclei. The densities of oxygen ρ_O and hydrogen ρ_H are presented relative to the bulk values for these quantities, $\rho_{O,bulk}$ and $\rho_{H,bulk}$. Superimposed on the figure are space-filling representations of graphene (green) and representative configurations of water molecules at three different orientations and*

distances relative to the graphene surface; graphene and water molecules are rendered on the scale of the abscissa (z).

The equivalent circuit model[77] describing the graphene-solution interface is shown in the inset of **Figure 6.2.2 b**. The interfacial capacitance C_i (~ µF cm^{-2})[78] of the graphene/solution interface can be ignored in the DC measurement used here, so the Faradaic current i is determined by the electrostatic potential ψ_S of the Stern plane due to adsorbed charges near the graphene surface and the charge transfer resistance R_{ct} (~ 6.7 MΩ cm^2)[74] between the graphene and the ionic solution: $i = \psi_S/R_{ct}$. The measured sensitivity of the GE, 0.12 ± 0.01 pA/pH, is equivalent to 6.8 ± 0.7 mV/pH at the Stern plane, in good agreement with the value[67] of ~ 6 mV/pH reported by others for experiments on graphene FETs in ionic aqueous solution using an electrolytic gate.

The current-pH dependence can be fit quantitatively using a model where the Grahame equation[79] is used to quantify the potential at the Stern plane associated with a surface charge density, σ_S, with two components: a constant (i.e., pH-independent) offset charge density and a set of ionizable defect sites in the graphene whose charge state varies with proton concentration through the the Langmuir-Freundlich isotherm[64,65]:

$$i = \psi_S/R_{ct} \qquad \textbf{(6. 2)}$$

$$\psi_S = \frac{2k_BT}{e}\sinh^{-1}\frac{\sigma_S}{\sqrt{8\epsilon\epsilon_0 k_BTc}} \qquad \textbf{(6.3)}$$

$$\sigma_S = \frac{\sigma_{max}}{1+10^{n(\mathrm{pK_a-pH})}\exp(-ne\psi_S/k_BT)} + \sigma_{off} \qquad \textbf{(6.4)}$$

In **Equation 6. 3**, k_B is the Boltzmann constant, T the absolute temperature, e the electronic charge, ϵ (ϵ_0) the relative (vacuum) permittivity, and $c = 150$ mM the ionic strength of the solution. In **Equation 6.4**, σ_{max} is the areal charge density of ionizable

groups (i.e., graphene defects), pK_a is the dissociation constant, and n the degree of heterogeneity. The parameter σ_{off} allows for the presence of a surface charge density that is independent of pH.

Combining **Equation 6.2**-**6.4**, we obtain an excellent fit to the measured current-pH response, where σ_{max}, n, pK_a, and σ_{off} are the fit parameters (solid line in **Figure 6.2.2 b**). The best fit value for σ_{max} is - 0.077 $\pm$ 0.005 C m^{-2}, consistent with earlier reports for graphene and carbon nanotubes[70,80,81] with values in the range from - 0.01 to - 0.08 C m^{-2}. The best fit value for σ_{off} is 0.007 $\pm$ 0.002 C m^{-2}, which we discuss further in the following paragraph. The best fit values for $n = 0.24 \pm 0.03$ and $pK_a = 6.5 \pm 0.1$ show reasonable agreement with values of $n = 0.3$ and $pK_a = 7.6$ found by others for single-wall carbon nanotubes (SWCNs) in KCl solution[81]. Our value for pK_a is also in the range 4.3 – 9.8 from earlier reports for ionizable groups on graphene[82].

The pH-independent areal charge density σ_{off} characterizes an intrinsic electric double layer at the graphene-water interface. To provide a molecular basis for this quantity, we first simulated the distribution of water molecules associated with defect-free graphene in contact with pure water with molecular dynamics. The charge density obtained from the simulation was then used to calculate the potential difference as a function of distance from the graphene (**Figure 6.2.2 c**). (See Simulation Section for details.) At the graphene surface, a potential of $\Phi = +360$ mV is calculated relative to bulk water. Excess hydrogen density compared to oxygen density close to the graphene surface ($z < 0.3$ nm) leads to the positive potential. Considering the double-layer capacitance at the graphene-solution interface, ~ 1.3 μF cm^{-2} (assuming the hydrogen-graphene distance of 0.12

nm)[78], the corresponding charge density is approximately 0.005 C m^{-2}, in good agreement with the value of σ_{off} inferred from the experiment (0.007 ± 0.002 C m^{-2}).

pH Response of Graphene Electrode to Complex Biofluids

Building on this understanding of GE operation in an idealized PBS sample, we conducted experiments to explore the use of GEs in more complex biological solutions. As a first step, we used a GE to measure the Faradaic current as a function of pH in a 0.1 μM equine spleen ferritin (Sigma Aldrich F4503) solution in PBS. Ferritin is a globular protein complex of 24 subunits found in most tissues and in serum (pH ~ 7.0) that stores iron oxide and releases it in a controlled fashion. Ferritin is known to disassemble and release the stored iron ions for pH below ~ 2.0 [83], with partial disassembly beginning to occur for pH below 4.2 [84]. Since kapton degrades at low pH below 2.0[85], the GEs for this experiment were fabricated on oxidized silicon substrates. First, we measured the Faradaic current for the ferritin solution as a function of pH over the range 1.0 – 7.0, and then we conducted the same measurement for a pure PBS solution to determine a baseline response (data not shown). The pH of all solutions was adjusted in steps of ~ 1.0 pH unit by adding 150 mM hydrochloride acid solution.

In order to observe the signature of ferritin disassembly, we focused on the *relative* Faradaic current **(Figure 6.2.3),** obtained by subtracting the baseline Faradaic current for PBS from that for the 5 μM ferritin solution. The relative Faradaic current increases abruptly at pH near 2.0, exactly in the range where ferritin disassembles and positively charged iron ions enclosed in the intact globular ferritin 24-mer are released. Furthermore, there is a noticeable increase in the relative Faradaic current in the pH range 2.0 - 4.0, in agreement with the expectation that partial disassembly of horse spleen

ferritin occurs in this range[84]. Thus, the pH dependence of the relative Faradaic current for the ferritin solution, although not analytically interpretable, is a sensitive probe of biomolecular processes that substantially change the electrostatic environment of the GE.
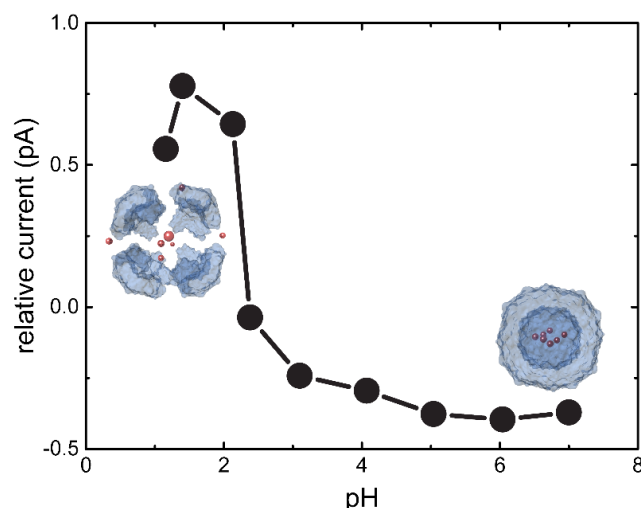
Figure 6.2.3. *pH-dependence of the relative current for the ferritin solution, defined as the difference between the Faradaic current for the ferritin solution and the baseline current for PBS.*

To test the GE performance in a complex human bio-fluid, we investigated its response to pH changes in a sample of human serum (ThermoFisher) diluted with PBS to bring it to physiological ionic strength ~ 150 mM. The pH range tested was 6.0 (typical extracellular pH for a tumor) to 7.6 (typical for normal tissue), which covers the range of pH variation that can be induced by non-metastatic/metastatic tumor.[5556,71,72] The GE Faradaic current was measured over the same pH range in PBS at ionic strengths of 139.5mM, 150 mM, and 160.5 mM (**Figure 6.2.4 a**), corresponding to the variation ionic strength expected in extracellular fluid (~7%)[73]. Over the relevant pH range, the Faradaic current varied by nearly 0.3 pA (~ 45%), with an estimated pH resolution < 0.2 pH unit

and sensitivity of 0.144 ± 0.0098 pA/pH. For fixed pH, the variation of Faradaic current over the range of ionic strengths tested was only $0.01 - 0.02$ pA, more than an order of magnitude smaller.

For human serum, the Faradaic charge transfer (**Figure 6.2.4 b**) had a more gradual time dependence than that for PBS (**Figure 6.2.2 a**). The variation of the GE Faradaic current with time in serum was well described by simple relaxation with a single time constant τ to a constant value that we term the steady-state Faradaic current (**Figure 6.2.4 b**). At a pH of 7.60 (**Figure 6.2.4 b,c**), the time constant was $\tau = 3.81 \pm 0.09$ s, and over the range of pH tested, this time constant varied by ± 0.5 s. This relaxation time is presumed to reflect equilibration processes such as non-specific adsorption of organic and inorganic components in human serum[86] onto the graphene surface, in rough agreement with earlier reports of the saturation time scale for non-specific adsorption of protein onto graphene (~ 30 s) measured with graphene FETs[75].

The magnitude of the Faradaic current measured in serum (**Figure 6.2.4 d**) is smaller by $0.1 - 0.4$ pA over the whole pH range than that for PBS. The reduced current magnitude is ascribed to the inhibition of electronic communication to the GE by biomolecules adsorbed onto its surface[87,88].

The differential current with respect to the pH ($\Delta I / \Delta[pH]$) can be derived from the current-pH response (**Figure 6.2.4a**), with results shown in **Figure 6.2.4 d**. The differential current response shows two different behaviors over the tested range: it is positive for pH 6.1 to 6.6 (saturating at ~ 0.47 pA/pH), and it is negative for pH 6.6 to 7.6 (saturating at ~ -0.23 pA/pH) with an abrupt transition at pH ~ 6.6. Since tumor development almost exclusively leads to acidosis with very rare exceptions[89], tumor-

induced pH decrease will result in either Faradaic current reduction in the pH range of 6.1 to 6.6 or increase in the range of 6.6 to 7.6 (**Figure 6.2.4e**). Thus for tumor diagnosis, the range of the pH can be determined from the current variation and further the pH can be identified based on the current-pH response.
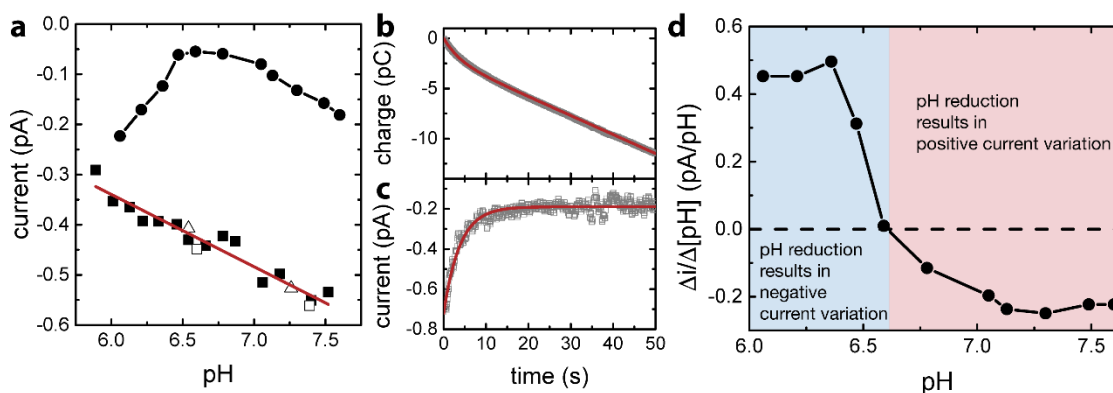
Figure 6.2.4. *(a) Faradaic current for human serum sample diluted to ionic strength of 150.0 mM (solid circles) and for phosphate buffer solution (PBS) as a function of pH in the physiological range. PBS measurements were made at ionic strength values of 139.5 mM (hollow squares), 150.0 mM (solid squares), and 160.5 mM (hollow triangles). The red curve is a linear fit to the PBS data. (b, c) Time-dependence of the Faradaic charge transfer (panel b) and Faradaic current (panel c) for human serum at pH = 7.60. The red curves in b and c are fits to a model where the Faradaic current is described by a single relaxation time. (d) Differential current with respect to pH calculated based on the current response to serum in a.*

Conclusions

In summary, we have demonstrated the use of flexible graphene microelectrodes for monitoring of pH in idealized and complex bio-solutions, specifically PBS, 5 μM ferritin solution, and human serum. The measurement signal is the zero-bias, sub-pA Faradaic current between the GE and the solution, making this a low-power, minimally perturbative approach. For PBS, the variation of the current with pH can be understood quantitatively in a model where the current reflects the potential of the Stern layer, which

is derived from an intrinsic (positive) charge associated with the graphene-water interface and ionizable (negative) charged groups whose density is described by a Langmuir-Freundlich adsorption isotherm. The charge density intrinsic to the graphene-water interface derived from the model is in excellent agreement with that found *via* molecular dynamics simulation. For the ferritin solution, the relative Faradaic current, compared to a PBS baseline, shows a strong feature at pH ~ 2.0, reflecting the disassembly of the ferritin cage and release of iron atoms. For human serum, the microelectrode rapidly (~ 20 s) reaches equilibrium with the solution. The Faradaic current and the current variation together can be used for identifying pH changes on the scale of that induced by a tumor. This electrode-based technique is therefore potentially suitable for use as a miniature portable or implantable pH-sensor for early-stage cancer diagnosis.

Graphene growth Please refer to Appendix A

Graphene device fabrication Please refer to chapter 4.1 of this thesis.

Biosample preparation Equine spleen ferritin (Sigma Aldrich F4503) samples were prepared at 0.1 μM concentration in full PBS solution (ionic strength 150 mM). Delipidated and dialyzed human serum (ThermoFisher 31876) was diluted by 1.73 times in DI-water, resulting in ionic strength of ~ 150 mM. The pH for solutions of ferritin or human serum was adjusted by adding diluted chloride acid or sodium hydroxide solution.

Simulation Section

The simulations consisted of two sheets of graphene, generated by the Nanotube Builder plug-in of the Visual Molecular Dynamics software (VMD)[90], separated by 20 Å each in contact with atomistic water molecules. Periodic boundary conditions were used and the

graphene sheets were positioned parallel to the *x-y* plane. The *x-y* dimensions of a periodic rectangular box were selected such that each sheet and its images formed a defect-free, continuous sheet of graphene. Each sheet had dimensions of 50.348 Å by 45.376 Å. The pair of parallel sheets was centered within the box in the z-dimension, and the distance between the two sheets was 20.000 Å. Each sheet contained 924 carbon atoms, the positions of which were constrained throughout the simulation. Water molecules were added with VMD's Solvate plug-in. Water was present above and below the sheets with a vacuum between them. The initial dimensions of the box were 51.577 Å by 46.794 Å by 119.942 Å and the system contained a total of 7153 water molecules.

The simulations were carried out in the NPT ensemble at 300 K and 1.0 atm. The area of the periodic box in the *x-y* plane was held constant, and the cell length in the *z* direction was allowed to vary. The CHARMM36[91-93] force field parameters were used with the NAMD software package[94]. The water model was the three-site TIPS3P model[95-97]. The charge on each hydrogen atom is $+ 0.417e$ and $- 0.834e$ on each oxygen atom, where *e* is the elementary charge. Bond distances in water molecules were constrained using the SHAKE algorithm[98]. Temperature was controlled with a Langevin thermostat with a damping coefficient of 1.0 ps^{-1}. Pressure was controlled with a Langevin piston barostat[99,100] with a period of 200 fs and a damping time of 100 fs. The particle mesh Ewald method was used to calculate long-range electrostatics beyond 14.0 Å, with a grid spacing of 1.0 Å. A 2 fs time step was used. The system was minimized for 20,000 steps, then heated incrementally to 300 K in steps of 5 K and 50 K over 160 ps. The system was equilibrated for 200 ps, then run for 10 ns, with configurations sampled every

1 ps. For each configuration, the charge density of the water molecules was calculated as a function of distance from the plane containing the carbon atoms of graphene.

The electric potential (ϕ) as a function of distance from graphene (z) was calculated from the charge density (ρ) using the Poisson equation[101,102]:

$$\frac{d^2\phi(z)}{dz^2} = -\frac{\rho(z)}{\varepsilon_0} \qquad \textbf{(6.5)}$$

where ε_0 is the vacuum permittivity, 8.854×10^{-12} C m^{-1} V^{-1} (F/m) or 5.526×10^{-5} e nm^{-1} mV^{-1}. This equation is integrated twice under the boundary conditions that electric field and potential are zero in bulk, to give

$$\phi(z) - \phi(z_0) = -\frac{1}{\varepsilon_0}\int_{z_0}^{z} dz' \int_{z_0}^{s} \rho(z'')\, dz'' \quad \textbf{(6.6)}$$

$$= -\frac{1}{\varepsilon_0}\int_{z_0}^{z} (z-z')\,\rho(z')dz'$$

where the final expression is obtained using integration by parts. The bulk, reference value of z_0 used was 4.4 nm.

6.3 Graphene Microelectrode Sensors for Ferritin-Nanoparticle Assembly Detection

The work presented here also appears in the publication: *Jinglei Ping, Katherine W. Pulsipher, Ramya Vishnubhotla, Jose A. Villegas, Tacey L. Hicks, Stephanie Honig, Jeffery G. Saven, Ivan J. Dmochowski, A. T. Charlie Johnson*, Chemical Science (**2017**)

Abstract

The characterization of protein-nanoparticle assemblies in solution remains a challenge. We demonstrate a technique based on a graphene microelectrode for structural-functional analysis of model systems composed of nanoparticles enclosed in open-pore and closed-pore ferritin molecules. The method readily resolves the difference in accessibility of the enclosed nanoparticle for charge transfer and offers the prospect for quantitative analysis of pore-mediated transport shed light on the spatial orientation of the protein subunits on the nanoparticle surface, faster and with higher sensitivity than conventional catalysis methods.

Introduction

The ability to attach functional biomolecules to nanoparticle surfaces has spurred development of nano-therapeutic[103], diagnostic,[104] and biosensing[105,106] agents, as well as novel nano-structures[107] and devices.[108] Methods for controlling the number and orientation of oligonucleotides and peptides at nanoparticle surfaces have been established,[108] but it remains challenging to create nanoparticle-protein assemblies with native-like protein structure and function.[109,110] One emerging paradigm is a thermophilic ferritin protein[111,112] whose 24 self-assembling four-helix bundles maintain native stoichiometry and secondary structure when encapsulating a single 6-nm gold nanoparticle (AuNP).[113-115] However, the assembly configuration in

solution remains unknown because conventional methods for characterizing protein structure, such as X-ray crystallography[84] are not suitable for liquid-phase protein-nanoparticle conjugates.

Here, we demonstrate a non-perturbing method using a graphene microelectrode[74] for structural-functional analysis of an ordered AuNP-ferritin protein assembly that differs substantively from an unstructured protein corona. Charge flowing from the AuNP through ferritin pores transfers into the graphene microelectrode and is recorded by an electrometer. The measurements are consistent with a pore diameter of 4.5-nm, providing evidence that ferritin maintains native-like quaternary structure upon AuNP encapsulation. This work highlights the design and characterization of nanoparticle-protein assemblies with tunable ionic conductivity and chemical reactivity, and demonstrates a new tool for sensitively probing protein-nanomaterial interactions.

Results and Discussion

Ferritin is a multimeric iron-storage protein comprising 24 protein subunits that self-assemble to form a hollow, ~8 nm inner diameter cage. The *Archaeoglobus fulgidus* ferritin (AfFtn) used here is a unique archaeal ferritin that forms a tetrahedral arrangement of its four-helix-bundle subunits, yielding four wide (4.5-nm), triangular pores spanning the 2-nm protein shell[116] (**Fig. 6.3.1a**). Stoichiometric addition of 6-nm gold nanoparticles (AuNPs) to disassembled apo-AfFtn induces AfFtn assembly around individual AuNPs capped with bis(*p*-sulfonatophenyl) phenylphosphine (BSSP),[113-115] while maintaining its native thermal stability, stoichiometry, ferroxidase activity, and secondary structure.[113] However, it is not understood whether AfFtn assembles in its native quaternary structure upon AuNP

encapsulation, maintaining the large triangular pores, or whether subunits assemble in a more typical ferritin closed-pore conformation or adsorb in an unordered fashion.
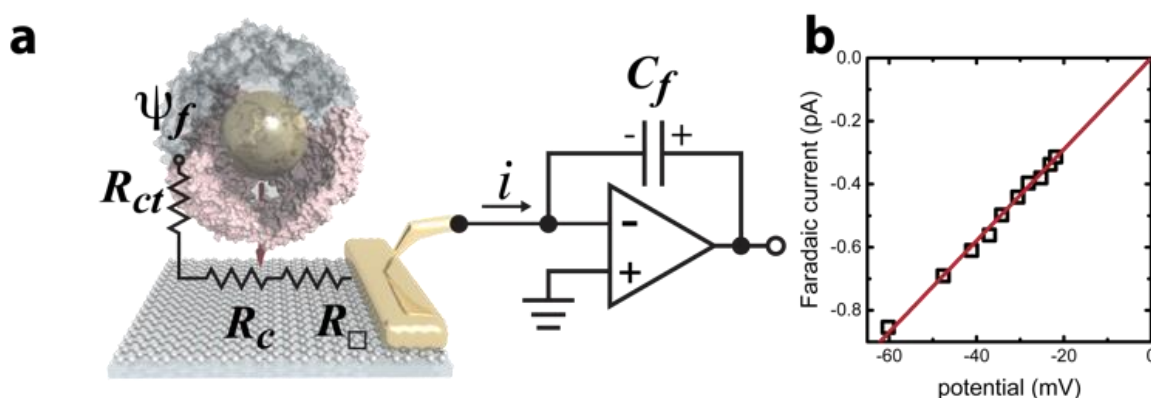
Figure 6.3.1. *(a) Schematic of the setup for measuring spontaneous Faradaic charge transfer across a pore to a graphene microelectrode in buffer solution and circuit diagram. (b) Faradaic current as a function of electrostatic potential in the buffer solution above graphene. The red line is a linear fit to the data.*

A graphene microelectrode was used to quantify Faradaic current through a ferritin-AuNP assembly and thereby gain information about the arrangement of AfFtn subunits on the AuNP surface (i.e. differentiate between open- and closed-pore forms of the AfFtn shell). The experimental setup (**Fig. 6.3.1a**) consisted of a graphene-based microelectrode connected to the inverting input of an electrometer[74] (Keithley 6517a). The electrostatic potential above a protein assembly in fluid, ψ_f, drives a sub-picoampere Faradaic current, i, through the series resistance of the charge-transfer at the graphene-solution interface[74] ($R_{ct} \sim 100$ GΩ), the graphene

sheet ($R_\square \sim 10^2 - 10^3$ Ω/□), and the graphene-gold contact[117] ($R_\mathrm{c} \sim 10$ Ω). Transferred charge accumulates on the feedback capacitor and is read out on the electrometer. Because there is no extrinsic bias voltage between the solution and the microelectrode, heat dissipation (aW µm^{-2}) and electrical perturbation (~pA) to the protein structure[118] are minimized. In a previous report[75] we documented the intrinsic low noise level for microelectrode measurements in an idealized buffer solution as well as excellent agreement between the data and theoretical models of the behaviour of the electric double layer above graphene.

The Faradaic current i is proportional to the potential ψ_f: $i = \psi_f / R_{ct}$. We applied a phosphate buffer solution to the graphene microelectrode and measured the Faradaic current while the electrostatic potential above the graphene surface was tuned by varying the buffer ionic strength c (**Fig. 6.3.1b**). The variation of ψ_f with ionic strength was inferred from the graphene equation for the electric double layer. The fit to the data corresponds to a constant charge-transfer resistance $R_{ct} =$ 69 ± 2 GΩ, and the fit passes through the origin as expected (0.6 ± 0.9 fA).

The assembly state of AfFtn in solution is affected by ionic strength: it assembles into the native 24mer cage at high ionic strength and disassembles into dimers at low ionic strength.[116] For quantifying trans-pore current *via* the enclosed AuNP, the current baseline for the AuNP-ferritin system was determined by measuring the Faradaic current of an AfFtn mutant (E65R, termed AfFtn-R), which remains a 24mer even in low ionic strength solution. (See Supplementary Fig. S1.) The solution (200 µL; 20 nM) was applied to the microelectrode, and a sparse layer of non-specifically bound protein allowed to form and equilibrate (Supplementary Fig.

S2). As the ionic strength of the solution was varied from 40 mM to 640 mM, a 15-sec time trace of Faradaic charge transfer (**Fig. 6.3.2a**) for AfFtn-R or AfFtn was used to extract the corresponding Faradaic current (**Fig. 6.3.2b**). Because of its excellent linearity, this 15-sec time trace is sufficient to determine the Faradaic current with high accuracy: indeed, for all figures in this report, the statistical errors associated with the electronic measurement are smaller than the size of the plotted points, and the observed scatter in the data is ascribed to experimental variation in the biofluid that is difficult to control. The solutions showed nearly identical Faradaic current at high ionic strength where both ferritins form stable 24mer assemblies, but the currents differed significantly at low ionic strength, where only AfFtn disassembles into dimers. The measured current for the AfFtn-R solution (black circles in **Fig 6.3.2b**) and the Faradaic current difference between the solutions of AfFtn and AfFtn-R (**Fig. 6.3.2c**) are well explained by models based on known properties of the electric double layer and AfFtn assembly. In particular, we infer a dissociation constant for AfFtn of 210 ± 60 mM, in agreement the value found from liquid chromatography measurements. (See Supplementary Section for details.)

To assess the configuration of AfFtn subunits on the surface of an AuNP, we measured the real-time Faradaic charge transfer for solutions of AuNPs (I_{AuNP}, see Supplementary Fig. S3), and of AuNP-ferritin assemblies based upon the wild-type ferritin AfFtn and a recently identified mutant, AfFtn-AA (K150A/R151A), which features an octahedral arrangement of its subunits with "closed" (< 1 nm) pores.[119] Representative data are shown in Supplementary Fig. S4. If AfFtn and AfFtn-AA

maintain their native quaternary structure upon AuNP encapsulation, the AuNP surface should be less accessible for AfFtn-AA compared to AfFtn, and there should therefore be less charge transfer.

We used the Faradaic current of AfFtn-R as the baseline for assembled (24mer) ferritin, which leads to several strict requirements for accurate quantification of trans-pore current. First, ferritin must remain assembled with the AuNP enclosed. This is satisfied as 24mer assemblies of both AuNP-AfFtn and AuNP-AfFtn-AA are stable in the range of ionic strengths tested (40 – 340 mM).[113] Second, all AuNPs must be encapsulated by ferritin with no free AuNPs in solution. As shown in Supplementary Fig. S5 and S6, more than 99% of AuNPs were enclosed in a ferritin protein shell as confirmed by TEM and gel electrophoresis. We also verified that AuNPs were stable in the range of ionic strengths used without aggregation (Supplementary Fig. S7).
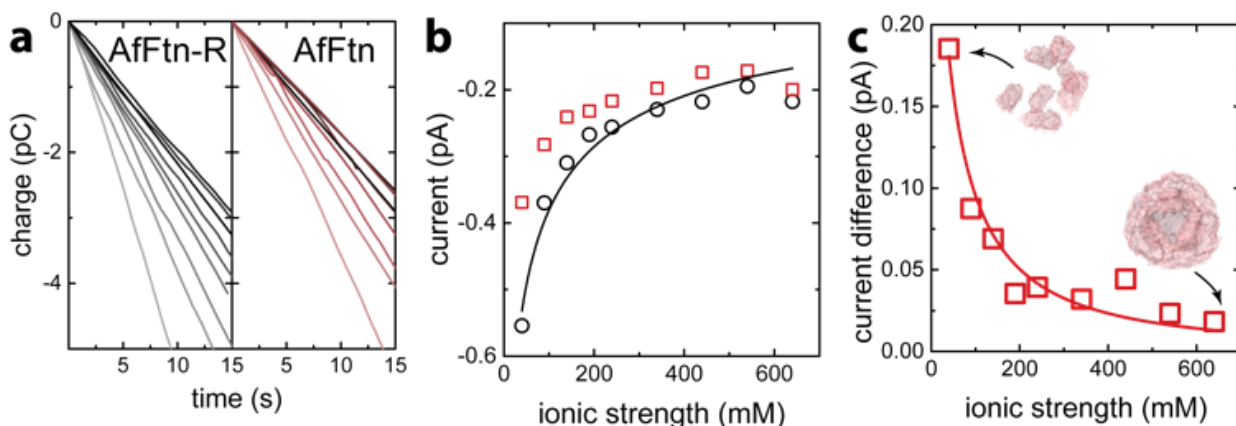
Figure 6.3.2. *(a) Time trace of the charge transfer between a graphene microelectrode and mutant A. fulgidus E65R ferritin solution (AfFtn-R), and wild-type A. fulgidus ferritin solution (AfFtn). The ionic strength of the solution increases as the grey-level of the data increases. (b) Faradaic current for AfFtn-R (black circles) and AfFtn (red squares) based on the data in panel a. The black curve is a fit to the data for AfFtn-R using Supplemental*

*Eqn. (1S). (**c**) Faradaic current difference for AfFtn compared to AfFtn-R; the red curve is a fit based on Supplemental Eqn. (25).*

To quantify Faradaic current contributed by enclosed AuNPs, we calculated the difference between the current for AuNP-AfFtn (AuNP-AfFtn-AA), $I_{AuNP\text{-}AfFtn}$ ($I_{AuNP\text{-}AfFtn\text{-}AA}$) and the baseline ($I_{AfFtn\text{-}R}$): $\Delta I = I_{AuNP\text{-}AfFtn} - I_{AfFtn\text{-}R}$ ($I_{AuNP\text{-}AfFtn\text{-}AA} - I_{AfFtn\text{-}R}$), with results plotted in **Fig. 6.3.3a**. For AuNP-AfFtn, ΔI varied by ~0.12 pA through the range of ionic strength, with a minimum at ~240 mM. For AuNP-AfFtn-AA, ΔI was much smaller and essentially constant at -0.020 ± 0.005 pA. For AuNP-AfFtn, the plot of ΔI *vs.* I_{AuNP} (**Fig. 6.3.3b**) followed a linear trend with slope $a = 0.59 \pm 0.05$, suggesting that the efficiency of Faradaic charge transfer *via* AuNPs enclosed in open-pore AfFtn is ~60% of that for bare AuNPs. In contrast, for AuNP-AfFtn-AA, we found a slope $a = 0.03 \pm 0.03$, suggesting that the ferritin closed pores completely suppress this charge transfer pathway.
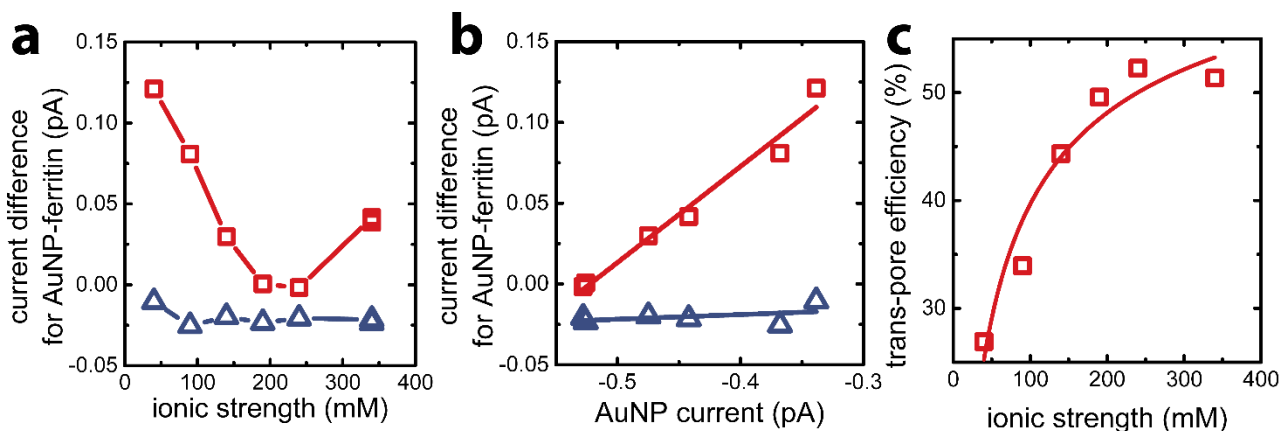
Figure 6.3.3. (*a*) *Difference in Faradaic current for solutions of AuNP-enclosed in A. fulgidus mutant ferritin K150A/R151A (AuNP-AfFtn-AA, blue triangles) and AuNP-enclosed in wild-type ferritin (AuNP-AfFtn, red squares) compared to the baseline current set by a solution of E65R ferritin (AfFtn-R). Two data points, which almost*

This analysis suggests that the Faradaic current carried by the ferritin-AuNP system has

two components: i) pore-mediated current *via* the AuNP and ii) current associated with

the protein shell, quantified by $I_{AfFtn-R}$. We define the trans-pore efficiency $\xi(c) =$

$|aI_{AuNP}(c)|/(|aI_{AuNP}(c)| + |I_{AfFtn-R}(c)|)$ to quantify the fraction of the total current

carried by the enclosed AuNPs. The efficiency increases monotonically by ~100% as the

ionic strength increases from 40 mM to 340 mM (**Fig. 6.3.3c**). In contrast to molecular

diffusion through the pore, which is driven by a concentration gradient, the Faradaic

current depends on the gradient of the electrostatic potential. Thus, negative charge at the

edge of the AfFtn pores can suppress the (negative) Faradaic current *via* the enclosed

AuNP over length scales given by the Debye screening length $\lambda_D[nm] = 0.304/\sqrt{c[M]}$.

Thus we expect that the efficiency will be affected by ionic strength approximately as

$\xi = A(4.5 - k\lambda_D[nm])^2$ where A is a factor scaling area to efficiency, 4.5 nm is the pore

diameter for AfFtn, and k is ~1. The charge-transfer efficiency is well fit by this equation

(**Fig. 6.3.3c**) with best fit value $k = 1.2 \pm 0.1$. This experiment demonstrates the

capability of graphene microelectrode measurements to differentiate between open- and

closed-pore structures in ferritin-nanoparticle assemblies, confirms the solvent

accessibility of enclosed AuNPs, and provides strong evidence that the AfFtn pore

maintains a native-like structure in the presence of the enclosed AuNP.

For confirmation and comparison, we used conventional catalysis methods to

differentiate between wild-type AuNP-AfFtn and AuNP-AfFtn-AA: dehalogenation

of a bisiodinated boron dipyrromethene derivative (I-BODIPY) and reduction of 4-nitrophenol. More AuNP surface area should be exposed in the AfFtn-containing sample compared to AfFtn-AA, and should therefore have greater AuNP catalytic activity. The reactions were monitored by different spectroscopic techniques: an increase in fluorescence at 507 nm was observed for the I-BODIPY dehalogenation reaction,[120] and a decrease in absorbance at 400 nm was observed for the 4-nitrophenol reduction.[121] The mechanism for AuNP-catalyzed dehalogenation of I-BODIPY is not well-understood but appears to be pseudo-zero order based on our data, similar to what was observed for dehalogenation of iodobenzene by AuNPs.[122] An induction period was observed in the 4-nitrophenol reduction, similar to polymer-coated AuNP systems.[123-126] This induction period has been attributed to diffusion of reagents to the AuNP surface and surface rearrangement of the AuNP before reaction can occur.[124] We expect similar effects to be in play for our AfFtn-coated AuNPs.

As shown in **Fig. 6.3.4 a**, the rate of increase in the fluorescence intensity in the AuNP-AfFtn solution (0.0081 ± 0.0002 A.U./min) is approximately 4 times larger than the AuNP-AfFtn-AA solution (0.0019 ± 0.0002 A.U./min). For the 4-nitrophenol reduction, AuNP-AfFtn had roughly twice the catalytic rate constant, $k = (7.4 \pm 0.7) \times 10^{-3}$ s^{-1} vs. $(4.0 \pm 0.3) \times 10^{-3}$ s^{-1} for AuNP-AfFtn-AA (**Fig. 6.3.4 b**). Neither ferritin contributed to the catalytic activity; see Supplementary Fig. S8. For the catalytic assays, the difference in signal for AuNP-AfFtn versus AuNP-AfFtn-AA is only four-fold and two-fold for the I-BODIPY and 4-nitrophenol reactions, respectively. In contrast, the difference between AuNP-AfFtn and AuNP-AfFtn-AA

for the microelectrode is nearly 20-fold (**Fig. 6.3.3 c**). Thus, our methodology based on graphene microelectrode is comparatively rapid (seconds *vs* tens of minutes), has the potential for a quantitative estimate of the pore diameter through direct charge-transfer measurement through the protein shell, and could overcome limitations in sensitivity imposed by the AuNP catalytic reactions. Finally, the electrode-based method only requires relatively small amounds of sample solution (~ tens of μL) compared to the catalytic method, which also requires significant amounts of additional reagents (I-BODIPY, 4-nitrophenol, and NaBH₄).
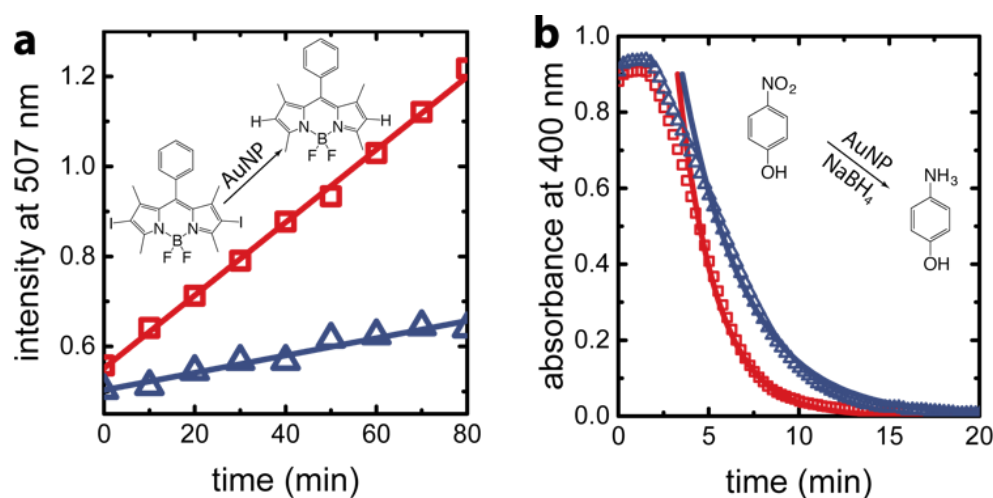
Figure 6.3.4 (*a*) *Real-time fluorescence intensity of I-BODIPY dehalogenation catalyzed by AuNP-AfFtn-AA (blue triangles) and AuNP-AfFtn (red squares) solutions. For each measurement, 10 nM AuNP-AfFtn and 1 μM I-BODIPY were mixed in 50 mM HEPES, pH 7.0 (100 μL total volume). (**b**) Real-time UV-visible spectroscopy of reduction of 4-nitrophenol catalyzed by AuNP-AfFtn-AA and AuNP-AfFtn solutions. For each measurement, 5 nM AuNP-AfFtn and 50 μM 4-nitrophenol were mixed in a cuvette. Freshly prepared aqueous NaBH₄ was added to a final concentration of 2.5 mM and total sample volume of 1 mL. The solid curves are fits based on first-order kinetics. The corresponding catalytic reactions are shown in panels a-b.*

Conclusions

We have developed a graphene microelectrode device as a sensitive tool for structure-function analysis of AuNP-ferritin assemblies in solution. This all-electronic method has multiple advantages for identifying protein pores compared to conventional AuNP catalysis methods, and it has the potential to be developed into a direct measurement of the pore-mediated charge-transfer process. Our approach could provide a way to explore protein structure at nm-scale and, more broadly, to explore interactions of biomolecules with inorganic nanomaterials in complex biofluids--systems shown to offer significant promise in bio-imaging, sensing,[106] catalysis and templated nanoparticle synthesis.[7]

Graphene growth Please refer to Appendix A

Graphene device fabrication The graphene-copper growth substrate was coated with 500-nm layer of poly(methylmethacrylate) (PMMA, MicroChem), and the PMMA-graphene film was floated off the surface by immersion in 0.1 M NaOH solution with the graphene-copper growth substrate connected to the cathode of a power supply. The PMMA-graphene film was transferred onto a 300 nm SiO_2 /Si wafer with an array of 5 nm/40 nm Cr/Au contact electrodes that were previously fabricated using photolithography. Al_2O_3 (5 nm) was deposited on the whole wafer as a sacrificial layer, and 50 µm $\times$ 100 µm graphene microelectrodes were defined by photolithography with photoresist PMGI (MicroChem) and S1813 (MICROPOSIT) and oxygen plasma etching. The Al_2O_3 layer on top of the microelectrode areas was removed by the basic photoresist developer MIF-319 (MICROPOSIT). After removal of the photoresist residues with 1165 (MICROPOSIT), another passivation layer of photoresist SU-8 (MicroChem) was

applied to the device, and the wells exposing the microelectrodes were defined via photolithography.

Computational Design of AfFtn-R The crystal structure of wild-type AfFtn (PDB 1SQ3) reveals a trimeric interface lined with negatively charged amino acids. We hypothesized that a high ionic strength solution allows for assembly by shielding the electrostatic repulsion between subunits at this interface. Therefore, a point mutation that inserts a positive charge along the interface, with potential for forming salt bridges to a neighboring subunit, could stabilize the 24mer cage at low ionic strengths.

We employed the statistical computational aided design strategy to guide the selection of stabilizing point mutations.[127-130] Calculations were carried out using atomic coordinates from chains G, H and J of AfFtn in PDB structure 1S3Q[2]. For each calculation, all amino acids were considered at the site selected, except for cysteine and proline. All other sites other than the site of interest were constrained to the wild-type identity and crystal structure conformation. Side-chain conformational states were taken from a rotamer library, and all possible conformations were considered.[131] Hydrogen atoms were placed according to the CHARMM19 topology files[93]. Energies were calculated using the CHARMM19 dihedral, van der Waals, and electrostatic terms were considered, with a non-bonded cut-off of 8 Å. Amino acid probability profiles were generated by summing the rotamer probabilities of each amino acid type. Sites 34 and 65 of AtFtn are at the center of the carboxylate-rich pore. Analysis of these sites using the statistical computational design strategy recovered wild-type (glutamic acid, E) as the most

162

probable amino acid at site 34. The most probable conformation possesses a favorable interaction with a neighboring positively charged lysine residue at site 39. This site was not selected for mutation. At site 65, the positively charged arginine (R) was the most probable residue. This site was chosen for mutation, and the arginine variant E65R was selected for expression.

Ferritin mutagenesis The pAF0834 plasmid containing the AfFtn gene was provided by the laboratory of Dr. Eric Johnson at the California Institute of Technology. AfFtn-R was made by site-directed mutagenesis using the Stratagene QuikChange kit. The primers were obtained from Integrated DNA Technologies: sense (5′-3′) GATTTCGTTTCCCGTCGCGGTGGCCGTG, antisense (5′-3′) CACGGCCACCGCGACGGGAAACGAAATC. The mutated cDNA was transformed into XL1-Blue Supercompetent *E. coli* cells (Stratagene) according to the manufacturer's protocol. The plasmid was isolated using a QIAprep Spin Miniprep kit (Qiagen). All sequencing was performed by the University of Pennsylvania DNA Sequencing Facility. The AfFtn-AA plasmid was purchased from DNA2.0 and transformed the same as AfFtn-R.

Ferritin expression/purification Production and purification of AfFtn and mutants was performed as previously published,[115] with some modifications. The plasmid was transformed into BL21-Codon Plus(DE3)-RP competent *E. coli* cells (Stratagene) in TB medium (1 L containing 100 mg ampicillin, 35 mg chloramphenicol) at 37 °C with shaking at 225 rpm until OD_{600} ~0.8 was reached. Expression was induced with 1 mM isopropyl β-D-1-thiogalactopyranoside (IPTG, Lab Scientific) and incubation at 37 °C was continued for 4 h. Cells were centrifuged

and stored at -20 °C, followed by resuspension in buffer (20 mM phosphate, 20 mM NaCl, pH 7.6) with an EDTA-free protease inhibitor cocktail tablet (ThermoFisher Scientific). Cell lysis was performed by treatment with lysozyme (~1 mg/mL final concentration) and sonication (amplitude of 30, 1 s on, 1 s off, 10 min total processing time). Cellular debris was removed by centrifugation (6 krpm, 30 min, 4 °C), and the supernatant was treated with nuclease (Pierce universal nuclease, ThermoFisher Scientific) after addition of $MgCl_2$ to a final concentration of 2 mM for 15 min at room temperature. The solution was heat shocked to remove most endogenous *E. coli* proteins (10 min at 80 °C). After pelleting the precipitated *E. coli* proteins by centrifugation (9 krpm, 60 min, 4 °C), the supernatant was buffer exchanged to ensure complete ferritin assembly (2.5 M NaCl, 2 mM EDTA, 20 mM phosphate, pH 7.6), and purified further using size exclusion chromatography (HiLoad 16/60 column, GE Healthcare). The purity of the protein was determined to be >95% by denaturing PAGE gel (4-15% Tris-HCl, Mini-Protean TGX gel), as seen in Supplementary Fig. S9a. Protein concentration was determined using the Bio-Rad Protein Assay (based on the Bradford method), using bovine gamma globulin as the standard. Proteins were also characterized by MALDI-TOF-MS, TEM, and DLS (see Fig. S9b, Fig. S9c and Table S1 in Supplementary Information). Protein stock solutions were 0.22 μm filtered and stored at 4 °C until use in experiments. Multiple stock solutions of ferritins were used for experiments to ensure reproducibility.

AfFtn solution and AfFtn-R solution preparation Protein samples were prepared at 10 μM concentration in phosphate buffer (20 mM phosphate, pH 7.6),

using NaCl to vary ionic strength (40, 90, 140, 190, 240, 340, 440, 540, 640 mM). To ensure accurate ionic strengths, samples were buffer exchanged on a Zebaspin column (ThermoFisher Scientific) equilibrated with the appropriate buffer. Samples were incubated overnight at 4 °C to allow for equilibration.

AuNP-AfFtn solution and AuNP-AfFtn-AA solution preparation

Citrate-capped 6-nm AuNPs were purchased from TedPella. The citrate was exchanged for bis(p-sulfonatophenyl)phenylphosphine (BSPP, Strem Chemicals) as described previously132. For device measurements, 1 mL samples were prepared at 0.3 mg/mL protein, 0.6 μM 6-nm AuNP-BSPP in 20 mM phosphate pH 7.6 and equilibrated at room temperature for 48 h with gentle agitation to ensure encapsulation. Protein NP samples were buffer-exchanged into various ionic strengths (40, 90, 140, 190, 240, 340 mM) using 10DG columns (Bio-Rad) equilibrated with the appropriate phosphate buffer. The 10DG column also helped ensure that only encapsulated AuNPs remained in the samples, as confirmed by TEM and native gel electrophoresis (see Supplementary Fig. S5 and S6). The first two fractions were combined, and AuNP concentration was verified by UV-vis spectroscopy. Because bare AuNPs cannot elute on a 10DG column, buffer exchange for the AuNP samples without protein was done using Zebaspin columns equilibrated at the same ionic strengths. All samples were diluted to 2 mL to match the lowest concentration sample (20 nM). All samples were measured on the same device on the same day they were prepared, to minimize bulk AuNP aggregation.

Preparation of I-BODIPY I-BODIPY was prepared following the method of

Zuber et al.[133] A dark red solid product was obtained with a mass of 31.8 mg (69.7%

yield). ^{1}H NMR (CD$_2$Cl$_2$): 7.54 (3H, m), 7.29-7.28 (2H, m), 2.62 (6H, s), 1.40 (6 H, s). Mass was verified using MALDI-TOF-MS with α-cyano-4-hydroxycinnamic acid (CHCA) as matrix. For characterization data, see Supplementary Fig. S10.

Fluorescence measurements For the AuNP-catalyzed dehalogenation reaction, 10 nM AuNP-AfFtn and 1 µM I-BODIPY were mixed in 50 mM HEPES buffer (pH 7.0). Steady-state fluorescence was monitored using a Varian Cary Eclipse fluorimeter, with PMT detector voltage at 800 V, excitation wavelength of 465 nm, and temperature of 25 °C.

4-Nitrophenol reduction A solution of 5 nM AuNP-AfFtn and 50 µM 4-nitrophenol (Fluka) was mixed in a cuvette. Freshly prepared aqueous NaBH$_4$ (Fluka) was added to a final concentration of 2.5 mM and total sample volume of 1 mL. Absorbance at 200—1100 nm was measured every 15 s at 25 °C using an Agilent 8453 UV-visible spectrometer. To determine the rate constant k, the data were fit to a first-order reaction, after subtracting the induction time (197 s):

$$\text{Abs} = \varepsilon[A]_0 e^{-kt} \qquad \qquad \textbf{(6.7)}$$

where Abs is the measured absorbance, ε the extinction coefficient of 4-nitrophenol at 400 nm (18000 M^{-1} cm^{-1}), $[A]_0$ the initial concentration of 4-nitrophenol (50 µM), and t the time.

6.4 Graphene Sensors for Quantification of Neuropeptide-Receptor Interaction

The work presented here also appears in the publication: "Ping, Vishnubhotla, Xi, Ducos, Saven, Liu, Johnson", ACS Nano, **2018,** 12 (5)

Abstract

Opioid neuropeptides play a significant role in pain perception, appetite regulation, sleep, memory, and learning. Advances in understanding of opioid peptide physiology are held back by the lack of methodologies for real-time quantification of affinities and kinetics of the opioid neuropeptide−receptor interaction at levels typical of endogenous secretion (<50 pM) in biosolutions with physiological ionic strength. To address this challenge, we developed allelectronic opioid−neuropeptide biosensors based on graphene microelectrodes functionalized with a computationally redesigned water-soluble μ-opioid receptor. We used the functionalized microelectrode in a bias-free charge measurement configuration to measure the binding kinetics and equilibrium binding properties of the engineered receptor with [D-Ala2, N-MePhe4, Gly-ol]-enkephalin and β-endorphin at picomolar levels in real time.

Introduction

Endogenous opioid neuropeptides are an important class of neurotransmitters that play a critical role in stress response, analgesia, addiction, pain management, and cardiovascular control[134]. The dysregulation of endogenous opioid neuropeptides may result in neurologic and psychiatric disorders such as depression, borderline personality disorder, as well as Alzheimer's, Huntington's, and Parkinson's[135-137]. Thus, understanding

opioid−neuropeptide physiology and the downstream applications in pharmacology[138], anesthesia and surgery[139], and therapeutics[140] is highly significant. Conventional voltammetry methods can be used to real-time detect neuropeptides, with relatively low sensitivity, >100 nM [141]. Quantification of opioid neuropeptides at low levels typical in human plasma (<50 pM) [142,143], a crucial enabling step in neuropeptide investigation, currently relies on liquid chromatography and n-rounds mass spectroscopy (LC-MSn), which is incompatible with real-time analysis. This method is highly invasive as the biofluid must be sampled for analysis, and it suffers from low spatial resolution, low throughput, and high cost[144]. Another emerging technique for neuropeptide quantification, biotransistors based on low-dimensional nanomaterials such as silicon nanowires[145] and graphene[29], is not suitable for use in vivo or in ionic complex biofluids due to limitations on sensitivity caused by the Debye screening effect[78]. Here, we demonstrate all-electronic real-time recording of neuropeptide−receptor interactions in solution with physiological ionic strength (∼150 mM) using graphene microelectrodes[74,146,147] functionalized with an engineered water-soluble μ-opioid receptor (wsMOR)[29,148,149]. The wsMOR is a computationally redesigned variant of the membrane protein that, unlike the native MOR, is stable in aqueous solution. The target molecules for our experiments were [D-Ala2, N-MePhe4, Glyol]- enkephalin and β-endorphin, both opioid peptides with high specificity for the native MOR. Conventional electrochemical methods, which include one or more additional electrodes to apply a voltage bias and/or to measure the potential of the solution, may lose sensitivity at low target concentration due to nonspecific adsorption on the additional electrodes[150]. To overcome this limitation, our approach is to monitor the spontaneous, zero-bias Faradaic

charge transfer from the solution into the microelectrode ($\sim$pC/s)[74,146]. We show that this

current varies systematically with the analyte concentration, providing picomolar

sensitivity in a solution with physiological salt content. We used this approach to quantify

the association rate constant, $2.8 \pm 0.1 \times 10^7$ M^{-1} min^{-1}, and the dissociation rate

constant, 0.089 ± 0.001 min^{-1}, for binding between the engineered wsMOR and

enkephalin. The Faradaic current measured after the electrode equilibrated with the

solution varied systematically with the concentration of the target analytes, enkephalin

and β-endorphin, with a limit of detection at the picomolar level. This methodology

offers a pathway toward in vivo quantification of neuropeptide secretion with high

sensitivity and spatiotemporal resolution for interrogating and understanding

neurophysiological and biopsychological effects of neuropeptides.

Results and Discussion

The experimental setup for Faradaic charge measurement[74] is shown in **Figure 6.4.1 a**

(see "Methods" for more information regarding the measurement). All measurements

were conducted in full-strength phosphate buffer solution ($1\times$ PBS). Faradaic charge

transfer occurred through the series combination of the solution diffuse layer resistance

($\sim$10 kΩ)[151], the graphene$-$solution interface charge transfer resistance ($R_{ct} \sim$ 100 GΩ)[74],

the sheet resistance of graphene ($\sim$10^2$-$10^3 Ω/$\square$), and the graphene$-$gold contact

resistance ($\sim$10 Ω)[117]. The charge transfer rate, $\sim$pC/s, was thus primarily determined by

the charge transfer resistance R_{ct}, which is independent of ionic strength[146]. Charge

transferred from the solution to graphene accumulated on the feedback capacitor, C_f, of

the electrometer to produce the readout voltage. For graphene microelectrodes, the

effective potential that drives the spontaneous Faradaic current decays logarithmically with increasing ionic strength[74], instead of the much faster exponential decrease that is characteristic of transistor-based devices. The charge transfer signal was, for this reason, readily detected at physiological ionic strength. As discussed below, our observations are consistent with the view that target binding modulates charge transfer through physical blocking of charge transfer sites.
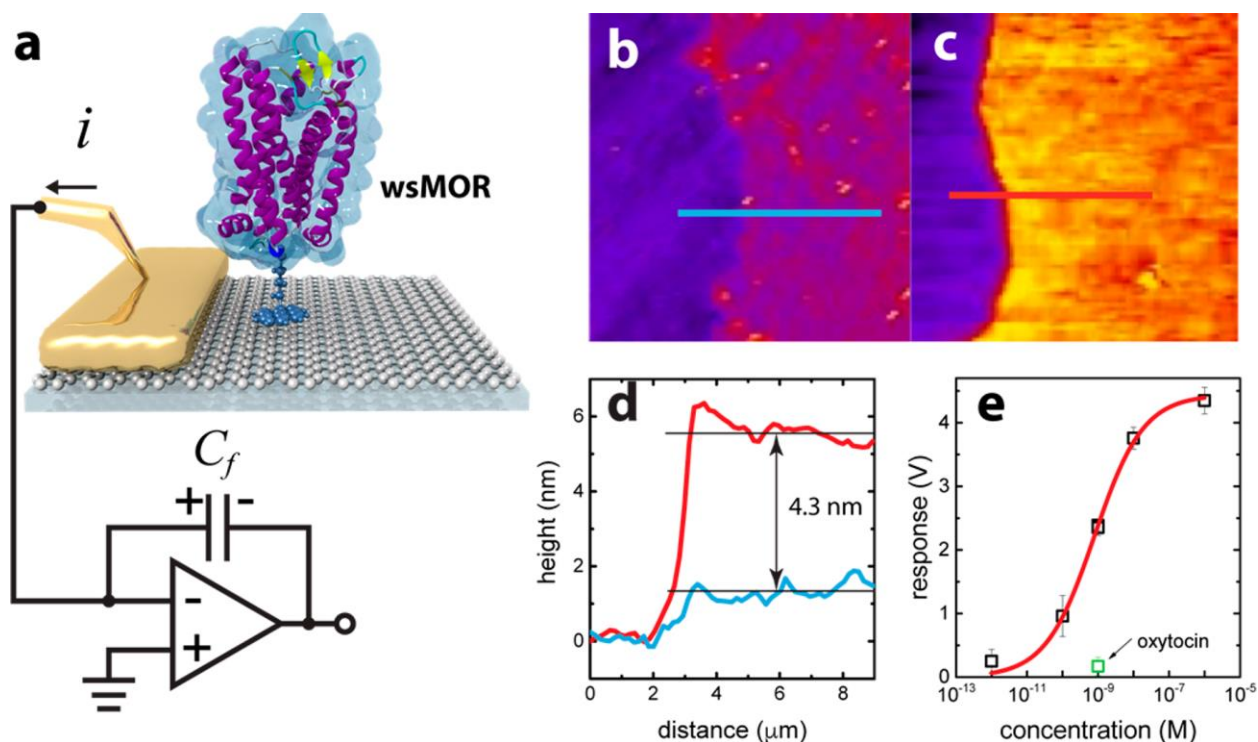
Figure 6.4.1. *(a) Schematic of the electronic setup for measurement of charge transfer from a biosolution to a graphene microelectrode functionalized with water-soluble μ-opiod receptor (wsMOR). (b) AFM image of monolayer graphene on SiO2/Si. (c) AFM image of wsMOR functionalized graphene on SiO2/Si. (d) Line scans indicated in panels b and c, showing the change in apparent height due to functionalization with wsMOR. (e) Response of a graphene transistor-based neuropeptide biosensor to solutions of varying concentration of [D-Ala2, N-MePhe4, Gly-ol]-enkephalin in low-salt buffer (0.002× PBS). Red curve is a fit to a model based on the Hill−Langmuir equation. The green data point is the result of a negative control experiment against oxytocin.*

For fabrication of graphene-based microelectrode arrays, large-area graphene sheets were prepared by chemical vapor deposition and transferred using a low-contamination

bubbling method[52] onto a Si/SiO$_2$ substrate with prefabricated 45 nm thick Cr/Au

electrodes. Graphene microelectrodes (50 μm × 50 μm) were then defined with

photolithography and plasma etching, and the metal contacts were passivated by a

hardbaked, ~20 μm thick SU-8 (MicroChem) layer so that charge transfer could occur

only at the graphene−solution interface (see Methods for further details of the fabrication

process). The graphene microelectrodes were functionalized with the computationally

redesigned wsMOR. The functionalization process parameters (i.e., solution

concentrations and incubation times) were optimized to maximize the density of

immobilized wsMOR. One key factor was a relatively long incubation time (>20 h) in a 1

mM solution of the linker molecule 1- pyrenebutyric acid N-hydroxysuccinimide ester

(PBASE, Sigma-Aldrich) in methanol, a crucial enabling step for highquality

functionalization (see the "Supporting Information" section for details). PBASE is a

bifunctional linker with an aromatic pyrenyl group that irreversibly adsorbs onto the basal

plane of graphene through a noncovalent π−π interaction[152,153]. The PBASE-covered

microelectrodes were next exposed to wsMOR (3 μg/mL) in 1× PBS. The succinimide

groups in the PBASE layer conjugated with primary amine groups on the surface of

wsMOR molecules to form stable amide bonds that immobilized wsMOR. The process

led to a high density of PBASE and wsMOR on the graphene surface[74,154], which

appeared as a uniform brush-like layer when imaged by atomic force microscopy (AFM),

as shown in **Figure 6.4.1c**. The apparent height of wsMOR as determined from AFM line

scans (**Figure 6.4.1 d**) was ~4.3 nm, in good agreement with expectations given the

wsMOR mass of 46 kDa[78]. We used the measured Dirac voltage shift induced by

wsMOR binding and the expected charge state of the wsMOR to estimate the density of

the wsMOR functionalization at 550 μm−2 (details are provided in the "Supporting

Information" section). This value is smaller than that in our earlier report[155] of 1300

μm−2 for single stranded DNA 22-mers immobilized on graphene using a very similar

procedure, which is attributed to the effect of the larger size of the wsMOR on the surface

packing efficiency. Before performing graphene microelectrode measurements of the

real-time binding properties of wsMOR in ionic solution, we characterized the

equilibrium dissociation constant and verified specific binding between wsMOR and

enkephalin by using biosensors based on wsMOR-functionalized graphene field-effect

transistors (GFETs)[29]. The experimental details are provided in the 'Supporting

Information" section. Typically, a biosensor response R against the target at

concentration c is described by the Hill−Langmuir equation[156]:

$$R = A \frac{\left(c/K_A\right)^n}{1 + \left(c/K_A\right)^n} \tag{6.7}$$

where A is the magnitude of the sensor response, KA is the concentration producing half

occupation, and n is the Hill coefficient. We measured the current−gate voltage (I−V_G)

characteristics of the wsMOR/GFETs in the dry state and quantified the sensor response

R as the shift of the Dirac voltage, ΔV_D, which varied systematically with the

concentration

of enkephalin in a low-salt buffer (0.002× PBS). As shown in **Figure 6.4.1e**, ΔV_D was

well fit by **Equation 6.7**, with the fit parameters A = 4.4 ± 0.1 V, K_A = 0.79 ± 0.10 nM,

and n = 0.6 ± 0.1. The fit value for the value of K_A was in very good agreement with the

value of 1.2−3.1 nM obtained by optical assays for the binding between native MOR and enkephalin[157,158]. The best fit value for the Hill coefficient n was smaller than the value obtained from radioligand binding assays, ∼1.0, [159] but consistent that in our earlier report for DNA hybridization on graphene, 0.56 ± 0.07,[155] which is ascribed to the interaction between graphene, the receptor, and the analyte (wsMOR and enkephalin in this case). We also tested the GFET biosensor response against oxytocin, an endogeneous neuropeptide that is known not to bind specifically to native MOR [160]. The response of the biotransistors to 1 nM oxytocin solution was very small, 0.17 V (**Figure 6.4.1 e**), indicating a low level of nonspecific binding of oxytocin to the wsMOR. We note that the transistor-based biosensor, although suitable for quantifying the enkephalin−receptor dissociation constant, suffers from the Debye screening effect[78], which required that the target be presented in a low-salt buffer solution for real-time testing. Now we discuss real-time measurements of the neuropeptide− wsMOR interaction using the graphene microelectrodes. The graphene microelectrode was exposed to 1× PBS at full ionic strength (∼150 mM). To determine the sensor response to enkephalin at different concentrations, drops of enkephalin solution at successively larger concentrations were placed onto the device; after each drop was applied, the feedback capacitor of the electrometer was discharged, and then a charge transfer time trace was acquired. Time traces of the Faradaic charge transfer, Q(t), for three different concentrations are shown in **Figure 6.4.2 a**, with the corresponding Faradaic currents, i(t) = dQ/dt, shown in **Figure 6.4.2 b**. From **Figure 6.4.2 b**, we see that the Faradaic current for 0.2 pM enkephalin decreased gradually over tens of minutes and saturated after more than 30 min, which is ascribed to an increase in Rct caused by enkephalin binding to wsMOR on

the graphene microelectrode so that charge transfer sites were physically blocked[146]. In contrast, for a target concentration of 22 nM, the current decreased much more quickly and saturated after about 6 min. To quantify the binding kinetics, we fit the current i(t) with a single-time relaxation model[161] describing ligand−receptor binding:

$$i(t) = i_A(c) - i_B(c)(1 - e^{-t/\tau}) \tag{6.8}$$

where $i_A(c)$ is an offset current at t = 0, τ is the saturation time constant, and $i_A(c) - i_B(c)$ is the saturation current for long times as the system reaches equilibrium (for practical purposes, this requires $t \geq 3\tau$). For 0.2 pM enkephalin, the best fit value is $\tau = 11.2 \pm 0.7$ min, whereas for 22 nM, $\tau = 1.40 \pm 0.02$ min, a factor of about 8.0 times smaller.
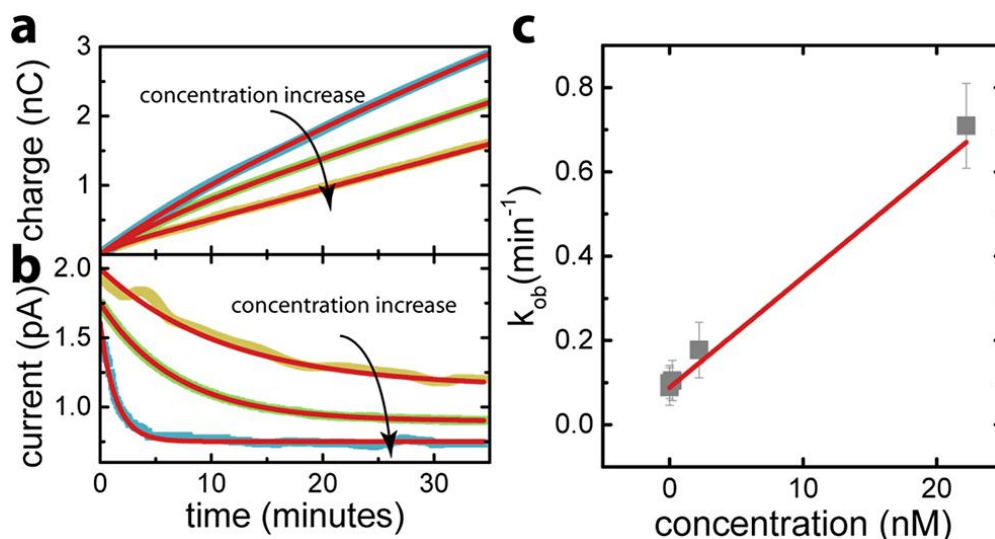
Figure 6.4.2. *(a) Real-time Faradaic charge transfer into graphene for 0.2 pM (blue), 2.2 nM (green), and 22 nM (yellow) [D-Ala2, NMePhe4, Gly-ol]-enkephalin in phosphate buffer solution. (b) Extracted Faradaic current as a function of time. The red curves in both panels are exponential fits characterized by a single time constant τ, as discussed in the main text. (c) Plot of the inverse of the time constant (k_{ob} = 1/τ) as a function of concentration. The red line is a linear fit to the data.*

For ligand−receptor binding, the observed saturation rate $k_{ob} = 1/\tau$ depends on the target concentration c through the relation $k_{on} = (k_{ob} - k_{off})/c$, where k_{on} and k_{off} are the

association rate constant and the dissociation rate constant, respectively[161]. The measurement presented in **Figure 6.4.2 c**, is well described by this relationship, and the best fit values for k_{on} and k_{off} are $2.8 \pm 0.1 \times 10^7$ M−1 min−1 and 0.089 ± 0.001 min−1, respectively. These values are in good agreement with those determined using radioligand binding assays: $k_{on} = 8.5 \times 10^7$ M−1 min−1,[162] and $k_{off} = 0.155 \pm 0.001$ min−1.[163] The corresponding dissociation constant $K_A = k_{off} / k_{on}$, is 3.1 ± 0.2 nM, slightly higher than the value derived from the FET sensor measurement, 0.79 ± 0.10 nM, but in good agreement with that found using optical assays, 1.2−3.1 nM [157,158], for native MOR and enkephalin binding. To investigate the use of the functionalized graphene microelectrode as an enkephalin biosensor, the limiting value of Faradaic current as t → ∞, iA(c) − iB(c), was obtained by fitting the measured charge transfer to **Equation 6.8**, and the sensor response was taken to be a relative Faradaic current compared to that measured when the microelectrode was exposed to pure PBS. As shown in **Figure 6.4.3**, the variation of the relative Faradaic current with enkephalin concentration was well fit by the Hill−Langmuir formula **Equation 6.7**, with high signal-to-noise ratio. The best fit values of the parameters are the amplitude A = −0.56 ± 0.01 pA, the concentration producing half occupation, $K_A = 3.6 \pm 0.4$ nM (in excellent agreement with the value obtained by kinetic measurements discussed above), and the Hill coefficient, n = 0.5 ± 0.1, again reduced below 1.0 by interactions between graphene, the receptor, and the enkephalin target.

We applied the same methodology to β-endorphin, a second neuropeptide known to bind to native MOR. As demonstrated in **Figure 6.4.3**, the neuropeptide biosensor response varied systematically with target concentration with high signal-to noise ratio and again

could be well fit by **Equation 6.7**. The best fit value for the dissociation constant was K_A = 1.5 ± 0.2 nM, in good agreement with the value obtained via radioligand arrays, 2−6 nM [164]; the value for n was 0.6 ± 0.1, in the range typical of functionalized graphene sensors. We found that the best fit value for the amplitude A = −0.89 ± 0.03 pA for β-endorphin is ~1.6 times larger than the amplitude found for enkephalin. This is ascribed to greater inhibition of charge diffusion[87,88] by β-endorphin compared to that of enkephalin due to the former's greater molecular weight and thus size. It is possible that the signal strength for the microelectrode sensor depends on multiple attributes of the target, such as size, chirality, and charge, making this an interesting topic for future exploration. Remarkably, for both enkephalin and β-endorphin, the excellent signal-to-noise performance leads to a detection limit in the picomolar range, suggesting this sensor system is capable of resolving the mean secretion level of enkephalin (~15 pM)[142] or β-endorphin (~40 pM)[143] characteristic of human plasma.
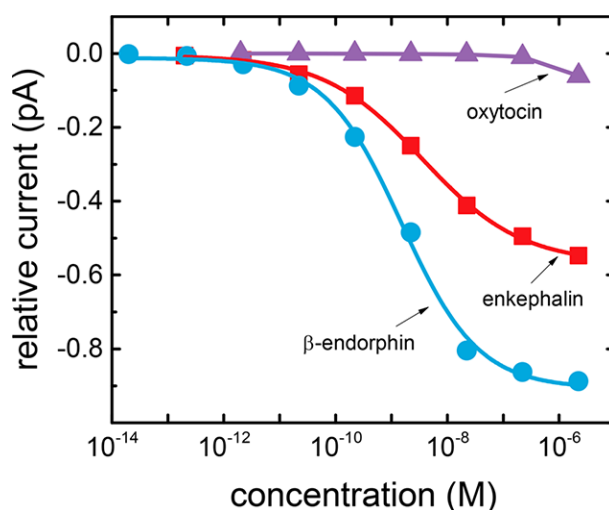
Figure 6.4.3. *Relative Faradaic current for the [D-Ala2, N-MePhe4, Glyol]- enkephalin, β-endorphin, and oxytocin as a function of concentration. The error bars (<femtoamp level) are smaller than the data points.*

To evaluate the reproducibility of the opioid–neuropeptide biosensors, we tested six different devices for enkephalin and two devices for β-endorphin. The device-to-device variation in the response amplitude was ±15%, whereas the dissociation constants for both targets were consistent at ±10%. We also investigated the selectivity of the wsMOR-functionalized neuropeptide biosensors by testing against oxytocin as a negative control (**Figure 6.4.3**). The response of the biosensor to oxytocin was essentially negligible at concentrations below 1 μM, providing strong evidence that the sensor response reflects specific binding of the target and wsMOR.

Conclusions

We demonstrated the use of graphene microelectrodes functionalized with a soluble variant of the human MOR for neuropeptide detection with high sensitivity (picomolar level) and specificity in biofluids with physiological ionic strength. The kinetics and equilibrium binding properties of two neuropeptides, [D-Ala2, N-MePhe4, Gly-ol]-enkephalin and β-endorphin, were investigated and quantified. The results were in excellent agreement with benchmarks set by conventional radioligand and optical assays, as well as neuropeptide biosensors based on field-effect transistors that were measured in the dry state. The size of the active sensor region for this work was 50 μm × 50 μm, on the scale of larger neurons, but this could be reduced to the scale of the smallest neurons (~4 μm) using optical lithography. The measurement time was ~30 min, which enabled determination of the relevant fitting parameters with high precision. If a microelectrode sensor was precalibrated so the time constant for a given concentration was known, then it might be possible to determine the concentration more rapidly by simply fitting the first

few minutes of the time trace (**Figure 6.4.2**). These all-electronic biosensors are therefore potentially suitable for development for use in *in vitro* clinical testing or implantable systems for interrogating neuropeptide secretion with high spatial and time resolution.

Methods

Graphene Growth Please refer to Appendix A

Graphene Device Fabrication The graphene−copper growth substrate was coated with a 500 nm layer of poly(methyl methacrylate) (PMMA, MICROCHEM), and the PMMA−graphene film was floated off the surface by immersion in a 0.1 M NaOH solution with the graphene−copper growth substrate connected to the cathode of a power supply. The PMMA−graphene film was transferred onto a silicon wafer with an array of 5 nm/40 nm Cr/Au contact electrodes that was previously fabricated using photolithography. After removal of PMMA with acetone, the graphene film was cleaned by annealing at 250 °C in 1000 sccm argon and 400 sccm hydrogen for 1 h. For the FET-based devices, 2 μm × 10 μm graphene channels were defined by photolithography (photoresist S1813, MICROCHEM) and oxygen plasma etching. For the graphene microelectrodes, 50 μm × 50 μm graphene electrodes were defined by photolithography (photoresist AZ 5214 E, MICROCHEM) followed by oxygen plasma etching. A layer of photoresist SU-8 (MICROCHEM) was then applied to the device, and the passivation layer covering the electrodes was defined by photolithography.

Graphene Functionalization Graphene electrodes were incubated in 1 mM 1-pyrenebutyric acid N-hydroxysuccinimide ester solution in ethanol for 20 h and then

washed thoroughly with methanol and deionized water to fully remove residual solute and solvent. Next, the devices were incubated in 3 μg/mL wsMOR solution in PBS (137 mM sodium chloride, 2.7 mM potassium chloride, 10 mM phosphate, pH 7.4) for 1 h for protein immobilization. After wsMOR functionalization, the PBASE that had not bound to wsMOR was passivated by exposing the chips to PBS with pH 8.6 for 1 h, much longer than the half-life of PBASE at this pH (∼10 min) [165].

Charge Transfer Measurement Using Graphene Microelectrodes.

The noninverting input of the operational amplifier in an electrometer (Keithley 6517a) was grounded. The inverting input was connected to the graphene microelectrode, which connected the microelectrode to a virtual ground, so all charge transferred into the microelectrode was delivered to the feedback capacitor C_f in **Figure 6.4.1 a** to produce the measured voltage readout. To start the measurement, the microelectrode was exposed to a solution of wsMOR at known concentration in 1× PBS (137 mM sodium chloride, 2.7 mM potassium chloride, 10 mM phosphate, pH 7.4), and a time trace of the sensor response was taken immediately.

Supporting Information

The Supporting Information is available at DOI: 10.1021/acsnano.7b07474

Chapter 6 Conclusions

The unique properties of graphene make it suitable for detection of small molecules in both the dry and liquid states, and on rigid and flexible substrates. This chapter explores the ways that graphene can be used beyond nucleic acid and drug target sensing, which include protein biomarker detection and pH sensing for fluids ranging from phosphate buffer solution (PBS) to human serum. In addition, graphene may also be used for detecting the open-closed structure of a protein, in this case, ferritin, based on a Faradaic charge transfer due to enclosing a gold nanoparticle within and open- pore protein. Finally, this chapter shows that graphene may be used for quantifying opioid neuropeptide-receptor interactions, which could be useful for physiological sensing such as pain perception and appetite regulation.

From this chapter, it is evident that graphene is an excellent material for sensing individual molecules, and for studying the interactions between a probe and its target. Furthermore, this chapter demonstrates that graphene sensing can be carried out without the more traditional field-effect transistor sensing mechanisms, and instead, with the use of graphene microelectrodes (GE).

Chapter 6 Reference

1   www.cancer.org/cancer/breast-cancer/about/how-common-is-breast-cancer.html.

2   Koutras, A. K. & Evans, T. R. J. The epidermal growth factor receptor family in breast cancer. *OncoTargets Ther.* **1**, 5-19 (2008).

3   Kim, J. H. *et al.* Expression of HER-2 and nuclear localization of HER-3 protein in canine mammary tumors: histopathological and immunohistochemical study. *Vet J* **189**, 318-322 (2011).

4   Karamouzis, M. V., Badra, F. A. & Papavassiliou, A. G. Breast cancer: The upgraded role of HER-3 and HER-4. *Int. J. Biochem. Cell Biol.* **39**, 851-856 (2007).

5   te Velde, E. A. *et al.* HER-family gene amplification and expression in resected pancreatic cancer. *Eur J Surg Oncol* **35**, 1098-1104 (2009).

6   Doster, A. R., Yhee, J. Y., Kim, J. H., Im, K. S. & Sur, J. H. CDX-2 and HER-3 Expression in Canine Gastric and Colorectal Adenocarcinomas. *J. Comp. Pathol.* **145**, 12-19 (2011).

7   Ledel, F., Hallstrom, M., Ragnhammar, P., Ohrling, K. & Edler, D. HER3 expression in patients with primary colorectal cancer and corresponding lymph node metastases related to clinical outcome. *Eur J Cancer* **50**, 656-662 (2014).

8   Reschke, M. *et al.* HER3 is a determinant for poor prognosis in melanoma. *Clin Cancer Res* **14**, 5188-5197 (2008).

9   Quinn, C. M. *et al.* c-erbB-3 protein expression in human breast cancer: comparison with other tumour variables and survival. *Histopathology* **25**, 247-252 (1994).

10   Naidu, R., Yadav, M., Nair, S. & Kutty, M. K. Expression of c-erbB3 protein in primary breast carcinomas. *Br J Cancer* **78**, 1385-1390 (1998).

11   Lin, S.-H. *et al.* Soluble ErbB3 Levels in Bone Marrow and Plasma of Men with Prostate Cancer. *Clin. Cancer Res.* **14**, 3729-3736 (2008).

12   Kitano, H. Systems biology: a brief overview. *Science* **295**, 1662-1664 (2002).

13   Srinivas, P. R., Kramer, B. S. & Srivastava, S. Trends in biomarker research for cancer detection. *Lancet Oncol.* **2**, 698-704 (2001).

14   Brindle, K. New approaches for imaging tumour responses to treatment. *Nat. Rev. Cancer* **8**, 94 (2008).

15   Imaging and cancer: A review. *Mol. Oncol.* **2**, 115-152 (2008).

16   Mosmann, T. Rapid colorimetric assay for cellular growth and survival: application to proliferation and cytotoxicity assays. *J. Immunol. Methods* **65**, 55-63 (1983).

17   Zhang, J., Campbell, R. E., Ting, A. Y. & Tsien, R. Y. Creating new fluorescent probes for cell biology. *Nat. Rev. Mol. Cell Biol.* **3**, 906 (2002).

18   Lerner, M. B. *et al.* Toward quantifying the electrostatic transduction mechanism in carbon nanotube molecular sensors. *J Am Chem Soc* **134**, 14318-14321 (2012).

19   Tang, X. *et al.* Carbon Nanotube DNA Sensor and Sensing Mechanism. *Nano Letters* **6**, 1632-1636 (2006).

20   Cella, L. N., Chen, W., Myung, N. V. & Mulchandani, A. Single-Walled Carbon Nanotube-Based Chemiresistive Affinity Biosensors for Small Molecules: Ultrasensitive Glucose Detection. *J. Am. Chem. Soc.* **132**, 5024-5026 (2010).

21   Ko, J. W. *et al.* Multi-Order Dynamic Range DNA Sensor Using a Gold Decorated SWCNT Random Network. *ACS Nano* **5**, 4365-4372 (2011).

22   Wei, G., Xu, F., Li, Z. & Jandt, K. D. Protein-Promoted Synthesis of Pt Nanoparticles on Carbon Nanotubes for Electrocatalytic Nanohybrids with Enhanced Glucose Sensing. *J. Phys. Chem. C* **115**, 11453-11460 (2011).

23   Lerner, M. B. *et al.* Hybrids of a Genetically Engineered Antibody and a Carbon Nanotube Transistor for Detection of Prostate Cancer Biomarkers. *ACS Nano* **6**, 5143-5149 (2012).

24   Lerner, M. B., Dailey, J., Goldsmith, B. R., Brisson, D. & Johnson, A. T. Detecting Lyme disease using antibody-functionalized single-walled carbon nanotube transistors. *Biosens Bioelectron* **45**, 163-167 (2013).

25   Mohanty, N. & Berry, V. Graphene-Based Single-Bacterium Resolution Biodevice and DNA Transistor: Interfacing Graphene Derivatives with Nanoscale and Microscale Biocomponents. *Nano Letters* **8**, 4469-4476 (2008).

26   Lu, J., Do, I., Drzal, L. T., Worden, R. M. & Lee, I. Nanometal-Decorated Exfoliated Graphite Nanoplatelet Based Glucose Biosensors with High Sensitivity and Fast Response. *ACS Nano* **2**, 1825-1832 (2008).

27   Ohno, Y., Maehashi, K. & Matsumoto, K. Label-Free Biosensors Based on Aptamer-Modified Graphene Field-Effect Transistors. *J. Am. Chem. Soc.* **132**, 18012-18013 (2010).

28   Mao, S., Yu, K., Lu, G. & Chen, J. Highly sensitive protein sensor based on thermally-reduced graphene oxide field-effect transistor. *Nano Res.* **4**, 921 (2011).

29   Lerner, M. B. *et al.* Scalable Production of Highly Sensitive Nanosensors Based on Graphene Functionalized with a Designed G Protein-Coupled Receptor. *Nano Letters* **14**, 2709-2714 (2014).

30   Park, K. H. *et al.* Exfoliation of Non-Oxidized Graphene Flakes for Scalable Conductive Film. *Nano Letters* **12**, 2871-2876 (2012).

31   Shin, D.-W. *et al.* A Facile Route To Recover Intrinsic Graphene over Large Scale. *ACS Nano* **6**, 7781-7788 (2012).

32   Reina, A. *et al.* Large Area, Few-Layer Graphene Films on Arbitrary Substrates by Chemical Vapor Deposition. *Nano Letters* **9**, 30-35 (2009).

33   Chang-Hsiao, C. *et al.* Electrical Probing of Submicroliter Liquid Using Graphene Strip Transistors Built on a Nanopipette. *Small* **8**, 43-46 (2012).

34   Chen, R. J. *et al.* Noncovalent functionalization of carbon nanotubes for highly specific electronic biosensors. *Proc. Natl. Acad. Sci.* **100**, 4984-4989 (2003).

35   Yin, P. T., Kim, T.-H., Choi, J.-W. & Lee, K.-B. Prospects for graphene-nanoparticle-based hybrid sensors. *Phys. Chem. Chem. Phys.* **15**, 12785-12799 (2013).

36   Claussen, J.C. *et al.* Nanostructuring Platinum Nanoparticles on Multilayered Graphene Petal Nanosheets for Electrochemical Biosensing. *Adv. Funct. Mater.* **22**, 3399-3405 (2012).

37   San, B. H. *et al.* Combining Protein-Shelled Platinum Nanoparticles with Graphene to Build a Bionanohybrid Capacitor. *ACS Nano* **8**, 12120-12129 (2014).

38   Yin, Z. *et al.* Real-time DNA detection using Pt nanoparticle-decorated reduced graphene oxide field-effect transistors. *Nanoscale* **4**, 293-297 (2012).

39   Vikash, S., Nitin, K. P., Ashok, M. & Rajesh. Platinum nanoparticles-single-walled carbon nanotubes hybrid based chemiresistive sensor array for myoglobin detection. *Mater. Res. Express* **3**, 035006 (2016).

40   Choi, Y. *et al.* Dissecting Single-Molecule Signal Transduction in Carbon Nanotube Circuits with Protein Engineering. *Nano Letters* **13**, 625-631 (2013).

41   Wang, Y. y. *et al.* Raman Studies of Monolayer Graphene: The Substrate Effect. *J. Phys. Chem. C* **112**, 10637-10640 (2008).

42   Tao, L. *et al.* Synthesis of High Quality Monolayer Graphene at Reduced Temperature on Hydrogen-Enriched Evaporated Copper (111) Films. *ACS Nano* **6**, 2319-2325 (2012).

43   Wenbo, L. *et al.* Self-assembly Synthesis of High-density Platinum Nanoparticles on Chemically Reduced Graphene Sheets. *Chemistry Letters* **40**, 104-105 (2011).

44   D'Souza, J. W. *et al.* Combining anti-ERBB3 antibodies specific for domain I and domain III enhances the anti-tumor activity over the individual monoclonal antibodies. *PLoS One* **9** (2014).

45   Ma, F. *et al.* Adsorption of cysteine molecule on intrinsic and Pt-doped graphene: A first-principle study. *J. Mol. Struct.: THEOCHEM* **955**, 134-139 (2010).

46   Cui, X., Freitag, M., Martel, R., Brus, L. & Avouris, P. Controlling Energy-Level Alignments at Carbon Nanotube/Au Contacts. *Nano Letters* **3**, 783-787 (2003).

47   Rajesh, Das, B. K., Srinives, S. & Mulchandani, A. ZnS nanocrystals decorated single-walled carbon nanotube based chemiresistive label-free DNA sensor. *Appl. Phys. Lett.* **98**, 013701 (2011).

48   Mao, S., Lu, G., Yu, K., Bo, Z. & Chen, J. Specific protein detection using thermally reduced graphene oxide sheet decorated with gold nanoparticle-antibody conjugates. *Adv. Mater.* **22**, 3521-3526 (2010).

49   Hill, A. The Possible Effects of The Aggregation of The Molecules of Haemoglobin on its Dissociation Curves. *J. Physiol.*, 4 (1910).

50   Sonuc, M. N. & Sezginturk, M. K. Ultrasensitive electrochemical detection of cancer associated biomarker HER3 based on anti-HER3 biosensor. *Talanta* **120**, 355-361 (2014).

51   Canbaz, M. Ç., Şimşek, Ç. S. & Sezgintürk, M. K. Electrochemical biosensor based on self-assembled monolayers modified with gold nanoparticles for detection of HER-3. *Anal. Chim. Acta* **814**, 31-38 (2014).

52   Gao, L. *et al.* Repeated growth and bubbling transfer of graphene with millimetre-size single-crystal grains using platinum. *Nature Communications* **3**, 699 (2012).

53   Horak, E. *et al.* Isolation of scFvs to In Vitro Produced Extracellular Domains of EGFR Family Members. *Cancer Biother. Radiopharm.* **20**, 603-613 (2005).

54   Korostynska, O., Arshak, K., Gill, E. & Arshak, A. Review paper: materials and techniques for in vivo pH monitoring. *IEEE Sensors J.* **8**, 20-28 (2008).

55   Bizzarri, R. *et al.* Development of a novel GFP-based ratiometric excitation and emission pH indicator for intracellurlar studies. *Biophys J.* **90**, 3300-3314 (2006).

56   Vinnakota, K., Kemp, M. L. & Kushmerick, M. J. Dynamics of muscle glycogenolysis modeled with pH time course computation and pH-dependent reaction equilibria and enzyme kinetics. *Biophys J.* **91**, 1264-1287 (2006).

57   Tannock, I. F. & Rotin, D. Acid pH in tumors and its potential for therapeutic exploitation. *Cancer Res.* **49**, 4373-4384 (1989).

58   Tung, C.-H., Qi, J., Hu, L., Han, M. S. & Kim, Y. A quick respnsive fluorogenic pH probe for ovarian tumor imaging. *Theranostics* **5**, 1166-1174 (2015).

59   Anderson, M., Moshinikova, A., Engelman, D. M., Reshetnyak, Y. K. & Andreev, O. A. Probe for the measurement of cell surface pH in vivo and ex vivo. *Proc. Natl. Acad. Sci. U. S. A.* **113**, 8177-8181 (2016).

60   Ma, X. *et al.* Ultra-pH-sensitive nanoprobe library with broad pH tunability and fluorescence emissions. *J. Am. Chem. Soc.* **136**, 11085-11092 (2014).

61   Zhang, X., Liu, Y. & Gillies, R. J. Tumor pH and Its Measurement. *J. Nucl. Med.* **51**, 1167-1170 (2010).

62   Chung, C. *et al.* Biomedical applications of graphene and graphene oxide. *Acc. Chem. Res.* **46**, 2211-2224 (2013).

63   Sohn, I. Y. *et al.* pH sensing characteristics and biosensing application of solution-gated reduced graphene oxide field-effect transistors. *Biosens. Bioelectron.* **45**, 70-76 (2013).

64   Mailly-Giacchetti, B. *et al.* pH sensing properties of graphene solution-gated field-effect transistors. *J. Appl. Phys.* **114**, 084505 (2013).

65   Ang, P. K., Chen, W., Wee, A. T. & Loh, K. P. Solution-gated epitaxial graphene as pH sensor. *J Am Chem Soc* **130**, 14392-14393 (2008).

66   Lee, M. H. *et al.* Apparent pH sensitivity of solution-gated graphene transistors. *Nanoscale* **7**, 7540-7544 (2015).

67   Fu, W. *et al.* Graphene Transistors Are Insensitive to pH Changes in Solution. *Nano Letters* **11**, 3597-3600 (2011).

68   Cheng, Z., Li, Q., Li, Z., Zhou, Q. & Fang, Y. Suspended Graphene Sensors with Improved Signal and Reduced Noise. *Nano Letters* **10**, 1864-1868 (2010).

69   Jürgen, R. *et al.* Characteristics of solution gated field effect transistors on the basis of epitaxial graphene on silicon carbide. *J. Phys. D: Appl. Phys.* **43**, 345303 (2010).

70   Heller, I. *et al.* Influence of electrolyte composition on liquid-gated carbon nanotube and graphene transistors. *Journal of the American Chemical Society* **132**, 17149-17156 (2010).

71   Estrella, V. *et al.* Acidity generated by the tumor microenvironment drives local invasion. *Cancer Res.* **73**, 1524-1538 (2012).

72   Webb, B. A., Chimenti, M., Jacobson, M. P. & Barber, D. L. Dysregulated pH: a perfect storm for cancer progression. *Nature Reviews* **11**, 671-677 (2011).

73   Madelin, G., Kline, R., Walvick, R. & Regatte, R. R. A method for estimating intracellular sodium concentration and extracellular volume fraction in brain in vivo using sodium magnetic resonane imaging. *Scientific Reports* **4**, 1-7 (2014).

74   Ping, J. & Johnson, A. T. C. Quantifying the intrinsic surface charge density and charge-transfer resistance of graphene-solution interface through bias-free low-level charge measurement. *Applied Physics Letters* **109**, 013103 (2016).

75   Ohno, Y., Maehashi, K., Yamashiro, Y. & Matsumoto, K. Electrolyte-Gated Graphene Field-Effect Transistors for Detecting pH and Protein Adsorption. *Nano Letters* **9**, 3318-3322 (2009).

76   Li, X. *et al.* Large-Area Synthesis of High-Quality and Uniform Graphene Films on Copper Foils. *Science* **324**, 1312-1314 (2009).

77   Kuzum, D. *et al.* Transpartent and flexible low noise graphene electrodes for simultaneous electrophysiology and neuroimaging. *Nature Communications* **5**, 1-10 (2014).

78   Ping, J., Xi, J., Saven, J. G., Liu, R. & Johnson, A. T. C. Quantifying the effect of ionic screening on protein-decorated graphene transistors. *Biosensors and Bioelectronics*, (2017).

79   Israelachvili, J. *Intermolecular and surface forces: Revised third edition.* (Acadmeic Press, 2011).

80   Zuccaro, L., Krieg, J., Desideri, A., Kern, K. & Balasubramanian, K. Tuning the isoelectric point of graphene by electrochemical functionalization. *Sci Rep* **5** (2015).

81   Back, J. H. & Shim, M. pH-Dependent Electron-Transport Properties of Carbon Nanotubes. *J. of Phys. Chem. B.* **110**, 23736-23741 (2006).

82   Yoon, J.-C., Thiyagarajan, P., Ahn, H.-J. & Jang, J.-H. A case study: effect of defects in CVD-grown graphene on graphene enhanced Raman spectroscopy. *RSC Adv.* **5**, 62772-62777 (2015).

83   Crichton, R. R. & Bryce, C. F. A. Subunit interactions in horse spleen apoferritin. Dissociation by extremes of pH. *Biochem. J.* **133**, 289-299 (1973).

84   Kim, M. *et al.* pH-Dependent Structures of Ferritin and Apoferritin in Solution: Disassembly and Reassembly. *Biomacromolecules* **12**, 1629-1640 (2011).

85   Delasi, R.. Aqueous degradation of polyimides. *J. Appl. Polym. Sci.* **15**, 2965-2974 (1971).

86   Krebs, H. A. Chemical Composition of Blood Plasma and Serum. *Biochemistry* **19**, 409-430 (1950).

87   Wang, C.H. et. al, Adsorption and Direct Electron Transfer from Hemoglobin into a Three-Dimensionally Ordered Macroporous Gold Film. *Avd. Funct. Mater.* **15**, 1267-1275 (2005).

88   Kim, B. S., Hayes, R. A. & Ralston, J. The adsorption of anionic naphthalene derivatives at the graphite-aqueous solution interface. *Carbon* **33**, 25-34 (1995).

89   Chong, W. H., Molinolo, A. A., Chen, C. C. & Collins, M. T. Tumor-induced osteomalacia. *Endocrine-related Cancer* **18**, R53-R77 (2011).

90   Humphrey, W., Dalke, A. & Schulten, K. VMD–Visual Molecular Dynamics. *Journal of Molecular Graphics* **14**, 33-38 (1996).

91   Best, R. B. *et al.* Optimization of the additive CHARMM all-atom protein force field targeting improved sampling of the backbone phi, psi and side-chain chi1 and chi2 dihedral angles. *J. Chem. Theory Comput.* **8**, 3257-3273 (2012).

92   MacKerellJr., A. D., Feig, M. & Brooks, C. L. Improved treatment of the protein backbone in empirical force fields. *J. Am. Chem. Soc.* **126**, 698-699 (2004).

93   MacKerell, J., A. D. *et al.* All-atom emprirical potential for molecular modeling and dynamics studies of proteins. *J. Phys. Chem. B* **102**, 3586-3616 (1998).

94   Phillips, J. C. *et al.* Scalable molecular dynamics with NAMD. *Journal of Computational Chemsitry* **26**, 1781-1802 (2005).

95   Brooks, B. R. *et al.* CHARMM: A program for macromolecular energy, minimization, and dynamics calculations. *Journal of Computational Chemsitry* **4**, 187-217 (1983).

96   Jorgensen, W. L., Chandrasekhar, J., Madura, J. D., Impey, R. W. & Klein, M. L. Comparison of simple potential functions for simulating liuqid water. *J. Chem. Phys.* **79**, 926-935 (1983).

97   Neria, E., Fischer, S. & Karplus, M. Simulation of activation free energies in molecular systems. *J. Chem. Phys.* **105**, 1902-1921 (1996).

98   Ryckaert, J. P., Ciccotti, G. & Berendsen, H. J. C. Numerical integration of the cartesian equations of motion of a system with constraints: molecular dynamics of n-alkanes. *J. Comput. Phys.* **23**, 317-341 (1977).

99   Martyna, G. J., Tobia, D. J. & Klein, M. L. Constant pressure molecular dynamics algorithms. *J. Chem. Phys.* **101**, 4177-4189 (1994).

100   Feller, S. E., Zhang, Y., Pastor, R. W. & Brooks, B. R. Constant pressure molecular dynamics simulation: the langevin piston method. *J. Chem. Phys.* **103**, 4613-4621 (1995).

101   Gurtovenko, A. A. & Vattulainen, I. Calculation of the electrostatic potential of lipid bilayers from molecular dynamics simulations: methodological issues. *J. Chem. Phys.* **130**, 215107 (2009).

102   Tieleman, D. P. & Berendsen, H. J. C. Molecular dynamics simulations of a fully hydrated dipalmitoylphosphatidylcholine bilayer with different macroscopic boundary conditions and paramters. *J. Chem. Phys.* **105**, 4871-4880 (1996).

103   Fantechi, E. *et al.* A Smart Platform for Hyperthermia Application in Cancer Treatment: Cobalt-Doped Ferrite Nanoparticles Mineralized in Human Ferritin Cage. *ACS Nano* **8**, 4705-4719 (2014).

104   Kumar, S., Aaron, J. & Sokolov, K. Directional conjugation of antibodies to nanoparticles for synthesis of multiplexed optical contrast agents with both delivery and targeting moieties. *Nature Protocols* **3**, 314-320 (2008).

105   Medintz, I. L., Uyeda, H. T., Goldman, E. R. & Mattoussi, H. Quantum dot bioconjugates for imaging, labelling and sensing. *Nature Materials* **4**, 435-446 (2005).

106   Rana, S. *et al.* A multichannel nanosensor for instantaneous readout of cancer drug mechanisms. *Nature Nanotechnology* **10**, 65-69 (2015).

107   Suzuki, Y. *et al.* Self-assembly of coherently dynamic, auxetic, two-dimensional protein crystals. *Nature* **533**, 369-373 (2016).

108   Nel, A. E. *et al.* Understanding biophysicochemical interactions at the nano-bio interface. *Nature Materials* **8**, 543-556 (2009).

109   Lundqvist, M. *et al.* Nanoparticle size and surface properties determine the protein corona with possible implications for biological impacts. *Proceedings of the*

National Academy of Sciences of the United States of America **105**, 14265-14270 (2008).

110   Maity, B., Abe, S. & Ueno, T. Observation of gold sub-nanocluster nucleation within a crystalline protein cage. *Nature Communications* **8**, 14820 (2017).

111   Theil, E. C., Tosha, T. & Behera, R. K. Solving biology's iron chemistry problem with ferritin protein nanocages. *Accounts of chemical research* **49**, 784-791 (2016).

112   Uchida, M., Kang, S., Reichhardt, C., Harlen, K. & Douglas, T. The ferritin superfamily: supramolecular tmeplates for materials synthesis. *Biochimica et Biophysica Acta* **1800**, 834-845 (2010).

113   Cheung-Lau, J. C., Liu, D., Pulsipher, K. W., Liu, W. & Dmochowski, I. J. Engineering a well-ordered, functional protein-gold nanoparticle assembly. *J. Inorg. Biochem.* **130**, 59-68 (2014).

114   Swift, J., Butts, C. A., Cheung-Lau, J., Yerubandi, V. & Dmochowski, I. J. Efficient self-assembly of Archaeoglobus fulgidus ferritin around metallic cores. *Langmuir* **25**, 5219-5225, (2009).

115   Pulsipher, K. W. & Dmochowski, I. J. in *Methods in Molecular Biology* Vol. 1252 (ed B. P. Orner) 27-37 (Springer New York, 2015).

116   Johnson, E., Cascio, D., Sawaya, M. R., Gingery, M. & Schroder, I. Crystal structures of a tetrahedral open pore ferritin from the hyperthermophilic archaeon Archaeoglobus fulgidus. *Structure* **13**, 637-648, (2005).

117   Qi, Z. J. *et al.* Correlating atomic structure and transport in suspended graphene nanoribbons. *Nano Lett.* **14**, 4238-4244 (2014).

118   Luo, Y., Ergenekan, C. E., Fischer, J. T., Tan, M.-L. & Ichiye, T. The Molecular Determinants of the Increased Reduction Potential of the Rubredoxin Domain of Rubrerythrin Relative to Rubredoxin. *Biophys. J.* **98**, 560-568 (2010).

119   Sana, B. *et al.* The role of nonconserved residues of Archaeoglobus fulgidus ferritin on its unique structure and biophysical properties. *J. Biol. Chem.* **288**, 32663-32672, (2013).

120   Park, J., Choi, S., Kim, T.-I. & Kim, Y. Highly selective fluorescence turn-on sensing of gold ions by a nanoparticle generation/C-I bond cleavage sequence. *Analyst* **137**, 4411-4414 (2012).

121   Esumi, K., Miyamoto, K. & Yoshimura, T. Comparison of PAMAM-Au and PPI-Au nanocomposites and their catalytic activity for reduction of 4-nitrophenol. *J. Colloid Interface Sci.* **254**, 402-405 (2002).

122   Corma, A. *et al.* Gold catalyzes the Sonogashira coupling reaction without the requirement of palladium impurities. *Chem Commun (Camb)* **47**, 1446-1448, (2011).

123   Gu, S. *et al.* Kinetic Analysis of the Catalytic Reduction of 4-Nitrophenol by Metallic Nanoparticles. *The Journal of Physical Chemistry C* **118**, 18618-18625, (2014).

124   Wunder, S., Lu, Y., Albrecht, M. & Ballauff, M. Catalytic Activity of Faceted Gold Nanoparticles Studied by a Model Reaction: Evidence for Substrate-Induced Surface Restructuring. *ACS Catalysis* **1**, 908-916 (2011).

125   Kuroda, K., Ishida, T. & Haruta, M. Reduction of 4-nitrophenol to 4-aminophenol over Au nanoparticles deposited on PMMA. *Journal of Molecular Catalysis A: Chemical* **298**, 7-11, (2009).

126   Wunder, S., Polzer, F., Lu, Y., Mei, Y. & Ballauff, M. Kinetic analysis of catalytic reduction of 4-nitrophenol by metallic nanoparticles immobilized in spherical polyelectrolyte brushes. *Journal of Physical Chemistry C* **114**, 8814-8820 (2010).

127   Kono, H. & Saven, J. G. Statistical theory for protein combinatorial libraries. Packing interactions, backbone flexibility, and the sequence variability of a main-chain structure. *J. Mol. Biol.* **306**, 607-628 (2001).

128   Calhoun, J. R. *et al.* Computational design and characterization of a monomeric helical dinuclear metalloprotein. *J. Mol. Biol.* **334**, 1101-1115 (2003).

129   Bender, G. M. *et al.* De novo design of a single-chain diphenylporphyrin metalloprotein. *J. Am. Chem. Soc.* **129**, 10732-10740 (2007).

130   Butts, C. A. *et al.* Directing noble metal ion chemistry within a designed ferritin protein. *Biochemistry* **47**, 12729-12739, (2008).

131   Dunbrack, R. L., Jr. Rotamer libraries in the 21st century. *Curr. Opin. Struct. Biol.* **12**, 431-440 (2002).

132   Marchetti, A. *et al.* Ferritin is used for iron storage in bloom-forming marine pennate diatoms. *Nature* **457**, 467-470 (2009).

133   Zuber, A. *et al.* Detection of gold nanoparticles with different sizes using absorption and fluorescence based method. *Sens. Actuators, B* **227**, 117-127, (2016).

134   Akil, H. *et al.* Endogenous opioids: biology and function. *Annu Rev Neurosci* **7**, 223-255 (1984).

135   Kennedy, S. E., Koeppe, R. A., Young, E. A. & Zubieta, J. K. Dysregulation of endogenous opioid emotion regulation circuitry in major depression in women. *Arch Gen Psychiatry* **63** (2006).

136   Prossin, A. R., Love, T. M., Koeppe, R. A., Zubieta, J. K. & Silk, K. R. Dysregulation of regional endogenous opioid function in borderline personality disorder. *Am J Psychiatry* **167**, 925-933 (2010).

137   Gulya, K. The opioid system in neurologic and psychiatric disorders and in their experimental models. *Pharmacol. Ther.* **46**, 395-428 (1990).

138   Deval, E. *et al.* Acid-sensing ion channels (ASICs): pharmacology and implication in pain. *Pharmacol Ther* **128**, 549-558 (2010).

139   Sprouse-Blum, A. S., Smith, G., Sugai, D. & Parsa, F. D. Understanding endorphins and their importance in pain management. *Hawaii Med J* **69**, 70-71 (2010).

140   Bonnet, A.-M. Involvement of Non-Dopaminergic Pathways in Parkinson's Disease. *CNS Drugs* **13**, 351-364 (2000).

141   Schmidt, A. C., Dunaway, L. E., Roberts, J. G., McCarty, G. S. & Sombers, L. A. Multiple Scan Rate Voltammetry for Selective Quantification of Real-Time Enkephalin Dynamics. *Anal. Chem.* **86**, 7806-7812 (2014).

142   Clement-Jones, V. *et al.* Increased beta-endorphin but not met-enkephalin levels in human cerebrospinal fluid after acupuncture for recurrent pain. *Lancet* **2**, 946-949 (1980).

143   Bruehl, S., Chung, O. Y., Burns, J. W. & Diedrich, L. Trait anger expressiveness and pain-induced beta-endorphin release: support for the opioid dysfunction hypothesis. *Pain* **130**, 208-215 (2007).

144   DiFeliceantonio, A. G., Mabrouk, O. S., Kennedy, R. T. & C. Berridge, K. Enkephalin surges in dorsal neostriatum as a signal to eat. *Current biology : CB* **22**, 1918-1924 (2012).

145   Duan, X. *et al.* Quantification of the affinities and kinetics of protein interactions using silicon nanowire biosensors. *Nat. Nanotech.* **7**, 401-407 (2012).

146   Ping, J. *et al.* pH Sensing Properties of Flexible, Bias-Free Graphene Microelectrodes in Complex Fluids: From Phosphate Buffer Solution to Human Serum. *Small* **13**, 14 (2017).

147   Ping, J. *et al.* Structural-functional analysis of engineered protein-nanoparticle assemblies using graphene microelectrodes. *Chem Sci* **8**, 5329-5334 (2017).

148   Perez-Aguilar, J. M. *et al.* A Computationally Designed Water-Soluble Variant of a G-Protein-Coupled Receptor: The Human Mu Opioid Receptor. *PLoS One* **8** (2013).

149   Zhao, X. *et al.* Characterization of a computationally designed water-soluble human mu-opioid receptor variant using available structural information. *Anesthesiology* **121**, 866-875 (2014).

150   Bogomolova, A. *et al.* Challenges of Electrochemical Impedance Spectroscopy in Protein Biosensing. *Anal. Chem.* **81**, 3944-3949 (2009).

151   Bard, A. J. F., L. R. *Electrochemical Methods: Fundamentals and Applications*. (Wiley, 2000).

152   Katz, E. Application of bifunctional reagents for immobilization of proteins on a carbon electrode surface: Oriented immobilization of photosynthetic reaction centers. *J. Electroanal. Chem.* **365**, 157-164 (1994).

153   Chen, R. J., Zhang, Y., Wang, D. & Dai, H. Noncovalent Sidewall Functionalization of Single-Walled Carbon Nanotubes for Protein Immobilization. *J. Am. Chem. Soc.* **123**, 3838-3839 (2001).

154   Liu, Y. *et al.* Giant enhancement in vertical conductivity of stacked CVD graphene sheets by self-assembled molecular layers. *Nat Commun* **5** (2014).

155   Ping, J., Vishnubhotla, R., Vrudhula, A. & Johnson, A. T. C. Scalable Production of High-Sensitivity, Label-Free DNA Biosensors Based on Back-Gated Graphene Field Effect Transistors. *ACS Nano* **10**, 8700-8704, (2016).

156   Weiss, J. N. The Hill equation revisited: uses and misuses. *FASEB Journal* **11**, 835-841 (1997).

157   Zhao, G.-M., Qian, X., Schiller, P. W. & Szeto, H. H. Comparison of [Dmt1] DALDA and DAMGO in Binding and G Protein Activation at μ, δ, and κ Opioid Receptors. *J. Pharmacol. Exper. Therap.* **307**, 947-954 (2003).

158   Schiller, P. W. *et al.* Synthesis and in vitro opioid activity profiles of DALDA analogues. *Eur J Med Chem* **35**, 895-901 (2000).

159   DeWire, S. M. *et al.* A G protein-biased ligand at the mu-opioid receptor is potently analgesic with reduced gastrointestinal and respiratory dysfunction compared with morphine. *J Pharmacol Exp Ther* **344**, 708-717 (2013).

160   Gimpl, G., Reitz, J., Brauer, S. & Trossen, C. Oxytocin receptors: ligand binding, signalling and cholesterol dependence. *Prog Brain Res* **170**, 193-204 (2008).

161   Limbird, L. E. *Cell Surface Receptors: A Short Course on Theory and Methods*. (Springer, 2005).

162   Zajac, J. M. & Roques, B. P. Differences in binding properties of mu and delta opioid receptor subtypes from rat brain: kinetic analysis and effects of ions and nucleotides. *J Neurochem* **44**, 1605-1614 (1985).

163   Yabaluri, N. & Medzihradsky, F. Reversible modulation of opioid receptor binding in intact neural cells by endogenous guanosine triphosphate. *Mol Pharmacol* **48**, 690-695 (1995).

164   Howard, A. D., de La Baume, S., Gioannini, T. L., Hiller, J. M. & Simon, E. J. Covalent labeling of opioid receptors with radioiodinated human beta-endorphin. Identification of binding site subunit. *J. Biol. Chem.* **260**, 10833-10839 (1985).

165   Lahiri, J., Isaacs, L., Tien, J. & Whitesides, G. M. A Strategy for the Generation of Surfaces Presenting Ligands for Studies of Binding Based on an Active Ester as a Common Reactive Intermediate: A Surface Plasmon Resonance Study. *Anal. Chem.* **71**, 777-790 (1999).

Chapter 7: Thesis Conclusions and Future Work

Graphene is a relatively new material, having been discovered in 2004 through mechanical exfoliation, and winning its discoverers the Nobel Prize in physics in 2010. Since then, it has been widely studied, intriguing scientists with its remarkable properties, including its high electron mobility, robustness, and sensitivity. Over the last decade, scientists have found many ways to incorporate graphene into applications and engineerable devices.

At the beginning of this work, we discussed the growth of graphene *via* CVD on a copper foil substrate, which, arguably, is the most critical step in the process, as without good quality graphene, multiple problems can arise, such as: 1) difficulty transferring the graphene, causing tears and wrinkles in the film, 2) discontinuous films, causing "peel off" of the graphene during lithography, resulting in low device yield, 3) poor quality devices not suitable for low-concentration detection. Because Raman spectroscopy, atomic force microscopy and optical microscopy have all separately characterized different aspects of the graphene and verified its high quality, the graphene described here was suitable for a myriad of sensing projects.

The low-contamination transfer process of graphene was carried out *via* an electrolysis bubble method, leading to minimal tearing as well as a clean graphene film. The fabrication of these graphene field-effect transistors was explained, which produced dozens of devices in one array (52 per chip, and up to > 500 in one round of lithography) with a yield greater than 90%.

Using these graphene sensor arrays, this thesis focused on the detection of synthetic small biomolecules and market drugs for eventual drug diagnostics and therapeutic drug monitoring (TDM).

From Chapter 5, we conclude that graphene functionalized with single strand DNA is adept at detecting target ssDNA down to concentrations of ~ 1 aM, which is a promising limit of detection, as certain nucleic acid strands are proven biomarkers for various cancers[1-3], and up-regulate or down-regulate in human samples in the attomolar range[4]. Additionally, these GFETs can be used to sense a long target with a short probe. Graphene devices functionalized with aptamers can detect therapeutic drugs in concentrations much lower than what is found in the human body, ~ 1-10 ng/mL, indicating that this technique is viable for point-of-care diagnostics.

Chapter 6 highlights further uses of graphene beyond nucleic acid detection and therapeutic drug monitoring. This chapter presents experiments for the detection of protein biomarkers and pH sensing of complex fluids through flexible devices. It also establishes a method for detecting micro-assemblies, in this case, protein-nanoparticle assemblies through charge transfer, and, finally, shows that it can be used for measuring the binding properties of neuropeptides and their receptors, further demonstrating the versatility of this nanomaterial as a sensing medium.

With the technology to detect biomolecules in small concentrations at the point-of-care, the medical community could finally have a standard, early-disease diagnostic method, and could diagnose ailments for which there are currently no standard forms of early detection, such as ovarian cancer[5], colon cancer[6], or pancreatic cancer[7]. Additionally,

doctors would be able to determine drug compliance of medications used to treat dangerous diseases like HIV, or monitor the pH of a patient's body fluids.

Early disease detection, through a rapid and inexpensive methodology, would serve the purpose of prolonging life spans. Furthermore, rapid therapeutic drug monitoring would replace the need for expensive lab techniques which are time-inefficient, and simultaneously, through the monitoring of drug compliance for dangerous diseases like HIV, can also prolong a patient's lifespan by decades.

Apart from saving lives, there is a less evident benefit to biosensors, and that is a lower cost of medical treatments for ailments such as cancer, which can cost the average patient tens of thousands of dollars, and sometimes, hundreds of thousands, depending on insurance policies or additional treatment for relapse. Therapeutic drug monitoring for HIV can help prevent the development of AIDS, and the treatment of illnesses due to AIDS. By reducing the cost of these medical treatments through diagnosing and treating cancer in its early stages, or by preventing the development of a more dangerous disease through TDM, the average medical costs per patient could be drastically lowered, and could impact the entire American health care system.

Because graphene is biocompatible, it serves as an appropriate medium for diagnostics with human samples. Future work in the area of sensing with graphene could extend towards biomarker detection in low concentrations in blood plasma, therapeutic drugs in urine, VOCs through breath/plasma samples, or glucose in sweat. However, many challenges exist for testing in human samples that do no present themselves in synthetic samples, such as high background signals from urea or daily diet in urine samples, signals from proteins, hormones, and electrolytes in blood plasma, and salt in sweat samples.

Consequently, the first step in this type of experiment would be to measure the background signal of the sample's solution compared to the signal of deionized water. This step would determine if the background signal of the sample creates a significant background noise. The noisier the background signal, the more difficult low-concentration detection will be.

Next, one would need to procure samples from patients with various degrees of the ailment when detecting biomarkers, for example, early stage, late stage, and healthy, to record a signal difference between these groups and use this information to learn more about the progression of the disease in the body. For therapeutic drug monitoring, one would need to obtain urine samples from patients taking a certain medication versus those taking a similar medication, or no medication at all, for comparison.

For this type of technology to come to fruition and be a viable clinical option, it needs to be mass-produced and marketed properly. This means that high-quality graphene needs to be grown in industry in very large areas, and the whole sensing system needs to be easily operable (hand-held), affordable, and of course, accurate. There are still many steps to be taken before this method can be considered a standard detection method for real-life situations, although there is documentation of these types of devices being manufactured and used for disease diagnostics[8].

These biosensing techniques could also extend towards other types of chemical sensing apart from market drugs, for example, explosive detection by the military, or more effective sensors for gas leaks in labs or homes. Each of the biomolecular or chemical sensors described herein could be applicable for low-concentration detection, for which

there are either no existing technologies, or for which existing technologies are unaffordable and difficult to operate.

Biosensing and chemical sensing with nanomaterials represents a relatively new and promising field of interdisciplinary science and engineering that might someday replace certain forms of current medical technology. As of now, graphene is the only material known to exceed the electron mobility of any other at room temperature, with high sensitivity and mechanical strength, making it ideal for sensitive detection.

This thesis demonstrates the versatility and promise of a sensing material that was discovered less than 20 years ago. Provided that all the appropriate challenges are addressed and overcome, such graphene sensors could one day be used for applications in a variety of sectors, most notably, the healthcare sector.

Chapter 7 References

1   Schwarzenbach, H., Hoon, D. S. B. & Pantel, K. Cell-free nucleic acids as biomarkers in cancer patients. *Nature Reviews Cancer* **11**, 426 (2011).

2   Wang, J. *et al.* MicroRNAs in Plasma of Pancreatic Ductal Adenocarcinoma Patients as Novel Blood-Based Biomarkers of Disease. *Cancer Prevention Research* **2**, 807-813 (2009).

3   Jakupciak, J. P. *et al.* Mitochondrial DNA as a Cancer Biomarker. *The Journal of Molecular Diagnostics* **7**, 258-267 (2005).

4   Cardoso, A. R., Moreira, F. T. C., Fernandes, R. & Sales, M. G. F. Novel and simple electrochemical biosensor monitoring attomolar levels of miRNA-155 in breast cancer. *Biosens Bioelectron* **80**, 621-630 (2016).

5   Rauh-Hain, J. A., Krivak, T. C., del Carmen, M. G. & Olawaiye, A. B. Ovarian Cancer Screening and Early Detection in the General Population. *Reviews in Obstetrics and Gynecology* **4**, 15-21 (2011).

6   Lionis, C. & Petelos, E. Early detection of colorectal cancer: barriers to screening in the primary care setting. *Family Practice* **28**, 589-591 (2011).

7   Reynolds, R. B. & Folloder, J. Clinical Management of Pancreatic Cancer. *Journal of the Advanced Practitioner in Oncology* **5**, 356-364 (2014).

8   Lerner, M. B. *et al.* Large scale commercial fabrication of high quality graphene-based assays for biomolecule detection. *Sens. Actuators B: Chem.* **239**, 1261-1267 (2017).

Chapter 8: Note about Thesis Dedication

This thesis is dedicated first and foremost to my maternal grandmother, Radha Rani Kuruganti, and to my maternal grandfather, Dr. K.V.L. Sarma.

Born in India in 1937, my grandfather was a physicist who earned his PhD at the University of Wisconsin, Madison in 1967 in theoretical neutrino physics. He went on as a postdoctoral researcher at Carnegie Mellon University and eventually returned to India to be a researcher at the Tata Institute of Fundamental Research (TIFR) in Mumbai, where he continued to work until his death in 1997.
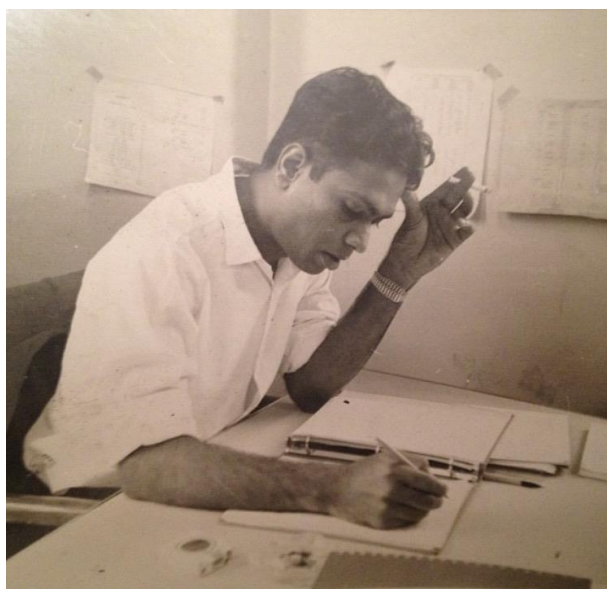
Figure 8.1.1 *My grandfather at work at the University of Wisconsin, 1960s.*

My grandmother, also born in India in 1941, did not finish high school, as was common for Indian women of that generation. Nonetheless, she followed my grandfather to the United States during his time as a graduate student, leaving her two small children, my mother and uncle, in India for two years to be cared for by her in-laws. Despite not

speaking any English upon her arrival in America, she managed to secure a job helping

PhD student Edward Dettmann in his research with scanning, measuring and data

analysis to encode the coordinates of proton tracks in the physics department at the

University of Wisconsin, Madison. It was through this position that she learned English,

and her contributions have been mentioned in Dr. Dettmann's thesis. With the money she

earned from this job, she purchased plane tickets for my mother and uncle to join her and

my grandfather in America.

Figure 8.1.2 *My grandmother at the University of Wisconsin in the lab where she worked (1960s)*

This dedication is bittersweet, as I feel regretful of the fact that my grandfather passed

before I could discuss science with him, but simultaneously inspired, not just by his

work, but by the work my grandmother took part in without knowing English and without

an education. With such little freedom and few resources, she still made her contribution

to science, which makes me believe that for myself and my peers, there are no limits, as we have been given many more opportunities for success.

Appendix A: CVD Graphene Growth Recipe

1) Clean furnace, thermal blocks and quartz plate with propanol-2 (IPA) only → acetone leaves a residue and can contribute to contamination of the furnace, so avoid it.

2) Cut a piece of copper foil (Alfa Aesar, 99.8%, 25 μm thickness) to approximately 3 x 4 inches

3) Sonicate foil in acetone for 10 minutes, rinse with IPA and dry with compressed N_2. (This cleaning step is to ensure that there are fewer defects on the surface of the foil, and that the surface is clean upon entering the furnace.)

4) Place foil on quartz plate and orient the plate and thermal blocks in the following positions in the furnace, shown below in **Figure AA.1**.
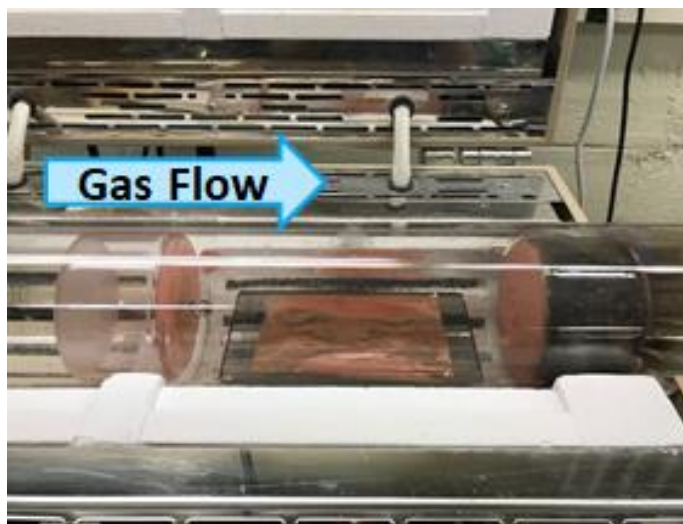
Figure AA.1 CVD furnace showing placement of copper foil and gas flow direction.

5) Place small amount of vacuum grease on the O-ring of the furnace and spread evenly to ensure a tight seal, and close the furnace with the metal plate and screws located on the chiller.

6) Turn the N_2 switch from "off" to "auto" on the furnace and set the flow rate to 200 sccm on the computer program.

7) After about 20 seconds, flip the N_2 switch to "purge" to increase the flow rate from 200 sccm to 500 sccm.

8) After 5 minutes of N_2 flow at 500 sccm, open the pressure valve *very* slowly to begin pumping gases out of the tube.

9) After another 5 minutes of N_2 flow, flip the switch back to "auto", at which point the flow rate will turn down to 200 sccm and, after 30 seconds, to "off", to lower the rate to 0 sccm. (The reason for this middle step is to prevent a drastic pressure change, which can shift the placement of the thermal blocks in the sealed furnace. At this point, the pressure should read somewhere between 50-60 mTorr.

10) Close the nitrogen tank and open the methane and hydrogen tanks, and turn the appropriate switches from "off" to "auto".

11) The desired growth recipe is chosen in the program on the computer connected to the furnace – all recipes are automated.

12) Gases will flow for about 30 minutes to purge the system of the nitrogen, at which point   the timer will beep.

13) Click "OK" on the computer screen pop-up, and immediately after, hold down the "run/hold" button the furnace. This will begin the heat ramp-up step.

14) The recipe will run for about 2.5 hours, which includes ramp up, anneal, and graphene growth. When the recipe is done, the system will beep.

15) A notification pop-up will appear on the screen – click "OK" on the notification and immediately "stop" the furnace (do NOT turn it off) and crank it open 2 inches. Clicking "OK" allows the program to go to the next step.

16) When the second alarm sounds, wait until the furnace reaches at most 900 C (for both thermocouples), click "OK" on the notification, and slide the furnace to the right, to increase the cooling rate. (It is very important not to slide the furnace until both thermocouples are at *most* 900 C, as doing so before could crack the ceramic inside the furnace, due to a drastic temperature change).

17) After sliding the furnace, one must wait for the temperature of both thermocouples to reach at most 500 C, click "OK" on the notification, and open the furnace all the way, at which point the methane turns off.

18) Keep the furnace in this position until the next alarm sounds, which will be when the furnace reaches around 80 C. Click "OK" on the notification and the H_2 will turn off. (For safety reasons, it is beneficial to continue waiting another 20 or 30 minutes after the hydrogen is turned off to allow the system to cool further, as 80 C could easily cause burns).

Note: the alarm always sounds a minute or two before the thermocouples reach the appropriate temperature. Allow the alarm to sound, and it will stop ringing on its own after a few seconds. Always wait for the thermocouples to reach the necessary temperature <u>before</u> clicking "OK" on the notification.

19) To vent the system, open the N_2 tank and slowly increase the flow rate to 500 sccm.

20) Close the pressure valve, allowing the nitrogen to fill the tube. When the pressure on the pressure gauge reaches room pressure (760 Torr), unscrew the metal plate and remove the thermal blocks and the foil on the quartz substrate. All tanks should be closed and the furnace (and all the quartz that goes in the furnace) should be cleaned with IPA. The Cu foil, now with graphene, can be wrapped in aluminum foil, gently, so as not to cause any wrinkles, and stored in a dry box at room temperature.

Additional growth method: A second method of cleaning involves sonicating in nitric acid for 40 seconds, followed by three sonication baths of DI water, each for 2 minutes, to remove the nitric acid residue and dried with N_2. The desire for nitric acid use over acetone is the strength of the acid over acetone, and its ability to etch away the top most layers of the Cu foil, leaving as few defects as possible. This results in a larger grain size of the graphene. One must be careful not to leave the foil in the nitric acid for too long, because too few defects on the Cu foil is also detrimental, as the graphene in fact grows around defects on the Cu foil's surface. In this thesis, the main method for foil cleaning is acetone, as it has been extremely effective and less dangerous than nitric acid use.

Appendix B: CVD Hexagonal Boron Nitride Growth Recipe

1) Cut a piece of copper foil roughly 1 x 3 inches (Alfa Aesar, 99.8%, 25 μm thickness) and sonicate in acetone for 10 minutes, then rinse with IPA and dry with N_2.

2) Center the appropriate growth tube in the center of the furnace.

3) Place the foil in the center of the 1 inch tube, so as to ensure even temperature spread and therefore uniform growth.

4) Using a pair of tweezers, place an ammonia borane (AB) pellet (Sigma Aldrich) in the center of a glass tube on the precursor holder.

5) Place the precursor holder at the right end of the tube (downstream of gas flow) about 20 cm from the right edge of the furnace.

6) Secure both ends of the furnace with the available O-rings and endcaps, to prevent gas leaks.

7) Open the argon and hydrogen tanks and associated mass flow controllers

8) Set the flow rates to the following: Argon: 500 sccm, H_2: 50 sccm

9) Set the furnace to 1050 C and wait 30 minutes for the ramp up/anneal steps.

10) After 30 minutes, lower the H_2 flow to 20 sccm and slide the precursor closer to the furnace, about 7.5 cm away from the edge.

11) Keep the precursor here for about 10 minutes, or until the pellet begins to expand

12) After 10 minutes, slide the precursor back to its original position about 20 cm away from the furnace.

13) Next, increase the Ar flow rate to 1000 sccm and lower the H2 to 10 sccm.

14) Turn off the furnace and slide it to the left (down stream of gas flow), about 1.5-2 inches from the foil.

15) Cool the furnace to below 100 C, and turn off the gases.

16) Remove copper foil, wrap in aluminum foil, and store in dry box for future use.

Appendix C: GFET Fabrication Recipe

1) Spin-coat wafer with a protective layer of polymethylglutarimide (PMGI, Microchem) at 4,000 rotations per minute (rpm) for 45 seconds.

2) Bake wafer at 210 C for 5 minutes.

3) spin coated a layer of S1813 (Microchem) at 5,000 rpm for 45 seconds atop the PMGI layer.

4) Bake wafer at 100 C for 2 minutes.

5) Place wafer in Suss Microtech mask aligner with appropriate contact mask and expose to UV light .

6) Develop wafer in MF-319 developer (Microposit) for ~30 seconds to reveal the pattern on the wafer.

7) Place wafer in thermal evaporator (PVD-75 Lesker) and deposit electrodes of chromium (5 nm) and gold (40 nm), the purpose of the chromium being to ensure proper adhesion of the gold to the wafer.

8) After evaporation, place wafer in 1165 (Microposit) to lift off excess metals. Mild pipetting and/or sonication is required to help remove these excess metals.

9) Place wafer in acetone to remove 1165 residue.

10) Rinse wafer with isopropyl alcohol (propanol-2, "IPA"). The patterning process and final substrate are shown in **Fig. AC.1** below.
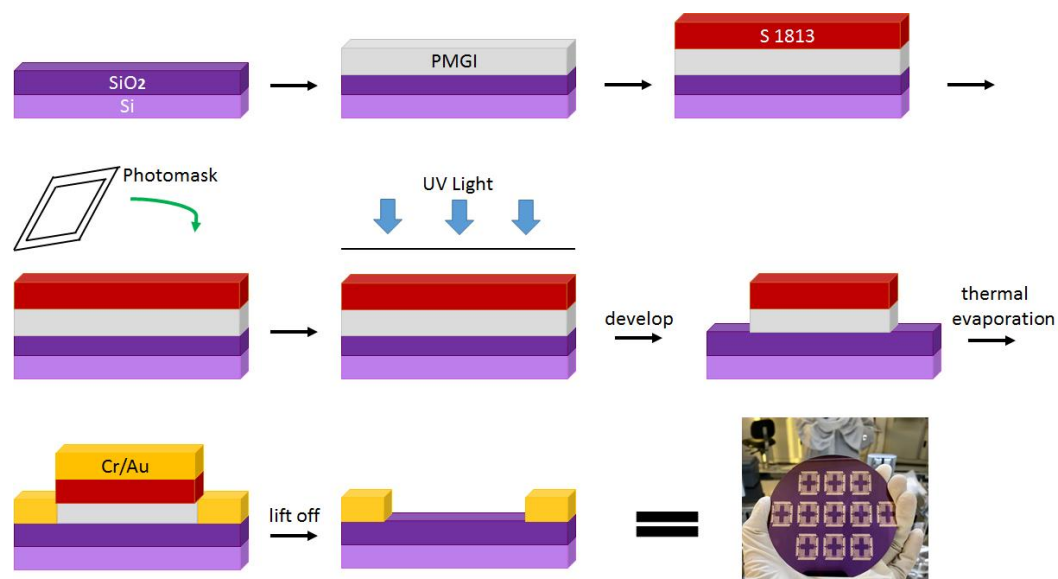
Figure AC.1 *Patterning schematic of a Si/SiO$_2$ wafer with chromium and gold electrodes (of thicknesses 5 nm and 40 nm, respectively). Each rectangle shown on the wafer in the bottom right hand corner represents one "chip", with each chip comprised of 52 devices, each with its own source and drain. In one round of lithography, we can have several hundred devices.*

11) Break wafer into individual chips using diamond scribe along vertical and horizontal axes of wafer.

12) Transfer graphene onto a chip through the electrolysis bubble transfer method (Chapter 3.1).

13) Leave graphene/PMMA film to dry on substrate for ~ 1 hour.

14) Bake chip at 150 C for 2 minutes to ensure proper adhesion of graphene to the SiO$_2$.

15) Wash chip with acetone and soak in an acetone bath for 10 minutes to remove PMMA.

16) Rinse with IPA and dry with compressed N$_2$.

17) Spin-coat chip with a protective layer of PMGI at 4,000 rpm for 45 seconds. This protective layer prevents the graphene from coming into contact with the next photoresist, which adheres more strongly to the graphene.

18) Bake chip at 125 C for 5 minutes.

19) Spin-coat a layer of S1813 onto the chip at 5,000 rpm for 45 seconds atop the PMGI layer.

20) Bake chip a second time, at 100 C for 2 minutes.

21) Place chip in Suss Microtech mask aligner with appropriate alignment mask

22) Expose chip to UV light to expose unwanted areas of graphene (everything except channels) in dimensions 10 x 100 µm

23) Develop in MF-319 for ~30 seconds to remove unwanted photoresist.

24) Rinse with DI water.

25) Place chip in plasma etcher to remove excess graphene, that is, not part of the FET channels, under the following conditions: O_2 plasma at 1.25 Torr under a power of 50 Watts for 30 seconds.

26) Clean chip in 1165, acetone, and IPA to remove excess photoresist on the channels in the following time order/time increments: 1165 (Microposit) for 2 minutes, 1165 for 5 minutes, acetone for 10 minutes, IPA for two minutes

27) Dry chip with compressed N_2. The steps are shown in **Figure AC.2**.

Figure AC2. *Fabrication of graphene channels on patterned substrate, resulting in an array of graphene field effect transistors (GFETs)*
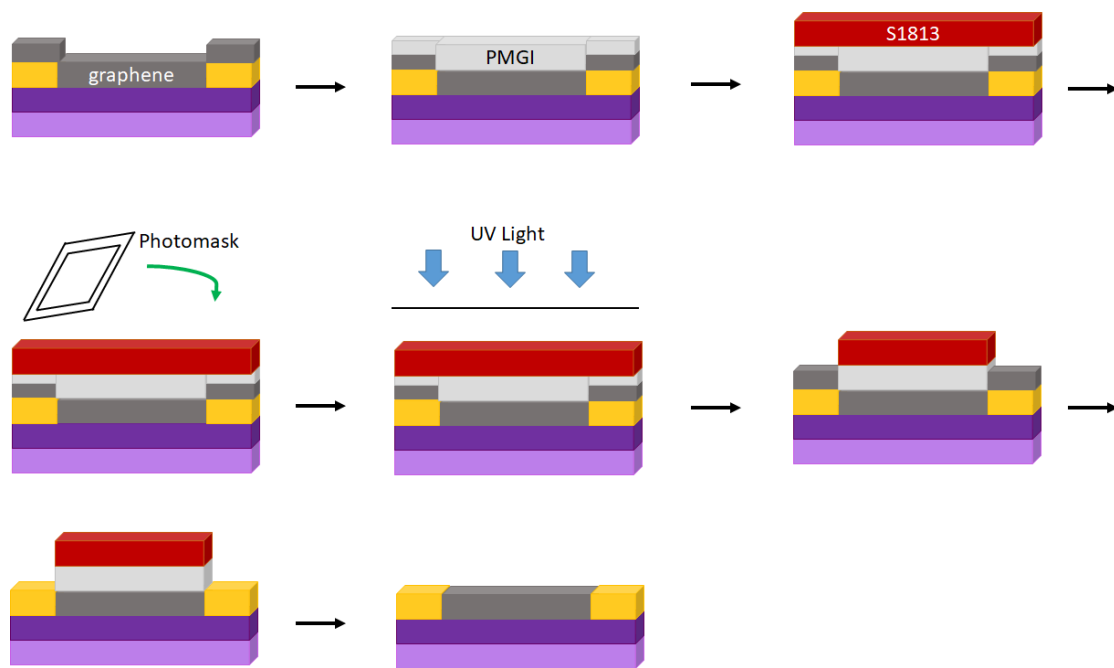
Bibliography

Akil, H., S. J. Watson, et al. (1984). "Endogenous opioids: biology and function." Annu Rev Neurosci **7**: 223-255.

Aliakbarinodehi, N., P. Jolly, et al. (2017). "Aptamer-based Field-Effect Biosensor for Tenofovir Detection." Scientific Reports **7**: 44409.

An, J. H., S. J. Park, et al. (2013). "High-Performance Flexible Graphene Aptasensor for Mercury Detection in Mussels." ACS Nano **7**(12): 10563-10571.

Anderson, M., A. Moshnikova, et al. (2016). "Probe for the measurement of cell surface pH in vivo and ex vivo." Proc. Natl. Acad. Sci. **113**(29): 8177-8181.

Andes, D., A. Pascual, et al. (2009). "Antifungal Therapeutic Drug Monitoring: Established and Emerging Indications." Antimicrob. Agents Chemother. **53**(1): 24-34.

Ang, P. K., W. Chen, et al. (2008). "Solution-gated epitaxial graphene as pH sensor." J Am Chem Soc **130**(44): 14392-14393.

Back, J. H. and M. Shim (2006). "pH-Dependent Electron-Transport Properties of Carbon Nanotubes." J. of Phys. Chem. B. **110**(47): 23736-23741.

Baker, E. S. and M. T. Bowers (2007). "B-DNA Helix Stability in a Solvent-Free Environment." J. Am. Soc. Mass. Spectrom **18**(7): 1188-1195.

Bard, A. J. F., L. R. (2000). Electrochemical Methods: Fundamentals and Applications. New York, Wiley.

Basu, J. and C. Roychaudhuri (2016). Attomolar Sensitivity of FET Biosensor Based on Smooth and Reliable Graphene Nanogrids.

Best, R. B., X. Zhu, et al. (2012). "Optimization of the Additive CHARMM All-Atom Protein Force Field Targeting Improved Sampling of the Backbone ϕ, ψ and Side-Chain χ1 and χ2 Dihedral Angles." J. Chem. Theor. Comp. **8**(9): 3257-3273.

Bizzarri, R., C. Arcangeli, et al. (2006). "Development of a Novel GFP-based Ratiometric Excitation and Emission pH Indicator for Intracellular Studies." Biophys. J. **90**(9): 3300-3314.

Bogomolova, A., E. Komarova, et al. (2009). "Challenges of Electrochemical Impedance Spectroscopy in Protein Biosensing." Anal. Chem. **81**(10): 3944-3949.

Bolotin, K. I., K. J. Sikes, et al. (2008). "Temperature-Dependent Transport in Suspended Graphene." Physical Review Letters **101**(9): 096802.

Bolotin, K. I., K. J. Sikes, et al. (2008). "Ultrahigh electron mobility in suspended graphene." <u>Solid State Communications</u> **146**(9): 351-355.

Bonnet, A.-M. (2000). "Involvement of Non-Dopaminergic Pathways in Parkinson's Disease." <u>CNS Drugs</u> **13**(5): 351-364.

Brindle, K. (2008). "New approaches for imaging tumour responses to treatment." <u>Nat. Rev. Cancer</u> **8**: 94.

Brooks, B. R., R. E. Bruccoleri, et al. (1983). "CHARMM: A program for macromolecular energy, minimization, and dynamics calculations." <u>J. Comp. Chem.</u> **4**(2): 187-217.

Bruehl, S., O. Y. Chung, et al. (2007). "Trait anger expressiveness and pain-induced beta-endorphin release: support for the opioid dysfunction hypothesis." <u>Pain</u> **130**(3): 208-215.

Butts, C. A., J. Swift, et al. (2008). "Directing Noble Metal Ion Chemistry within a Designed Ferritin Protein." <u>Biochemistry</u> **47**(48): 12729-12739.

Cai, B., S. Wang, et al. (2014). "Ultrasensitive Label-Free Detection of PNA–DNA Hybridization by Reduced Graphene Oxide Field-Effect Transistor Biosensor." <u>ACS Nano</u> **8**(3): 2632-2638.

Cai, H., M. A. Stott, et al. (2016). "On-chip wavelength multiplexed detection of cancer DNA biomarkers in blood." <u>Biomicrofluidics</u> **10**(6): 064116.

Calhoun, J. R., H. Kono, et al. (2003). "Computational design and characterization of a monomeric helical dinuclear metalloprotein." <u>J Mol Biol</u> **334**(5): 1101-1115.

Canbaz, M. Ç., Ç. S. Şimşek, et al. (2014). "Electrochemical biosensor based on self-assembled monolayers modified with gold nanoparticles for detection of HER-3." <u>Anal. Chim. Acta</u> **814**: 31-38.

Cardoso, A. R., F. T. C. Moreira, et al. (2016). "Novel and simple electrochemical biosensor monitoring attomolar levels of miRNA-155 in breast cancer." <u>Biosens Bioelectron</u> **80**: 621-630.

Cella, L. N., W. Chen, et al. (2010). "Single-Walled Carbon Nanotube-Based Chemiresistive Affinity Biosensors for Small Molecules: Ultrasensitive Glucose Detection." <u>J. Am. Chem. Soc.</u> **132**(14): 5024-5026.

Chai, C., Z. Xie, et al. (2011). SELEX (Systematic Evolution of Ligands by EXponential Enrichment), as a Powerful Tool for Deciphering the Protein–DNA Interaction Space. <u>Plant Transcript. Fact.: Meth. Prot.</u>**:** 249-258.

Chen, C. H., C.-T. Lin, et al. (2012). "Electrical Probing of Submicroliter Liquid Using Graphene Strip Transistors Built on a Nanopipette." Small **8**(1): 43-46.

Chen, R. J., S. Bangsaruntip, et al. (2003). "Noncovalent functionalization of carbon nanotubes for highly specific electronic biosensors." Proc. Natl. Acad. Sci. **100**(9): 4984-4989.

Chen, R. J., Y. Zhang, et al. (2001). "Noncovalent Sidewall Functionalization of Single-Walled Carbon Nanotubes for Protein Immobilization." J. Am. Chem. Soc. **123**(16): 3838-3839.

Chen, T.-Y., P. T. K. Loan, et al. (2013). "Label-free detection of DNA hybridization using transistors based on CVD grown graphene." Biosens. Bioelectron. **41**: 103-109.

Cheng, Z., Q. Li, et al. (2010). "Suspended Graphene Sensors with Improved Signal and Reduced Noise." Nano Letters **10**(5): 1864-1868.

Cheung-Lau, J. C., D. Liu, et al. (2014). "Engineering a well-ordered, functional protein-gold nanoparticle assembly." J. Inorg. Biochem. **130**: 59-68.

Choi, Y., T. J. Olsen, et al. (2013). "Dissecting Single-Molecule Signal Transduction in Carbon Nanotube Circuits with Protein Engineering." Nano Letters **13**(2): 625-631.

Chong, W. H., A. A. Molinolo, et al. (2011). "Tumor-induced osteomalacia." Endocr. Relat. Cancer **18**(3): 11-0006.

Chung, C., Y.-K. Kim, et al. (2013). "Biomedical Applications of Graphene and Graphene Oxide." Accounts of Chemical Research **46**(10): 2211-2224.

Claussen, J. C., K. Anurag, et al. (2012). "Nanostructuring Platinum Nanoparticles on Multilayered Graphene Petal Nanosheets for Electrochemical Biosensing." Adv. Funct. Mater. **22**(16): 3399-3405.

Clement-Jones, V., L. McLoughlin, et al. (1980). "Increased beta-endorphin but not met-enkephalin levels in human cerebrospinal fluid after acupuncture for recurrent pain." Lancet **2**(8201): 946-949.

Corma, A., R. Juarez, et al. (2011). "Gold catalyzes the Sonogashira coupling reaction without the requirement of palladium impurities." Chem. Commun. **47**(5): 1446-1448.

Crichton, R. R. and C. F. A. Bryce (1973). "Subunit interactions in horse spleen apoferritin. Dissociation by extremes of pH." Biochem. J. **133**(2): 289-299.

Cui, X., M. Freitag, et al. (2003). "Controlling Energy-Level Alignments at Carbon Nanotube/Au Contacts." Nano Letters **3**(6): 783-787.

Cui, Y., Q. Wei, et al. (2001). "Nanowire nanosensors for highly sensitive and selective detection of biological and chemical species." Science **293**(5533): 1289-1292.

Darmostuk, M., S. Rimpelova, et al. (2015). "Current approaches in SELEX: An update to aptamer selection technology." Biotechnol. Adv. **33**(6, Part 2): 1141-1161.

Dean, C. R., A. F. Young, et al. (2010). "Boron nitride substrates for high-quality graphene electronics." Nature Nanotechnology **5**: 722.

DeIasi, Russell (1971). "Aqueous degradation of polyimides." J. Appl. Polym. Sci. **15**(12): 2965-2974.

Deval, E., X. Gasull, et al. (2010). "Acid-sensing ion channels (ASICs): pharmacology and implication in pain." Pharmacol Ther **128**(3): 549-558.

DeWire, S. M., D. S. Yamashita, et al. (2013). "A G protein-biased ligand at the mu-opioid receptor is potently analgesic with reduced gastrointestinal and respiratory dysfunction compared with morphine." J Pharmacol Exp Ther **344**(3): 708-717.

DiFeliceantonio, A. G., O. S. Mabrouk, et al. (2012). "Enkephalin surges in dorsal neostriatum as a signal to eat." Current biology : CB **22**(20): 1918-1924.

Dolton, M. J., R. J. M. Brüggemann, et al. (2014). "Understanding Variability in Posaconazole Exposure Using an Integrated Population Pharmacokinetic Analysis." Antimicrob. Agents Chemother. **58**(11): 6879-6885.

Dolton, M. J., G. Mikus, et al. (2014). "Understanding variability with voriconazole using a population pharmacokinetic approach: implications for optimal dosing." J Antimicrob Chemother **69**(6): 1633-1641.

Dore, G. J., D. A. Cooper, et al. (2004). "Efficacy of Tenofovir Disoproxil Fumarate in Antiretroviral Therapy-Naive and -Experienced Patients Coinfected with HIV-1 and Hepatitis B Virus." J. Infect. Dis. **189**(7): 1185-1192.

Doster, A. R., J. Y. Yhee, et al. (2011). "CDX-2 and HER-3 Expression in Canine Gastric and Colorectal Adenocarcinomas." J. Comp. Pathol. **145**(1): 12-19.

Dresselhaus, M. S., G. Dresselhaus, and P. Avouris (2001). "Carbon nanotubes : synthesis, structure, properties, and applications." Topics in applied physics: 447.

Drummond, T. G., M. G. Hill, et al. (2003). "Electrochemical DNA sensors." Nat. Biotechnol. **21**: 1192.

D'Souza, J. W., S. Reddy, et al. (2014). "Combining anti-ERBB3 antibodies specific for domain I and domain III enhances the anti-tumor activity over the individual monoclonal antibodies." PLoS One **9**(11).

Duan, X., Y. Li, et al. (2012). "Quantification of the affinities and kinetics of protein interactions using silicon nanowire biosensors." <u>Nat. Nanotech.</u> **7**(6): 401-407.

Dunbrack, R. L., Jr. (2002). "Rotamer libraries in the 21st century." <u>Curr Opin Struct Biol</u> **12**(4): 431-440.

Ellington, A. D. and J. W. Szostak (1990). "In vitro selection of RNA molecules that bind specific ligands." <u>Nature</u> **346**: 818.

Estrella, V., T. Chen, et al. (2013). "Acidity generated by the tumor microenvironment drives local invasion." <u>Cancer Res</u> **73**(5): 1524-1535.

Esumi, K., K. Miyamoto, et al. (2002). "Comparison of PAMAM-Au and PPI-Au nanocomposites and their catalytic activity for reduction of 4-nitrophenol." <u>J Colloid Interface Sci</u> **254**(2): 402-405.

Fantechi, E., C. Innocenti, et al. (2014). "A Smart Platform for Hyperthermia Application in Cancer Treatment: Cobalt-Doped Ferrite Nanoparticles Mineralized in Human Ferritin Cages." <u>ACS Nano</u> **8**(5): 4705-4719.

Feller, S. E., Y. Zhang, et al. (1995). "Constant pressure molecular dynamics simulation: The Langevin piston method." <u>J. Chem. Phys.</u> **103**(11): 4613-4621.

Ferrari, A. C. (2007). "Raman spectroscopy of graphene and graphite: Disorder, electron–phonon coupling, doping and nonadiabatic effects." <u>Solid State Communications</u> **143**(1): 47-57.

Ferrari, A. C., J. C. Meyer, et al. (2006). "Raman Spectrum of Graphene and Graphene Layers." <u>Physical Review Letters</u> **97**(18): 187401.

Fu, W., C. Nef, et al. (2011). "Graphene Transistors Are Insensitive to pH Changes in Solution." <u>Nano Letters</u> **11**(9): 3597-3600.

Galbiati, M., A. C. Stoot, et al. (2017). "Real-time oxide evolution of copper protected by graphene and boron nitride barriers." <u>Scientific Reports</u> **7**: 39770.

Gan, L. and Z. Luo (2013). "Turning off Hydrogen To Realize Seeded Growth of Subcentimeter Single-Crystal Graphene Grains on Copper." <u>ACS Nano</u> **7**(10): 9480-9488.

Gannett, W., W. Regan, et al. (2011). "Boron nitride substrates for high mobility chemical vapor deposited graphene." <u>Applied Physics Letters</u> **98**(24): 242105.

Gao, L., W. Ren, et al. (2012). "Repeated growth and bubbling transfer of graphene with millimetre-size single-crystal grains using platinum." <u>Nature Communications</u> **3**: 699.

Gao, Z., H. Kang, et al. (2016). "Scalable Production of Sensor Arrays Based on High-Mobility Hybrid Graphene Field Effect Transistors." ACS Applied Materials & Interfaces **8**(41): 27546-27552.

Geim, A. K. and K. S. Novoselov (2007). "The rise of graphene." Nature Materials **6**: 183.

Ghannoum, M. A. and L. B. Rice (1999). "Antifungal agents: mode of action, mechanisms of resistance, and correlation of these mechanisms with bacterial resistance." Clin Microbiol Rev **12**(4): 501-517.

Gimpl, G., J. Reitz, et al. (2008). "Oxytocin receptors: ligand binding, signalling and cholesterol dependence." Prog Brain Res **170**: 193-204.

Goldsmith, B. R., Y. Lu, et al. (2009). "Temperature dependence of the noise amplitude in graphene and graphene oxide." Phys. Status Solidi (RRL) **3**(6): 178-180.

Grebe, S. K. G. and R. J. Singh (2011). "LC-MS/MS in the Clinical Laboratory – Where to From Here?" Clin. Biochem. Rev. **32**(1): 5-31.

Greenfield, N. J. (2006). "Using circular dichroism spectra to estimate protein secondary structure." Nat. Protoc. **1**(6): 2876-2890.

Gu, S., S. Wunder, et al. (2014). "Kinetic Analysis of the Catalytic Reduction of 4-Nitrophenol by Metallic Nanoparticles." J. Phys. Chem. C **118**(32): 18618-18625.

Gulya, K. (1990). "The opioid system in neurologic and psychiatric disorders and in their experimental models." Pharmacol. Ther. **46**(3): 395-428.

Guo, Z., C. H. Taubes, et al. (2008). "DNA on a Tube: Electrostatic Contribution to Stiffness." The journal of physical chemistry. B **112**(50): 16163-16169.

Gurtovenko, A. A. and I. Vattulainen (2009). "Calculation of the electrostatic potential of lipid bilayers from molecular dynamics simulations: methodological issues." J Chem Phys **130**(21): 3148885.

Halperin, A., A. Buhot, et al. (2004). "Sensitivity, Specificity, and the Hybridization Isotherms of DNA Chips." Biophys. J. **86**(2): 718-730.

Han, M. Y., B. Özyilmaz, et al. (2007). "Energy Band-Gap Engineering of Graphene Nanoribbons." Physical Review Letters **98**(20): 206805.

Hasegawa, H., K. Sode, et al. (2008). "Selection of DNA aptamers against VEGF165 using a protein competitor and the aptamer blotting method." Biotechnol Lett **30**(5): 829-834.

Heller, I., J. Kong, et al. (2006). "Electrochemistry at Single-Walled Carbon Nanotubes: The Role of Band Structure and Quantum Capacitance." J. Am. Chem. Soc. **128**(22): 7353-7359.

Hill, A. (1910). "The Possible Effects of The Aggregation of The Molecules of Haemoglobin on its Dissociation Curves." J. Physiol.(40): 4.

Hoffman, D. M., G. L. Doll, et al. (1984). "Optical properties of pyrolytic boron nitride in the energy range 0.05---10 eV." Physical Review B **30**(10): 6051-6056.

Horak, E., T. Heitner, et al. (2005). "Isolation of scFvs to In Vitro Produced Extracellular Domains of EGFR Family Members." Cancer Biother. Radiopharm. **20**(6): 603-613.

Howard, A. D., S. de La Baume, et al. (1985). "Covalent labeling of opioid receptors with radioiodinated human beta-endorphin. Identification of binding site subunit." J. Biol. Chem. **260**(19): 10833-10839.

Hu, R., T. Liu, et al. (2015). "DLISA: A DNAzyme-Based ELISA for Protein Enzyme-Free Immunoassay of Multiple Analytes." Anal. Chem. **87**(15): 7746-7753.

Huang, L., H. Xu, et al. (2014). "Graphene/Si CMOS Hybrid Hall Integrated Circuits." Sci. Rep. **4**: 5548.

Huang, P., L. Jing, et al. (2013). "Diazonium Functionalized Graphene: Microstructure, Electric, and Magnetic Properties." Accounts of Chemical Research **46**(1): 43-52.

Humphrey, W., A. Dalke, et al. (1996). "VMD: Visual molecular dynamics." J. Mol. Graph. **14**(1): 33-38.

Hwang, M. T., P. B. Landon, et al. (2016). "Highly specific SNP detection using 2D graphene electronics and DNA strand displacement." Proc. Natl. Acad. Sci. **113**(26): 7088-7093.

Israelachvili, J. (2011). "Intermolecular and Surface Forces", Revised Third Edition

Jager, N. G. L., R. M. van Hest, et al. (2016). "Therapeutic drug monitoring of anti-infective agents in critically ill patients." Expert Rev. Clin. Pharmacol. **9**(7): 961-979.

Jakupciak, J. P., W. Wang, et al. (2005). "Mitochondrial DNA as a Cancer Biomarker." The Journal of Molecular Diagnostics **7**(2): 258-267.

Jiadong, Z., L. Fucai, et al. (2017). "Large-Area and High-Quality 2D Transition Metal Telluride." Advanced Materials **29**(3): 1603471.

Jing, M. and M. T. Bowser (2011). "Methods for measuring aptamer-protein equilibria: a review." Anal Chim Acta **686**(1-2): 9-18.

Johnson, E., D. Cascio, et al. (2005). "Crystal Structures of a Tetrahedral Open Pore Ferritin from the Hyperthermophilic Archaeon Archaeoglobus fulgidus." Structure **13**(4): 637-648.

Jorgensen, W. L., J. Chandrasekhar, et al. (1983). "Comparison of simple potential functions for simulating liquid water." J. Chem. Phys. **79**(2): 926-935.

Jürgen, R., Z. Wenying, et al. (2010). "Characteristics of solution gated field effect transistors on the basis of epitaxial graphene on silicon carbide." J. Phys. D: Appl. Phys. **43**(34): 345303.

Justino, C. I. L., A. R. Gomes, et al. (2017). "Graphene based sensors and biosensors." TrAC Trends in Analytical Chemistry **91**: 53-66.

Kakatkar, A., T. S. Abhilash, et al. (2015). "Detection of DNA and poly-l-lysine using CVD graphene-channel FET biosensors." Nanotechnology **26**(12): 0957-4484.

Kammer, M. N., I. R. Olmsted, et al. (2014). "Characterizing aptamer small molecule interactions with backscattering interferometry." Analyst **139**(22): 5879-5884.

Karamouzis, M. V., F. A. Badra, et al. (2007). "Breast cancer: The upgraded role of HER-3 and HER-4." Int. J. Biochem. Cell Biol. **39**(5): 851-856.

Katz, E. (1994). "Application of bifunctional reagents for immobilization of proteins on a carbon electrode surface: Oriented immobilization of photosynthetic reaction centers." J. Electroanal. Chem. **365**(1): 157-164.

Ke, X., M. Xenia, et al. (2014). "Graphene- and aptamer-based electrochemical biosensor." Nanotechnology **25**(20): 205501.

Kennedy, S. E., R. A. Koeppe, et al. (2006). "Dysregulation of endogenous opioid emotion regulation circuitry in major depression in women." Arch Gen Psychiatry **63**(11).

Kim, B. S., R. A. Hayes, et al. (1995). "The adsorption of anionic naphthalene derivatives at the graphite-aqueous solution interface." Carbon **33**(1): 25-34.

Kim, D. J., H. C. Park, et al. (2013). "Electrical Graphene Aptasensor for Ultra-Sensitive Detection of Anthrax Toxin with Amplified Signal Transduction." Small **9**(19): 3352-3360.

Kim, J. H., K. S. Im, et al. (2011). "Expression of HER-2 and nuclear localization of HER-3 protein in canine mammary tumors: histopathological and immunohistochemical study." Vet J **189**(3): 318-322.

Kim, K. S., Y. Zhao, et al. (2009). "Large-scale pattern growth of graphene films for stretchable transparent electrodes." Nature **457**: 706.

Kim, M., Y. Rho, et al. (2011). "pH-Dependent Structures of Ferritin and Apoferritin in Solution: Disassembly and Reassembly." Biomacromolecules **12**(5): 1629-1640.

Kim, S. O. and H. J. Kim (1994). "Fabrication of n-metal–oxide semiconductor field effect transistor with Ta2O5 gate oxide prepared by plasma enhanced metalorganic chemical vapor deposition." J. of Vacuum Sci & Tech B **12**(5): 3006-3009.

Kitano, H. (2002). "Systems biology: a brief overview." Science **295**(5560): 1662-1664.

Ko, J. W., J.-M. Woo, et al. (2011). "Multi-Order Dynamic Range DNA Sensor Using a Gold Decorated SWCNT Random Network." ACS Nano **5**(6): 4365-4372.

Ko, K. Y., J.-G. Song, et al. (2016). "Improvement of Gas-Sensing Performance of Large-Area Tungsten Disulfide Nanosheets by Surface Functionalization." ACS Nano **10**(10): 9287-9296.

Kobayashi, K. and J. Yamauchi (1995). "Electronic structure and scanning-tunneling-microscopy image of molybdenum dichalcogenide surfaces." Physical Review B **51**(23): 17085-17095.

Koehn, J., Y. Ding, et al. (2015). "A Simple, Efficient, and Sensitive Method for Simultaneous Detection of Anti-HIV Drugs Atazanavir, Ritonavir, and Tenofovir by Use of Liquid Chromatography-Tandem Mass Spectrometry." Antimicrob. Agents Chemother. **59**(11): 6682-6688.

Kono, H. and J. G. Saven (2001). "Statistical theory for protein combinatorial libraries. Packing interactions, backbone flexibility, and the sequence variability of a main-chain structure." J Mol Biol **306**(3): 607-628.

Korendovych, I. V., A. Senes, et al. (2010). "De Novo Design and Molecular Assembly of a Transmembrane Diporphyrin-Binding Protein Complex." J. Am. Chem. Soc. **132**(44): 15516-15518.

Korostynska, O., K. Arshak, et al. (2008). Review Paper: Materials and Techniques for In Vivo pH Monitoring.

Koutras, A. K. and T. R. J. Evans (2008). "The epidermal growth factor receptor family in breast cancer." Onco Targets Ther. **1**: 5-19.

Kuila, T., S. Bose, et al. (2012). "Chemical functionalization of graphene and its applications." Progress in Materials Science **57**(7): 1061-1105.

Kumar, S., J. Aaron, et al. (2008). "Directional conjugation of antibodies to nanoparticles for synthesis of multiplexed optical contrast agents with both delivery and targeting moieties." Nat Protoc **3**(2): 314-320.

Kuroda, K., T. Ishida, et al. (2009). "Reduction of 4-nitrophenol to 4-aminophenol over Au nanoparticles deposited on PMMA." J. Mol. Catal. A: Chem. **298**(1): 7-11.

Kuzum, D., H. Takano, et al. (2014). "Transparent and flexible low noise graphene electrodes for simultaneous electrophysiology and neuroimaging." Nat. Commun. **5**: 5259.

Kwon, O. S., S. J. Park, et al. (2012). "Flexible FET-Type VEGF Aptasensor Based on Nitrogen-Doped Graphene Converted from Conducting Polymer." ACS Nano **6**(2): 1486-1493.

Kybert, N. J., M. B. Lerner, et al. (2013). "Differentiation of Complex Vapor Mixtures Using Versatile DNA–Carbon Nanotube Chemical Sensor Arrays." ACS Nano **7**(3): 2800-2807.

Lahiri, J., L. Isaacs, et al. (1999). "A Strategy for the Generation of Surfaces Presenting Ligands for Studies of Binding Based on an Active Ester as a Common Reactive Intermediate: A Surface Plasmon Resonance Study." Anal. Chem. **71**(4): 777-790.

Laundau, L. D. (1937). "Zur Theorie der phasenumwandlungen II." Physikalische Zeitschrift der Sowjetunion **11**: 26-35.

Lea, W. A. and A. Simeonov (2011). "Fluorescence polarization assays in small molecule screening." Expert Opin Drug Discov **6**(1): 17-32.

Ledel, F., M. Hallstrom, et al. (2014). "HER3 expression in patients with primary colorectal cancer and corresponding lymph node metastases related to clinical outcome." Eur J Cancer **50**(3): 656-662.

Lee, J., P. Dak, et al. (2014). "Two-dimensional Layered MoS2 Biosensors Enable Highly Sensitive Detection of Biomolecules." Scientific Reports **4**: 7352.

Lee, M. H., B. J. Kim, et al. (2015). "Apparent pH sensitivity of solution-gated graphene transistors." Nanoscale **7**(17): 7540-7544.

Lerner, M. B., J. D'Souza, et al. (2012). "Hybrids of a Genetically Engineered Antibody and a Carbon Nanotube Transistor for Detection of Prostate Cancer Biomarkers." ACS Nano **6**(6): 5143-5149.

Lerner, M. B., J. M. Resczenski, et al. (2012). "Toward quantifying the electrostatic transduction mechanism in carbon nanotube molecular sensors." J Am Chem Soc **134**(35): 14318-14321.

Lerner, M. B., J. Dailey, et al. (2013). "Detecting Lyme disease using antibody-functionalized single-walled carbon nanotube transistors." Biosens Bioelectron **45**: 163-167.

Lerner, M. B., N. Kybert, et al. (2013). "Scalable, non-invasive glucose sensor based on boronic acid functionalized carbon nanotube transistors." Applied Physics Letters **102**(18): 183113.

Lerner, M. B., F. Matsunaga, et al. (2014). "Scalable Production of Highly Sensitive Nanosensors Based on Graphene Functionalized with a Designed G Protein-Coupled Receptor." Nano Letters **14**(5): 2709-2714.

Lerner, M. B., D. Pan, et al. (2017). "Large scale commercial fabrication of high quality graphene-based assays for biomolecule detection." Sens. Actuators B: Chem. **239**: 1261-1267.

Letowski, J., R. Brousseau, et al. (2004). "Designing better probes: effect of probe size, mismatch position and number on hybridization in DNA oligonucleotide microarrays." J. Microbiol. Methods **57**(2): 269-278.

Li, H., J. Wu, et al. (2014). "Preparation and Applications of Mechanically Exfoliated Single-Layer and Multilayer MoS2 and WSe2 Nanosheets." Accounts of Chemical Research **47**(4): 1067-1075.

Li, H., Y. Zhu, et al. (2017). "Graphene field effect transistors for highly sensitive and selective detection of K+ ions." Sensors and Actuators B: Chemical **253**: 759-765.

Li, L., G. Yichuan, et al. (2018). "A General Method for the Chemical Synthesis of Large-Scale, Seamless Transition Metal Dichalcogenide Electronics." Advanced Materials **30**(12): 1706215.

Li, X., W. Cai, et al. (2009). "Large-Area Synthesis of High-Quality and Uniform Graphene Films on Copper Foils." Science **324**(5932): 1312-1314.

Li, X. and H. Zhu (2015). "Two-dimensional MoS2: Properties, preparation, and applications." J. Materiomics **1**(1): 33-44.

Limbird, L. E. (2005). Cell Surface Receptors: A Short Course on Theory and Methods. New York, Springer.

Lin, S.-H., Y.-C. Lee, et al. (2008). "Soluble ErbB3 Levels in Bone Marrow and Plasma of Men with Prostate Cancer." Clin. Cancer Res. **14**(12): 3729-3736.

Lionis, C. and E. Petelos (2011). "Early detection of colorectal cancer: barriers to screening in the primary care setting." Family Practice **28**(6): 589-591.

Liu, J., Z. Cao, et al. (2009). "Functional Nucleic Acid Sensors." Chem. Rev. **109**(5): 1948-1998.

Liu, Y., L. Yuan, et al. (2014). "Giant enhancement in vertical conductivity of stacked CVD graphene sheets by self-assembled molecular layers." Nat Commun **5**(5461).

Lu, J., I. Do, et al. (2008). "Nanometal-Decorated Exfoliated Graphite Nanoplatelet Based Glucose Biosensors with High Sensitivity and Fast Response." ACS Nano **2**(9): 1825-1832.

Lundqvist, M., J. Stigler, et al. (2008). "Nanoparticle size and surface properties determine the protein corona with possible implications for biological impacts." Proc. Natl. Acad. Sci. **105**(38): 14265-14270.

Luo, Y., C. Chen, et al. (2016). "Tungsten disulfide (WS2) based all-fiber-optic humidity sensor." Optics Express **24**(8): 8956-8966.

Luo, Y., C. E. Ergenekan, et al. (2010). "The Molecular Determinants of the Increased Reduction Potential of the Rubredoxin Domain of Rubrerythrin Relative to Rubredoxin." Biophys. J. **98**(4): 560-568.

Luo, Z., Y. Lu, et al. (2011). "Effect of Substrate Roughness and Feedstock Concentration on Growth of Wafer-Scale Graphene at Atmospheric Pressure." Chemistry of Materials **23**(6): 1441-1447.

Ma, D., J. Shi, et al. (2015). "A universal etching-free transfer of MoS2 films for applications in photodetectors." Nano Research **8**(11): 3662-3672.

Ma, F., Z. Zhang, et al. (2010). "Adsorption of cysteine molecule on intrinsic and Pt-doped graphene: A first-principle study." J. Mol. Struct.: THEOCHEM **955**(1): 134-139.

Ma, X., Y. Wang, et al. (2014). "Ultra-pH-Sensitive Nanoprobe Library with Broad pH Tunability and Fluorescence Emissions." J. Am. Chem. Soc. **136**(31): 11085-11092.

MacKerell, A. D., D. Bashford, et al. (1998). "All-Atom Empirical Potential for Molecular Modeling and Dynamics Studies of Proteins." J. Phys. Chem. B **102**(18): 3586-3616.

MacKerell, A. D., Jr., M. Feig, et al. (2004). "Improved treatment of the protein backbone in empirical force fields." J Am Chem Soc **126**(3): 698-699.

Madelin, G., R. Kline, et al. (2014). "A method for estimating intracellular sodium concentration and extracellular volume fraction in brain in vivo using sodium magnetic resonance imaging." Sci. Rep. **4**: 4763.

Mailly-Giacchetti, B., A. Hsu, et al. (2013). "pH sensing properties of graphene solution-gated field-effect transistors." J. Appl. Phys. **114**(8): 084505.

Maity, B., S. Abe, et al. (2017). "Observation of gold sub-nanocluster nucleation within a crystalline protein cage." Nat. Commun. **8**: 14820.

Malard, L. M., M. A. Pimenta, et al. (2009). "Raman spectroscopy in graphene." Physics Reports **473**(5): 51-87.

Mao, S., G. Lu, et al. (2010). "Specific protein detection using thermally reduced graphene oxide sheet decorated with gold nanoparticle-antibody conjugates." Adv. Mater. **22**(32): 3521-3526.

Mao, S., K. Yu, et al. (2011). "Highly sensitive protein sensor based on thermally-reduced graphene oxide field-effect transistor." Nano Res. **4**(10): 921.

Marchetti, A., M. S. Parker, et al. (2009). "Ferritin is used for iron storage in bloom-forming marine pennate diatoms." Nature **457**(7228): 467-470.

Martyna, G. J., D. J. Tobias, et al. (1994). "Constant pressure molecular dynamics algorithms." J. Chem. Phys. **101**(5): 4177-4189.

Medintz, I. L., H. T. Uyeda, et al. (2005). "Quantum dot bioconjugates for imaging, labelling and sensing." Nat Mater **4**(6): 435-446.

Menezes, M. G., R. B. Capaz, et al. (2014). "Ab initio quasiparticle band structure of ABA and ABC-stacked graphene trilayers." Physical Review B **89**(3): 035431.

Mohanty, N. and V. Berry (2008). "Graphene-Based Single-Bacterium Resolution Biodevice and DNA Transistor: Interfacing Graphene Derivatives with Nanoscale and Microscale Biocomponents." Nano Letters **8**(12): 4469-4476.

Mosmann, T. (1983). "Rapid colorimetric assay for cellular growth and survival: application to proliferation and cytotoxicity assays." J. Immunol. Methods **65**(1-2): 55-63.

Nagatoishi, S., Y. Tanaka, et al. (2007). "Circular dichroism spectra demonstrate formation of the thrombin-binding DNA aptamer G-quadruplex under stabilizing-cation-deficient conditions." Biochem Biophys Res Commun **352**(3): 812-817.

Naidu, R., M. Yadav, et al. (1998). "Expression of c-erbB3 protein in primary breast carcinomas." Br J Cancer **78**(10): 1385-1390.

Naylor, C. H., N. J. Kybert, et al. (2016). "Scalable Production of Molybdenum Disulfide Based Biosensors." ACS Nano **10**(6): 6173-6179.

Naylor, C. H., Parkin, W.M. et al. (2017). "Large-area synthesis of high-quality monolayer 1T'-WTe 2 flakes." 2D Materials **4**(2): 021008.

Neenu, V., M. Umesha, et al. (2009). "Binding of DNA Nucleobases and Nucleosides with Graphene." ChemPhysChem **10**(1): 206-210.

Nel, A. E., L. Mädler, et al. (2009). "Understanding biophysicochemical interactions at the nano–bio interface." Nat. Mater. **8**: 543.

Nemes-Incze, P., Z. Osváth, et al. (2008). "Anomalies in thickness measurements of graphene and few layer graphite crystals by tapping mode atomic force microscopy." Carbon **46**(11): 1435-1442.

Neria, E., S. Fischer, et al. (1996). "Simulation of activation free energies in molecular systems." J. Chem. Phys. **105**(5): 1902-1921.

Neto, A. H. C., F. Guinea, et al. (2009). "The electronic properties of graphene." Reviews of Modern Physics **81**(1): 109-162.

Novoselov, K. S., A. K. Geim, et al. (2005). "Two-dimensional gas of massless Dirac fermions in graphene." Nature **438**: 197.

Novoselov, K. S., A. K. Geim, et al. (2004). "Electric Field Effect in Atomically Thin Carbon Films." Science **306**(5696): 666-669.

Ohno, Y., K. Maehashi, et al. (2010). "Label-Free Biosensors Based on Aptamer-Modified Graphene Field-Effect Transistors." J. Am. Chem. Soc. **132**(51): 18012-18013.

Ohno, Y., K. Maehashi, et al. (2009). "Electrolyte-Gated Graphene Field-Effect Transistors for Detecting pH and Protein Adsorption." Nano Letters **9**(9): 3318-3322.

Okahata, Y., M. Kawase, et al. (1998). "Kinetic Measurements of DNA Hybridization on an Oligonucleotide-Immobilized 27-MHz Quartz Crystal Microbalance." Anal. Chem. **70**(7): 1288-1296.

Panchakarla, L. S., K. S. Subrahmanyam, et al. (2009). "Synthesis, Structure, and Properties of Boron- and Nitrogen-Doped Graphene." Advanced Materials **21**(46): 4726-4730.

Paramasivan, S., I. Rujan, et al. (2007). "Circular dichroism of quadruplex DNAs: applications to structure, cation effects and ligand binding." Methods **43**(4): 324-331.

Park, J., S. Choi, et al. (2012). "Highly selective fluorescence turn-on sensing of gold ions by a nanoparticle generation/C-I bond cleavage sequence." Analyst **137**(19): 4411-4414.

Park, K. H., B. H. Kim, et al. (2012). "Exfoliation of Non-Oxidized Graphene Flakes for Scalable Conductive Film." Nano Letters **12**(6): 2871-2876.

Park, S. J., O. S. Kwon, et al. (2012). "Ultrasensitive Flexible Graphene Based Field-Effect Transistor (FET)-Type Bioelectronic Nose." Nano Lett. **12**(10): 5082-5090.

Park, W. B., N. H. Kim, et al. (2012). "The effect of therapeutic drug monitoring on safety and efficacy of voriconazole in invasive fungal infections: a randomized controlled trial." Clin Infect Dis **55**(8): 1080-1087.

Peierls, R. (1935). "Quelques propriétés typiques des corps solides." Annales de l'institut Henri Poincaré **5**(3): 177-222.

Perez-Aguilar, J. M., J. Xi, et al. (2013). "A Computationally Designed Water-Soluble Variant of a G-Protein-Coupled Receptor: The Human Mu Opioid Receptor." PLoS One **8**(6).

Peterson, A. W., L. K. Wolf, et al. (2002). "Hybridization of Mismatched or Partially Matched DNA at Surfaces." J. Am. Chem. Soc. **124**(49): 14601-14607.

Pham, V. P., H.-S. Jang, et al. (2017). "Direct growth of graphene on rigid and flexible substrates: progress, applications, and challenges." Chem. Soc. Rev. **46**(20): 6276-6300.

Phillips, J. C., R. Braun, et al. (2005). "Scalable molecular dynamics with NAMD." J Comput Chem **26**(16): 1781-1802.

Ping, J. and M. S. Fuhrer (2014). "Carbon impurities on graphene synthesized by chemical vapor deposition on platinum." J. Appl. Phys. **116**(4): 044303.

Ping, J. and A. T. C. Johnson (2016). "Quantifying the intrinsic surface charge density and charge-transfer resistance of the graphene-solution interface through bias-free low-level charge measurement." Appl. Phys. Lett. **109**(1): 013103.

Ping, J., Vishnubhotla, R. et al. (2016). "Scalable Production of High-Sensitivity, Label-Free DNA Biosensors Based on Back-Gated Graphene Field Effect Transistors." ACS Nano **10**(9): 8700-8704.

Ping, J., J. Xi, et al. (2017). "Quantifying the effect of ionic screening with protein-decorated graphene transistors." Biosens. Bioelectron. **89**: 689-692.

Ping, J., K. W. Pulsipher, et al. (2017). "Structural-functional analysis of engineered protein-nanoparticle assemblies using graphene microelectrodes." Chem Sci **8**(8): 5329-5334.

Ping, J., J. E. Blum, et al. (2017). "pH Sensing Properties of Flexible, Bias-Free Graphene Microelectrodes in Complex Fluids: From Phosphate Buffer Solution to Human Serum." Small **13**(30): 14.

Pohl, F. M. and T. M. Jovin (1972). "Salt-induced co-operative conformational change of a synthetic DNA: equilibrium and kinetic studies with poly (dG-dC)." J Mol Biol **67**(3): 375-396.

Prossin, A. R., T. M. Love, et al. (2010). "Dysregulation of regional endogenous opioid function in borderline personality disorder." Am J Psychiatry **167**(8): 925-933.

Pulsipher, K. and I. Dmochowski (2015). Ferritin Encapsulation and Templated Synthesis of Inorganic Nanoparticles.

Qi, Z. J., S. J. Hong, et al. (2015). "Electronic Transport in Heterostructures of Chemical Vapor Deposited Graphene and Hexagonal Boron Nitride." Small **11**(12): 1402-1408.

Qi, Z. J., J. A. Rodríguez-Manzo, et al. (2014). "Correlating Atomic Structure and Transport in Suspended Graphene Nanoribbons." Nano Letters **14**(8): 4238-4244.

Quinn, C. M., J. L. Ostrowski, et al. (1994). "c-erbB-3 protein expression in human breast cancer: comparison with other tumour variables and survival." Histopathology **25**(3): 247-252.

Rahman, M. S., M. R. Hasan, et al. (2018). "A novel graphene coated surface plasmon resonance biosensor with tungsten disulfide (WS2) for sensing DNA hybridization." Optical Materials **75**: 567-573.

Rajesh, B. K. Das, et al. (2011). "ZnS nanocrystals decorated single-walled carbon nanotube based chemiresistive label-free DNA sensor." Appl. Phys. Lett. **98**(1): 013701.

Rajesh, G. Zhaoli, et al. (2016). "Genetically Engineered Antibody Functionalized Platinum Nanoparticles Modified CVD-Graphene Nanohybrid Transistor for the Detection of Breast Cancer Biomarker, HER3." Adv. Mater. Inter. **3**(17).

Rana, S., N. D. B. Le, et al. (2014). "A multichannel nanosensor for instantaneous readout of cancer drug mechanisms." Nat. Nanotech. **10**: 65.

Rauh-Hain, J. A., T. C. Krivak, et al. (2011). "Ovarian Cancer Screening and Early Detection in the General Population." Reviews in Obstetrics and Gynecology **4**(1): 15-21.

Reina, A., X. Jia, et al. (2009). "Large Area, Few-Layer Graphene Films on Arbitrary Substrates by Chemical Vapor Deposition." Nano Letters **9**(1): 30-35.

Reschke, M., D. Mihic-Probst, et al. (2008). "HER3 is a determinant for poor prognosis in melanoma." Clin Cancer Res **14**(16): 5188-5197.

Reynolds, R. B. and J. Folloder (2014). "Clinical Management of Pancreatic Cancer." Journal of the Advanced Practitioner in Oncology **5**(5): 356-364.

Ryckaert, J.-P., G. Ciccotti, et al. (1977). "Numerical integration of the Cartesian Equations of Motion of a System with Constraints: Molecular Dynamics of n-Alkanes." J. Comp. Phys. **23**: 317-341.

San, B. H., J. A. Kim, et al. (2014). "Combining Protein-Shelled Platinum Nanoparticles with Graphene to Build a Bionanohybrid Capacitor." ACS Nano **8**(12): 12120-12129.

Sana, B., E. Johnson, et al. (2013). "The Role of Nonconserved Residues of Archaeoglobus fulgidus Ferritin on Its Unique Structure and Biophysical Properties." J. Biol. Chem. **288**(45): 32663-32672.

Sarkar, D., W. Liu, et al. (2014). "MoS2 Field-Effect Transistor for Next-Generation Label-Free Biosensors." ACS Nano **8**(4): 3992-4003.

Sassolas, A., B. D. Leca-Bouvier, et al. (2008). "DNA Biosensors and Microarrays." Chem. Rev. **108**(1): 109-139.

Schiller, P. W., T. M. Nguyen, et al. (2000). "Synthesis and in vitro opioid activity profiles of DALDA analogues." Eur J Med Chem **35**(10): 895-901.

Schmidt, A. C., L. E. Dunaway, et al. (2014). "Multiple Scan Rate Voltammetry for Selective Quantification of Real-Time Enkephalin Dynamics." Anal. Chem. **86**(15): 7806-7812.

Schmidt, H., S. Wang, et al. (2014). "Transport Properties of Monolayer MoS2 Grown by Chemical Vapor Deposition." Nano Letters **14**(4): 1909-1913.

Schwarzenbach, H., D. S. B. Hoon, et al. (2011). "Cell-free nucleic acids as biomarkers in cancer patients." Nature Reviews Cancer **11**: 426.

Schwierz, F. (2010). "Graphene transistors." Nature Nanotech. **5**: 487.

Sheehan, D. J., C. A. Hitchcock, et al. (1999). "Current and Emerging Azole Antifungal Agents." Clin. Microbiol. Rev. **12**(1): 40-79.

Shin, D.-W., H. M. Lee, et al. (2012). "A Facile Route To Recover Intrinsic Graphene over Large Scale." ACS Nano **6**(9): 7781-7788.

Shokri, A. and N. Salami (2016). "Gas sensor based on MoS2 monolayer." Sensors and Actuators B: Chemical **236**: 378-385.

Sips, R. (1948). "On The Structure of a Catalyst Surface." J. Chem. Phys. **16**: 490-495.

Sohn, I. Y., D. J. Kim, et al. (2013). "pH sensing characteristics and biosensing application of solution-gated reduced graphene oxide field-effect transistors." Biosens. Bioelectron. **45**: 70-76.

Sonuc, M. N. and M. K. Sezginturk (2014). "Ultrasensitive electrochemical detection of cancer associated biomarker HER3 based on anti-HER3 biosensor." Talanta **120**: 355-361.

Sprouse-Blum, A. S., G. Smith, et al. (2010). "Understanding endorphins and their importance in pain management." Hawaii Med J **69**(3): 70-71.

Squires, T. M., R. J. Messinger, et al. (2008). "Making it stick: convection, reaction and diffusion in surface-based biosensors." Nat. Biotechnol. **26**: 417.

Srinivas, P. R., B. S. Kramer, et al. (2001). "Trends in biomarker research for cancer detection." Lancet Oncol. **2**(11): 698-704.

Stoltenburg, R., N. Nikolaus, et al. (2012). "Capture-SELEX: Selection of DNA Aptamers for Aminoglycoside Antibiotics." J. Anal Methods Chem. **2012**: 14.

Suzuki, Y., G. Cardone, et al. (2016). "Self-assembly of coherently dynamic, auxetic, two-dimensional protein crystals." Nature **533**(7603): 369-373.

Swift, J., C. A. Butts, et al. (2009). "Efficient Self-Assembly of Archaeoglobus fulgidus Ferritin around Metallic Cores." Langmuir **25**(9): 5219-5225.

Tang, X., S. Bansaruntip, et al. (2006). "Carbon Nanotube DNA Sensor and Sensing Mechanism." Nano Letters **6**(8): 1632-1636.

Tannock, I. F. and D. Rotin (1989). "Acid pH in tumors and its potential for therapeutic exploitation." Cancer Res **49**(16): 4373-4384.

Tao, L., J. Lee, et al. (2012). "Synthesis of High Quality Monolayer Graphene at Reduced Temperature on Hydrogen-Enriched Evaporated Copper (111) Films." ACS Nano **6**(3): 2319-2325.

te Velde, E. A., A. C. Franke, et al. (2009). "HER-family gene amplification and expression in resected pancreatic cancer." Eur J Surg Oncol **35**(10): 1098-1104.

Theil, E. C., T. Tosha, et al. (2016). "Solving Biology's Iron Chemistry Problem with Ferritin Protein Nanocages." Acc Chem Res **49**(5): 784-791.

Tieleman, D. P. and H. J. C. Berendsen (1996). " Molecular dynamics simulations of a fully hydrated dipalmitoylphosphatidylcholine bilayer with different macroscopic boundary conditions and parameters." J. Chem. Phys. **105**: 4871-4880.

Trushin, M. and J. Schliemann (2007). "Minimum Electrical and Thermal Conductivity of Graphene: A Quasiclassical Approach." Phys. Rev. Lett. **99**(21): 216602.

Tuerk, C. and L. Gold (1990). "Systematic evolution of ligands by exponential enrichment: RNA ligands to bacteriophage T4 DNA polymerase." Science **249**: 505-510.

Tung, C.-H., J. Qi, et al. (2015). "A Quick Responsive Fluorogenic pH Probe for Ovarian Tumor Imaging." Theranostics **5**(10): 1166-1174.

Uchida, M., S. Kang, et al. (2010). "The ferritin superfamily: Supramolecular templates for materials synthesis." Biochim Biophys Acta **8**: 834-845.

Van Ngoc, H., Y. Qian, et al. (2016). "PMMA-Etching-Free Transfer of Wafer-scale Chemical Vapor Deposition Two-dimensional Atomic Crystal by a Water Soluble Polyvinyl Alcohol Polymer Method." Scientific Reports **6**: 33096.

Vikash, S., K. P. Nitin, et al. (2016). "Platinum nanoparticles-single-walled carbon nanotubes hybrid based chemiresistive sensor array for myoglobin detection." Mater. Res. Express **3**(3): 035006.

Vinnakota, K., M. L. Kemp, et al. (2006). "Dynamics of Muscle Glycogenolysis Modeled with pH Time Course Computation and pH-Dependent Reaction Equilibria and Enzyme Kinetics." Biophys. J. **91**(4): 1264-1287.

Vishnubhotla, R., J. Ping, et al. (2017). "Scalable graphene aptasensors for drug quantification." AIP Advances **7**(11): 115111.

Wallace, P. R. (1947). "The Band Theory of Graphite." Physical Review **71**(9): 622-634.

Wang, C., X. Cui, et al. (2016). "A label-free and portable graphene FET aptasensor for children blood lead detection." Scientific Reports **6**: 21711.

Wang, C. H., C. Yang, et al. (2005). "Adsorption and Direct Electron Transfer from Hemoglobin into a Three-Dimensionally Ordered Macroporous Gold Film." Avd. Funct. Mater. **15**(8): 1267-1275.

Wang, D.-W., X.-H. Wang, et al. (2017). "MoTe2: A Promising Candidate for SF6 Decomposition Gas Sensors with High Sensitivity and Selectivity." iEEE Electron Dev. Lett. **9**(2): 292-295.

Wang, G., J. Liu, et al. (2017). "Selection and characterization of DNA aptamer against glucagon receptor by cell-SELEX." Sci. Rep. **7**(1): 7179.

Wang, H., A. Hsu, et al. (2010). "Graphene-Based Ambipolar RF Mixers." IEEE Electron Device Letters **31**(9): 906-908.

Wang, J., J. Chen, et al. (2009). "MicroRNAs in Plasma of Pancreatic Ductal Adenocarcinoma Patients as Novel Blood-Based Biomarkers of Disease." Cancer Prevention Research **2**(9): 807-813.

Wang, J., F. Ma, et al. (2017). "Graphene, hexagonal boron nitride, and their heterostructures: properties and applications." RSC Advances **7**(27): 16801-16822.

Wang, X., H. Feng, et al. (2013). "Controlled Synthesis of Highly Crystalline MoS2 Flakes by Chemical Vapor Deposition." Journal of the American Chemical Society **135**(14): 5304-5307.

Wang, Y., S. Springer, et al. (2015). "Detection of tumor-derived DNA in cerebrospinal fluid of patients with primary tumors of the brain and spinal cord." Proceedings of the National Academy of Sciences **112**(31): 9704-9709.

Wang, Y. y., Z. h. Ni, et al. (2008). "Raman Studies of Monolayer Graphene: The Substrate Effect." J. Phys. Chem. C **112**(29): 10637-10640.

Webb, B. A., M. Chimenti, et al. (2011). "Dysregulated pH: a perfect storm for cancer progression." Nat. Rev. Cancer **11**: 671.

Wei, G., F. Xu, et al. (2011). "Protein-Promoted Synthesis of Pt Nanoparticles on Carbon Nanotubes for Electrocatalytic Nanohybrids with Enhanced Glucose Sensing." J. Phys. Chem. C **115**(23): 11453-11460.

Weiss, J. N. (1997). "The Hill equation revisited: uses and misuses." FASEB Journal **11**(11): 835-841.

Wenbo, L., Z. Dongyuan, et al. (2011). "Self-assembly Synthesis of High-density Platinum Nanoparticles on Chemically Reduced Graphene Sheets." Chemistry Letters **40**(1): 104-105.

Wenrong, Y., R. K. R., et al. (2010). "Carbon Nanomaterials in Biosensors: Should You Use Nanotubes or Graphene?" Ange. Chemi. Internatl. Ed. **49**(12): 2114-2138.

Wiedman, G. R., Y. Zhao, et al. (2017). "An Aptamer-Based Biosensor for the Azole Class of Antifungal Drugs." mSphere **2**(4).

Wunder, S., Y. Lu, et al. (2011). "Catalytic Activity of Faceted Gold Nanoparticles Studied by a Model Reaction: Evidence for Substrate-Induced Surface Restructuring." ACS Catalysis **1**(8): 908-916.

Wunder, S., F. Polzer, et al. (2010). "Kinetic Analysis of Catalytic Reduction of 4-Nitrophenol by Metallic Nanoparticles Immobilized in Spherical Polyelectrolyte Brushes." J. Phys. Chem. C **114**(19): 8814-8820.

Xiaochen, D., S. Yumeng, et al. (2010). "Electrical Detection of DNA Hybridization with Single-Base Specificity Using Transistors Based on CVD-Grown Graphene Sheets." Adv. Mater. **22**(14): 1649-1653.

Xu, G., J. Abbott, et al. (2014). "Electrophoretic and field-effect graphene for all-electrical DNA array technology." Nat. Commun. **5**: 4866.

Xuesong, L., C. Luigi, et al. (2016). "Synthesis of Graphene Films on Copper Foils by Chemical Vapor Deposition." Advanced Materials **28**(29): 6247-6252.

Yabaluri, N. and F. Medzihradsky (1995). "Reversible modulation of opioid receptor binding in intact neural cells by endogenous guanosine triphosphate." Mol Pharmacol **48**(4): 690-695.

Yi-Hsien, L., Z. Xin-Quan, et al. (2012). "Synthesis of Large-Area MoS2 Atomic Layers with Chemical Vapor Deposition." Advanced Materials **24**(17): 2320-2325.

Yin, P. T., T.-H. Kim, et al. (2013). "Prospects for graphene-nanoparticle-based hybrid sensors." Phys. Chem. Chem. Phys. **15**(31): 12785-12799.

Yin, Z., Q. He, et al. (2012). "Real-time DNA detection using Pt nanoparticle-decorated reduced graphene oxide field-effect transistors." Nanoscale **4**(1): 293-297.

Yoon, J.-C., P. Thiyagarajan, et al. (2015). "A case study: effect of defects in CVD-grown graphene on graphene enhanced Raman spectroscopy." RSC Adv. **5**(77): 62772-62777.

Zajac, J. M. and B. P. Roques (1985). "Differences in binding properties of mu and delta opioid receptor subtypes from rat brain: kinetic analysis and effects of ions and nucleotides." J Neurochem **44**(5): 1605-1614.

Zhang, J., R. E. Campbell, et al. (2002). "Creating new fluorescent probes for cell biology." Nat. Rev. Mol. Cell Biol. **3**: 906.

Zhang, L., M. F. Miles, et al. (2003). "A model of molecular interactions on short oligonucleotide microarrays." Nat. Biotechnol. **21**: 818.

Zhang, X., S. Li, et al. (2011). "A new photoelectrochemical aptasensor for the detection of thrombin based on functionalized graphene and CdSe nanoparticles multilayers." Chem. Commun. **47**(17): 4929-4931.

Zhang, X., Y. Lin, et al. (2010). "Tumor pH and its measurement." J. Nucl. Med. **51**(8): 1167-1170.

Zhang, Y., H. Zhou, et al. (2001). "Stretching Single-Stranded DNA: Interplay of Electrostatic, Base-Pairing, and Base-Pair Stacking Interactions." Biophys. J. **81**(2): 1133-1143.

Zhao, G.-M., X. Qian, et al. (2003). "Comparison of [Dmt1] DALDA and DAMGO in Binding and G Protein Activation at μ, δ, and κ Opioid Receptors." J. Pharmacol. Exper. Therap. **307**(3): 947-954.

Zhao, X., Y. Li, et al. (2014). "Interactive Oxidation–Reduction Reaction for the in Situ Synthesis of Graphene–Phenol Formaldehyde Composites with Enhanced Properties." ACS Appl. Mater. Interf. **6**(6): 4254-4263.

Zhao, X., J. M. Perez-Aguilar, et al. (2014). "Characterization of a computationally designed water-soluble human mu-opioid receptor variant using available structural information." Anesthesiology **121**(4): 866-875.

Zheng, C., L. Huang, et al. (2015). "Fabrication of Ultrasensitive Field-Effect Transistor DNA Biosensors by a Directional Transfer Technique Based on CVD-Grown Graphene." ACS Applied Materials & Interfaces **7**(31): 16953-16959.

Zhihong, F., X. Yuan, et al. (2017). "Highly sensitive MoTe 2 chemical sensor with fast recovery rate through gate biasing." 2D Materials **4**(2): 025018.

Zhu, J., J. Wu, et al. (2016). "Thickness-dependent bandgap tunable molybdenum disulfide films for optoelectronics." RSC Adv. **6**(112): 110604-110609.

Zuber, A., M. Purdey, et al. (2016). "Detection of gold nanoparticles with different sizes using absorption and fluorescence based method." Sens. Actuat. B **227**: 117-127.

Zuccaro, L., J. Krieg, et al. (2015). "Tuning the isoelectric point of graphene by electrochemical functionalization." Sci Rep **5**(11794).

www.cancer.org/cancer/breast-cancer/about/how-common-is-breast-cancer.html.